

Auswirkungen einer langfristigen fettreichen Ernährung und anschließender Ernährungsumstellung auf Verhaltensmerkmale und Mikroglia im Mausmodell

Dissertation
zur Erlangung des akademischen Grades
Dr. rer. med.

an der Medizinischen Fakultät
der Universität Leipzig

eingereicht von: M. Sc. Judith Leyh

Geburtsdatum / Geburtsort: 11.03.1989 in Berlin

angefertigt an / im: der Medizinischen Fakultät der Universität Leipzig /
Institut für Anatomie

Betreuer: Prof. Dr. med. Ingo Bechmann

Beschluss über die Verleihung des Doktorgrades vom: 18.07.2023

Inhaltsverzeichnis

1. Einleitung.....	3
1.1 Mikroglia.....	3
1.1.1 Funktion der Mikroglia	3
1.1.2 Morphologie der Mikroglia	5
1.1.3 Darstellung der Mikroglia mit Iba1.....	7
1.2 Automatisierte Klassifizierung und Quantifizierung mikroglialer morphologischer Phänotypen	7
1.3 Verhaltensphänotypisierung von Mäusen	8
1.4 Morbus Alzheimer	9
1.5 Adipositas	10
1.5.1 Mikrogliale Reaktion auf fettreiche Ernährung und Adipositas	11
1.5.2 Adipositas als Risiko für M. Alzheimer	13
1.5.3 Mausmodelle für Adipositas	14
2. Fragestellungen	16
3. Publikationen.....	17
3.1 Classification of Microglial Morphological Phenotypes Using Machine Learning	17
3.2 Long-term diet-induced obesity does not lead to learning and memory impairment in adult mice	39
4. Zusammenfassung.....	81
5. Literaturverzeichnis.....	85
6. Darstellung des eigenen wissenschaftlichen Beitrags.....	97
7. Erklärung über die eigenständige Abfassung der Arbeit.....	99
8. Lebenslauf	100
9. Publikationsliste	101
10. Danksagung	102

1. Einleitung

1.1 Mikroglia

Im Gehirn arbeiten nicht nur etwa 100 Milliarden Neuronen, sondern auch Gliazellen, deren Gesamtzahl die der Neuronen um das Zehnfache übersteigt und die entscheidend zur Gehirnentwicklung und -funktion beitragen ¹. Zu diesen nicht-neuronalen Zellen gehören Makroglia (Astrozyten, Oligodendrozyten) sowie Mikroglia, wobei letztere etwa 7 % aller Gliazellen ausmachen und in jeder Hirnregion zu finden sind ². Erstmals visualisiert und detailliert beschrieben wurden mikrogliale Zellen vom spanischen Neurowissenschaftler Pío del Río-Hortega im Jahr 1919 ^{3,4}. Mikroglia sind einzigartige, langlebige Zellen im zentralen Nervensystem (ZNS) und gehören zusammen mit den nicht-parenchymalen Makrophagen zum Monozyten-Makrophagen-System ⁵⁻⁷. Sie stammen von Vorläuferzellen im Dottersack ab und wandern während der Embryogenese aus diesem in das Gehirn ein ^{7,8}. Dort bilden sie die erste Linie des Immun- und Verteidigungssystems, indem sie fortlaufend die Umgebung mit ihren mobilen Fortsätzen abtasten und schnell sowie effektiv Veränderungen und Störungen im ZNS, z. B. durch Infektionen, erkennen und entsprechend reagieren können ⁹. Mikrogliazellen übernehmen neben Abwehrfunktionen (Phagozytose, Zytotoxizität, Antigenpräsentation) wichtige Aufgaben zur Aufrechterhaltung der Homöostase im ZNS ¹⁰⁻¹². Sie sind an Gedächtnisfunktionen beteiligt, indem sie synaptische Verbindungen eliminieren können und bilden damit die Grundlage für Lernprozesse ¹³. Durch die Hochregulation von phagozytischen Funktionen, Änderung ihrer Morphologie und Expression einer Reihe von bioaktiven Effektormolekülen können Mikroglia spezifisch auf pathologische Veränderungen reagieren ¹⁴.

1.1.1 Funktion der Mikroglia

Mikroglia unter physiologischen Bedingungen

Mikroglia sind im gesamten Parenchym des ZNS lokalisiert, während die nicht-parenchymalen Makrophagen in den ZNS umgebenden Kompartimenten wie den Hirnhäuten, dem perivaskulären Raum sowie dem Plexus choroideus angesiedelt sind ^{15,16}. Die mikrogliale Zelldichte ist abhängig von der jeweiligen Region des ZNS ¹⁷. Unter physiologischen Bedingungen wird die Zellpopulation der Mikroglia im adulten humanen und murinen Gehirn nicht durch periphere Immunzellen ergänzt, sondern bleibt durch eine langsame Selbsterneuerung mittels Proliferation und Zelltod bestehen ¹⁸⁻²³. Mit Hilfe von Einzelzellansätzen wurde die mikrogliale Zellsignatur aufgezeigt. Die Analysen offenbarten erhebliche Unterschiede zwischen im ZNS ansässigen Makrophagen- und Mikrogliapopulationen. Zusätzlich weisen Mikroglia eine hirnrregions- und altersabhängige Heterogenität auf ²⁴⁻²⁷. Im gesunden Zustand zeichnet sich ihr Profil durch eine hohe Expression von homöostatischen Markern wie TMEM119 (Transmembrane protein 119), P2RY12 (Purinergic

receptor P2Y12), SIGLECH (Sialic-acid-binding immunoglobulin-like lectin H) und GPR34 (G protein-coupled receptor 34) aus ^{24,28-30}. Die Signatur der adulten Mikroglia ist geschlechtsspezifisch, wobei Mikroglia weiblicher Mäuse neuroprotektive, Mikroglia männlicher Mäuse hingegen eher inflammatorische Merkmale aufweisen ³¹. Mikroglia sorgen während der Entwicklung für das synaptische Pruning („Beschneiden, Stutzen“), überwachen im Erwachsenenalter die Funktion von Synapsen und eliminieren synaptische Verbindungen, wobei Letzteres die Markierung unerwünschter Synapsen durch Komplementfaktoren erfordert. Damit ermöglichen sie gedächtnisassoziierte Funktionen wie Lernen und synaptische Plastizität ³²⁻³⁸. Die Eliminierung von Synapsen ist jedoch auch ein Kennzeichen des Alterns und von neurodegenerativen Erkrankungen wie Morbus Alzheimer ³⁹⁻⁴¹. Darüber hinaus bieten Mikroglia ihren benachbarten Zellen trophische Unterstützung, indem sie neurotrophe Faktoren wie NGF (Nerve growth factor), BDNF (Brain-derived neurotrophic Factor), FGF (Fibroblast growth factor) sowie IGF (Insulin-like growth factor) absondern. Dadurch regulieren sie die neuronale Funktion und die Synapsenbildung ^{13,30,42}. NGF und BDNF können wiederum die Funktionen der Mikroglia beeinflussen ⁴³⁻⁴⁸.

Mikroglia unter pathologischen Bedingungen und bei Alterung

Mikrogliazellen spielen nicht nur während der Entwicklung und im Erwachsenenalter eine wesentliche Rolle, sondern haben auch unter pathologischen Bedingungen eine wichtige Bedeutung. Als immunkompetente Makrophagen des ZNS können sie mittels ihrer spezialisierten Oberflächenrezeptoren Veränderungen in der Umgebung erkennen und Krankheitserreger, apoptotische Zellen und Zelltrümmer, Toxine sowie Myelinreste entfernen ^{11,13,49-52}. Damit sorgen sie für das Abklingen von Entzündungen, was für die Reparatur des Hirnparenchyms notwendig ist ^{53,54}. Die mikrogliale Phagozytose von freiem Myelin, welches bei demyelinisierenden Erkrankungen und im Alter vermehrt vorliegt, ist Voraussetzung für die Remyelinisierung und die Gewebereparatur ^{53,55-57}. Mit zunehmendem Alter weisen Mikroglia eine verminderte phagozytäre Kapazität auf und akkumulieren übermäßige Mengen von Myelinresten, was zur Bildung von Cholesterinkristallen, zur Ruptur der phagolysosomalen Membran und zur Aktivierung von Inflammasomen führt ^{53,58-61}. Der Abbau von Beta-Amyloid (A β) durch Mikroglia nimmt ebenfalls mit fortschreitendem Alter ab und mikrogliale Zellen scheinen in Zusammenhang mit der Alzheimer-Krankheit beeinträchtigt oder sogar dysfunktional zu sein. Sie sind folglich nicht mehr in der Lage, pathologisches A β zu beseitigen ^{62,63}. Die komplexe Rolle der Mikroglia bei neurodegenerativen Erkrankungen wie der Alzheimer- und der Parkinson-Krankheit sowie der amyotrophen Lateralsklerose ist Gegenstand laufender umfangreicher Forschung ^{64,65}. Die Beteiligung dysfunktionaler Mikroglia wird Studien zufolge auch an neuropsychiatrischen Erkrankungen wie Schizophrenie, bipolaren Störungen, Autismus oder Depression diskutiert ^{66,67}.

Gealterte Mikroglia haben eine reduzierte Selbsterneuerungskapazität und können dysfunktional oder seneszent werden⁶⁸⁻⁷⁰. Seneszente Mikroglia weisen eine erhöhte Expression von p16^{Ink4a} auf und sind bei neurodegenerativen Pathologien häufig nachweisbar, während ihre Beseitigung eine Gliose und neuropathologische Prozesse verhindern⁷⁰. Darüber hinaus sind seneszente Mikroglia weniger effizient bei der Aufrechterhaltung der Eisenhomöostase und unterliegen einer oxidativen, eisenabhängigen, nicht-apoptischen Form des Zelltods, der Ferroptose⁷¹⁻⁷³. Die Geschwindigkeit der mikroglialen Motilität verlangsamt sich mit zunehmendem Alter erheblich, was zu einer verminderten Überwachung des umliegenden Gewebes, einem beeinträchtigten Kontakt mit Synapsen und einer schlechten Erholung nach Verletzungen führt^{60,74}. Des Weiteren können gealterte Mikroglia immunologisch "geprimt" werden, d. h., sie zeigen eine übertriebene Entzündungsreaktion auf Stimuli und weisen eine erhöhte Expression von proinflammatorischen Zytokinen sowie Antigenpräsentationsmolekülen auf⁷⁵.

Bei neurodegenerativen Erkrankungen verlieren Mikroglia ihr homöostatisches Profil und entwickeln eine krankheitsassoziierte Signatur, die durch eine erhöhte Expression von APOE (Apolipoprotein E), AXL (Tyrosine-protein kinase receptor UFO), CSF1 (Colony-stimulating factor 1), CLEC7a (C-type lectin domain family 7a), CD11c (ITGAX, Integrin subunit alpha X), CST7 (Cystatin F) und BHLHE40 (Basic helix-loop-helix family member E40) gekennzeichnet ist^{30,76-81}. Mikrogliale Reaktionen im Zusammenhang mit neurodegenerativen Erkrankungen können geschlechtsabhängig sein. In einem Alzheimer-Mausmodell beispielsweise entwickeln sich Mikroglia weiblicher Mäuse schneller in einen aktivierten Zustand als Mikroglia von männlichen Mäusen, in dem sie MHC (Major histocompatibility complex)-Klasse II und Alzheimer-Risikogene exprimieren⁸².

Neuroinflammation ist einerseits eine für die Geweberegeneration erforderliche, lebenswichtige und schützende Reaktion auf Verletzungen, andererseits beeinträchtigt sie in ihrer chronischen Form neuronale sowie gliale Funktionen und wird als ein Merkmal neurodegenerativer Erkrankungen angesehen⁸³⁻⁸⁶. Der Übergang mikroglialer Zellen von einem homöostatischen in einen krankheitsbedingten Zustand, die Erschöpfung gealterter Mikroglia und die damit verbundene gestörte Phagozytose könnten neben zusätzlichen Lebensstilfaktoren die Krankheitsentwicklung fördern⁸¹.

1.1.2 Morphologie der Mikroglia

Die Morphologie reifer Mikroglia ist im Zustand des Abtastens ihrer Mikroumgebung und unter physiologischen Bedingungen durch einen kleinen Zellkörper und lange, sehr feine, stark verzweigte Fortsätze gekennzeichnet. Dies ermöglicht den mikroglialen Zellen, das lokale Hirnparenchym auf Anzeichen von Infektionen, Traumata, Ischämie, Zell- und Gewebeschäden oder homöostatische

Störungen hin zu untersuchen^{9,87}. In diesem stationären Zustand wurden die stark verzweigten Mikroglia früher als "ruhend" beschrieben. Neuere Studien haben allerdings gezeigt, dass diese Zellen hochdynamisch sind und demnach vielmehr als "überwachende" Zellen bezeichnet werden sollten^{88,89}. Sogenannte DAMPs (Damage-Associated Molecular Patterns), bei denen es sich um Schad- oder Gefahrensignale in Form von freigesetzten Molekülen von Krankheitserregern und verletzten Zellen handelt, lösen mikrogliale Immunreaktionen aus. Diese führen zu einer Rückbildung der Fortsätze, einer Vergrößerung und Verdickung des Zellsomas sowie einer morphologischen Umwandlung von einer verzweigten zu einer aktivierten Morphologie und schließlich zu einer amöboiden Zellform^{90,91}. Amöboide Mikroglia sind durch vollständig eingezogene Fortsätze und ein geschwollenes Zellsoma gekennzeichnet⁹². Die schnelle morphologische Umwandlung der Mikroglia ermöglicht es diesen Zellen, zum Ort der Verletzung zu wandern oder schädliche Ablagerungen und Eindringlinge zu phagozytieren^{9,87,88}. Bemerkenswerterweise besitzen Mikroglia zwischen der verzweigten, aktivierten und amöboiden Zellform eine Vielzahl von morphologischen Übergangszuständen, die möglicherweise krankheitsspezifische funktionelle Zellzustände widerspiegeln. Ihre räumliche Organisation und genaue Rolle im geschädigten oder erkrankten Gehirn sind jedoch noch unklar⁹³⁻⁹⁵. In neueren Studien wurde eine weitere Morphologie von Mikroglia in Mäusen beschrieben, sogenannte stäbchenförmige Mikrogliazellen, von denen Franz Nissl bereits 1899 berichtete⁹⁶⁻¹⁰⁰. Stäbchenartige Mikroglia weisen keine planaren Fortsätze auf und zeigen eine verringerte Anzahl sekundärer Verzweigungen sowie eine Verengung des Zellsomas^{97,101}. Im Gehirn alter Menschen wurde mit der mikroglialen Dystrophie ein weiterer morphologischer Phänotyp beschrieben, der möglicherweise die mikrogliale Seneszenz widerspiegelt^{8,18,102,103}. Gehirne von Alzheimer-Patienten zeigen eine Prävalenz von Mikroglia mit einer dystrophen Morphologie im Hippocampus und mehreren kortikalen Bereichen^{69,104,105}. Kennzeichen dystropher/seneszenter Mikroglia sind lysosomale Einschlüsse, unregelmäßig geformte Zellkörper, verkürzte und scheinbar fragmentierte Zellfortsätze sowie eine verringerte phagozytotische und makropinozytotische Funktion. Dies führt zu verminderten neuroprotektiven Fähigkeiten^{56,69,106,107}. Die mikrogliale Pathologie bei der Alzheimer-Krankheit ist durch eine inhomogene Verteilung vom zytoplasmatischen Protein Iba1 charakterisiert. Iba1-positive Verbindungen unterhalb der lichtmikroskopischen Auflösung (0,182 µm) lassen die Mikrogliazellen fragmentiert erscheinen¹⁰⁸.

Morphologische Analysen liefern im Gegensatz zur Einzelzell-RNA-Sequenzierung, die die volle Bandbreite mikroglialer Funktionen und phänotypischer Vielfalt hervorhebt sowie diese Zellen umfassend auf molekularer Ebene charakterisiert, räumliche Informationen für ein vollständiges Verständnis der Hirnhomöostase und der Mechanismen der Krankheitsprogression. Physiologische und pathologische Bedingungen, regionale Verteilung, Speziespezifität, neurologische Erkrankungen

und Gewebeverletzungen im ZNS können die Heterogenität und damit die Morphologie der Mikroglia beeinflussen^{25–27,109–112}.

1.1.3 Darstellung der Mikroglia mit Iba1

Das Protein Iba1 (Ionized calcium binding adaptor molecule 1) ist mittlerweile der am häufigsten verwendete Marker für immunhistochemische Untersuchungen der Mikrogliazellen und wurde erstmals 1998 beschrieben^{113,114}. Dieses kalziumbindende Protein, welches an der Membrankräuselung, der Aktinvernetzung und der Phagozytose beteiligt ist, wird von allen mikroglialen Subpopulationen^{113,115–117} sowie peripheren Makrophagen exprimiert^{115,118–120}. Es markiert allerdings sowohl perivaskuläre als auch meningeale Makrophagen sowie ins Gehirn einwandernde myeloide Zellen wie Monozyten. Meningeale und perivaskuläre Iba1-positive Makrophagen können aufgrund ihrer Lage innerhalb von Hirnhäuten bzw. Gefäßen identifiziert werden. Infiltrierende mit Iba1 markierte Monozyten lassen sich aufgrund ihrer Zellform von den verzweigten Mikroglia unterscheiden, können allerdings im Extrazellulärraum des Gehirns auch ramifizieren¹²¹. Iba1 ist ein zytoplasmatischer Mikroglia-Marker, der sowohl den Zellkörper als auch die Zellfortsätze markiert und somit alle morphologischen Phänotypen der Mikrogliazellen zuverlässig anfärbt^{106,121}. Iba1 fördert die Proliferation sowie Migration von Immunzellen und erhöht die Expression von inflammatorischen Zytokinen sowie Chemokinen¹²². Trotz seiner häufigen Verwendung und Charakterisierung als mikroglialer Aktivierungsmarker sind noch nicht alle Funktionen von Iba1 gänzlich bekannt. Obgleich seine Beteiligung an der Phagozytose weitestgehend bestätigt ist, zeigten IRF8 (Interferon regulatory factor 8)-defiziente Mikroglia zwar signifikant verminderte Iba1-Level, aber keine Defizite bei der Phagozytose¹²³. IRF8 ist unter anderem ein entscheidender Transkriptionsfaktor für die Umwandlung der Mikroglia in deren reaktiven Phänotyp und damit ein wichtiger Regulator der mikroglialen Motilität^{124,125}.

1.2 Automatisierte Klassifizierung und Quantifizierung mikroglialer morphologischer Phänotypen

Es gibt zahlreiche Studien zur automatischen Erkennung und Quantifizierung von Iba1- oder CD11b-positiven Zellen im gesunden oder verletzten Gehirn von Nagern^{126–135}. Die automatisierte Klassifizierung mikroglialer morphologischer Phänotypen erfolgte bisher weitestgehend anhand ausgewählter quantitativer Parameter wie bspw. der konvexen Hüllfläche, dem Somaumfang, der Anzahl, Länge und Verzweigung der Fortsätze, dem Fortsatzvolumen, der Zirkularität, der Solidität, der fraktalen Dimension und der Lakunarität (Lückenhaftigkeit)^{128,131–133,135–137}. Da diese Ansätze jedoch aufgrund der naturgemäß begrenzten Anzahl von Kriterien und ihrer manuellen Auswahl

während eines einzelnen Experiments das Risiko eines Selektionsbias bergen, sind ausgefeiltere Konzepte erforderlich, um die bestmögliche Genauigkeit bei morphologischen Klassifizierungen zu erreichen. Im Bereich des maschinellen Lernens, einem Teilbereich der künstlichen Intelligenz, hat es in den letzten Jahren rasante Fortschritte gegeben. Das maschinelle Lernen kann automatisiert Wissen aus Erfahrung generieren, Lernalgorithmen trainieren, Zusammenhänge identifizieren und unbekannte Muster erkennen. Das aus Beispieldaten entwickelte komplexe Modell lässt sich anschließend auf einen neuen, potentiell unbekanntem Datensatz anwenden, um damit Vorhersagen treffen, Prozesse optimieren, komplexe Aufgaben lösen und Ziele erreichen zu können¹³⁸. Künstliche neuronale Netze gehören zu den Algorithmen des maschinellen Lernens und sind dem menschlichen Gehirn nachempfunden. Es sind somit abstrahierte Modelle von verbundenen künstlichen Neuronen. Weist ein künstliches neuronales Netzwerk besonders tiefe Netzstrukturen auf, wird von Deep Learning gesprochen¹³⁹. Ein künstliches neuronales Netzwerk setzt sich aus der Eingabeschicht (Input Layer), der verborgenen Schicht (Hidden Layer) und einer Ausgabeschicht (Output Layer) zusammen. Eine spezialisierte Form des künstlichen neuronalen Netzes ist das gefaltete neuronale Netz (Convolutional Neural Network (CNN)), welches besonders effizient mit großen Mengen an Eingabedaten arbeiten kann und damit für den Bereich der Bilderkennung besonders gut geeignet ist¹⁴⁰. Die Funktionsweise des CNN ist biologischen Vorgängen nachempfunden und sein Aufbau ähnelt dem visuellen Kortex des Gehirns. Die verborgene Schicht basiert bei CNNs auf einer Abfolge von Faltungs- und Poolingoperationen. Bei einer Faltung wird ein Filter zur Extraktion von Bildmerkmalen (Kernel) über die Daten gelegt und währenddessen eine Faltung gerechnet, was mit einer Multiplikation vergleichbar ist. Die Neuronen werden aktualisiert und die anschließende Einführung einer Poolingschicht sorgt für vereinfachte Ergebnisse, sodass ausschließlich wichtige Informationen erhalten bleiben. Dies führt zur Minimierung von bspw. zwei- oder dreidimensionalen Eingabedaten. Durch die kontinuierliche Fortführung dieses Verfahrens ergibt sich am Ende in der Ausgabeschicht ein Vektor, die verbundene Schicht (Fully Connected Layer). Dieser Vektor hat vor allem in der Klassifikation eine besondere Bedeutung, da er ebenso viele Neuronen wie Klassen enthält und die entsprechende Zuordnung über eine Wahrscheinlichkeit bewertet^{139,141,142}. Vorteile eines CNN gegenüber herkömmlichen nicht gefalteten neuronalen Netzen sind die wesentlich geringere Speicheranforderung und die stark verkürzte Trainingszeit. CNNs wurden bereits für Bilder von intrazellulären Aktin-Netzwerken¹⁴³, Mehrkanal-Einzelzellbilder¹⁴⁴ und zur Charakterisierung Iba1-immunopositiver Mikroglia beim Schädel-Hirn-Trauma verwendet¹³⁵.

1.3 Verhaltensphänotypisierung von Mäusen

Messbare Aspekte des Verhaltens bei Mäusen, die Symptome für psychiatrische und neurologische Erkrankungen darstellen können, betreffen die Sensorik, Motorik, Emotionalität sowie Lern- und

Gedächtnisfähigkeiten¹⁴⁵. Zur Untersuchung der allgemeinen sensorischen und motorischen Fähigkeiten können Reflexe wie der Vibrissen-, Ohrmuschel- und Krümmungsreflex verwendet werden¹⁴⁶. Für die Analyse des emotionalen Verhaltens wird bei Mäusen häufig ihre Handlungsweise in ungewohnten Situationen geprüft. In solchen Situationen stehen sie im Konflikt zwischen Neugier, Erkundung der bisher unbekanntem Umgebung und der Vermeidung möglicher Gefahren¹⁴⁵. Mit Open-Field- (offenes Gelände), Light-Dark-Box- (Helligkeit) oder Elevated-Plus-Maze-Tests (Höhe) werden verschiedene Aspekte der Ängstlichkeit untersucht¹⁴⁷. Die am häufigsten verwendeten Tests im Zusammenhang mit depressivem Verhalten sind der Forced-Swim- und der Tail-Suspension-Test. Hierbei werden Mäuse für wenige Minuten in eine scheinbar ausweglose Situation gebracht und gemessen, ob sie aktiv oder passiv versuchen, diese zu bewältigen. Passivität wird als depressives Verhalten gewertet, was die Motivation in Lern- und Gedächtnistests beeinflussen könnte^{145,148}. Für Demenzerkrankungen relevante Lern- und Gedächtnisfunktionen, wie Orientierungsvermögen und Arbeitsgedächtnis, werden z. B. in Labyrinthtests wie dem Y-Maze (Kurzzeitgedächtnis) oder dem Morris-Water-Maze (Lernen und Langzeitgedächtnis) gemessen¹⁴⁵.

1.4 Morbus Alzheimer

Morbus (M.) Alzheimer oder andere Demenzformen spielen laut WHO mit schätzungsweise 55 Millionen Erkrankten weltweit und 1,6 Millionen allein in Deutschland bereits jetzt eine herausragende Rolle¹⁴⁹. Das Bundesministerium für Familie, Senioren, Frauen und Jugend prognostiziert für Deutschland bis zum Jahr 2050 einen Anstieg auf 2,8 Millionen Betroffene¹⁵⁰. Der progrediente Verlauf einer Demenz stellt eine enorme Herausforderung für betroffene Personen, deren Familien und für das Gesundheitssystem dar. Die häufigste Ursache einer Demenz ist die irreversible Alzheimer-Erkrankung. Die Neurodegeneration beginnt im transentorhinalen Kortex und greift auf andere Hirnregionen über, was sich klinisch mit Gedächtnisverlust, kognitiven Beeinträchtigungen sowie Veränderungen in Persönlichkeit und Verhalten manifestiert. Die Krankheit beginnt jedoch bereits etwa 10 bis 20 Jahre vor dem Auftreten der Symptome und entwickelt sich zunächst asymptomatisch über ein langes präklinisches Stadium¹⁵¹. M. Alzheimer schreitet bei Patienten mit leichter kognitiver Beeinträchtigung allmählich zum Prodromalstadium (frühe Krankheitsphase) und setzt sich später zu einer leichten, mittelschweren und schließlich schweren Demenz fort, die sich in einer zunehmenden Unfähigkeit zur Durchführung alltäglicher Aktivitäten äußert¹⁵². Zwei wesentliche neuropathologische Kennzeichen der Alzheimerschen Krankheit im Gehirn sind extrazelluläre senile Plaques aus Ablagerungen von A β -Peptiden und intrazelluläre neurofibrilläre Tangles (NFTs), die durch hyperphosphoryliertes Tau-Protein gebildet werden¹⁵¹.

Ein wichtiger genetischer Risikofaktor für die Entwicklung einer spät beginnenden Alzheimer-Erkrankung ist das *APOE*-Gen, das für das Apolipoprotein E (*APOE*) kodiert. *APOE* ist ein Bestandteil von Plasmalipoproteinen in der Peripherie, in der Zerebrospinalflüssigkeit und in der interstitiellen Flüssigkeit des Parenchyms im ZNS¹⁵³. Astrozyten und Mikroglia sind die Hauptproduzenten von *APOE*, einem wichtigen Lipidtransportprotein, das eine zentrale Rolle bei der Entwicklung, Erhaltung und Reparatur des ZNS spielt^{154,155}. *APOE* erfüllt wichtige Funktionen beim Cholesterin-/Lipidtransport, der Immunmodulation, der Synapsenregeneration und es reguliert den Abbau von A β sowie mehrere wichtige Signalwege¹⁵³. Beim Menschen gibt es drei gängige Versionen des *APOE*-Gens: das $\epsilon 2$ -, das $\epsilon 3$ - und das $\epsilon 4$ -Allel. *APOE* $\epsilon 3$ ist das häufigste Allel (weltweite Prävalenz: $\approx 79\%$) und wird nicht mit dem Alzheimer-Risiko in Verbindung gebracht. Personen, die das $\epsilon 4$ -Allel ($\approx 14\%$) tragen, haben ein erhöhtes Alzheimer-Risiko, während das Tragen des $\epsilon 2$ -Allels ($\approx 7\%$) schützend wirkt^{156,157}. Einer bevölkerungsbasierten Kohortenstudie zufolge liegt die Lebenszeitinzidenz von leichter kognitiver Beeinträchtigung oder Demenz bei 30-35 % für *APOE4*-homozygote Personen, bei 20-25 % für *APOE4*-heterozygote Personen ($\epsilon 3/\epsilon 4$ und $\epsilon 2/\epsilon 4$) und bei 10-15 % für Nicht-*APOE4*-Träger ($\epsilon 3/\epsilon 3$, $\epsilon 3/\epsilon 2$ und $\epsilon 2/\epsilon 2$)^{153,158}. Verglichen mit Nicht-*APOE4*-Trägern wird bei heterozygoten *APOE4*-Trägern ein drei- bis fünffach und bei homozygoten *APOE4*-Trägern ein zehn- bis fünfzehnfach erhöhtes Erkrankungsrisiko für M. Alzheimer angenommen. Die Penetranz ist trotz dieses großen Effekts unvollständig, denn einige homozygote Träger der *APOE4*-Genvariante sind auch im sehr hohen Alter (> 95 Jahre) nicht in ihrer kognitiven Gesundheit beeinträchtigt. Die Wahrscheinlichkeit, dass homozygote Träger des $\epsilon 4$ -Allels vor dem 85. Lebensjahr eine Alzheimer-Erkrankung entwickeln, beträgt bei Männern 50 % und bei Frauen 60 %. Neben der Homozygotie für das Hochrisikogen *APOE4* müssen demzufolge zusätzliche Faktoren für die Entwicklung von M. Alzheimer eine Rolle spielen¹⁵⁹. Bei der Alzheimer-Pathologie wird *APOE* von Mikrogliazellen stark hochreguliert, was bei Tieren und Menschen mit mikroglialer Aktivierung, erhöhter Gefäßsteifigkeit, gesteigerter vaskulärer A β -Ablagerung und erhöhten systemischen Entzündungswerten verbunden ist^{77,151,160}. Kürzlich wurde ein großer Einfluss der westlichen Ernährung auf die Entwicklung von M. Alzheimer bei *APOE4*-Trägern gefunden¹⁶¹. Diese Personen weisen nicht nur ein erhöhtes Risiko für die Entwicklung von M. Alzheimer, sondern auch für das metabolische Syndrom, eine Kombination aus Diabetes, Bluthochdruck und Adipositas, auf^{156,161-163}.

1.5 Adipositas

Nichtübertragbare Krankheiten wie Herz-Kreislauf- und Atemwegserkrankungen, Krebs sowie Diabetes mellitus machen mehr als 70 % der vorzeitigen Todesfälle weltweit aus und sind damit die Hauptursache für Sterblichkeit und frühzeitige Erwerbsunfähigkeit¹⁶⁴. Adipositas ist ein Hauptrisikofaktor für nichtübertragbare Krankheiten und wird je nach Schweregrad der Erkrankung

und Komorbidität mit einer verringerten Lebenserwartung von schätzungsweise 5 bis 20 verlorenen Jahren assoziiert ¹⁶⁵⁻¹⁶⁸. Die Weltgesundheitsorganisation (WHO) definiert Adipositas als abnorme oder übermäßige Fettansammlung, die die Gesundheit beeinträchtigen kann und bei einem Body Mass Index (BMI) $\geq 30 \text{ kg/m}^2$ diagnostiziert wird. Sie ist durch ein chronisches Energieungleichgewicht gekennzeichnet, d. h., die Energieaufnahme übersteigt den Energieverbrauch und führt zu einer Gewichtszunahme ¹⁶⁹. Übergewicht bei einem BMI über 25 wird bereits mit einer höheren Sterblichkeit in Verbindung gebracht und stellt bereits einen Risikofaktor für verschiedene Krankheiten wie Stoffwechselkrankheiten (z. B. Typ-2-Diabetes und Fettleber), Herz-Kreislauf-Erkrankungen (Bluthochdruck, Herzinfarkt und Schlaganfall), Muskel-Skelett-Erkrankungen (Arthrose), M. Alzheimer, Depression und einige Krebsarten (z. B. Brust-, Eierstock-, Prostata-, Leber-, Nieren- und Dickdarmkrebs) dar. Zudem kann Adipositas zu einer verminderten Lebensqualität, Arbeitslosigkeit, geringerer Produktivität und sozialen Nachteilen führen ¹⁶⁸. Nach Angaben der WHO hat sich die weltweite Prävalenz von Adipositas seit 1975 fast verdreifacht und im Jahr 2019 starben etwa 1,5 Millionen Menschen an den direkten Folgen einer Diabeteserkrankung. Hochrechnungen zufolge werden im Jahr 2025 21 % der Frauen und 18 % der Männer weltweit fettleibig sein ¹⁶⁹⁻¹⁷². Umweltfaktoren, die das Ungleichgewicht zwischen Energiezufuhr und -verbrauch begünstigen, könnten Gründe für diese weltweite Epidemie sein. Studien deuten darauf hin, dass eine Zunahme der Menge und der Energiedichte von verzehrten Lebensmitteln, insbesondere die gesteigerte Fettaufnahme in der Nahrung, sowie eine Abnahme der körperlichen Aktivität für die Zunahme der Adipositas in der Bevölkerung verantwortlich sind ¹⁷³⁻¹⁷⁶. Zudem ergaben epidemiologische Studien eine positive Korrelation zwischen einem erhöhten Fettgehalt in der Nahrung und einer erhöhten Inzidenz von Adipositas ¹⁷⁷⁻¹⁸⁰. Darüber hinaus wurde in einer genomweiten Assoziationsstudie ein Einzelnukleotid-Polymorphismus im Gen für Fettmasse und Adipositas (FTO) identifiziert, welcher mit einem 1,67-fach erhöhten Risiko für Adipositas im Vergleich zu Personen ohne dieses Allel assoziiert ist ^{175,181}. Schließlich könnten auch soziale Faktoren eine entscheidende Rolle spielen. Das Risiko einer Person adipös zu werden, erhöht sich um 57 %, wenn ein Freund adipös ist oder um 37-40 %, wenn die Person ein adipöses Geschwisterkind oder einen adipösen Ehepartner hat ^{175,182}. Angesichts der hohen Zahlen sind große Bemühungen erforderlich, um Adipositas zu behandeln sowie die Prozesse, die dieser Krankheit zugrunde liegen, besser zu verstehen.

1.5.1 Mikrogliale Reaktion auf fettreiche Ernährung und Adipositas

Der funktionale und morphologische Phänotyp von Mikrogliazellen wird durch den westlichen Lebensstil und die ernährungsbedingte Adipositas ^{183,184} sowie durch das Mikrobiom, welches die für die Reifung der Mikroglia erforderlichen kurzkettigen Fettsäuren liefert ¹⁸⁵, beeinflusst. Mikroglia

reagieren auf eine unterschiedlich lang andauernde fettreiche Ernährung in Form einer hypothalamischen Mikrogliose, welche durch eine morphologische Aktivierung und Akkumulation mikroglialer Zellen sowie Entzündungssignale gekennzeichnet ist ^{186–188}. Bereits ein Tag einer fettreichen Ernährung induziert eine Entzündung im Hypothalamus, die sich in einer erhöhten Anzahl von Makrophagen/Mikroglia und einer erhöhten mRNA-Expression von proinflammatorischen Biomarkern äußert ¹⁸⁶. Kürzlich wurde jedoch gezeigt, dass Mikroglia ihren Zellpool ohne signifikante Substitution durch zirkulierende Monozyten nach ihrer Etablierung im frühen postnatalen Leben beibehalten können, selbst unter den Bedingungen einer chronischen fettreichen Ernährung ¹⁸⁹. Eine Studie an Nagetieren mit übermäßig fettreicher Ernährung zeigte, dass den mikroglialen Zellen im mediobasalen Hypothalamus für Mikroglia spezifische Marker wie TMEM119 und P2RY12 fehlen ¹⁸⁸. Eine fettreiche Diät induziert zudem die Expression vom mitochondrialen Uncoupling Protein 2 (UCP2) in hypothalamischen Mikrogliazellen. Dieses Protein spielt eine wichtige Rolle bei der Funktion von Mitochondrien wie z. B. der kontrollierten Erzeugung reaktiver Sauerstoffspezies (ROS). Einhergehend mit der Überexpression von Ucp2 treten auch funktionelle und morphologische Veränderungen in den Mitochondrien von Mikroglia des Nucleus arcuatus auf ¹⁹⁰. Neben dem Hypothalamus, der eine zentrale Rolle bei der Kontrolle von Appetit und Gewicht innerhalb des ZNS einnimmt, hat sich auch gezeigt, dass der Hippocampus, eine für die Gedächtniskonsolidierung und den Gedächtnisabruf entscheidende Hirnregion, sehr anfällig für die Auswirkungen von Adipositas oder schlechter Ernährung ist ^{191–194}. Eine frühe Belastung mit einer fettreichen Nahrung (P21-60) induziert entzündliche Veränderungen im Hippocampus von Mäusen, die eine Zunahme der Somafläche von Iba1-positiven Zellen zeigen ¹⁹⁵. Eine langfristige fettreiche Ernährung (> 20 Wochen) führt auch zu einer Aktivierung mikroglialer Zellen im Hippocampus, einer erhöhten Anzahl von Iba1-positiven Zellen in diesem Hirnbereich und zu kognitiven Defiziten ^{184,196–198}. Im Gegensatz dazu zeigte eine Untersuchung der langfristigen Auswirkungen einer fett- und kohlenhydratreichen Ernährung im Hippocampus von Ratten, dass der von Iba1-positiven Zellen bedeckte Flächenanteil nach einjährigem Verzehr reduziert war. Außerdem wurde bei dieser Diätform im Vergleich zu den Kontrollen keine mikrogliale Hypertrophie, die auf einen aktivierten Zustand hindeutet, festgestellt ¹⁹⁹.

Obwohl die Adipositas-induzierte mikrogliale Aktivierung bei Nagetieren, insbesondere im Hypothalamus und Hippocampus, gut belegt ist, gibt es nur wenige Literaturdaten, die die Folgen chronischer Adipositas im menschlichen Gehirn beschreiben. Baufeld und Kollegen (2016) identifizierten sowohl bei adipösen als auch bei nicht adipösen Personen ausschließlich im Hypothalamus eine mikrogliale Dystrophie/Zytorrhesis, die in ihrem Ausmaß signifikant mit dem BMI der untersuchten Personen korrelierte ¹⁸⁷. Das Auftreten von dystrophen Mikroglia im menschlichen Hypothalamus bei allen untersuchten Individuen könnte auch dem fortgeschrittenen Alter

geschuldet sein ^{187,200}. Da Mikroglia langlebige Immunzellen im Gehirn sind und ihre Population normalerweise nicht durch aus dem Blut stammende Monozyten ergänzt wird, zeigen sie mit zunehmendem Alter Anzeichen von Seneszenz ^{8,18,103}. Gehirne von Alzheimerpatienten zeigen eine Prävalenz von Mikroglia mit einer dystrophen/seneszenten Morphologie im Hippocampus und anderen kortikalen Bereichen ^{69,104,105}. Selbst im Hypothalamus von Zebrafischen mit ernährungsbedingter Fettleibigkeit wurde eine Zunahme dystropher Mikroglia sowie eine mikrogliale Aktivierung festgestellt ²⁰¹.

Die westliche Ernährung, welche durch eine hohe Zufuhr von gesättigten Fetten und Zucker sowie eine geringe Zufuhr von Ballaststoffen charakterisiert ist, trägt mit der chronischen Phagozytose des lipidreichen Myelins wahrscheinlich zur Bildung dieses dystrophen/seneszenten Phänotyps in Mikrogliazellen und zur Immundysfunktion im normalen gealterten Gehirn bei ^{56,187}.

1.5.2 Adipositas als Risiko für M. Alzheimer

Typ-2-Diabetes ^{202,203}, Bluthochdruck ²⁰⁴ und Adipositas ²⁰⁵⁻²⁰⁷ stellen bedeutende Risikofaktoren für neurodegenerative Erkrankungen wie vaskuläre Demenz und M. Alzheimer dar. Neben genetischen (nicht modifizierbaren) Risikofaktoren gibt es immer mehr Hinweise darauf, dass modifizierbare Umweltfaktoren wie unausgewogene Ernährung und Bewegungsmangel die Entwicklung von M. Alzheimer begünstigen, da sie Erkrankungen wie Diabetes, Adipositas, Hypercholesterinämie oder Bluthochdruck verursachen ¹⁵¹. Modifizierbare Faktoren machen fast 40 % aller Risikofaktoren für M. Alzheimer aus ^{208,209} und können den Verlauf des präklinischen Stadiums bei asymptomatischen Personen bis zur Lebensmitte stark beeinflussen ¹⁵¹.

Eine Vielzahl an Humandaten belegt einen klaren Zusammenhang zwischen ernährungsbedingter Adipositas und dem Auftreten von leichter kognitiver Beeinträchtigung und Demenz ²¹⁰⁻²¹³. Adipositas erhöht das Risiko eines kognitiven Abbaus und der Entwicklung von M. Alzheimer im Erwachsenenalter um ein Vielfaches ^{214,215}. Umfangreiche Metaanalysen beim Menschen bestätigen, dass Adipositas im mittleren Lebensalter (45-65 Jahre) im Gegensatz zu Adipositas im späten Lebensalter (> 65 Jahre) das Risiko für Demenz und M. Alzheimer signifikant erhöht ^{207,216-218}. Die Art der entwickelten Adipositas (metabolisch gesund oder ungesund) scheint eine wichtige Komponente für das Risiko einer Alzheimer-Erkrankung zu sein ²¹⁹.

Adipöse Personen haben ein verringertes Kortex- und Hippocampusvolumen, einen erhöhten Hirnatrophiegrad, eine geringere Leistung bei verschiedenen Gedächtnisaufgaben und Defizite bei exekutiven Funktionen ²²⁰⁻²²³. Eine Gewichtsreduzierung führt bei Menschen mit Adipositas zu verbesserten Aufmerksamkeits- und exekutiven Funktionsleistungen ^{224,225}. Eine wichtige und kritische Hirnregion für die Gedächtniskonsolidierung und den Gedächtnisabruf ist die

Hippocampusformation^{192,193}, eine Struktur, die nachweislich sehr anfällig für die Auswirkungen von Adipositas oder schlechter Ernährung ist^{191,194}. Mäuse, die mit einer fettreichen Diät gefüttert wurden, zeigten eine Gewichtszunahme, die mit erhöhten Aβ-Spiegeln und einer verringerten Neurogenese im Hippocampus sowie Defiziten bei kognitiven Aufgaben einherging^{184,226–231}. Mehrere Forschungsarbeiten haben gezeigt, dass Nagetiere, die über Monate hinweg übermäßig viel Fett und Zucker zu sich genommen haben, bei Gedächtnisaufgaben, die vom Hippocampus abhängen, beeinträchtigt sind^{232–235}. Ernährungsstudien mit erwachsenen Nagetieren und Menschen weisen darauf hin, dass bereits wenige Tage einer fettreichen Ernährung ausreichen, um die Funktion des Hippocampus zu beeinträchtigen^{191,236–240}. Zwei Publikationen berichteten kürzlich, dass eine fettreiche Nahrung für 7 bis 9 Tage bei männlichen Ratten im Jugendalter (P20 bis P29) mit einem gestörten sozialen Wiedererkennungsgedächtnis und einer beeinträchtigten präfrontalen Plastizität einhergeht, was mit einer Störung des vom Hippocampus abhängigen Gedächtnisses und der Plastizität verbunden ist^{241,242}. Mehrere Studien deuten darauf hin, dass eine fettreiche Ernährung in der Jugend (P21 bis P60) schädlichere Auswirkungen auf die vom Hippocampus abhängige Plastizität und das Gedächtnis hat als eine solche Diät im Erwachsenenalter (ab P61)^{243–245}. Es gibt auch immer mehr Hinweise dafür, dass eine veränderte Hippocampusfunktion bei Adipositas die adaptive Entscheidungsfindung in Bezug auf Essen und Ernährung beeinträchtigen kann²⁴⁶. Darüber hinaus deuten zahlreiche Daten darauf hin, dass eine fettreiche Nahrung Signalwege mit schädlichen Auswirkungen nicht nur im Hippocampus, sondern auch im Kortex aktivieren kann^{247–249}.

Bei ernährungsbedingter Adipositas führen neben anderen Faktoren erhöhte Konzentrationen zirkulierender Fettsäuren und ein Anstieg der sezernierten proinflammatorischen Zytokine zu einer fortschreitenden systemischen Entzündung, die eine mikrogliale Aktivierung, Endothelschäden und eine Störung der Blut-Hirn-Schranke auslöst. Diese Ereignisse führen schließlich zu einer Entzündung des Gehirns. Diese Neuroinflammation ist abhängig vom Grad der Adipositas, dem Alter, der Zusammensetzung der Ernährung und der untersuchten Struktur des ZNS. Sie führt letztlich allmählich zum Verlust von Synapsen und zum Absterben von Neuronen^{250,251}.

1.5.3 Mausmodelle für Adipositas

Erkenntnisse über Gesundheitsprobleme im Zusammenhang mit Adipositas werden hauptsächlich aus epidemiologischen Studien am Menschen gewonnen. Für die Untersuchung der molekularen Mechanismen bei der Entwicklung von Adipositas und den damit einhergehenden Problemen sind Tiermodelle jedoch unverzichtbar. Es stehen zwei Arten von Mausmodellen für Adipositas zur Verfügung: genetische und ernährungsbedingte Modelle. Das erste genetische Mausmodell für Adipositas war die Agouti-Maus. Sie weist unter anderem Adipositas im Erwachsenenalter, Typ-2-Diabetes und Hyperleptinämie auf²⁵². Eine weitere wichtige Entdeckung war die leptindefiziente

ob/ob-Maus im Jahr 1949²⁵³. Aufgrund der Schlüsselrolle von Leptin bei der Appetitkontrolle zeigen diese Mäuse eine unkontrollierte Nahrungsaufnahme, werden dadurch fettleibig und entwickeln einen Diabetes Typ 2. Ähnlich wie die *ob/ob*-Maus wird die *db/db*-Maus aufgrund einer Mutation im Leptinrezeptorgen adipös, die auch die Leptin-Signalübertragung im Hypothalamus beeinträchtigt²⁵². Neben den genetischen Mausmodellen werden auch Mausmodelle für ernährungsbedingte Adipositas verwendet, um den Einfluss von Veränderungen in der Ernährung auf den adipösen Phänotyp zu untersuchen²⁵². Es stehen zahlreiche Futtermittel mit unterschiedlichem Fett- oder Zuckergehalt zur Verfügung, um die Gegebenheiten beim Menschen zu imitieren. Da eine fettreiche Ernährung beim Menschen zu Adipositas führt und eine positive Korrelation zwischen der Fettaufnahme in der Nahrung und dem Auftreten von Fettleibigkeit besteht, konzentrieren sich die meisten Studien auf fettreiche Diäten^{151,173,174,178,180,231}. Außerdem zeigen eine Reihe der bisher erwähnten Studien eine spezifische Reaktion der Mikroglia auf eine fettreiche Ernährung, weshalb für diese Arbeit das Modell der ernährungsbedingten Adipositas und ein Futter mit 60 % Kalorien aus Fett verwendet wurde^{183,186–188,254}.

2. Fragestellungen

Adipositas ist weltweit zu einem der größten Gesundheitsprobleme geworden, das Millionen von Menschen betrifft und nicht nur zu verschiedenen Folgeerkrankungen wie Herz-Kreislauf-Erkrankungen, Diabetes und Krebs beiträgt, sondern auch ein Risiko für M. Alzheimer darstellt. In Tiermodellen zeigte sich, dass Mikrogliazellen, die neuroprotektiven und immunkompetenten Makrophagen des Gehirns, auf eine fettreiche Ernährung reagieren.

Die vorliegende Arbeit befasst sich zum einen mit der Entwicklung eines Klassifizierungsverfahrens mikroglialer morphologischer Phänotypen und zum anderen mit den Folgen einer langfristigen fettreichen Ernährung (24 Wochen) sowie einer anschließenden Ernährungsumstellung für das Verhalten und dem Einfluss der Nahrung auf die Morphologie mikroglialer Zellen in verschiedenen Hirnregionen von Mäusen. Aus der in der Einleitung dargestellten Studienlage ergaben sich folgende Fragestellungen:

1. Lassen sich verschiedene morphologische Phänotypen der Mikrogliazellen in einem effizienten, zeitsparenden und objektiven Verfahren klassifizieren und quantifizieren?
2. Welche Auswirkungen hat eine langfristige fettreiche Ernährung auf die allgemeine Gesundheit (äußeres Erscheinungsbild, sensorische und motorische Fähigkeiten) und verschiedene Verhaltensmerkmale (Kurz- und Langzeitgedächtnis, Lernen, Motivation) im Mausmodell?
3. Weisen Mäuse unter dem Einfluss einer fettreichen Ernährung über einen langen Zeitraum dystrophe Mikroglia auf?
4. Beeinflusst eine langfristige fettreiche Ernährung die Morphologie der murinen Mikroglia im Hypothalamus, Hippocampus und Kortex?
5. Sind etwaige Veränderungen nach einer Umstellung von einer fettreichen auf eine normale Ernährung reversibel?

Für die Bearbeitung der ersten Frage wurden männliche Wildtyp-C57BL/6J-, Leptinrezeptor-defiziente *db/db*- und *db/+*-Mäuse sowie ein Mausmodell des ischämischen Schlaganfalls verwendet. Zur Klärung der weiteren Fragestellungen wurden 8 Wochen alte männliche Wildtyp-C57BL/6J-Mäuse genutzt, denen für 24 Wochen eine normale Diät (11 kcal% Fett) oder eine fettreiche Diät (59 kcal% Fett) verabreicht wurde. Um die letzte Frage zu beantworten, wurden ebenfalls 8 Wochen alte männliche Wildtyp-C57BL/6J-Mäuse verwendet, die eine Ernährungsumstellung zurück auf normales Futter für 4 bzw. 12 Wochen nach unterschiedlich langen Phasen einer fettreichen Ernährung (4, 12 oder 24 Wochen) erhalten haben. Im Rahmen dieser Arbeit wurden immunhistochemische Färbungen und Immunfluoreszenzfärbungen, Verhaltenstests sowie RT-qPCR-Analysen durchgeführt.

3. Publikationen

3.1 Classification of Microglial Morphological Phenotypes Using Machine Learning

Judith Leyh^{1*}, Sabine Paeschke^{1*}, Bianca Mages¹, Dominik Michalski², Marcin Nowicki¹,
Ingo Bechmann¹, Karsten Winter¹

¹Institute of Anatomy, University of Leipzig, Leipzig, Germany

²Department of Neurology, University of Leipzig, Leipzig, Germany

* These authors have contributed equally to this work and share first authorship



Classification of Microglial Morphological Phenotypes Using Machine Learning

Judith Leyh^{1†}, Sabine Paeschke^{1†}, Bianca Mages¹, Dominik Michalski², Marcin Nowicki¹, Ingo Bechmann¹ and Karsten Winter^{1*}

¹Institute of Anatomy, University of Leipzig, Leipzig, Germany, ²Department of Neurology, University of Leipzig, Leipzig, Germany

OPEN ACCESS

Edited by:

Renato Socodato,
Universidade do Porto, Portugal

Reviewed by:

Stefano Fumagalli,
Istituto di Ricerche Farmacologiche
Mario Negri (IRCCS), Italy
Stefano Garofalo,
Sapienza University of Rome, Italy

*Correspondence:

Karsten Winter
kwinter@rz.uni-leipzig.de

[†]These authors have contributed
equally to this work and share first
authorship

Specialty section:

This article was submitted to
Non-Neuronal Cells,
a section of the journal
Frontiers in Cellular Neuroscience

Received: 28 April 2021

Accepted: 07 June 2021

Published: 29 June 2021

Citation:

Leyh J, Paeschke S, Mages B,
Michalski D, Nowicki M, Bechmann I
and Winter K (2021) Classification of
Microglial Morphological Phenotypes
Using Machine Learning.
Front. Cell. Neurosci. 15:701673.
doi: 10.3389/fncel.2021.701673

Microglia are the brain's immunocompetent macrophages with a unique feature that allows surveillance of the surrounding microenvironment and subsequent reactions to tissue damage, infection, or homeostatic perturbations. Thereby, microglia's striking morphological plasticity is one of their prominent characteristics and the categorization of microglial cell function based on morphology is well established. Frequently, automated classification of microglial morphological phenotypes is performed by using quantitative parameters. As this process is typically limited to a few and especially manually chosen criteria, a relevant selection bias may compromise the resulting classifications. In our study, we describe a novel microglial classification method by morphological evaluation using a convolutional neuronal network on the basis of manually selected cells in addition to classical morphological parameters. We focused on four microglial morphologies, ramified, rod-like, activated and amoeboid microglia within the murine hippocampus and cortex. The developed method for the classification was confirmed in a mouse model of ischemic stroke which is already known to result in microglial activation within affected brain regions. In conclusion, our classification of microglial morphological phenotypes using machine learning can serve as a time-saving and objective method for post-mortem characterization of microglial changes in healthy and disease mouse models, and might also represent a useful tool for human brain autopsy samples.

Keywords: microglia, morphology, machine learning, stroke, hippocampus, cortex

INTRODUCTION

Microglia serve as the central nervous system (CNS)'s immunocompetent macrophages, which crucially contribute to homeostasis, plasticity, and learning by taking up pathogens, apoptotic cells, synaptic remnants, toxins, and myelin debris (Bradl and Lassmann, 2010; Sofroniew and Vinters, 2010; Goldmann and Prinz, 2013; Parkhurst et al., 2013; Nutma et al., 2020; Traiffort, 2020). Our current understanding is that these highly specialized brain-resident immune cells constantly monitor the brain's microenvironment enabling them to detect

Abbreviations: CNS, central nervous system; CNN, convolutional neural network; DAPI, 4',6-diamidino-2-phenylindole; PFA, paraformaldehyde; PBS, phosphate buffered saline; SRI, Schoenen ramification index; BBB, blood-brain barrier; DAMP, damage-associated molecular patterns; NF-L, neurofilament light; MAP2, microtubule-associated-protein-2; Coll IV, collagen IV; Iba1, ionized calcium-binding adapter molecule 1; ROI, Regions of interest; CLAHE, contrast limited adaptive histogram equalization; MCA, middle cerebral artery.

and respond to tissue damage, infection, or homeostatic perturbations (Nimmerjahn et al., 2005). In the scanning state and under physiological conditions, microglial morphology is characterized by a small cell body and very fine, highly ramified processes, which allow these cells to screen their local brain parenchyma for signs of pathogens or cellular damage. In this steady-state condition, highly branched microglia were previously described as “resting”, but recent studies revealed them to be greatly dynamic and microglia should rather be described as “surveilling” cells (Tremblay et al., 2011; Nimmerjahn, 2012). So-called damage-associated molecular patterns (DAMPs), which are warning mechanisms in the form of secreted or released molecules from pathogens and injured cells, initiate microglial immune responses triggering process retraction, cell soma size increase and thickening, and morphological transformation from a ramified toward an activated morphology and finally to an amoeboid cell form (Huang et al., 2015; Colonna and Butovsky, 2017). Amoeboid microglia are characterized by completely retracted processes and a swollen cell soma (Doorn et al., 2014). The rapid morphological transformation of microglia enables these cells to migrate to the site of injury or to phagocytose harmful debris and invaders (Davalos et al., 2005; Nimmerjahn et al., 2005; Tremblay et al., 2011). Remarkably, between the two classes at the ends of the microglial morphology spectrum, of either ramified or amoeboid cell shape, microglia exhibit a variety of morphological transition states, which may reflect disease-specific functional cell states, but their spatial organization and precise role in the damaged or diseased brain is still unclear (Stence et al., 2001; Fumagalli et al., 2013; Salamanca et al., 2019). Recent studies described a fourth morphology of microglia in mice, so-called rod-like microglial cells, which were already reported by Franz Nissl in 1899 (Nissl, 1899; Ziebell et al., 2012; Rojas et al., 2014; Bachstetter et al., 2017; Holloway et al., 2019). Rod-like microglia do not exhibit planar processes and show a decreased number of secondary branches as well as narrowing of cell and soma (Ziebell et al., 2012; Taylor et al., 2014).

Microglial cells are active participants in various pathological conditions such as neurodegenerative disorders, traumatic brain injury, and stroke. Ischemic stroke due to obstruction of blood vessels is a leading cause of morbidity and mortality worldwide and not only affects neurons, but also the glial network including microglia (del Zoppo, 2009; Deb et al., 2010; Campbell et al., 2019). Along with cerebral ischemia a rapid deramification of microglial cells occurs, while severe ischemic stroke is accompanied by an intense microgliosis followed by the production of both neuroprotective and detrimental mediators (Masuda et al., 2011; Zhao et al., 2017; Zhang, 2019). Activated microglia may be involved in the progression of the ischemic lesion, but their precise function during ischemia evolution remains unclear. While single-cell RNA sequencing recently highlighted the whole range of microglial functions reflected by their phenotypic diversity and comprehensively characterized these cells at the molecular level, it does not provide the spatial information for a full understanding of brain homeostasis and disease progression mechanisms. Physiological and pathological conditions including regional distribution, species specificity,

neurological disorders, and CNS tissue injuries can affect microglial heterogeneity (Grabert et al., 2016; Galatro et al., 2017; Gosselin et al., 2017; Soreq et al., 2017; Sousa et al., 2017; Heindl et al., 2018; Masuda et al., 2020).

There are numerous studies on automated detection and quantification of Iba1 or CD11b-positive cells in healthy or injured brain in rodents (Kozłowski and Weimer, 2012; Valous et al., 2013; Kongsui et al., 2014; Rey-Villamizar et al., 2014; Johnson and Walker, 2015; Zanier et al., 2015; Ding et al., 2017; Morrison et al., 2017; York et al., 2018; Kyriazis, 2019). Automated classification of microglial morphological phenotypes is performed by using quantitative parameters like *convex hull area*, *soma perimeter*, *process length*, *number of processes*, *process branching process volume*, *circularity*, *solidity*, *fractal dimension* and, *lacunarity* (Kongsui et al., 2014; Zanier et al., 2015; Fernández-Arjona et al., 2017, 2019; Morrison et al., 2017; York et al., 2018; Kyriazis, 2019). However, as these approaches hold the risk for a selection bias due to the naturally limited number of criteria and their manual selection during a single experiment, more elaborated concepts are needed to achieve the best possible accuracy in morphological classifications.

We here describe a novel classification method for analysis of microglial phenotypes by morphological evaluation using machine learning within the murine hippocampus and cortex with a focus on four microglial morphologies (ramified, rod-like, activated, amoeboid). In addition to classical morphological parameters, we used a convolutional neuronal network (CNN) for the classification of microglial phenotypes on the basis of manually selected cells. CNNs were already used for phenotype classification, for example for images of intracellular actin networks (Oei et al., 2019), multichannel single-cell images (Dürr and Sick, 2016), and Iba1-immunopositive microglia (Kyriazis, 2019). To confirm a reliable classification of different microglial morphological phenotypes, we finally applied our developed method in a mouse model of ischemic stroke which is already known to result in microglial activation.

MATERIALS AND METHODS

Animals and Diets

The experiments were performed using male wild-type C57BL/6J mice ($n = 36$) and leptin receptor-deficient *db/db* ($n = 37$) and *Lepr^{db/+}* (*db/+*) ($n = 36$) mice as well as male wild-type C57BL/6J mice which underwent 24 h of transient focal cerebral ischemia ($n = 6$) by occlusion of the middle cerebral artery (MCA) as described in Mages et al. (2021). In our study, the filament occluding the MCA was retracted after 1 h of ischemia, and reperfusion was allowed until animals were sacrificed 24 h after ischemia induction. All animals were kept in the local animal facility under standard conditions: 12 h dark/light cycle, group-housed with free access to water and food. We performed this study in accordance with the guidelines of the Animal Experimental Committee following the German Animal Welfare Act as well as the European guidelines (Directive 2010/63/EU) concerning the protection of laboratory animals. The study was carried out in compliance with the ARRIVE guidelines. All

experimental procedures and protocols were authorized by the local ethics committee of the state of Saxony (Landesdirektion Sachsen, Leipzig, approval nos. TVV 65/15, TVV 02/17, and TVV 41/17).

Tissue Preparation

Mice were anesthetized with isoflurane (Baxter GmbH, Unterschleißheim, Germany) and transcardially perfused with ice-cold phosphate buffered saline (PBS, pH 7.4) and 4% paraformaldehyde (PFA) in 0.2 M PBS. Brains were carefully removed from the skull and post-fixed for 24 h in 4% PFA in 0.2 M PBS. Perfused and fixed brains of male wild-type C57BL/6J mice as well as *db/db* and *db/+* mice were sliced into 20 μm thick coronal or horizontal floating sections using a vibratome (Leica VT 1200, Leica Biosystems, Wetzlar, Germany) before their storage in PBS, containing 0.2% sodium azide, until further processing. Tissue preparation of C57BL/6J mice subjected to experimental cerebral ischemia was performed as described in Mages et al. (2021).

Staining

For staining with rabbit anti-Iba1 (Synaptic Systems, Göttingen, Germany) to label microglia, floating brain sections were mounted onto microscopic slides followed by three wash steps with 0.3% Triton X-100 in 0.02M PBS for 10 min each time. Then, slices were incubated for 20 min in PBS containing 1.5% hydrogen peroxide at room temperature in order to quench the endogenous peroxidase activity. Afterward, brain sections were washed again three times with 0.3% Triton X-100 in PBS for 10 min each time, and slices were subsequently pretreated with 0.5% sodium borohydride in PBS for 30 min to reduce background staining. Thereafter, slices were thoroughly rinsed in 0.3% Triton X-100 in PBS and were blocked for 1 h in PBS blocking buffer containing 5% normal goat serum and 0.3% Triton X-100 at room temperature. Then, brain sections were incubated with the primary antibody Iba1 (1:500) diluted in PBS with 5% of normal goat serum. Incubation was done overnight at 4°C. The next day, brain sections were rinsed three times with 0.3% Triton X-100 in PBS and incubated with the biotinylated goat anti-rabbit IgG secondary antibody (1:100; Vector Laboratories, Burlingame, CA, USA) for 1 h at room temperature. After three wash steps with 0.3% Triton X-100 in PBS for 10 min each time, slices were incubated with VECTASTAIN Elite ABC HRP Kit (Vector Laboratories, Burlingame, CA, USA) for 30 min at room temperature. Thereafter, sections were washed with PBS and 0.05 M Tris, stained 5 min with the Vector SG HRP substrate (Vector Laboratories, Burlingame, CA, USA) producing a blue-gray reaction product, and were thoroughly rinsed in Tris and distilled water. Finally, brain sections were dried and covered with Entellan (Toluene; Merck KGaA, Darmstadt, Germany) and coverslips. For negative controls, the omission of primary antibodies, under otherwise identical conditions, resulted in the absence of any labeling (data not shown). A critical step for successful cell detection and classification was the reduction of background staining, which we overcame by performing a pre-treatment with 0.5% sodium borohydride in PBS. Prior

to this, other microglia-specific markers (P2RY12, TMEM119) were also explored but did not result in desired image quality regarding the resolution of cell processes and subsequent cell detection.

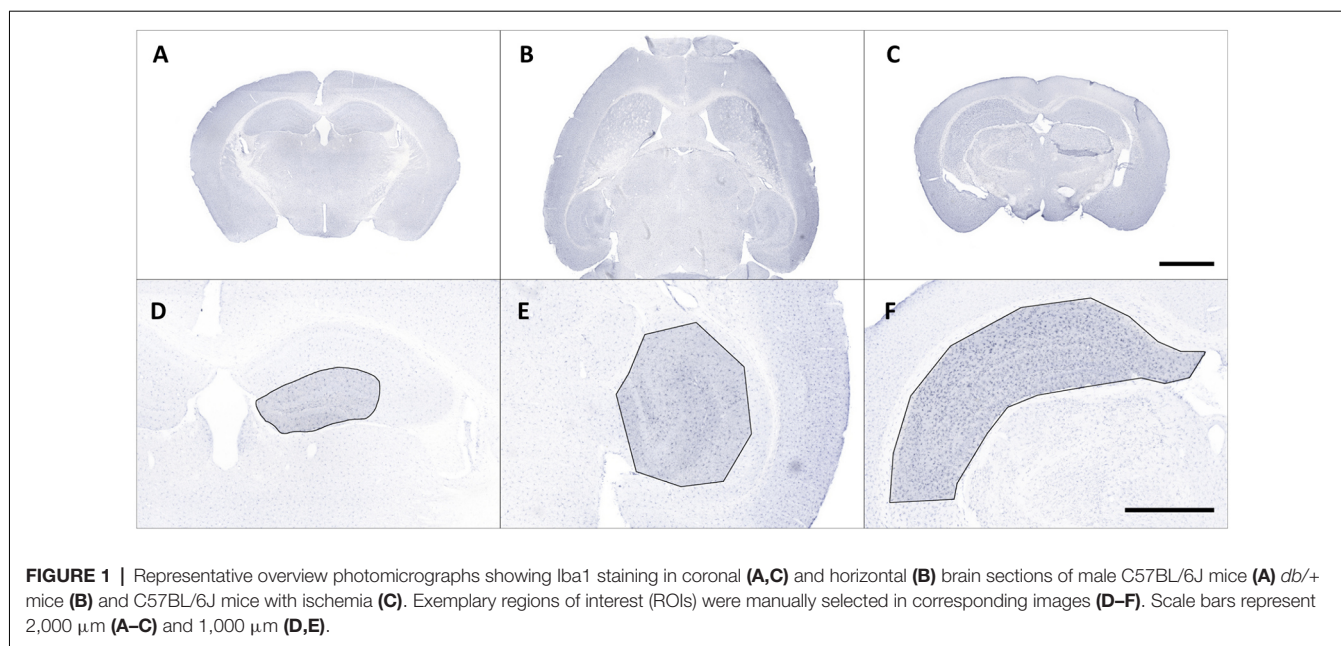
To define the ischemic area, which was subsequently used for microglial classification, the proteins MAP2 (microtubule-associated protein 2), NF-L (neurofilaments-light chain), and collagen IV (Coll IV) were used as ischemia-sensitive markers (Popp et al., 2009; Härtig et al., 2016, 2017; Mages et al., 2018) in animals which underwent transient MCA occlusion. In general, fluorescence staining was performed as described in Mages et al. (2018), whereas following antibodies and dilutions were used (Mages et al., 2018). Primary antibodies: Rabbit-anti-neurofilament L (1:200, Synaptic Systems, Göttingen, Germany); mouse-anti-MAP2 (clone HM-2; 1:500, Sigma, Taufkirchen, Germany); rabbit-anti-collagen IV (1:100, Merck Millipore, MD, USA). Secondary antibodies: AlexaFluor488-donkey-anti-mouse IgG, AlexaFluor586-donkey-anti-rabbit IgG, AlexaFluor647-donkey-anti-goat IgG, each 1:250, each Thermo Fisher, Waltham, MA, USA. Brain sections were scanned with an Axio Scan.Z1 slide scanner (Carl Zeiss Microscopy GmbH, Jena, Germany) and files were exported using the NetScope Viewer Pro Software (Net-Base Software GmbH, Freiburg i. Br., Germany). In line with earlier reports (Härtig et al., 2017; Mages et al., 2018) the ischemic area was characterized by a loss of MAP2 (**Supplementary Figure 1A**), whereas the NF-L- and Coll IV-related immunofluorescence intensities increased in these regions compared to the non-ischemic contralateral hemisphere (**Supplementary Figures 1B,C**). **Supplementary Figure 1D** shows the selected neocortical and hippocampal areas within the ipsilateral and contralateral hemispheres.

Image Acquisition and Processing

Iba1-stained brain sections were fully digitalized using a digital slide scanner (Pannoramic Scan II, 3D HISTECH Ltd., Budapest, Hungary) at 40 \times magnification and automatically stitched (**Figures 1A–C**). The scanner software (Pannoramic Scanner, version 1.23, 3D HISTECH Ltd., Budapest, Hungary) was operated in extended focus mode (eight levels with 1 μm axial distance) to combine images from several adjacent focal planes into one image with maximum depth of sharpness. This procedure enables coherent imaging of freely aligned cell processes within a shallow tissue volume instead of producing images with interrupted processes from a single focal plane.

Regions of interest (ROIs) were manually selected and corresponding images were exported from slide scanner data sets (Case Viewer, version 2.3, 3D HISTECH Ltd., Budapest, Hungary) with a pixel dimension of 0.122 μm (**Figures 1D–F**). Exported images were converted to grayscale and submitted to contrast limited adaptive histogram equalization (CLAHE; Heckbert, 1994) using Icy (version 2.0.3¹, de Chaumont et al., 2012). The resulting images were imported in Mathematica (version 11.2, Wolfram Research, Inc., Champaign, IL, USA), grayscale colors were inverted and tissue area was computed. Soma detection was performed in two steps. First, a series

¹<http://icy.bioimageanalysis.org>



of top hat (Gonzalez and Woods, 2016) and Gaussian filter operations was applied to the inverted images to suppress cell processes and enhance cell somata. Processed grayscale images were then binarized using Otsu's (cluster variance maximization) thresholding method (Otsu, 1979). The binarized images were cleared of smaller segments that did not match somata (artifacts or clumped cell processes) by using an empirically determined size threshold of 1,500 pixels and the remaining somata were reconstructed by morphological closing (Gonzalez and Woods, 2016) within a 7.5-pixel radius.

Process detection was performed in a hybrid fashion to preserve connections between cell somata and cell processes. In the first step, the inverted images were submitted to local adaptive segmentation (5-pixel radius) to detect all stained cells. In the second step, all processes within the inverted images were amplified by using a ridge-detecting image filter ("RidgeFilter", $\sigma = 5$) to enhance local structural coherence and the resulting images were also submitted to local adaptive segmentation (5-pixel radius). Both segmented images were subsequently added and merged with the respective somata image. Since some processes may appear separated from somata due to the imaging procedure, an additional reconstruction step was performed by connecting endpoints of processes to the respective somata within a 50-pixel radius. In the last step all images were cleared of processes without connections to any somata and all cells intersected by the border of the image area were removed.

The resulting images contained many connected cells which had to be separated from each other. Centroid coordinates of all somata were calculated and used as seed pixels for a parallel flood fill operation. Starting from the seeds this operation fills all pixels of the detected cells with a unique label, either to the cell borders or to the filling fronts of connected cells. After this step, all individual cells of an image were uniquely labeled. All final cell

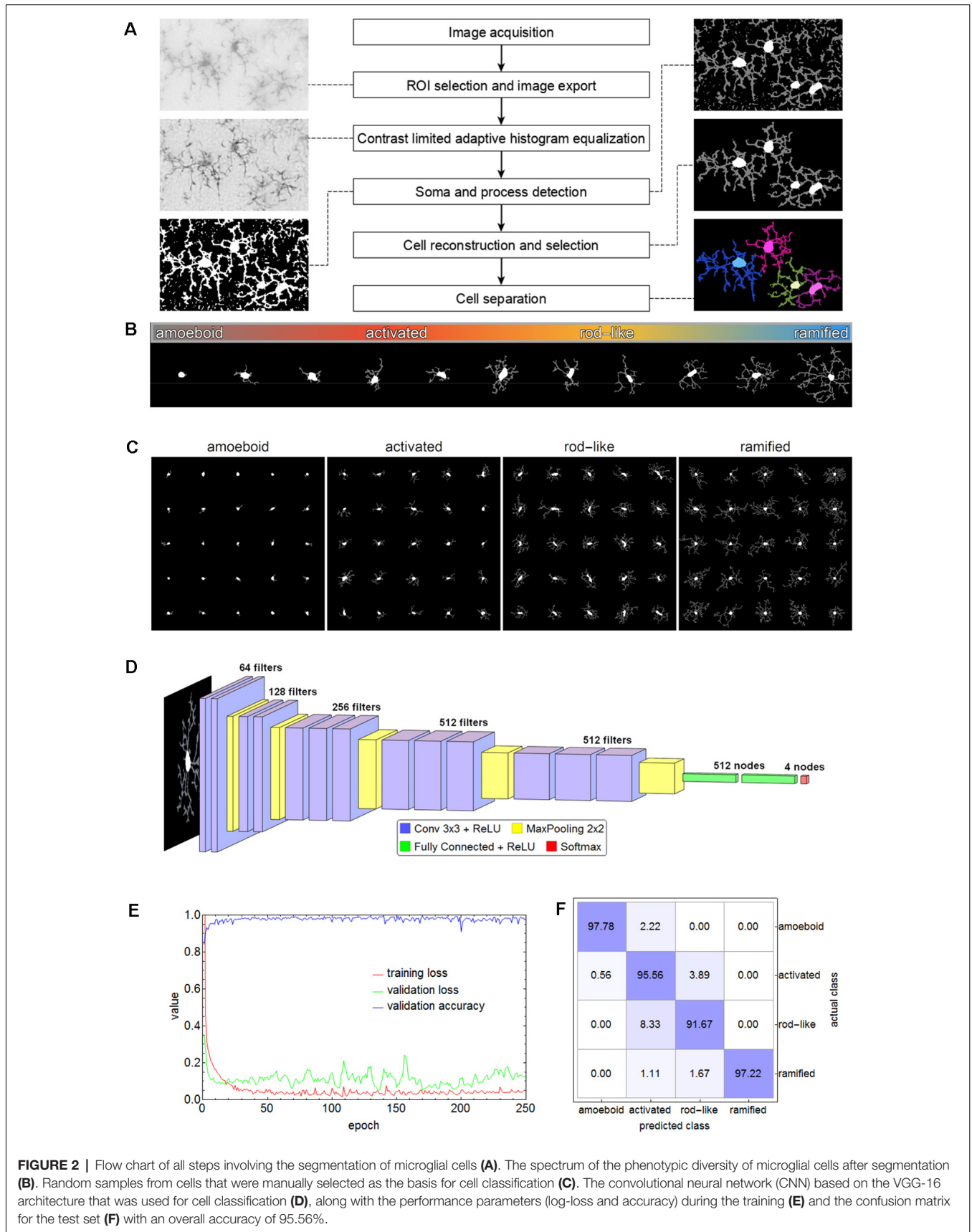
segmentations along with results of relevant intermediate steps were examined to ensure proper processing and detection.

For subsequent cell classification, the cells of all images were cropped from the original image area and exported as binary masks containing their complete shape (as well as in separate shapes for soma and processes, respectively) along with their original grayscale representation from the equalized grayscale images. Additionally, for visual inspection cell shapes were submitted to morphological thinning to compute the medial axes, the so-called skeleton, of all processes which was combined with the respective somata. **Figure 2A** shows a schematic overview of the applied methods.

Cell Classification of Microglial Cells in Wild-Type C57BL/6J, *db/db*, and *db/+* Mice

Microglial cells express a considerable phenotypic diversity (**Figure 2B**). After thorough inspection of all exported cell images, 1,000 cells per class were manually selected as the basis for cell classification and the corresponding cell images were cropped and rescaled to 128×128 pixels (**Figure 2C**). Images were split into training (70%), validation (15%), and test (15%) set. The test set was only used for the evaluation of the trained network. Images belonging to the training set were submitted to image augmentation (Shorten and Khoshgoftaar, 2019) to expand data diversity and make the classification more robust (Gao et al., 2017). A series of rotation and reflection image transforms was applied to each image, and after image augmentation, 3-fold cross-validation was performed.

A convolutional neural network (CNN) based on the VGG-16 architecture was selected for cell classification (Simonyan and Zisserman, 2015). The network consisted of 13 convolutional layers, five max-pooling layers, two fully connected layers, and a softmax layer of four nodes for the classes amoeboid, activated, rod-like, and ramified (**Figure 2D**). ReLU was



used as an activation function and after each activation, BatchNormalization was applied for regularization. “Adam” optimizer was used for optimization, the initial learning rate was set to 0.001, batch size was set to 64, and a dropout rate of 0.5 was applied to constrain the fully connected layers and to reduce overfitting. The CNN was trained on an off-the-shelf NVIDIA GeForce GTX 1080 with 8 GB GPU memory for 250 epochs, training time took about 5.8 h. The performance parameters (log-loss and accuracy) are shown in **Figure 2E**. Averaged values of the last 50 training rounds were as follows: training loss 0.0497, validation loss 0.2887, and validation accuracy 0.9726. Subsequently, the test set was submitted to the trained CNN. Overall accuracy was 95.56%, the confusion matrix is shown in **Figure 2F**. While 97.78% of the amoeboid and 97.22% of the ramified cells were correctly classified, the percentage dropped to 95.56% and 91.67% for activated and rod-like cells, respectively. The matrix shows that 3.89% of activated cells were misclassified as rod-like cells, while 8.33% were misclassified vice-versa, indicating the more prominent phenotype overlap between these two classes.

Classification and Quantitative Analysis of Microglial Cells in Ischemia Affected Regions

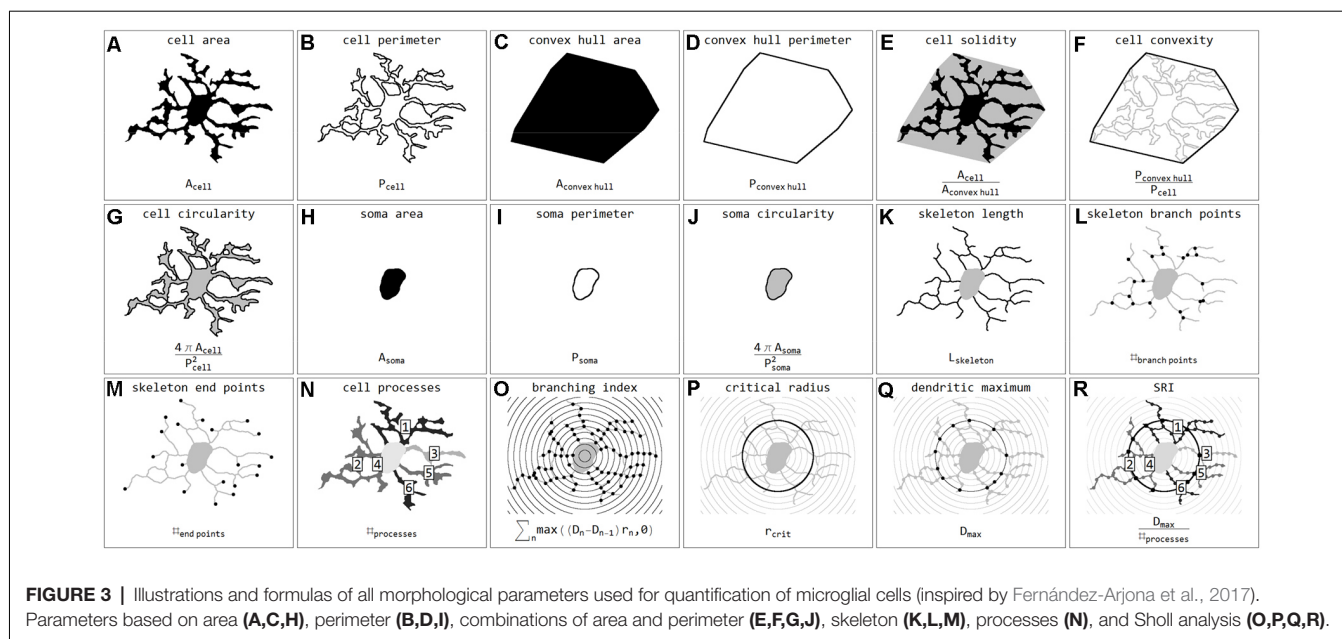
Stroke sections were submitted to the same image acquisition and cell extraction procedure mentioned above. Brain sections and ROIs were selected based on the ischemia-induced decrease of MAP2-related and increase of NFL- and Coll IV-related immunofluorescence intensities within cortical and hippocampal regions (**Supplementary Figure 1**). These regions were mirrored to the contralateral control hemisphere, thus capturing four ROIs per animal (Mages et al., 2021). The selection was performed and verified by experienced investigators. Exported cell masks (soma white, processes gray) were also scaled to 128×128 pixels and submitted to classification. In total 15,786 single cells from 24 stroke ROIs were classified. Individual cells were coded as labeled regions within the original image area. Labels were subsequently color-coded according to classification results. Final images were used for visualization and classification verification. Subsequently, cells were submitted to quantification and all calculated parameters are presented in **Figure 3**. Parameters include *areas* (μm^2) and *perimeters* (μm) of whole cells (**Figures 3A,B**), their *convex hulls* (the smallest convex set of pixels that encloses a cell; **Figures 3C,D**) and their somata (**Figures 3H,I**); *cell solidity* (the degree to which the area of a cell fills the area of its *convex hull*; **Figure 3E**) and *convexity* (the ratio of a cell's *convex hull perimeter* to the cell's actual perimeter; **Figure 3F**); *circularity* of cells and somata (the roundness, where 1 equals a perfect circle and values smaller than 1 indicate shapes that increasingly deviate from the shape of a circle; **Figures 3G,J**); *length* (μm) as well as the number of *branch* and *endpoints* (n) of the skeletonized *processes* (**Figures 3K–M**); and the number of *cell processes* (n ; **Figure 3N**). The number of cell processes was calculated by subtracting the dilated soma (3-pixel dilation) from the respective cell and counting the number of all isolated processes. Furthermore,

all cells were submitted to Sholl analysis (Sholl, 1953) and the cell's *branching index* (Garcia-Segura and Perez-Marquez, 2014; a measure to distinguish between cells of different ramification types; **Figure 3O**), *critical radius* (μm ; the radius with the maximum number of process crossings; **Figure 3P**), *dendritic maximum* (n ; the number of process crossings at the critical radius; **Figure 3Q**) and the *Schoenen ramification index* (SRI, Schoenen, 1982; a measure of the branching of a cell; **Figure 3R**) were calculated. Additionally, for whole images the segmented image area (%), representing the ratio of segmented pixels within the total image area (before cell detection), and the cell density (cells per mm^2) were computed.

NC (Nearest Centroid) Classification

To demonstrate the differences between CNN classification and conventional parameter-based classification, we applied an NC classification method to various parameter combinations (**Figure 4**). Morphological parameters of all manually selected cells that were used for the training of the CNN were calculated.

Initially—and to demonstrate the approach—we considered combinations consisting of only two parameters. **Figure 4** shows results for the following combinations: *cell area/skeleton length* (A–E), *cell perimeter/soma perimeter* (F–J), *cell circularity/soma circularity* (K–O). In the first step, scatter plots for parameter values of all manually selected cells were generated using a color scheme for the indication of the four classes (**Figures 4A,F,K**; ramified microglia: blue, rod-like microglia: orange, activated microglia: red, amoeboid microglia: gray). Class centroids (median values of the current parameters) were calculated for all four classes and added to the scatter plots (black dots). Subsequently, scatter plots were also generated for the same parameter combinations of all CNN classified cells (**Figures 4B,G,L**). NC classification was performed for all already CNN classified cells by calculating the distance of their parameter combinations to all four class centroids and assigning the class of the nearest centroid. The resulting NC clusters were also presented as scatter plots (**Figures 4D,I,N**) along with the four class centroids. Classification results were compared (**Figures 4E,J,O**) and the degree of conformity of both methods was determined by calculating the portion of consistently (sum of diagonal matrix values) to all (sum of all matrix values) classified cells. Additionally, the generated matrices were tested regarding their symmetry using the exact symmetry test for paired contingency tables (“nominalSymmetryTest”) from the “rcompanion” package for R. Classification differences between the two methods were also illustrated using an exemplary image section with the color coding from CNN classification (**Figure 4R**) and color codings from NC classifications (**Figures 4C,H,M**). Correlation analysis was performed for all two-parameter combinations using Spearman's rank correlation coefficient to characterize the distribution of parameter points of all CNN classified cells. Scatter plots and respective regression lines of selected parameter combinations are shown in **Supplementary Figure 3**. The degree of conformity (upper triangular matrix) and correlation coefficients (lower triangular matrix) of all two-parameter



combinations are shown in **Figure 5A**. Another correlation analysis was performed to investigate a potential association between the degree of conformity (CNN vs. NC classification) and the absolute correlation coefficient, or more precisely to answer the question whether NC classification accuracy can be correlated to the distribution of parameter points within the parameter space (**Figure 5B**).

Similar analyses (NC classification, degree of conformity, and test for matrix symmetry) were performed for combinations ranging from three up to 17 parameters (131,054 combinations in total; **Figure 5C**). The parameter SRI was omitted from all analyses since it could not be calculated for each cell (division by zero for cells with no processes). Furthermore, a number of parameter combinations, as well as singular parameters whose presence resulted in highest degrees of conformity, were identified.

Statistical Analysis

Statistical analysis was performed with IBM SPSS Statistics (version 22, IBM Corp., Armonk, NY, USA) and R (version 3.6.1; R Core Team²). Images were separated into analysis groups. For each group, the number of cells per class were counted, relative class proportions were calculated and respective stacked bar charts were generated. Group comparisons of class percentages were performed using the non-parametric density equality test (Li et al., 2009; “ndpdnq”, 999 bootstrap replications) from the “np” package for R. Descriptive statistics were calculated and box plots were generated. Data were tested for normal distribution using the Shapiro-Wilk Test (segmented image area and cell density) and Kolmogorov-Smirnov Test (grouped parameter data), and group comparisons were performed using Kruskal Wallis and Mann-Whitney-U tests. To adjust the *p*-value

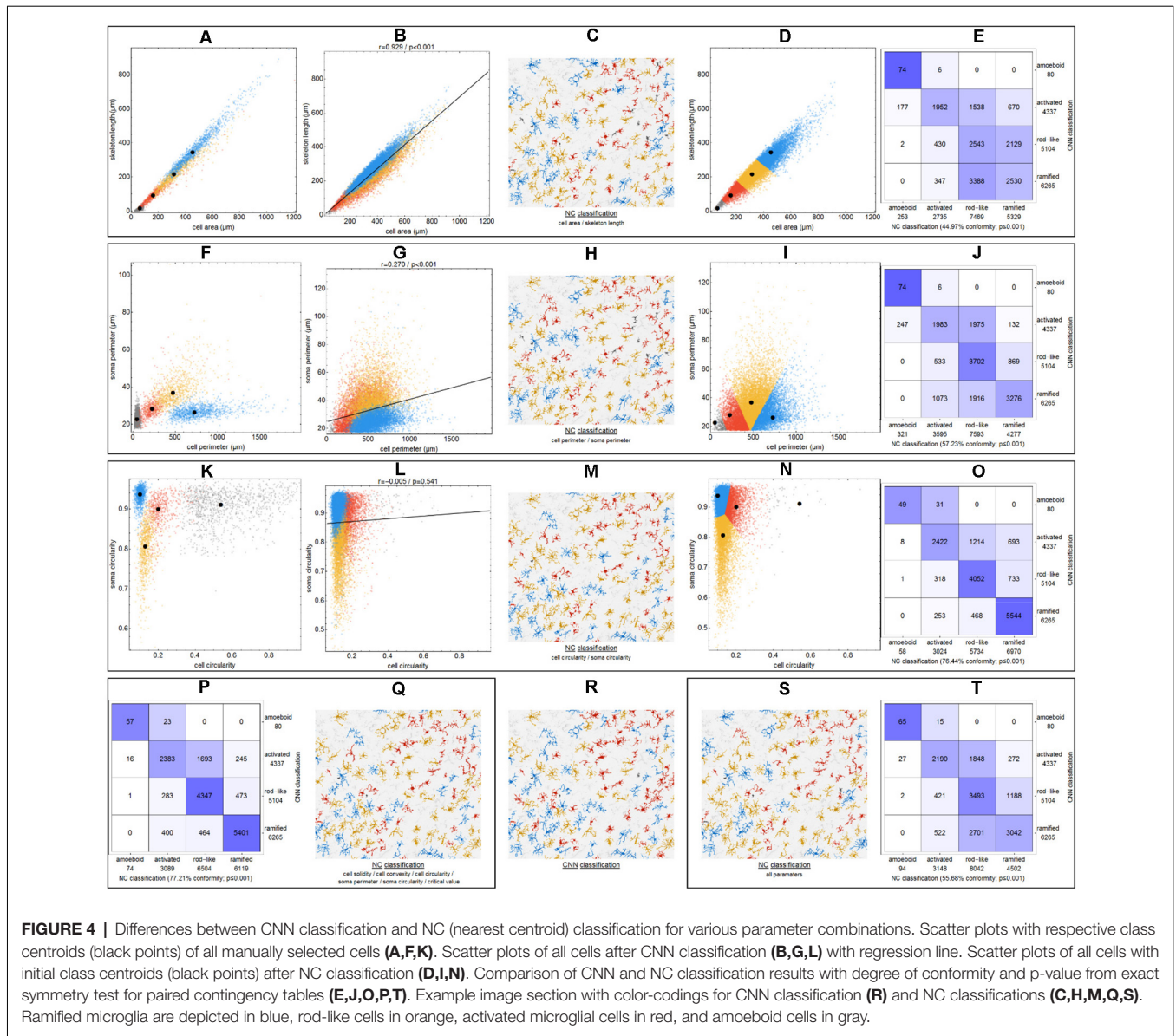
for multiple comparisons, *post hoc* Bonferroni correction was performed. The number of analyzed animals is indicated as “*n*” in the figure legend. Data are presented as the median and interquartile range (IQR). Significance was set as follows: $p < 0.05$ *, $p < 0.01$ **, $p < 0.001$ ***, $p < 0.0001$ ****.

RESULTS

Class Percentage of Microglial Morphological Phenotypes

We trained the CNN with microglial cells of different mouse strains, male wild-type C57BL/6J mice, *db/db*, and *db/+* mice, to obtain and cover a wide variety of microglial morphological phenotypes. Subsequently, we examined our microglial classification method in a mouse model of experimental cerebral ischemia (24 h after ischemia induction) known for microglial activation in the area of ischemic tissue damage (Härtig et al., 2017; Zhang, 2019). **Figure 6** shows representative images of Iba1 staining within the control neocortex (**Figure 6A**), ischemic neocortex (**Figure 6B**), control hippocampus (**Figure 6C**), and ischemic hippocampus (**Figure 6D**). Ischemia-affected regions in the hippocampus and neocortex presented more activated and rod-like Iba1-positive cells (which most probably correspond to microglia rather than infiltrated cells such as monocytes/macrophages at day one after experimental stroke; Jian et al., 2019; Rajan et al., 2019; Han et al., 2020) compared to the relevant brain areas within the contralateral hemisphere (**Figures 6A'–D'**). Classification of microglial morphological phenotypes using our neural network machine learning method confirmed the qualitative analysis of microglial phenotypes by morphological evaluation after staining with Iba1. Total class percentages within the ischemic neocortex and hippocampus were significantly different compared to the control neocortex or hippocampus (**Figure 7A**; control

²<http://www.R-project.org>

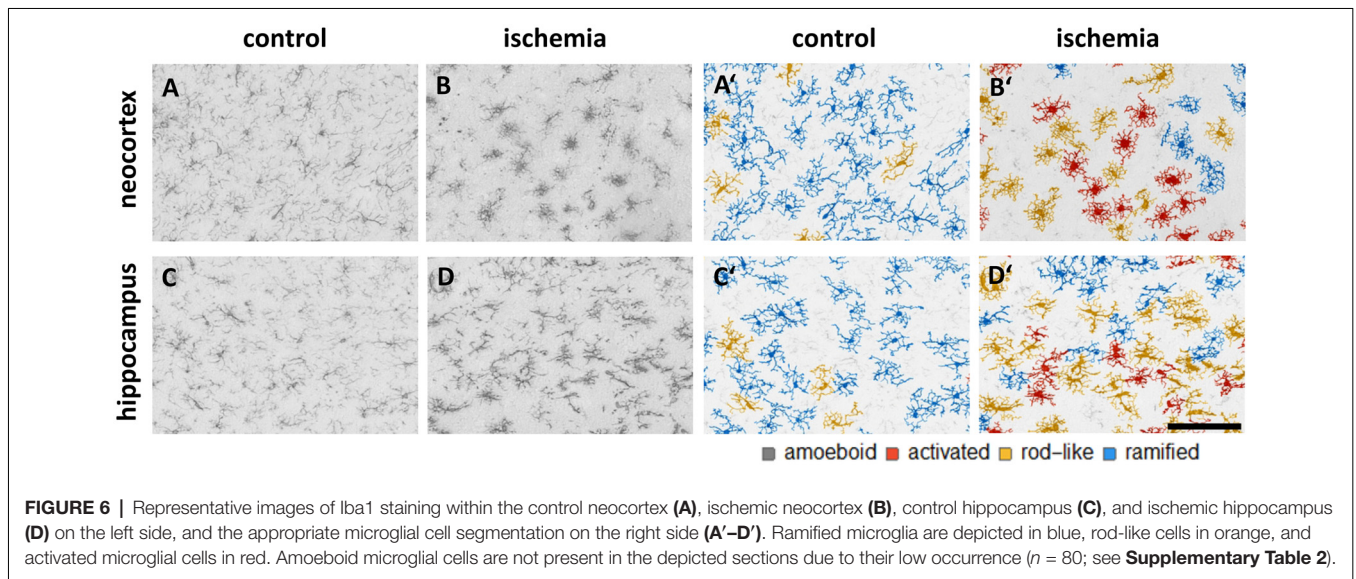
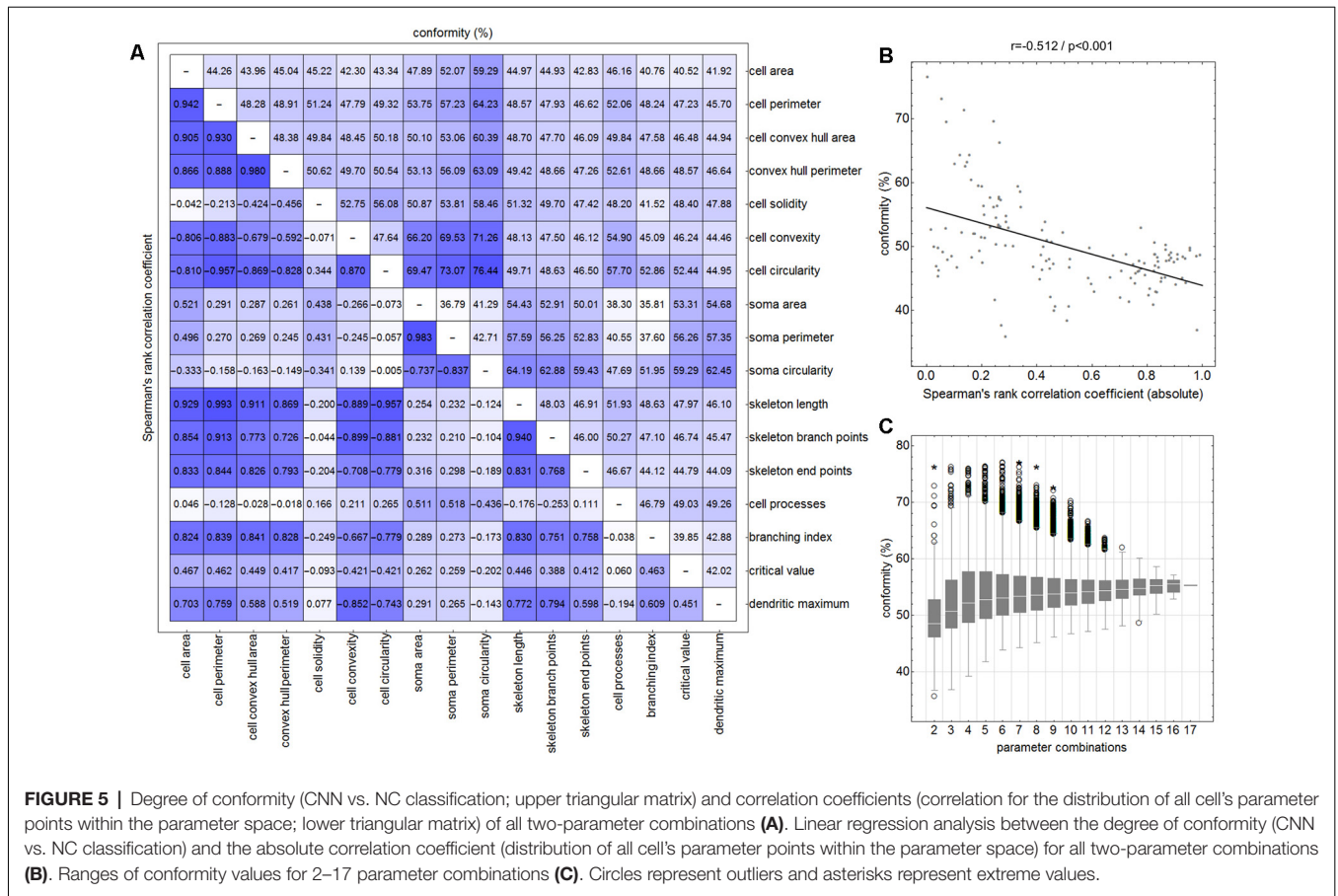


neocortex vs. ischemic neocortex *, control hippocampus vs. ischemic hippocampus *). Individual class percentages in the neocortex revealed significant increases of activated and rod-like microglial cells and a simultaneous decrease of ramified microglia within the ischemia-affected hemisphere compared to the control hemisphere. Amoeboid Iba1-positive cells did not differ between the ischemic and non-ischemic neocortex, as they were virtually absent (Figure 7B; activated microglia control vs. ischemic neocortex **, rod-like microglia control vs. ischemic neocortex **, ramified microglia control vs. ischemic **). Similarly, the percentages of activated and rod-like microglial cells within the ischemic hippocampus were significantly enhanced, whereas the amount of ramified microglia was lower compared to the control hippocampal area (Figure 7C; activated microglia control vs. ischemic hippocampus **, rod-like microglia control vs. ischemic hippocampus *, ramified

microglia control vs. ischemic hippocampus **). In contrast to the neocortex, we also detected a significant increase in amoeboid microglial cells within the ischemic hippocampus compared to the control hippocampus (Figure 7C, amoeboid microglia control vs. ischemic hippocampus *). The segmented image area did not reveal any differences within the neocortical and hippocampal regions (Supplementary Figure 2). Normalized microglial cell density (cells per mm²) was significantly enhanced within the ischemic hippocampus compared to the control hippocampal area and a slight trend was observed in the neocortex (Figure 7D).

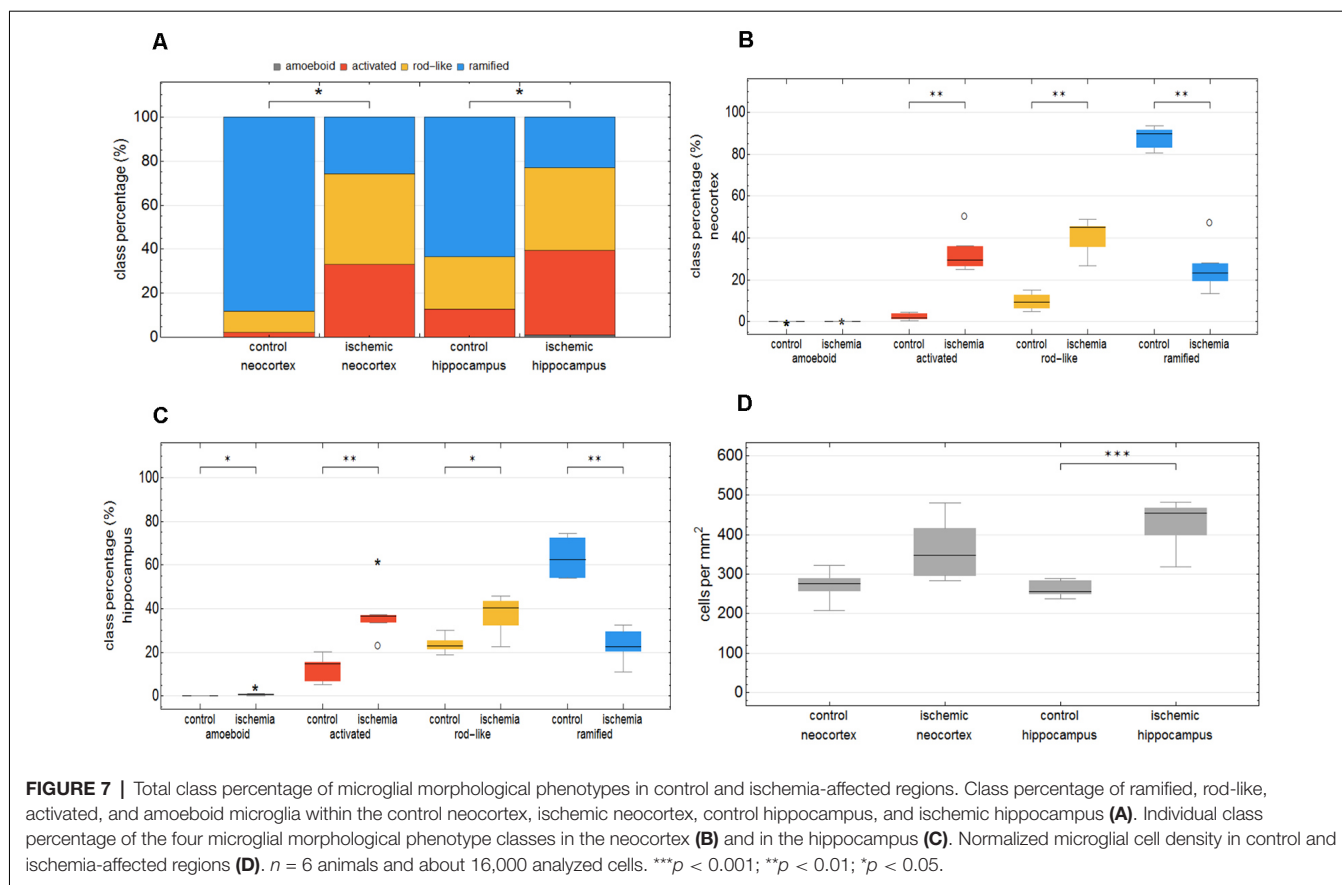
Quantification of Morphological Parameters

Eighteen morphological parameters (*cell area, cell perimeter, convex hull area, convex hull perimeter, cell solidity, cell convexity,*



cell circularity, soma area, soma perimeter, soma circularity, skeleton length, skeleton branch points and endpoints, cell processes, branching index, critical radius, dendritic maximum, SRI) were measured for each detected Iba1-positive cell ($n = 15786$).

Firstly, we looked at all Iba1-positive cells within control and ischemic areas of the neocortex and hippocampus (**Supplementary Table 1**). Microglia within control and ischemic-affected hemispheres differed significantly regarding the morphological parameters. We found lower values for cell



area, perimeter, convex hull area, soma area, skeleton length, branch and endpoints, branching index, dendritic maximum as well as SRI within the control and ischemic hippocampus compared to control and ischemic neocortex. Microglial cell convexity and circularity were greater in the hippocampus than in the neocortex. Control and ischemic areas in both brain regions showed differences in the morphology of microglial cells. Microglia had larger cell perimeters, convex hull areas, soma circularities, skeleton lengths, skeleton branch and endpoints, higher branching indices, and SRI within the control hemisphere compared to the ischemic-affected hemisphere (Supplementary Table 1).

To test whether our neural network machine learning method adequately classifies microglial cells into the four morphological phenotype groups, we merged all microglial cells of each morphological class within both control and ischemic brain regions. Supplementary Table 2 summarizes the 18 selected morphological parameters for amoeboid, activated, rod-like and ramified microglial cells. As expected, amoeboid microglia were characterized by the smallest values for cell area, perimeter, convex hull area, soma area, skeleton length, branch and endpoints, branching index, and SRI compared to the other morphological phenotypes. Amoeboid microglia's cell solidity and circularity showed high values. The classified activated phenotype of microglia had a smaller cell area, perimeter, and convex hull area and also fewer skeleton branches and endpoints

than ramified and rod-like microglial cells. Ramified microglia typically exhibit small somata and fine ramifications, which was demonstrated by a small soma area, big cell convex hull area, long skeleton length as well as a high branching index. Rod-like microglial cells projected similar skeleton lengths, branch and endpoints than ramified microglia, but exhibited a higher cell and soma area (Supplementary Table 2). All four morphological classes of microglia were significantly different among each other regarding the selected parameters.

After Fernández-Arjona et al. (2019) had recently categorized activated microglial cells according to their morphometric parameters, we further looked at the activated morphotype in more detail (Fernández-Arjona et al., 2019). Ischemic-affected regions displayed more activated microglial cells, which showed smaller cell and soma area, cell perimeter, convex hull area, skeleton length, and branching index in the control area compared to the ischemic-affected corresponding area (Figures 8A–E, Supplementary Tables 3, 4). Activated microglial cells within the ischemic neocortex showed larger cell and soma areas, cell perimeters and convex hull areas, skeleton lengths, and higher branching indices compared to the ischemic hippocampus (Figures 8A–E, Supplementary Tables 3, 4).

Cell area of all microglial cells positively correlated with soma area, cell perimeter, convex hull area, skeleton length, but not with cell solidity (Supplementary Figures 3A–E). Cell perimeter positively correlated with convex hull area, skeleton

length, and slightly negatively with *cell solidity* (Supplementary Figures 3F–H). *Convex hull area* positively correlated with *skeleton length* and is negatively associated with *cell solidity* (Supplementary Figures 3I,J). Control areas of both brain regions did not differ among each other concerning the above-mentioned six morphological parameters with the exception of *cell area*, *cell perimeter*, *convex hull area*, and *skeleton length* for ramified and rod-like cells (Figures 8A,C–E). Amoeboid microglia did not show any differences at all. We observed that rod-like microglia's *cell* and *soma area* as well as *cell solidity* are enhanced within the ischemic hemisphere compared to the control hemisphere (Figures 8A,B,F). In general, ramified cells exhibited small *soma areas*, big *cell perimeters*, and long *skeleton lengths* (Figures 8A,C,E).

Microglial *cell area* is expected to increase due to activation and soma enlargement yielding higher values of this morphological parameter for rod-like and activated microglia. The *cell perimeter* is estimated to be higher in ramified and rod-like cells. A decrease is characteristic of fewer ramifications. The more ramified is the microglial cell, the bigger is the *convex hull area*, thus leading to a smaller *cell solidity*. An increase of this parameter reveals the tendency of microglial cells to be more compact. *Cell circularity* is expected to be higher for amoeboid microglia. Typically, highly ramified microglia have a greater *skeleton length*, many *branches* and *endpoints*. The *branching index* is an additional measurement of microglial branching complexity. For instance, a small ramified microglial cell and an activated microglial cell may have a similar cell volume, but the activated microglia occupy more of its surrounding, therefore the *branching index* measure will be smaller. *SRI* constantly increases from an amoeboid toward an activated and rod-like morphology and to a ramified cell type (Figure 8 and Supplementary Table 2).

Since microglial cells are three-dimensional objects, the main limitation of our study is the two-dimensional way of image acquisition and subsequent image processing that does not properly allow to include all fine ramifications of different focal planes and can lead to underestimated cell parameters such as *area*, *perimeter*, or *skeleton length* for instance. Further, the thickness of brain slices is important to enable the analysis of entire microglial cells, each of which has its own territory of about 15–30 μm . Thin sections limit the accuracy of describing three-dimensional microglial morphology (Heindl et al., 2018). In line with Zanier et al. (2015), we used 20 μm and additionally 30 μm thick slices to ensure the detection of many non-overlapping microglial cells (Zanier et al., 2015). Another just recently published study used even thinner brain sections of 7 μm thickness (Ding et al., 2017). We had problems to properly separate Iba1-positive cells from each other using thicker sections.

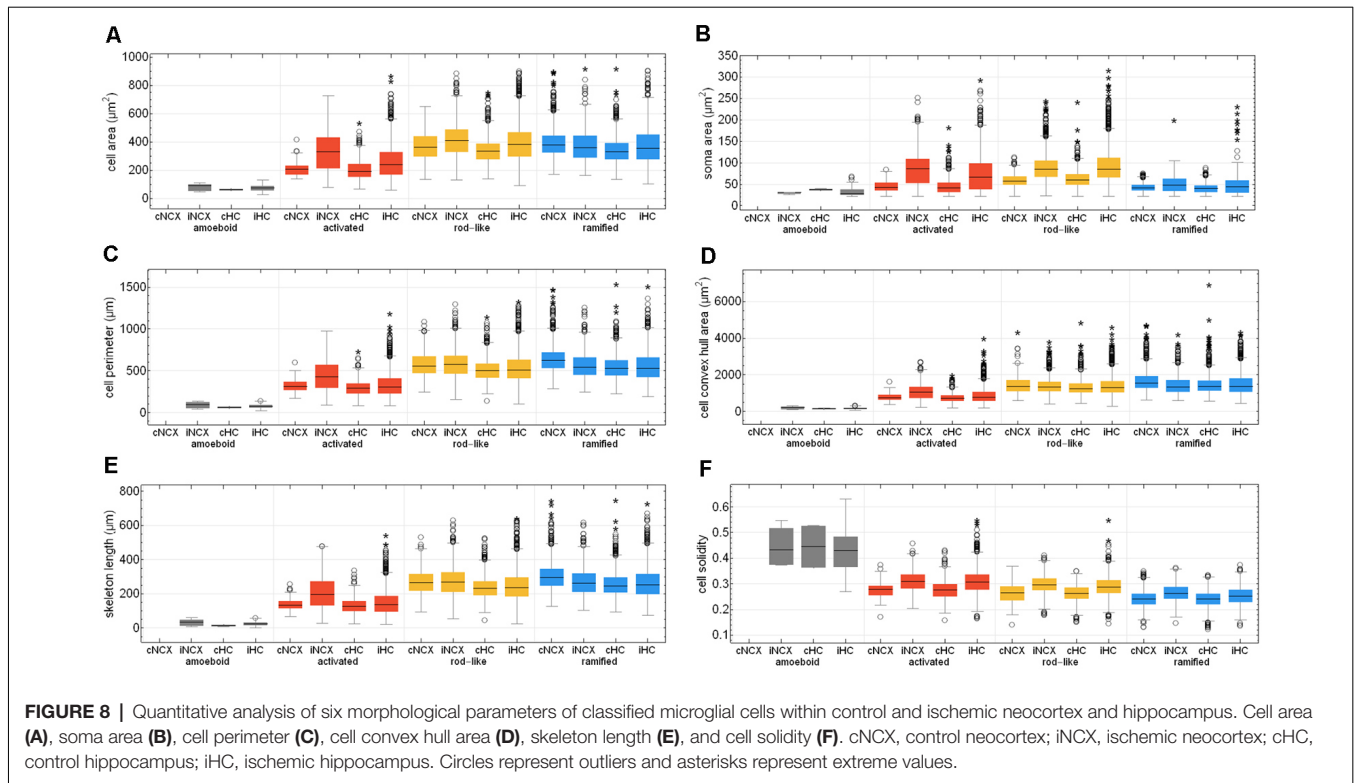
Comparison of CNN and NC Classification

The comparison of CNN and NC classification revealed detailed information regarding the relationship between individual morphological parameters. Figure 4 and Supplementary Figure 3 show some selected scatter plots and Figure 5A (lower triangular matrix) provides correlation coefficients for

all two-parameter combinations. Some parameters are closely related to each other (darker colored matrix cells; positively correlated: *cell perimeter* and *skeleton length*, negatively correlated: *cell perimeter* and *cell circularity*), while others show very weak correlation (lighter colored matrix cells; *cell area* and *cell solidity*). Parameters with close relationships and therefore strong absolute correlation coefficients express narrow spatial distributions near the regression line (Figure 4B). Parameters with weak to negligible absolute correlation coefficients tend to express broad and (but not always) less overlapping distributions (Figures 4G,L). NC classification is based on predefined centroids and cannot generate overlapping classes by design, which is a major pitfall for this approach. Therefore, NC classification results strongly depend on the shape and location of their respective point distributions in parameter space. This is also reflected in the comparison of CNN and NC classification in terms of their actual results: strongly correlating parameters show lower degrees of conformity (Figure 4E: 44.97%), while weakly correlating parameters show higher degrees of conformity (Figure 4O: 76.44%). Figure 5A (upper triangular matrix) provides values for the degree of conformity for all two-parameter combinations. As for correlation coefficients, these values are also emphasized with a color scheme and a certain pattern in relation to the matrix diagonal can be perceived. Correlation analysis of the degree of conformity (CNN vs. NC classification) and the absolute correlation coefficients revealed a moderate negative correlation (Figure 5B; $r = -0.512$, $p \leq 0.001$). In addition to the numerical comparison of both approaches, color-coded cell images were also generated. Figure 4R shows a section with color coding according to CNN classification. Color codings after NC classification are also presented for the following combinations: *cell area* and *skeleton length* (Figure 4C), *cell perimeter* and *soma perimeter* (Figure 4H) as well as *cell circularity* and *soma circularity* (Figure 4M). Lower degrees of conformity result in greater deviations from the CNN color-coding and classification differences are distributed across all four classes with one recognizable accumulation: NC classification tends to classify a larger proportion of activated cells as rod-like cells (Figures 4E–O).

A clear limitation of the CNN classification approach presented in this study was the number of cells that were selected for the training of the neural network. Although image augmentation was performed to dramatically increase the number of images for the training and validation set, this procedure may not fully replace the addition of cells with a completely different morphology. To counteract subjective influences during the manual selection of training images, this procedure was performed by four experienced investigators resulting in a more diverse set of cells belonging to the four classes—although this approach might have introduced too much morphological variability and overlap. These two factors may have attributed to misclassification and might be addressed to increase overall classification accuracy.

All possible combinations with more than three and up to 17 parameters (131,054 combinations in total, *SRI* was omitted from all analyses) were also investigated (Figure 5C).



Analyses revealed a peak degree of conformity at 77.21% with remaining NC overclassification of activated cells as rod-like cells (Figure 4P). However, the respective color-coding (Figure 4Q) largely resembles the CNN color-coding (Figure 4R). NC classification of all 17 parameters showed only a medium degree of conformity at 55.68% (Figure 4T), the respective color-coding is shown in Figure 4S. Certain parameters and combinations thereof are involved in NC classifications with higher—or even highest—degrees of conformity: *cell solidity*, *cell convexity*, *cell circularity*, *soma perimeter*, *soma circularity*, and *critical value*. Combinations of up to eight parameters could result in conformities of more than 75% (always with the participation of the parameters listed in the previous sentence), peak conformities of combinations with more parameters rapidly declined to less than 60%. The lowest conformities ranged down to 35.81% with parameters such as *skeleton branch points*, *skeleton endpoints* or *dendritic maximum*.

DISCUSSION

We can successfully confirm that our developed classification method of microglial morphological phenotypes works well by using a mouse model of transient MCA occlusion, which is one of the models that most closely simulate human ischemic stroke and is probably the most frequently used model in experimental stroke research (Engel et al., 2011; Fluri et al., 2015). Since microglial activation within the ischemia-affected brain regions has been well established (del Zoppo, 2009; Härtig et al., 2017; Zhang, 2019), this model was used as a

positive control to confirm a reliable detection of activated microglia by using the established machine learning method. In our study, we did not analyze neurons, but we assumed that neuronal damage or neuronal death is likely in ischemia-affected regions where microglia show activation processes to engulf cellular debris. Here, we showed that ischemia-affected regions in the hippocampus and neocortex presented more activated and rod-like microglial cells and consequently less ramified microglia compared to the relevant brain areas within the contralateral hemisphere. Michalski et al. (2017) recently demonstrated that Iba1-staining density and intensity were strongly increased in the ischemic core and ischemic border zone compared to the control area located at the contralateral, non-affected hemisphere (Michalski et al., 2017). This is in line with our data, which exhibit an increased microglial cell density in ischemia-affected brain regions. After an ischemic stroke, the blood-brain-barrier (BBB) is compromised (Latour et al., 2004; Sandoval and Witt, 2008; Krueger et al., 2015, 2017) and a BBB leakage coincides with an increased number of activated glial cells (Kuntz et al., 2014). Thus, a failing of the BBB integrity is followed by an infiltration of peripheral immune cells including neutrophils, lymphocytes, dendritic cells, and macrophages (microglia-derived and monocytes-derived macrophages) into the ischemic brain tissue (Kim and Cho, 2016; Jian et al., 2019). According to Rayasam et al. (2018), microglia in the CNS and peripheral immune cells are recruited to the ischemic hemisphere inducing an inflammatory response after stroke (Rayasam et al., 2018). Upon an ischemic event, microglial cells are the first responders and

become activated within 30 min after cerebral ischemia (Rupalla et al., 1998), peak at 2–3 days post-stroke, and persist for several weeks (Denes et al., 2007; Gelderblom et al., 2009). Activated microglia and monocytes/macrophages are similar in morphology and function, but recent studies in rodent models of transient cerebral ischemia reported that microglia dominate the ischemic brain at day 1 and 2 after ischemia. For instance, on day 1, only a small fraction of monocytes/macrophages was determined (<3%; Jian et al., 2019; Rajan et al., 2019; Han et al., 2020). Thus, the here detected higher microglial cell density within ischemia-affected brain regions after 1 day of transient ischemia is predominantly provoked by resident microglial cells of the activated and rod-like morphotypes. However, at this point, the given data cannot provide any conclusion on the temporal evolution of microglia phenotypes post-stroke and the time course of the alterations will have to be investigated (Mages et al., 2021). Furthermore, it cannot be ruled out that activated Iba1-positive cells might also include monocytes/macrophages.

Our findings show that the segmented image area did not reveal any differences within the neocortical and hippocampal regions. This parameter reflects the proportion of segmented pixels—or the raw count of all stained structures—within the image area before cell detection. The values are comparable since the tissue volume is evenly permeated by cells and their processes as the task of microglial cells is to evenly monitor the tissue. But their number and distribution depend on the activation state of the microglial cells. In slides with high cell density, the cell territories are smaller. There we found a larger proportion of somata with connected processes as well as fewer processes belonging to somata located outside the imaged tissue slice. These images are characterized by a larger share of activated and rod-like cells with comparatively larger somata and shorter processes. In slides with low cell density, the cell territories are larger. There we found a smaller proportion of somata with connected processes as well as more processes belonging to somata located outside the imaged tissue slice. These images are characterized by a larger share of ramified cells with comparatively smaller somata and longer processes.

For verification of our classification method of microglial morphological phenotypes, we analyzed several morphological parameters of about 16,000 Iba1-positive cells in accordance with recently published studies (Kongsui et al., 2014; Zanier et al., 2015; Fernández-Arjona et al., 2017, 2019). Comparing studies of Zanier et al. (2015) and Fernández-Arjona et al. (2017, 2019) with our work showed that the *cell area* of our classified group of activated microglial cells is highly distributed in different brain regions and is not bigger than ramified *cell's area* on average (Zanier et al., 2015; Fernández-Arjona et al., 2017, 2019). Here, we also examined rod-like microglial cells showing bigger *cell areas*. Activated and rod-like microglia in sum have bigger *cell areas* than ramified cells. In line with all studies including analysis of morphological parameters for microglial cells, we confirmed for instance larger *cell perimeters* and *convex hull areas* as well as smaller *cell soma areas* for ramified microglia.

Microglial cells are sensitive to fluctuations in blood flow and its reduction leads to a significant decrease in process activity and results in noticeable deramification and increased cell soma size (Masuda et al., 2011). Indeed, after ischemia, microglia tend to retract their fine, highly ramified processes leading to a reduced *skeleton length* what we have shown for all microglial cells within the ischemic neocortex and hippocampus as well as for activated compared to ramified cells. Reduced *branching indices* and *SRI* in ischemic compared to control regions confirmed this issue.

In contrast to Zanier et al. (2015), we distinguish between four different morphological classes of Iba1-stained cells in addition to an observation of all microglial cells after ischemia in control and ischemic-affected brain regions. The authors showed higher measurements for *cell area* and *cell perimeter* of CD11b-positive cells after transient MCA occlusion compared to naive mice. In line, we also used 20 μm thick brain slices for the analysis of microglial morphology (Zanier et al., 2015).

It has been recently shown by Fernández-Arjona et al. (2019) that, after injection of the enzyme neuraminidase within the lateral ventricle, activated microglial cells within the hypothalamus can be clustered in four different morphotypes characterized by various morphological parameters and IL-1 β expression levels. Here, we were unable to cluster activated microglia due to strong overlapping between different value ranges of morphological parameters, which can be an argument for morphological classification and against pure quantification. Moreover, the authors analyzed 150 activated cells, whereas we examined thousands of Iba1-positive cells. Clustering with fewer microglial cells showing extreme morphological characteristics of the activated morphotype is more efficient than with numerous microglia classified by their probability. We should also take into account the heterogeneity of microglial cell density and morphology across different brain regions. Microglial cell morphology is affected by the cellular architecture of specific brain areas. Fernández-Arjona et al. (2017) suggested the consideration of the brain location for future microglial morphological classification (Fernández-Arjona et al., 2017, 2019).

While the classification of microglial cells solely based on parameters from quantitative analysis has been proven to be a successful approach (Kongsui et al., 2014; Zanier et al., 2015; Fernández-Arjona et al., 2017, 2019; Morrison et al., 2017; York et al., 2018; Kyriazis, 2019), our results show that parameter values may differ considerably within individual classes. There partially is a wide spread in parameter values caused by the biological variance and it needs to be considered that the highest probability is pivotal for the final morphological classification of microglial cells.

Small morphological differences can indicate an incipient change in the activation state of microglial cells. Such changes are detectable by a CNN and could give an indication of pathological processes in the brain. While our CNN covers four morphological states, it is not yet known if different activation states are physiologically relevant. Furthermore, transitions between different phenotypes are fluent and subtle. While classification based on four discrete classes provides a good distinction of these phenotypes, there

is some latitude with regard to the morphology within these individual classes. There are differences in parameter expressions between different brain regions (activated microglia in the cortex differ from activated microglia in the hippocampus). Application of continuous scoring models like embedding visualization such as t-Distributed Stochastic Neighbor Embedding could be much more sensitive to even smaller morphological changes which should be explored in further studies.

CNN-based cell classification offers a powerful and interesting alternative to parameter-based cell classification. There are a number of morphological and topological parameters that are widely used to characterize microglial cells—some of them are basic properties (*cell area*, *skeleton length*, etc.), while others are combinations of multiple parameters (*circularity*, *branching index*, etc.). While we have presented 18 parameters in our study, there are many more that can be computed—and some parameters might be more significant for classification in a specific context than others.

Although the focus of this study is CNN-based cell classification, we also applied NC classification—a conventional parameter-based approach. While CNN classification is purely based on the shape of the cells, NC classification requires a set of morphological parameters that have to be computed prior to classification. As we have shown, it is not easy to determine a parameter set that is best suited for this task, since stronger parameter correlations may result in lower degrees of classification conformity. Without a thorough examination of all parameters for their interrelationships, it is not possible to make accurate predictions regarding their discriminatory power—but this would reach far beyond the scope of this study. While we have found potential parameter combinations and could compile a superficial ranking at best, the resulting classification quality is still inferior to results from CNN classification. Since NC classification is based on predefined centroids and class membership is assigned due to minimum centroid distances, different cluster shapes or sizes are not taken into account. Furthermore, this approach cannot generate overlapping classes by design, which—considering the high interpenetration of class point clusters—is a major strength of CNN classification. The NC approach also classifies a larger proportion of activated cells as rod-like cells, indicating a lower discriminatory power between these two classes. Due to the broad distribution of amoeboid cell parameters (*cell circularity* and *soma circularity*) or the strong overlap with clusters of the other three classes (*cell area* and *skeleton length*), amoeboid cells consistently show the highest number of NC misclassification in terms of their relative count. This is especially precarious regarding the low number of amoeboid cells within the images of our study.

Since it might be difficult to find suitable parameter combinations and specify thresholds for the assignment of cells to classes, we advocate for cell classification based on cell phenotype followed by quantitative analysis for morphological characterization. Cell classification based on CNNs does not require any parameters or combinations thereof, it is solely based on the cell's shape represented as an image matrix. Deep learning-based approaches are becoming more accessible to

researchers due to rapid technical progress and training CNNs on current graphics hardware with powerful GPUs gets increasingly time- and cost-efficient.

For the calculation of morphological parameters, a fully automatic approach was implemented and adapted to the characteristics of segmented cells. Manual analyses might be slightly better suited in cases of heterogeneous image quality or during interactive detection and reconstruction of interrupted cell processes, but they also greatly depend on the experience and endurance of the investigator. While automatic approaches require extensive testing and might introduce systematic errors, they are much faster than manual analyses and provide objective repeatability.

The proposed classification approach can be also applied to other staining and image acquisition setups as long as four key criteria are met: (1) staining quality and contrast must be sufficiently good to ensure reliable cell segmentation; (2) image resolution must be high enough to allow separation of cell processes during segmentation procedure; (3) tissue thickness must be chosen adequately to acquire (a) enough volume with a sufficient number of microglia showing an adequate amount of processes, while (b) avoiding overpopulated volumes with excessively interconnected network of ambiguously assignable cell processes; and (4) all segmented cells have to be adapted to match the input criteria for the CNN if an already trained CNN exists.

In the next step, we want to analyze microglia in scanned serial sections for 3D reconstruction and additionally in human brain tissue. Moreover, the morphological classification using machine learning can be transferred to other cell types like astrocytes and neurons.

In conclusion, our newly established classification method of microglial morphological phenotypes using machine learning represents an objective, unbiased and time-saving procedure that can serve as a powerful tool for post-mortem characterization of microglial changes in disease mouse models, and probably human brain autopsy samples.

DATA AVAILABILITY STATEMENT

The raw data supporting the conclusions of this article will be made available by the authors, without undue reservation.

ETHICS STATEMENT

The animal study was reviewed and approved by the local ethics committee of the state of Saxony (Landesdirektion Sachsen, Leipzig, approval nos. TVV 65/15, TVV 02/17, and TVV 41/17).

AUTHOR CONTRIBUTIONS

JL, SP, IB, and KW conceived and designed the study. KW performed image acquisition and image processing. DM and BM carried out the animal experiments of cerebral ischemia. JL carried out the animal experiments of male wild-type C57BL/6J mice. MN provided and SP carried out the animal experiments

of *db/db* and *db/+* mice. JL, SP, and KW analyzed the data and wrote the manuscript. All authors contributed to the article and approved the submitted version.

FUNDING

This work was funded by the Deutsche Forschungsgemeinschaft (DFG, German Research Foundation), SFB 1052 obesity mechanisms (Project number 209933838, SFB-1052/A9 to IB), supported by grants of the Deutsche Diabetes Gesellschaft: DDG 934300-002 (to MN), and the European Social Fund (ESF, grant 100270131 to DM).

REFERENCES

- Bachstetter, A. D., Ighodaro, E. T., Hassoun, Y., Aldeiri, D., Neltner, J. H., Patel, E., et al. (2017). Rod-shaped microglia morphology is associated with aging in 2 human autopsy series. *Neurobiol. Aging* 52, 98–105. doi: 10.1016/j.neurobiolaging.2016.12.028
- Bradl, M., and Lassmann, H. (2010). Oligodendrocytes: biology and pathology. *Acta Neuropathol. (Berl.)* 119, 37–53. doi: 10.1007/s00401-009-0601-5
- Campbell, B. C. V., De Silva, D. A., Macleod, M. R., Coutts, S. B., Schwamm, L. H., Davis, S. M., et al. (2019). Ischaemic stroke. *Nat. Rev. Dis. Primer* 5:70. doi: 10.1038/s41572-019-0118-8
- Colonna, M., and Butovsky, O. (2017). Microglia function in the central nervous system during health and neurodegeneration. *Annu. Rev. Immunol.* 35, 441–468. doi: 10.1146/annurev-immunol-051116-052358
- Davalos, D., Grutzendler, J., Yang, G., Kim, J. V., Zuo, Y., Jung, S., et al. (2005). ATP mediates rapid microglial response to local brain injury *in vivo*. *Nat. Neurosci.* 8, 752–758. doi: 10.1038/nn1472
- de Chaumont, F., Dallongeville, S., Chenouard, N., Hervé, N., Pop, S., Provoost, T., et al. (2012). Icy: an open bioimage informatics platform for extended reproducible research. *Nat. Methods* 9, 690–696. doi: 10.1038/nmeth.2075
- Deb, P., Sharma, S., and Hassan, K. M. (2010). Pathophysiologic mechanisms of acute ischemic stroke: an overview with emphasis on therapeutic significance beyond thrombolysis. *Pathophysiology* 17, 197–218. doi: 10.1016/j.pathophys.2009.12.001
- del Zoppo, G. J. (2009). Inflammation and the neurovascular unit in the setting of focal cerebral ischemia. *Neuroscience* 158, 972–982. doi: 10.1016/j.neuroscience.2008.08.028
- Denes, A., Vidyasagar, R., Feng, J., Narvainen, J., McColl, B. W., Kauppinen, R. A., et al. (2007). Proliferating resident microglia after focal cerebral ischaemia in mice. *J. Cereb. Blood Flow Metab.* 27, 1941–1953. doi: 10.1038/sj.jcbfm.9600495
- Ding, Y., Pardon, M. C., Agostini, A., Faas, H., Duan, J., Ward, W. O. C., et al. (2017). Novel methods for microglia segmentation, feature extraction and classification. *IEEE/ACM Trans. Comput. Biol. Bioinform* 14, 1366–1377. doi: 10.1109/TCBB.2016.2591520
- Doorn, K. J., Goudriaan, A., Blits-Huizinga, C., Bol, J. G. J. M., Rozemuller, A. J., Hoogland, P. V. J. M., et al. (2014). Increased amoeboid microglial density in the olfactory bulb of Parkinson's and Alzheimer's patients: microglia in olfactory bulb of AD and PD patients. *Brain Pathol.* 24, 152–165. doi: 10.1111/bpa.12088
- Dürr, O., and Sick, B. (2016). Single-cell phenotype classification using deep convolutional neural networks. *J. Biomol. Screen.* 21, 998–1003. doi: 10.1182/blood.2021011817
- Engel, O., Kolodziej, S., Dirnagl, U., and Prinz, V. (2011). Modeling stroke in mice - middle cerebral artery occlusion with the filament model. *J. Vis. Exp.* 47:2423. doi: 10.3791/2423
- Fernández-Arjona, M. del M., Grondona, J. M., Fernández-Llebrez, P., and López-Ávalos, M. D. (2019). Microglial morphometric parameters correlate with the expression level of IL-1 β and allow identifying different activated morphotypes. *Front. Cell. Neurosci.* 13:472. doi: 10.1016/j.clinbiochem.2021.06.001

ACKNOWLEDGMENTS

We thank Nicole Kaiser, Andreas Horn and the staff from the animal facility for their excellent technical assistance. We acknowledge support from Leipzig University for Open Access Publishing.

SUPPLEMENTARY MATERIAL

The Supplementary Material for this article can be found online at: <https://www.frontiersin.org/articles/10.3389/fncel.2021.701673/full#supplementary-material>.

- Fernández-Arjona, M. del M., Grondona, J. M., Granados-Durán, P., Fernández-Llebrez, P., and López-Ávalos, M. D. (2017). Microglia morphological categorization in a rat model of neuroinflammation by hierarchical cluster and principal components analysis. *Front. Cell. Neurosci.* 11:235. doi: 10.1016/j.clinbiochem.2021.06.001
- Fluri, F., Schuhmann, M., and Kleinschnitz, C. (2015). Animal models of ischemic stroke and their application in clinical research. *Drug Des. Devel. Ther.* 9, 3445–3454. doi: 10.2147/DDDT.S56071
- Fumagalli, S., Perego, C., Ortolano, F., and De Simoni, M.-G. (2013). CX3CR1 deficiency induces an early protective inflammatory environment in ischemic mice: fractalkine receptor and ischemic environment. *Glia* 61, 827–842. doi: 10.1002/glia.22474
- Galatro, T. F., Holtman, I. R., Lerario, A. M., Vainchtein, I. D., Brouwer, N., Sola, P. R., et al. (2017). Transcriptomic analysis of purified human cortical microglia reveals age-associated changes. *Nat. Neurosci.* 20, 1162–1171. doi: 10.1038/nn.4597
- Gao, Z., Wang, L., Zhou, L., and Zhang, J. (2017). HEp-2 cell image classification with deep convolutional neural networks. *IEEE J. Biomed. Health Inform.* 21, 416–428. doi: 10.1109/JBHI.2016.2526603
- García-Segura, L. M., and Pérez-Marquez, J. (2014). A new mathematical function to evaluate neuronal morphology using the Sholl analysis. *J. Neurosci. Methods* 226, 103–109. doi: 10.1016/j.jneumeth.2014.01.016
- Gelderblom, M., Leyppoldt, F., Steinbach, K., Behrens, D., Choe, C.-U., Siler, D. A., et al. (2009). Temporal and spatial dynamics of cerebral immune cell accumulation in stroke. *Stroke* 40, 1849–1857. doi: 10.1161/STROKEAHA.108.534503
- Goldmann, T., and Prinz, M. (2013). Role of Microglia in CNS Autoimmunity. *Clin. Dev. Immunol.* 2013, 1–8. doi: 10.1155/2013/208093
- Gonzalez, R. C., and Woods, R. E. (2016). *Digital Image Processing*, 3rd edition. Delhi, Chennai: Pearson Prentice-Hall.
- Gosselin, D., Skola, D., Coufal, N. G., Holtman, I. R., Schlachetzki, J. C. M., Sajti, E., et al. (2017). An environment-dependent transcriptional network specifies human microglia identity. *Science* 356:eaal3222. doi: 10.1126/science.aal3222
- Grabert, K., Michoel, T., Karavolos, M. H., Clohisey, S., Baillie, J. K., Stevens, M. P., et al. (2016). Microglial brain region-dependent diversity and selective regional sensitivities to aging. *Nat. Neurosci.* 19, 504–516. doi: 10.1038/nn.4222
- Han, D., Liu, H., and Gao, Y. (2020). The role of peripheral monocytes and macrophages in ischemic stroke. *Neurol. Sci.* 41, 3589–3607. doi: 10.1007/s10072-020-04777-9
- Härtig, W., Krueger, M., Hofmann, S., Preißler, H., Märkel, M., Frydrychowicz, C., et al. (2016). Up-regulation of neurofilament light chains is associated with diminished immunoreactivities for MAP2 and tau after ischemic stroke in rodents and in a human case. *J. Chem. Neuroanat.* 78, 140–148. doi: 10.1016/j.jchemneu.2016.09.004
- Härtig, W., Mages, B., Aleithe, S., Nitzsche, B., Altmann, S., Barthel, H., et al. (2017). Damaged neocortical perineuronal nets due to experimental focal cerebral ischemia in mice, rats and sheep. *Front. Integr. Neurosci.* 11:15. doi: 10.3389/fnint.2017.00015
- Heckbert, P. S. ed. (1994). *Graphics Gems IV*. Boston: AP Professional.

- Heindl, S., Gesierich, B., Benakis, C., Llovera, G., Duering, M., and Liesz, A. (2018). Automated morphological analysis of microglia after stroke. *Front. Cell. Neurosci.* 12:106. doi: 10.3389/fncel.2018.00106
- Holloway, O. G., Canty, A. J., King, A. E., and Ziebell, J. M. (2019). Rod microglia and their role in neurological diseases. *Semin. Cell Dev. Biol.* 94, 96–103. doi: 10.1016/j.semcdb.2019.02.005
- Huang, H., Tohme, S., Al-Khafaji, A. B., Tai, S., Loughran, P., Chen, L., et al. (2015). Damage-associated molecular pattern-activated neutrophil extracellular trap exacerbates sterile inflammatory liver injury: liver injury/regeneration. *Hepatology* 62, 600–614. doi: 10.1002/hep.27841
- Jian, Z., Liu, R., Zhu, X., Smerin, D., Zhong, Y., Gu, L., et al. (2019). The involvement and therapy target of immune cells after ischemic stroke. *Front. Immunol.* 10:2167. doi: 10.3389/fimmu.2019.02167
- Johnson, S. J., and Walker, F. R. (2015). Strategies to improve quantitative assessment of immunohistochemical and immunofluorescent labelling. *Sci. Rep.* 5:10607. doi: 10.1038/srep10607
- Kim, E., and Cho, S. (2016). Microglia and monocyte-derived macrophages in stroke. *Neurotherapeutics* 13, 702–718. doi: 10.1007/s13311-016-0463-1
- Kongsui, R., Beynon, S. B., Johnson, S. J., and Walker, F. R. (2014). Quantitative assessment of microglial morphology and density reveals remarkable consistency in the distribution and morphology of cells within the healthy prefrontal cortex of the rat. *J. Neuroinflammation.* 11:182. doi: 10.1186/s12974-014-0182-7
- Kozłowski, C., and Weimer, R. M. (2012). An automated method to quantify microglia morphology and application to monitor activation state longitudinally *in vivo*. *PLoS One* 7:e31814. doi: 10.1371/journal.pone.0031814
- Krueger, M., Bechmann, I., Immig, K., Reichenbach, A., Härtig, W., and Michalski, D. (2015). Blood–brain barrier breakdown involves four distinct stages of vascular damage in various models of experimental focal cerebral ischemia. *J. Cereb. Blood Flow Metab.* 35, 292–303. doi: 10.1038/jcbfm.2014.199
- Krueger, M., Härtig, W., Frydrychowicz, C., Mueller, W. C., Reichenbach, A., Bechmann, I., et al. (2017). Stroke-induced blood-brain barrier breakdown along the vascular tree—no preferential affection of arteries in different animal models and in humans. *J. Cereb. Blood Flow Metab.* 37, 2539–2554. doi: 10.1177/0271678X16670922
- Kuntz, M., Mysiorek, C., Pétrault, O., Pétrault, M., Uzbekov, R., Bordet, R., et al. (2014). Stroke-induced brain parenchymal injury drives blood-brain barrier early leakage kinetics: a combined *in vivo/in vitro* study. *J. Cereb. Blood Flow Metab.* 34, 95–107. doi: 10.1038/jcbfm.2013.169
- Kyriazis, A. D. (2019). An end-to-end system for automatic characterization of iba1 immunopositive microglia in whole slide imaging. *Neuroinformatics* 17, 373–389. doi: 10.1007/s12021-018-9405-x
- Latour, L. L., Kang, D.-W., Ezzeddine, M. A., Chalela, J. A., and Warach, S. (2004). Early blood-brain barrier disruption in human focal brain ischemia. *Ann. Neurol.* 56, 468–477. doi: 10.1002/ana.20199
- Li, Q., Maasoumi, E., and Racine, J. S. (2009). A nonparametric test for equality of distributions with mixed categorical and continuous data. *J. Econom.* 148, 186–200. doi: 10.1016/j.jeconom.2008.10.007
- Mages, B., Aleithe, S., Altmann, S., Blietz, A., Nitzsche, B., Barthel, H., et al. (2018). Impaired neurofilament integrity and neuronal morphology in different models of focal cerebral ischemia and human stroke tissue. *Front. Cell. Neurosci.* 12:161. doi: 10.3389/fncel.2018.00161
- Mages, B., Fuhs, T., Aleithe, S., Blietz, A., Hobusch, C., Härtig, W., et al. (2021). The cytoskeletal elements MAP2 and NF-L show substantial alterations in different stroke models while elevated serum levels highlight especially MAP2 as a sensitive biomarker in stroke patients. *Mol. Neurobiol.* doi: 10.1007/s12035-021-02372-3. [Epub ahead of print].
- Masuda, T., Croom, D., Hida, H., and Kirov, S. A. (2011). Capillary blood flow around microglial somata determines dynamics of microglial processes in ischemic conditions. *Glia* 59, 1744–1753. doi: 10.1002/glia.21220
- Masuda, T., Sankowski, R., Staszewski, O., and Prinz, M. (2020). Microglia heterogeneity in the single-cell era. *Cell Rep.* 30, 1271–1281. doi: 10.1016/j.celrep.2020.01.010
- Michalski, D., Pitsch, R., Pillai, D. R., Mages, B., Aleithe, S., Grosche, J., et al. (2017). Delayed histochemical alterations within the neurovascular unit due to transient focal cerebral ischemia and experimental treatment with neurotrophic factors. *PLoS One* 12:e0174996. doi: 10.1371/journal.pone.0174996
- Morrison, H., Young, K., Qureshi, M., Rowe, R. K., and Lifshitz, J. (2017). Quantitative microglia analyses reveal diverse morphologic responses in the rat cortex after diffuse brain injury. *Sci. Rep.* 7:13211. doi: 10.1038/s41598-017-13581-z
- Nimmerjahn, A. (2012). Two-photon imaging of microglia in the mouse cortex *in vivo*. *Cold Spring Harb. Protoc.* 2012:pdb.prot069294. doi: 10.1101/pdb.prot069294
- Nimmerjahn, A., Kirchhoff, F., and Helmchen, F. (2005). Resting microglial cells are highly dynamic surveillants of brain parenchyma *in vivo*. *Science* 308:6. doi: 10.1126/science.1110647
- Nissl, F. (1899). Über einige beziehungen zwischen nervenzellerkrankungen und gliösen erscheinungen bei verschiedenen psychosen. *Arch Psychiatr* 32, 1–21.
- Nutma, E., van Gent, D., Amor, S., and Peferoen, L. A. N. (2020). Astrocyte and oligodendrocyte cross-talk in the central nervous system. *Cells* 9:600. doi: 10.3390/cells9030600
- Oei, R. W., Hou, G., Liu, F., Zhong, J., Zhang, J., An, Z., et al. (2019). Convolutional neural network for cell classification using microscope images of intracellular actin networks. *PLoS One* 14:e0213626. doi: 10.1371/journal.pone.0213626
- Otsu, N. (1979). A threshold selection method from gray-level histograms. *IEEE Trans. Syst. Man Cybern.* 9, 62–66.
- Parkhurst, C. N., Yang, G., Ninan, I., Savas, J. N., Yates, J. R., Lafaille, J. J., et al. (2013). Microglia promote learning-dependent synapse formation through brain-derived neurotrophic factor. *Cell* 155, 1596–1609. doi: 10.1016/j.cell.2013.11.030
- Popp, A., Jaenisch, N., Witte, O. W., and Frahm, C. (2009). Identification of ischemic regions in a rat model of stroke. *PLoS One* 4:e4764. doi: 10.1371/journal.pone.0004764
- Rajan, W. D., Wojtas, B., Gielniewski, B., Gieryng, A., Zawadzka, M., and Kaminska, B. (2019). Dissecting functional phenotypes of microglia and macrophages in the rat brain after transient cerebral ischemia. *Glia* 67, 232–245. doi: 10.1002/glia.23536
- Rayasam, A., Hsu, M., Kijak, J. A., Kissel, L., Hernandez, G., Sandor, M., et al. (2018). Immune responses in stroke: how the immune system contributes to damage and healing after stroke and how this knowledge could be translated to better cures? *Immunology* 154, 363–376. doi: 10.1111/imm.12918
- Rey-Villamizar, N., Somasundar, V., Meghani, M., Xu, Y., Lu, Y., Padmanabhan, R., et al. (2014). Large-scale automated image analysis for computational profiling of brain tissue surrounding implanted neuroprosthetic devices using Python. *Front. Neuroinformatics* 8:39. doi: 10.3389/fninf.2014.00039
- Rojas, B., Gallego, B. I., Ramírez, A. I., Salazar, J. J., de Hoz, R., Valiente-Soriano, F. J., et al. (2014). Microglia in mouse retina contralateral to experimental glaucoma exhibit multiple signs of activation in all retinal layers. *J. Neuroinflammation* 11:133. doi: 10.1186/1742-2094-11-133
- Rupalla, K., Allegrini, P. R., Sauer, D., and Wiessner, C. (1998). Time course of microglia activation and apoptosis in various brain regions after permanent focal cerebral ischemia in mice. *Acta Neuropathol.* 96, 172–178. doi: 10.1007/s004010050878
- Salamanca, L., Mechawar, N., Murai, K. K., Balling, R., Bouvier, D. S., and Skupin, A. (2019). MIC-MAC: An automated pipeline for high-throughput characterization and classification of three-dimensional microglia morphologies in mouse and human postmortem brain samples. *Glia* 67:glia.23623. doi: 10.1002/glia.23623
- Sandoval, K. E., and Witt, K. A. (2008). Blood-brain barrier tight junction permeability and ischemic stroke. *Neurobiol. Dis.* 32, 200–219. doi: 10.1016/j.nbd.2008.08.005
- Schoenen, J. (1982). The dendritic organization of the human spinal cord: the dorsal horn. *Neuroscience* 7, 2057–2087. doi: 10.1016/0306-4522(82)90120-8
- Sholl, D. A. (1953). Dendritic organization in the neurons of the visual and motor cortices of the cat. *J. Anat.* 87, 387–406.
- Shorten, C., and Khoshgoftaar, T. M. (2019). A survey on image data augmentation for deep learning. *J. Big Data* 6:60. doi: 10.1186/s40537-019-0197-0
- Simonyan, K., and Zisserman, A. (2015). Very Deep Convolutional Networks for Large-Scale Image Recognition. *ArXiv14091556 Cs* [preprint].
- Sofroniew, M. V., and Vinters, H. V. (2010). Astrocytes: biology and pathology. *Acta Neuropathol.* 119, 7–35. doi: 10.1007/s00401-009-0619-8

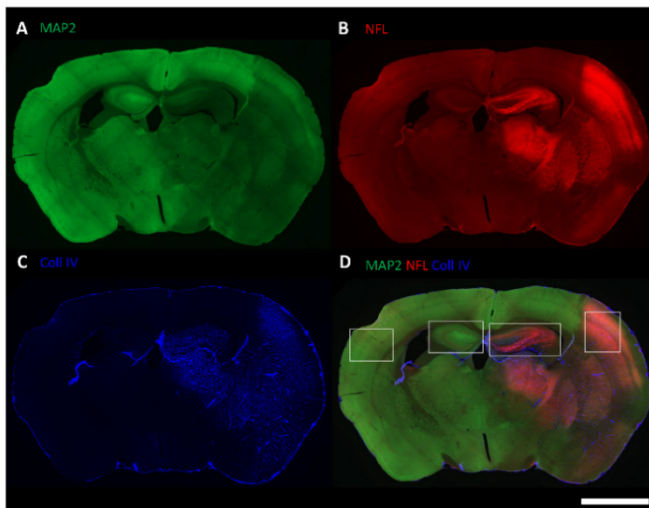
- Soreq, L., Rose, J., Soreq, E., Hardy, J., Trabzuni, D., Cookson, M. R., et al. (2017). Major shifts in glial regional identity are a transcriptional hallmark of human brain aging. *Cell Rep.* 18, 557–570. doi: 10.1016/j.celrep.2016.12.011
- Sousa, A. M. M., Zhu, Y., Raghanti, M. A., Kitchen, R. R., Onorati, M., Tebbenkamp, A. T. N., et al. (2017). Molecular and cellular reorganization of neural circuits in the human lineage. *Science* 358, 1027–1032. doi: 10.1126/science.aan3456
- Stence, N., Waite, M., and Dailey, M. E. (2001). Dynamics of microglial activation: a confocal time-lapse analysis in hippocampal slices. *Glia* 33, 256–266. doi: 10.1002/1098-1136(200103)33:3<256::aid-glia1024>3.0.co;2-j
- Taylor, S. E., Morganti-Kossmann, C., Lifshitz, J., and Ziebell, J. M. (2014). Rod microglia: a morphological definition. *PLoS One* 9:e97096. doi: 10.1371/journal.pone.0097096
- Traiffort, E. (2020). Astrocytes and microglia as major players of myelin production in normal and pathological conditions. *Front. Cell. Neurosci.* 14:21. doi: 10.3389/fncel.2020.00079
- Tremblay, M.-E., Stevens, B., Sierra, A., Wake, H., Bessis, A., and Nimmerjahn, A. (2011). The role of microglia in the healthy brain. *J. Neurosci.* 31, 16064–16069. doi: 10.1523/JNEUROSCI.4158-11.2011
- Valous, N. A., Lahrmann, B., Zhou, W., Veltkamp, R., and Grabe, N. (2013). Multistage histopathological image segmentation of Iba1-stained murine microglia in a focal ischemia model: Methodological workflow and expert validation. *J. Neurosci. Methods* 213, 250–262. doi: 10.1016/j.jneumeth.2012.12.017
- York, E. M., LeDue, J. M., Bernier, L.-P., and MacVicar, B. A. (2018). 3DMorph automatic analysis of microglial morphology in three dimensions from *ex vivo* and *in vivo* imaging. *eNeuro* 5:ENEURO.0266–18.2018. doi: 10.1523/ENEURO.0266-18.2018
- Zanier, E. R., Fumagalli, S., Perego, C., Pischiutta, F., and Simoni, M.-G. D. (2015). Shape descriptors of the “never resting” microglia in three different acute brain injury models in mice. *Intensive Care Med. Exp.* 18:39. doi: 10.1186/s40635-015-0039-0
- Zhang, S. (2019). Microglial activation after ischaemic stroke. *Stroke Vasc. Neurol.* 4, 71–74. doi: 10.1136/svn-2018-000196
- Zhao, S., Ma, L., Chu, Z., Xu, H., Wu, W., Liu, F., et al. (2017). Regulation of microglial activation in stroke. *Acta Pharmacol. Sin.* 38, 445–458. doi: 10.1038/aps.2016.162
- Ziebell, J. M., Taylor, S. E., Cao, T., Harrison, J. L., and Lifshitz, J. (2012). Rod microglia: elongation, alignment and coupling to form trains across the somatosensory cortex after experimental diffuse brain injury. *J. Neuroinflammation.* 9:247. doi: 10.1186/1742-2094-9-247

Conflict of Interest: The authors declare that the research was conducted in the absence of any commercial or financial relationships that could be construed as a potential conflict of interest.

Copyright © 2021 Leyh, Paeschke, Mages, Michalski, Nowicki, Bechmann and Winter. This is an open-access article distributed under the terms of the Creative Commons Attribution License (CC BY). The use, distribution or reproduction in other forums is permitted, provided the original author(s) and the copyright owner(s) are credited and that the original publication in this journal is cited, in accordance with accepted academic practice. No use, distribution or reproduction is permitted which does not comply with these terms.

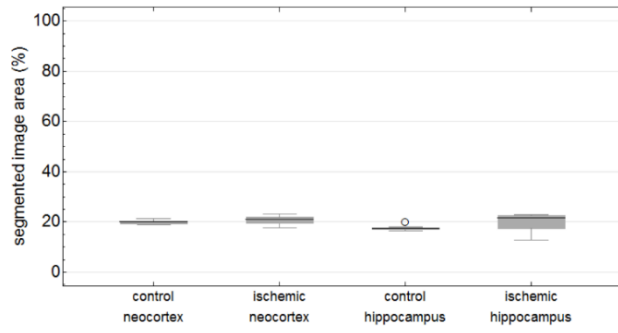
Classification of microglial morphological phenotypes using machine learning

Supplementary Materials



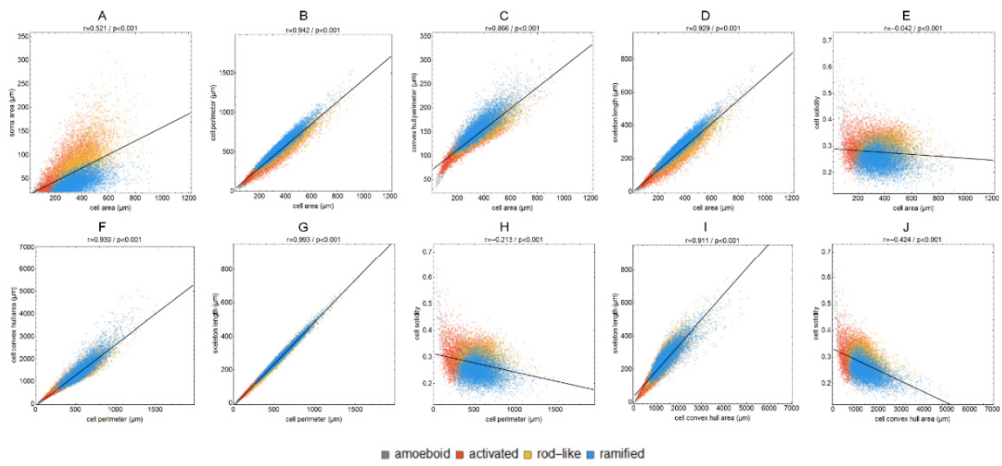
Supplementary Figure 1

Representative overview images of immunofluorescence staining for MAP2 (A), NFL (B), Coll IV (C), and triple immunofluorescence labelling of all applied markers (D) in mice 24 h after induction of experimental cerebral ischemia. Selected regions of interest in the hippocampus and neocortex within the ipsilateral, ischemia-affected hemisphere on the right and contralateral, control hemisphere on the left (F). Scale bar represents 200 μm .



Supplementary Figure 2

Percentage of segmented image area in control and ischemic neocortex and in control and ischemic hippocampus.



Supplementary Figure 3

Linear regression analysis between different microglial morphological parameters.

Supplementary Table 1: Morphological parameters of all microglial cells within control and ischemic neocortex and hippocampus.

parameter	control neocortex	ischemic neocortex	control hippocampus	ischemic hippocampus
cells	2024	4532	3105	6125
cell area [μm^2]	375.10 (123.58)	374.85 (179.01)	317.12 (122.22)	320.01 (192.19)
cell perimeter [μm]	611.19 (203.45)	527.89 (244.06)	497.69 (193.26)	436.27 (262.61)
convex hull area [μm^2]	1519.46 (655.09)	1263.45 (569.75)	1256.53 (588.97)	1110.21 (705.99)
convex hull perimeter [μm]	158.85 (37.14)	142.16 (34.81)	144.41 (35.58)	135.65 (43.06)
cell solidity	0.25 (0.04)	0.29 (0.05)	0.25 (0.05)	0.29 (0.06)
cell convexity	0.26 (0.05)	0.27 (0.08)	0.29 (0.07)	0.31 (0.11)
cell circularity	0.11 (0.02)	0.13 (0.03)	0.13 (0.03)	0.14 (0.05)
soma area [μm^2]	43.04 (13.83)	74.23 (49.85)	43.15 (21.13)	66.26 (53.10)
soma perimeter [μm]	25.09 (4.74)	35.27 (14.50)	25.70 (7.56)	33.59 (17.08)
soma circularity	0.93 (0.04)	0.88 (0.09)	0.91 (0.06)	0.87 (0.11)
skeleton length [μm]	290.63 (100.90)	247.78 (126.40)	231.87 (97.68)	200.57 (132.59)
skeleton branch points	28 (12)	25 (17)	21 (12)	18 (15)
skeleton end points	18 (7)	16 (7)	15 (7)	14 (9)
cell processes	3 (2)	4 (2)	3 (2)	4 (3)
branching index	224.62 (137.11)	189.61 (126.41)	176.97 (122.52)	160.44 (136.13)
critical radius	12.64 (2.92)	12.64 (3.89)	12.64 (2.92)	11.67 (4.86)
dendritic maximum	14 (4)	14 (5)	12 (5)	11 (5)
SRI	5 (4.10)	3.25 (3.08)	3.67 (3.5)	2.50 (2.08)

Values are expressed as median (and interquartile range).

Supplementary Table 2: Morphological parameters of classified microglial cells.

parameter	amoeboid	activated	rod-like	ramified
cells	80	4337	5104	6265
cell area [μm^2]	73.13 (33.92)	253.34 (189.69)	380.86 (166.35)	354.29 (137.28)
cell perimeter [μm]	76.12 (35.58)	333.22 (221.07)	533.51 (225.63)	557.59 (208.78)
convex hull area [μm^2]	172.62 (94.97)	842.47 (554.43)	1316.72 (565.99)	1420.09 (641.69)
convex hull perimeter [μm]	56.36 (17.12)	118.43 (36.28)	146.42 (33.65)	154.09 (36.48)
cell solidity	0.43 (0.12)	0.30 (0.06)	0.29 (0.05)	0.25 (0.05)
cell convexity	0.76 (0.19)	0.35 (0.13)	0.28 (0.07)	0.28 (0.06)
cell circularity	0.39 (0.11)	0.17 (0.05)	0.13 (0.03)	0.12 (0.02)
soma area [μm^2]	28.93 (13.00)	68.33 (61.50)	79.23 (41.88)	42.03 (18.9)
soma perimeter [μm]	20.59 (5.09)	33.02 (16.89)	38.65 (14.11)	25.01 (6.30)
soma circularity	0.93 (0.06)	0.89 (0.07)	0.82 (0.11)	0.92 (0.04)
skeleton length [μm]	24.59 (17.42)	149.47 (108.93)	247.72 (114.58)	264.81 (105.22)
skeleton branch points	1 (2)	13 (13)	24 (15)	25 (13)
skeleton end points	4 (2)	12 (8)	17 (8)	17 (7)
cell processes	3 (2)	4 (3)	4 (3)	3 (2)
branching index	17.5 (12.64)	116.69 (99.18)	197.39 (125.44)	211.01 (141.97)
critical radius	3.89 (1.94)	10.70 (4.86)	13.61 (2.92)	12.64 (2.92)
dendritic maximum	3 (1)	10 (6)	14 (5)	13 (4)
SRI	1 (0.58)	2.20 (1.75)	3 (2.67)	4.33 (4.00)

Values are expressed as median (and interquartile range).

Supplementary Table 3: Morphological parameters of classified microglial cells within control and ischemic neocortex and hippocampus.

parameter	amoeboid				activated				rod-like				ramified			
	control neocortex	ischemic neocortex	control hippocampus	ischemic hippocampus	control neocortex	ischemic neocortex	control hippocampus	ischemic hippocampus	control neocortex	ischemic neocortex	control hippocampus	ischemic hippocampus	control neocortex	ischemic neocortex	control hippocampus	ischemic hippocampus
cells	0	5	2	73	55	1541	415	2326	209	1872	747	2276	1760	1114	1941	1450
cell area [µm ²]	-	91.95 (40.32)	62.73 (8.57)	73.49 (31.26)	276.39 (66.33)	332.08 (218.45)	199.80 (91.64)	236.95 (159.95)	362.53 (142.42)	433.62 (162.15)	334.68 (106.66)	381.55 (171.74)	339.87 (129.67)	393.95 (153.71)	339.53 (114.26)	352.65 (175.65)
cell perimeter [µm]	-	83.06 (62.13)	62.21 (19.02)	76.35 (33.48)	312.16 (105.18)	429.68 (276.34)	289.35 (125.85)	336.75 (179.13)	558.33 (202.47)	574.82 (218.76)	503.10 (169.70)	506.60 (228.39)	621.36 (199.82)	545.45 (208.12)	527.82 (178.84)	526.71 (240.61)
convex hull area [µm ²]	-	222.12 (137.28)	147.71 (73.44)	172.17 (79.08)	741.59 (298.09)	1049.53 (626.64)	722.23 (316.63)	789.12 (485.57)	1365.52 (632.64)	1546.30 (507.88)	1241.22 (514.66)	1309.87 (631.18)	1556.47 (642.20)	1376.29 (644.55)	1360.11 (573.62)	1360.77 (746.93)
convex hull perimeter [µm]	-	67.65 (32.07)	50.95 (19.81)	56.54 (15.99)	199.84 (15.88)	128.17 (38.07)	108.83 (23.07)	114.59 (34.50)	148.15 (38.41)	147.20 (26.99)	142.89 (28.95)	146.58 (37.23)	161.32 (36.19)	148.59 (36.14)	151.19 (34.12)	152.47 (41.81)
cell solidity	-	0.43 (0.13)	0.44 (0.14)	0.43 (0.12)	0.28 (0.04)	0.31 (0.06)	0.28 (0.05)	0.31 (0.06)	0.22 (0.06)	0.30 (0.05)	0.26 (0.04)	0.28 (0.05)	0.24 (0.04)	0.26 (0.05)	0.24 (0.04)	0.25 (0.05)
cell convexity	-	0.73 (0.10)	0.81 (0.07)	0.76 (0.18)	0.36 (0.06)	0.39 (0.11)	0.38 (0.11)	0.38 (0.13)	0.27 (0.05)	0.26 (0.06)	0.29 (0.06)	0.029 (0.07)	0.26 (0.04)	0.27 (0.06)	0.29 (0.06)	0.29 (0.07)
cell circularity	-	0.37 (0.18)	0.46 (0.11)	0.38 (0.11)	0.16 (0.00)	0.15 (0.04)	0.17 (0.04)	0.18 (0.05)	0.12 (0.02)	0.12 (0.02)	0.13 (0.02)	0.13 (0.03)	0.11 (0.02)	0.12 (0.02)	0.12 (0.02)	0.13 (0.03)
soma area [µm ²]	-	30.49 (2.7)	38.01 (3.74)	28.69 (13.28)	43.94 (18.53)	86.28 (56.62)	40.91 (23.34)	66.64 (60.34)	56.94 (16.38)	85.16 (38.31)	60.97 (25.00)	84.45 (46.14)	41.83 (12.73)	48.54 (28.05)	39.87 (15.87)	44.15 (21.94)
soma perimeter [µm]	-	20.96 (1.33)	24.55 (1.50)	20.57 (5.54)	25.34 (5.70)	36.95 (14.27)	25.06 (7.39)	32.71 (17.00)	31.73 (6.97)	39.40 (12.37)	33.04 (9.89)	41.07 (16.39)	24.68 (4.34)	27.14 (8.52)	24.36 (5.55)	25.94 (9.00)
soma circularity	-	0.93 (0.02)	0.89 (0.01)	0.93 (0.00)	0.93 (0.04)	0.89 (0.06)	0.92 (0.05)	0.88 (0.06)	0.85 (0.07)	0.83 (0.10)	0.83 (0.06)	0.80 (0.12)	0.93 (0.03)	0.92 (0.04)	0.93 (0.04)	0.92 (0.05)
skeleton length [µm]	-	34.57 (33.08)	14.17 (10.34)	24.64 (16.58)	134.94 (45.02)	157.90 (139.42)	128.61 (62.31)	136.15 (91.79)	266.44 (98.87)	279.73 (114.77)	232.24 (85.00)	234.65 (113.18)	295.38 (98.38)	261.21 (108.84)	247.72 (87.95)	251.37 (120.50)
skeleton branch points	-	2 (4)	0	1 (2)	11 (7)	18 (17)	10 (7)	11 (11)	26 (13)	28 (17)	21 (13)	21 (14)	28 (11)	24 (14)	23 (11)	24 (14)
skeleton end points	-	4 (3)	4 (2)	4 (2)	10 (4)	14 (8)	10 (4)	11 (6)	17 (6)	18 (7)	16 (6)	17 (8)	18 (7)	17 (7)	16 (7)	17 (8)
cell processes	-	4 (1)	4 (2)	3 (2)	4 (2)	4 (3)	4 (2)	5 (3)	3 (3)	4 (3)	4 (2)	5 (2)	3 (2)	3 (2)	3 (2)	3 (2)
branching index	-	16.53 (10.70)	14.59 (1.94)	18.48 (12.64)	102.10 (48.62)	151.68 (115.71)	99.43 (56.4)	105.99 (141.97)	180.61 (139.39)	211.98 (124.46)	176.00 (102.10)	195.45 (128.35)	231.43 (134.19)	207.19 (149.09)	188.36 (128.35)	207.12 (159.47)
critical radius	-	3.89 (0)	4.86 (0)	3.89 (1.94)	9.72 (3.89)	11.67 (4.86)	9.72 (3.89)	9.72 (4.86)	13.61 (2.92)	13.61 (2.92)	12.64 (3.89)	13.61 (4.86)	12.64 (2.92)	12.64 (2.92)	12.64 (2.92)	12.64 (3.89)
dendritic maximum	-	4 (1)	3.5 (1)	3 (1)	10 (5)	12 (6)	9 (4)	9 (5)	14 (3)	15 (5)	13 (4)	13 (5)	14 (4)	14 (5)	13 (4)	12 (4)
SRI	-	0.83 (0.25)	0.90 (0.20)	1 (0.53)	2.67 (2.00)	2.69 (2.17)	2.20 (1.59)	2 (1.40)	4.09 (3.75)	3.40 (3.08)	3.25 (2.71)	2.50 (1.96)	5.00 (4.50)	4.33 (3.87)	4.33 (4.09)	3.50 (3.00)

Values are expressed as median (and interquartile range).

Supplementary Table 4: Morphological parameters of classified microglial cells within control and ischemic neocortex and hippocampus.

		cell area [µm ²]	cell perimeter [µm]	convex hull area [µm ²]	convex hull perimeter [µm]	cell solidity	cell convexity	cell circularity	soma area [µm ²]	soma perimeter [µm]	soma circularity	skeleton length [µm]	skeleton branch points	skeleton end points	cell processes	branching index	critical radius	dendritic maximum	SRI	
amoeboid	ICX vs cHC	ns	ns	ns	ns	ns	ns	ns	ns	ns	ns	ns	ns	ns	ns	ns	ns	ns	ns	
	ICX vs iHC	ns	ns	ns	ns	ns	ns	ns	ns	ns	ns	ns	ns	ns	ns	ns	ns	ns	ns	
	cHC vs iHC	ns	ns	ns	ns	ns	ns	ns	ns	ns	ns	ns	ns	ns	ns	ns	ns	ns	ns	
activated	ICX vs ICX	****	****	****	****	****	****	****	****	****	****	****	****	****	****	****	****	****	****	ns
	ICX vs cHC	ns	ns	ns	ns	ns	ns	ns	ns	ns	ns	ns	ns	ns	ns	ns	ns	ns	ns	ns
	ICX vs iHC	ns	ns	ns	ns	****	****	****	****	****	****	****	****	****	****	****	****	****	****	****
	ICX vs cHC	****	****	****	****	****	****	****	****	****	****	****	****	****	****	****	****	****	****	****
rod-like	ICX vs ICX	****	****	ns	****	****	****	****	****	****	****	****	****	****	****	****	****	****	****	****
	ICX vs cHC	****	****	ns	****	****	****	****	****	****	****	****	****	****	****	****	****	****	****	****
	ICX vs iHC	****	****	ns	****	****	****	****	****	****	****	****	****	****	****	****	****	****	****	****
	cHC vs iHC	****	ns	ns	ns	****	****	****	****	****	****	ns	ns	****	****	****	****	****	****	****
ramified	ICX vs ICX	****	****	****	****	****	****	****	****	****	****	****	****	****	****	****	****	****	****	****
	ICX vs cHC	****	****	****	****	ns	****	****	****	****	****	****	****	****	****	****	****	****	****	****
	ICX vs iHC	****	****	ns	ns	****	****	****	****	****	****	****	****	****	****	****	****	****	****	****
	cHC vs iHC	****	****	*	ns	****	****	****	****	****	****	****	****	****	*	****	****	****	****	****

cNCX – control neocortex; iNCX- ischemic neocortex; cHC- control hippocampus; iHC- ischemic hippocampus; ns – not significant; p < 0.05 *, p < 0.01 **, p < 0.001 ***, p < 0.0001 ****

3.2 Long-term diet-induced obesity does not lead to learning and memory impairment in adult mice

Judith Leyh¹, Karsten Winter¹, Madlen Reinicke², Uta Ceglarek^{2,3}, Ingo Bechmann¹, Julia Landmann¹

¹Institute of Anatomy, Faculty of Medicine, University of Leipzig, Leipzig, Germany

²Institute of Laboratory Medicine, Clinical Chemistry and Molecular Diagnostics, Faculty of Medicine, University of Leipzig, Leipzig, Germany

³Leipzig Research Center for Civilization Diseases (LIFE), Faculty of Medicine, University of Leipzig, Leipzig, Germany

RESEARCH ARTICLE

Long-term diet-induced obesity does not lead to learning and memory impairment in adult mice

Judith Leyh¹, Karsten Winter¹, Madlen Reinicke², Uta Ceglarek^{2,3}, Ingo Bechmann¹, Julia Landmann^{1*}

1 Institute of Anatomy, Faculty of Medicine, University of Leipzig, Leipzig, Germany, **2** Institute of Laboratory Medicine, Clinical Chemistry and Molecular Diagnostics, Faculty of Medicine, University of Leipzig, Leipzig, Germany, **3** Leipzig Research Center for Civilization Diseases (LIFE), Faculty of Medicine, University of Leipzig, Leipzig, Germany

* Julia.Landmann@medizin.uni-leipzig.de



OPEN ACCESS

Citation: Leyh J, Winter K, Reinicke M, Ceglarek U, Bechmann I, Landmann J (2021) Long-term diet-induced obesity does not lead to learning and memory impairment in adult mice. PLoS ONE 16(9): e0257921. <https://doi.org/10.1371/journal.pone.0257921>

Editor: Stephen D. Ginsberg, Nathan S Kline Institute, UNITED STATES

Received: May 27, 2021

Accepted: September 13, 2021

Published: September 29, 2021

Copyright: © 2021 Leyh et al. This is an open access article distributed under the terms of the [Creative Commons Attribution License](https://creativecommons.org/licenses/by/4.0/), which permits unrestricted use, distribution, and reproduction in any medium, provided the original author and source are credited.

Data Availability Statement: All relevant data are within the manuscript and its [Supporting information](#) files.

Funding: This study was supported by the Deutsche Forschungsgemeinschaft (DFG, German Research Foundation), SFB 1052 obesity mechanisms (Project number 209933838, SFB-1052/A9) with contributions granted to UC and IB.

Competing interests: The authors have declared that no competing interests exist.

Abstract

Obesity arising from excessive dietary fat intake is a risk factor for cognitive decline, dementia and neurodegenerative diseases, including Alzheimer's disease. Here, we studied the effect of long-term high-fat diet (HFD) (24 weeks) and return to normal diet (ND) on behavioral features, microglia and neurons in adult male C57BL/6J mice. Consequences of HFD-induced obesity and dietary changes on general health (coat appearance, presence of vibrissae), sensory and motor reflexes, learning and memory were assessed by applying a phenotypic assessment protocol, the Y maze and Morris Water Maze test. Neurons and microglia were histologically analyzed within the mediobasal hypothalamus, hippocampus and frontal motor cortex after long-term HFD and change of diet. Long periods of HFD caused general health issues (coat alterations, loss of vibrissae), but did not affect sensory and motor reflexes, emotional state, memory and learning. Long-term HFD increased the microglial response (increased Iba1 fluorescence intensity, percentage of Iba1-stained area and Iba1 gene expression) within the hypothalamus, but not in the cortex and hippocampus. In neither of these regions, neurodegeneration or intracellular lipid droplet accumulation was observed. The former alterations were reversible in mice whose diet was changed from HFD to ND. Taken together, long periods of excessive dietary fat alone do not cause learning deficits or spatial memory impairment, though HFD-induced obesity may have detrimental consequences for cognitive flexibility. Our data confirm the selective responsiveness of hypothalamic microglia to HFD.

1. Introduction

The consumption of a high-fat diet (HFD) and consequent obesity are associated with numerous disorders, including cardiovascular diseases, cancer, and metabolic disturbances such as in glucose metabolism and insulin resistance, as well as accumulation of adipose tissue [1–4]. Further, (diet-induced) obesity has been described to be linked with cognitive deficits and

access to water and food. Young adult male mice (8 weeks (wks) old) were fed with a normal diet (ND) (11 kcal% fat, 53 kcal% carbohydrates, 36 kcal% protein; V1124-300, ssniff Spezialdiäten, Soest, Germany) for 8, 16, 24, and 28 wks or a high-fat diet (HFD) (59 kcal% fat, 26 kcal% carbohydrates, 15 kcal% protein; E15772-34, ssniff Spezialdiäten GmbH, Soest, Germany) for 24 wks or received a dietary change back to ND for 4 or 12 wks after different periods of HFD (4, 12, 24 wks). Laboratory animals were divided into the following ten groups: 8 wks ND (n = 12), 4 wks HFD + 4 wks ND (n = 12, one animal died before the probe trial two of the MWM has been conducted), 16 wks ND (n = 24), 4 wks HFD + 12 wks ND (n = 12), 12 wks HFD + 4 wks ND (n = 12 each), 24 wks ND (n = 18), 12 wks HFD + 12 wks ND (n = 12), 24 wks HFD (n = 18), 28 wks ND (n = 12), 24 wks HFD + 4 wks ND (n = 12) (Fig 1A). Body weight was measured weekly during the whole experiment and daily during behavioral testing. For analysis of the consequences of diet or dietary change we set the following thresholds for a minimal weight gain compared to ND: 25% for 24 wks HFD, 20% for 24 wks HFD + 4 wks ND and 10% for 12 wks HFD + 4 wks ND. Mice which did not reach the threshold were excluded from analysis. All animal experiments were approved by the local state and university authorities. We performed this study in accordance with the guidelines of the Animal Experimental Committee following the German Animal Welfare Act as well as the European guidelines (Directive 2010/63/EU) concerning the protection of laboratory animals. All experimental procedures and protocols were authorized by the local ethics committee of the state of Saxony (Landesdirektion Sachsen, Leipzig, approval no. TVV 41/17).

2.2 Behavioral phenotyping

Behavioral testing was accomplished in a silent, separate room (dim illumination, constant temperature (23°C) and humidity) during the active phase of the animals. Mice had one hour to adjust to the testing room before experiments started. Tests were video-recorded and analyzed later using Video Mot2 software or evaluated and scored directly by an experienced researcher. All behavioral tests were conducted and analyzed by the same experimenter blinded to conditions. After each trial, all testing devices were cleaned with 70% ethanol. An overview of behavioral tests is illustrated in Fig 1B. Memory tests were performed first, followed by tests that required repeated handling. All animals and groups mentioned in 2.1 passed through all behavioral tests described below.

Y maze test. We investigated working and spatial memory following HFD or dietary change using a three-armed horizontal maze (each arm 5 cm x 25 cm) made of white opaque Plexiglas. Test details can be found in Landmann et al. (2019) [51]. Mice were placed in the center of the testing arena and had the liberty to explore the environment freely over 7 min, while the trial was video-recorded from above. Videos were converted to images using FFmpeg (Version 3.3.9, <https://ffmpeg.org>) and image processing was performed using Mathematica (Version 11.3, Wolfram Research Inc., Champaign, IL, USA). Mice were automatically detected. Based on all mouse positions the Y maze shape was reconstructed, all three arm end points as well as the central junction were automatically detected and the three maze arms were labeled. Mouse positions were assigned according to the labeled arms and respective sequential durations of stay of the mouse within the arms were calculated based on the frame rate. The percentage of spontaneous alternations between arms was calculated as follows: $[\text{number of alternations} / (\text{total number of arm entries} - 2)] * 100$ [52].

Morris Water Maze test. Applying the Morris Water Maze test (MWM) we studied learning and long-term memory adapted from previous studies [53, 54]. The set-up consisted of a swimming pool made of white opaque Plexiglas (diameter 120 cm, height 60 cm) with a removable transparent platform (diameter 10 cm, height 20 cm, 1 cm below the water surface).

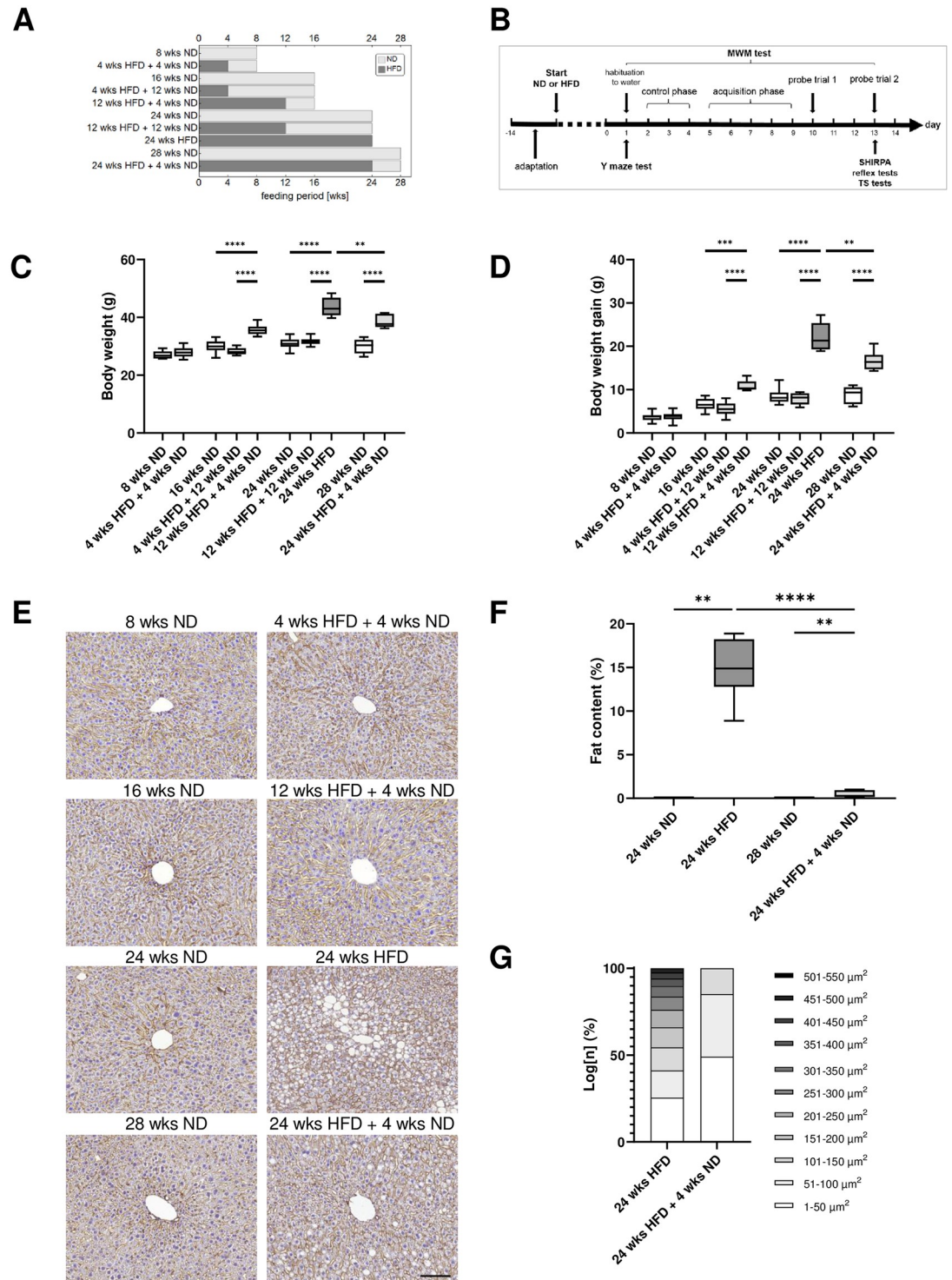


Fig 1. Effect of age, diet and dietary change on body weight and liver tissue. (A) Experimental groups and feeding period. (B) Experimental set-up and sequence of behavioral tests. Mice had 14 days to adapt until diet (ND or HFD) started. Study began with sensitive and cognitive tests (Y maze and MWM test) and terminated with SHIRPA, shorter reflex and tail suspension tests. For histochemical analysis, mice were sacrificed on day 14. (C) Body weight and (D) weight gain of C57BL/6J mice fed with HFD and/or ND for varying wks. (E) Representative liver sections stained for β -catenin and hematoxylin from mice maintained on HFD and/or ND for varying wks, scale bar corresponds to 50 μ m. (F) Quantification of percentage of lipids in β -catenin- and hematoxylin-stained liver sections and (G) quantitative analysis of the proportion (grouped according to size) of lipid droplets in hepatocytes revealed a long-term HFD-induced hepatic steatosis in mice. Data are presented as mean values and error bars

indicate SD; 8 wks ND n = 11 [5], 4 wks HFD + 4 wks ND n = 12 [5], 16 wks ND n = 24 [6], 4 wks HFD + 12 wks ND n = 12 [6], 12 wks HFD + 4 wks ND n = 8 [6], 24 wks ND n = 30 [12], 12 wks HFD + 12 wks ND n = 12 [6], 24 wks HFD n = 10 [6], 28 wks ND n = 12 [6], 24 wks HFD + 4 wks ND n = 7 [6]; in brackets, the number of animals used for liver analysis; (C, D): One-way ANOVA, Welch-ANOVA, unpaired t test, Kruskal-Wallis test; (F): Mann-Whitney test, unpaired t test; **** p < 0.0001; *** p < 0.001; ** p < 0.01.

<https://doi.org/10.1371/journal.pone.0257921.g001>

The water temperature was kept constantly at 23–24°C. Water was made opaque by non-toxic white water color. The testing area was separated from the experimenters' location and the other animals by an opaque folding screen. Animals in the swimming pool were video-recorded from above and tracked automatically (Video Mot2). Initially, we performed a habituation and a control phase to evaluate comparability of data due to visual and motoric capabilities between young and old as well as slim and obese mice (Fig 1B). After the Y maze test, mice were placed three times for 10 sec each onto the platform in the swimming pool for habituation to the water. If the mouse jumped into the water, the animal was carefully guided back to the platform. In the control session (three days), the location of the platform hidden underneath the water surface was indicated by a high contrast check mark. In the following acquisition phase over four days, mice should find the hidden platform using visual cues at the border of the basin. Each mouse was tested in three trials (max. 60 sec each) and was placed under red light between the trials. At day 10, after the training phase, memory retention was tested in probe trial one, where the platform was removed. After two days without training mice were tested again in probe trial two (Fig 1B). Fecal pellets and odors were removed from the water after each trial and water was changed daily.

SHIRPA. We followed a modified SHIRPA protocol (SmithKline Beecham, Harwell, Imperial College, Royal London Hospital, phenotype assessment) to assess general health of mice after different types and periods of nutrition. Mice's appearance and behavior were evaluated using following parameters and scores: palpebral closure (0 = eyes open; 1 = eyes closed), coat appearance (0 = tidy, well groomed; 1 = shaggy, dirty), skin color (0 = blanched, 1 = pink, 2 = deep red), whiskers (0 = absent, 1 = present), tail elevation (0 = dragging, 1 = horizontal extension, 2 = elevated/straub tail), body position (0 = inactive, 1 = active, 2 = excessively active), head tremble (0 = no reaction, 1 = mild shaking, 2 = strong shaking), gait (0 = fluid movement, 1 = irregular, anomalies), touch escape (0 = no reaction, 1 = reaction to touch, 2 = strong reaction to touch/jumps or flees prior), lacrimation (0 = absent, 1 = present), defecation (0 = absent, 1 = present), vocalization (0 = none, 1 = vocal) and biting (0 = none, 1 = present in response to handling). In order to evaluate the effect of diet or dietary change, we measured the body weight.

General reflexes. General sensory and motor abilities were estimated by the following reflexes: vibrissae reflex (0 = no reaction, 1 = reaction to whisker touch, 2 = strong reaction to whisker touch), pinna reflex (0 = no reaction, 1 = reaction to pinna touch, 2 = strong reaction to pinna touch) and writhe reflex (0 = absent, 1 = present) [51].

Tail suspension test. As described by Cryan et al. (2005), mice were suspended by the tail and video-recorded for three min to analyze their behavior to escape (learned helplessness) [55]. Thereby, we evaluated how emotionally stable and stress-resistant animals were, which could influence their performance in cognitive tasks. Time and latency spending active or inactive were measured. Each mouse was tested once and placed back in the home cage at the end. Video processing was conducted exactly as described for the Y maze experiments. Mice were automatically detected and change in segmented mouse size between consecutive frames was considered as an activity marker. Phases of activity and inactivity were automatically detected and durations were calculated based on the frame rate.

2.3 Tissue preparation

At the end of the feeding experiments mice were anesthetized with isoflurane (Baxter GmbH, Unterschleißheim, Germany) and transcardially perfused with ice-cold phosphate buffered saline (PBS, pH 7.4) and 4% paraformaldehyde (PFA) in 0.2 M PBS. Brains were carefully removed from the skull and post-fixed for 24 hours in 4% PFA in 0.2 M PBS before their storage in PBS, containing 0.2% sodium azide, until further processing. Livers of mice were collected for further analysis.

2.4 Histopathological assessment of liver tissue

Liver tissue was fixed with 4% PFA in 0.2 M PBS, dehydrated in graded ethanol series, dealcoholized in xylene and paraffin embedded. Paraffin blocks were sliced into five μm sections, stained with mouse anti- β -catenin (1:500; BD Transduction Laboratories, Franklin Lakes, New Jersey, USA) and counterstained with hematoxylin solution.

Whole β -catenin-stained sections were fully digitized at 20x magnification using a digital slide scanner (Pannoramic Scan II, 3D HISTECH Ltd., Budapest, Hungary). The scanner software (Pannoramic Scanner, version 1.23, 3D HISTECH Ltd., Budapest, Hungary) was operated in extended focus mode (three levels with 0.8 μm axial distance) to combine images from several adjacent focal planes into one image with maximum depth of sharpness. Regions of interest (ROIs) within the specimen were exported from slide scanner data sets (CaseViewer, Version 2.3, 3D HISTECH Ltd., Budapest, Hungary) as PNG images with pixel dimensions of 0.243 μm .

For quantification of hepatic lipid accumulation, PNG images were imported into Mathematica (Version 12.0, Wolfram Research Inc., Champaign, IL, USA) and tissue masks were computed using global thresholding ($t = 0.7$). These masks contained the tissue itself along with holes representing small and/or scattered lipid accumulations, fully formed vacuoles, vesicles as well as artifacts like cuts, fissures or incisions. Almost all lipid accumulations and vacuoles could be detected automatically by using empirically determined size thresholds ($200 < t < 4000$) as well as a roundness parameter (bounding disk coverage > 0.53) for the characterization of these holes. Masks of all remaining structures were superimposed onto the original images and these automatically generated pre-selections were inspected and corrected by hand using GIMP (Version 2.10.2, The GIMP team, <http://www.gimp.org>). Total tissue area and area of lipid accumulations or vacuoles were counted, and ratios were calculated. Furthermore, areas of all individual lipid accumulations and vacuoles were calculated and averaged per image.

2.5 Fluorescence labeling

For immunofluorescence staining with rabbit anti-Iba1 (ionized calcium-binding adaptor molecule 1; Synaptic Systems, Göttingen, Germany) to label microglia and guinea pig anti-NeuN (Synaptic Systems, Göttingen, Germany) to label neurons, perfused and fixed mouse brains were sliced into 50 μm thick coronal floating sections using a vibratome (Leica VT 1200, Leica Biosystems, Wetzlar, Germany). After three washing steps with 0.3% Triton X-100 in PBS for 10 min each time, slices were blocked for one hour in PBS blocking buffer containing 5% normal goat serum and 0.3% Triton X-100 at room temperature. Afterwards, coronal brain sections were incubated with the primary antibodies Iba1 (1:500) and NeuN (1:200) diluted in PBS with 1% of normal goat serum. Incubation was done overnight at 4°C. The next day, slices were rinsed three times with 0.3% Triton X-100 in PBS and incubated with the secondary antibodies goat anti-guinea pig Alexa Fluor 488 (1:200) (Thermo Fisher Scientific, Waltham, Massachusetts, USA) and goat anti-rabbit Alexa Fluor 568 (1:250) (Thermo Fisher

Scientific) for 2 hours at room temperature. Thereafter, sections were washed with PBS, stained five min with 4',6-diamidino-2-phenylindole (DAPI; Thermo Fisher Scientific) and were thoroughly rinsed in PBS. Finally, brain sections were mounted onto microscope slides and covered with Fluorescence Mounting Medium (DAKO, Agilent, Santa Clara, California, USA) and coverslips. For negative controls, the omission of primary antibodies, under otherwise identical conditions, resulted in the absence of any labeling.

2.6 Oil Red O staining

Perfused and fixed mouse brains were sliced with a vibratome (Leica VT 1200, Leica Biosystems, Wetzlar, Germany) into 20 μm thick coronal floating sections for Oil Red O Staining. Brain sections were washed three times with PBS for five min each time followed by incubation with 60% isopropanol for five min. Thereafter, slices were stained with Oil Red O solution [60% Oil Red O stock solution (5 mg/ml isopropanol)/40% water] for 15 min and washed once again three times with PBS for five min each time. Following a short incubation with 40% isopropanol, brain slices were thoroughly rinsed in PBS and counterstained with hematoxylin solution for one min. Finally, brain sections were mounted onto microscope slides and covered with Glycergel mounting medium (DAKO, Agilent, Santa Clara, California, USA) and coverslips.

2.7 Image acquisition and quantification of fluorescence staining

Microscopic images of Iba1 and NeuN staining were captured with a confocal microscope (LSM 700, Zeiss, Jena, Germany) applying a 20 \times /0.5 NA objective at constant exposure times within hypothalamic, hippocampal and neocortical regions. Confocal z-stack images were acquired using the ZEN 2 (blue edition) software (Zeiss) and an interval size of 2.0 μm for a total range of 30 μm ($n = 16$ optical slices per animal, 6–12 animals per condition). All in all, five ROIs, the mediobasal hypothalamus, the CA1 and CA3 region, the dentate gyrus, and the frontal motor cortex were acquired for each animal to quantify Iba1 and NeuN immunosignals. Two ROIs per animal within the mentioned brain areas were analyzed in coronal brain sections at Bregma -1.7 mm. Fluorescence intensity and staining area measurements of z-stack maximum intensity projections were processed using ImageJ software (National Institutes of Health, Bethesda, MD, USA). The percent area occupied by Iba1- or NeuN-immunopositive cells per ROI was measured after a threshold adjustment of the images. The total staining intensity was expressed by integrated density (mean gray value \times area) using the ROI manager and the background subtraction function of ImageJ. The reactive state of microglial cells is frequently measured by fluorescence intensity of Iba1 or by percentage of Iba1-stained area [37, 45, 56–59].

For quantitative analysis of microglial morphology, original confocal z-stack images were imported into Mathematica and maximum intensity projections of the Iba1 channels were computed. Microglia cells were automatically detected using a previously developed approach [60]. In brief, images were contrast enhanced, Iba1-positive structures (somata and processes) were segmented and all somata were identified. Processes not connected to any somata were removed and all interconnected microglia cells were separated from each other based on a parallel flood fill operation starting from the soma centroids. ROIs were drawn onto the maximum intensity projections and used for the masking of all detected cells. Remaining cells within the respective regions were uniquely labelled. Further, microglial cells were submitted to quantification and 17 parameters were calculated for each detected Iba1-positive cell ($n = 9186$). Parameters include *cell areas* (μm^2) and *perimeters* (μm) of whole cells, their *convex hulls* (the smallest convex set of pixels that encloses a cell) and their *soma*; *cell solidity* (the

degree to which the *area* of a cell fills the area of its *convex hull*) and *convexity* (the ratio of a cell's *convex hull perimeter* to the cell's actual perimeter); *circularity* of cells and soma (the roundness, where one equals a perfect circle and values smaller than one indicate shapes that increasingly deviate from the shape of a circle); *length* (μm) as well as number of *branch* and *end points* of the skeletonized *processes*; and the number of *cell processes*. Furthermore, all cells were submitted to Sholl analysis [61] and the cell's *branching index* [62] (a measure to distinguish between cells of different ramification types), *critical radius* (μm) (the radius with the maximum number of process crossings) and *dendritic maximum* (the number of process crossings at the critical radius) were calculated. Values for each parameter were averaged for all images of one animal to define the value per animal and per group, respectively. Additionally, for whole images the microglial cell density (cells per mm^2) was computed.

2.8 Image acquisition and quantification of Oil Red O staining

The staining of lipid droplets in coronal brain sections using Oil Red O solution was fully digitized using the same digital slide scanner and image export procedures mentioned above (see 2.4). The only exception was that the extended focus mode was set to 30 levels with $1.2 \mu\text{m}$ axial distance at 40x magnification to combine images from several adjacent focal planes into one image with maximum depth of sharpness resulting in exported PNG images with pixel dimensions of $0.122 \mu\text{m}$.

For quantification of lipid droplets, PNG images were imported into Mathematica, white-balanced and submitted to color deconvolution resulting in separate images for red (Oil Red O) and blue (hematoxylin) staining. Red images were background-corrected (ten pixel wide Gaussian filter), lipid droplets were segmented using local adaptive thresholding (100 pixel wide radius) and specks smaller than ten pixels were removed. Blue images were adjusted for brightness and gamma, nuclei were segmented using global thresholding (threshold value 0.15) followed by morphological closing (three pixel radius), and specks smaller than 200 pixels were removed. Due to the varying quality of Oil Red O staining segmented droplets were manually corrected using GIMP to remove tissue artifacts when necessary. Total tissue area, cell area, droplet area and red signal intensity were counted and ratios were calculated.

2.9 Quantitative RT-qPCR

Hypothalamus, hippocampus and frontal cortex were quickly dissected from the brain of mice fed with ND or HFD for 24 wks after transcatheter perfusion with ice-cold phosphate buffered saline (PBS, pH 7.4). Brain tissue was flash-frozen in liquid nitrogen and stored at -80°C until RNA isolation.

RNA isolation and cDNA synthesis: Messenger RNA (mRNA) of the hypothalamus, hippocampus and prefrontal murine cortices was isolated using RNeasy Mini Kit (Qiagen, Hilden, Germany) according to manufacturer's instructions. Reverse transcription was performed with the ProtoScript First Strand Synthesis Kit (New England Biolabs, Frankfurt am Main, Germany) using $1 \mu\text{g}$ total RNA as template.

RT2 Profiler™ PCR array: Gene expression of *Iba1* was analyzed using a RT2 Profiler™ PCR array. Primers were synthesized by the manufacturer Qiagen and are adsorbed on the bottom of each well in a 96-well microplate, one primer pair per well. Each PCR array plate includes three housekeeping genes (*Actb*, *Gapdh*, *B2m*) as well as controls for genomic DNA contamination, reverse transcription efficiency and general PCR performance. Thermal cycling and fluorescence detection were performed using the CFX96 Touch Real-Time PCR Detection System from Bio-Rad Laboratories GmbH (Feldkirchen, Germany). The utilized temperature protocol includes an initial melting for 10 min at 95°C , 40 cycles of amplification (15 s at 95°C ,

1 min at 60°C) followed by a melt curve. Relative gene expression was calculated using the $\Delta\Delta\text{Ct}$ method ($2^{-\Delta\Delta\text{Ct}}$). All Ct values of target cDNAs were normalized to the average of three housekeeping genes.

2.10 Statistical analysis

Behavioral data were tested for normal distribution using the D'Agostino & Pearson test. Non-parametric data (scored parameters or parameters not following a normal distribution) were analyzed by the Kruskal-Wallis test followed by Dunn's method for multiple comparisons or the Mann-Whitney test. For parametric data (following a normal distribution) one-way ANOVA and unpaired t test (equal SDs) or Welch-ANOVA and Welch's t test (unequal SDs), and for multifactorial data two-way ANOVA were performed using Tukey's method for multiple comparisons. Immunohistochemical data of liver tissue were tested for normal distribution using the Kolmogorov-Smirnov test and validated by Mann-Whitney (non-parametric) or unpaired t test (parametric). Data of immunofluorescence staining were tested for normal distribution using the Shapiro-Wilk test and were analyzed by one-way ANOVA followed by Tukey's method for multiple comparisons, unpaired t test or Welch-ANOVA followed by Dunnett's method for multiple comparisons. The qPCR data was tested for normal distribution using the Shapiro-Wilk test and differences between the ND and HFD group were validated by an unpaired t test. Analysis of data was performed separately within age-matched (4 sub-analyses: 8 wks ND vs. 4 wks HFD + 4 wks ND; 16 wks ND vs. 4 wks HFD + 12 wks ND vs. 12 wks HFD + 4 wks ND; 24 wks ND vs. 12 wks HFD + 12 wks ND vs. 24 wks HFD; 28 wks ND vs. 24 wks HFD + 4 wks ND) as well as diet-matched (3 sub-analyses: 8 vs. 16 vs. 24 vs. 28 wks ND; 4 wks HFD + 4 wks ND vs. 12 wks HFD + 4 wks ND vs. 24 wks HFD + 4 wks ND; 4 wks HFD + 12 wks ND vs. 12 wks HFD + 12 wks ND) groups. We compared age-matched mice to analyze the impact of diet and dietary change as well as diet-matched mice to examine the effect of age on behavioral features, microglia and neurons. For better clarity, only significant results of age-matched groups are presented in the figures and significant results of diet-matched groups are shown in [S1 Table](#). GraphPad Prism 9.2.0 (GraphPad Software, San Diego, CA, USA) was applied to perform statistical analyses of behavioral and histological data. Statistic details are given in the figure legends, result section and [S1 Table](#). Number of analyzed animals is indicated as "n" in the figure legend. Data are presented as mean \pm SD. Statistical significance was determined as follows: $p < 0.05$ *, $p < 0.01$ **, $p < 0.001$ ***, $p < 0.0001$ ****.

3. Results

3.1 HFD and dietary change have an effect on body weight and liver tissue

As expected, diet had a highly significant effect on mice's body weight and animals benefited significantly from a dietary change back to ND after HFD exposure ([Fig 1C](#); [S1 Table](#), ll. 1–3). Thereby, even a short period of four wks ND following a long-term HFD of 24 wks revealed a positive effect on the body weight ([Fig 1C](#); unpaired t test, $p = 0.0024$; [S1 Table](#), l. 4). Further, we observed a strong effect of age on body weight as well ([S1 Table](#), ll. 5–7). Older mice fed with ND gained significantly more body weight compared to younger animals ([Fig 1D](#); [S1 Table](#), l. 12).

To control the effectiveness of HFD, we performed staining of liver tissue with β -catenin and hematoxylin and found an increase in lipid accumulation after long-term HFD compared to mice fed with ND ([Fig 1E and 1F](#); Mann-Whitney test, $p = 0.0022$; [S1 Table](#), l. 15) as shown before [63, 64]. Mouse liver tissue in ND groups and groups that received short- and mid-term HFD (four and 12 wks) followed by a dietary change back to ND exhibited the typical

hepatolobular architecture and hepatocytes displayed their normal polygonal shape showing distinctive nuclei along with no signs of steatosis (Fig 1E). In contrast, we observed high amounts of lipid droplets (macrovesicular steatosis) after long-term HFD in liver tissue. However, already four wks ND after 24 wks HFD significantly improved the livers' fat content, but these mice exhibited even more lipid droplets in hepatocytes than their age-matched control group (Fig 1E and 1F; unpaired t test, $p < 0.0001$, Mann-Whitney test, $p < 0.0022$; S1 Table, ll. 16–17). Moreover, lipid droplet sizes showed a shift of hepatic lipid droplets toward smaller ones in mice that received long-term HFD followed by a dietary change. Long-term HFD alone also leads to hepatic lipid droplets of enormous size (Fig 1G).

3.2 Long periods of HFD lead to general health issues without modification of reflexes

General health parameters and basic reflexes were observed following the SHIRPA protocol (Fig 2). Long-time HFD caused impairment of the coat compared to age-matched control animals, which manifested in weak and scrubby fur with bare spots (Fig 2A; Kruskal-Wallis test, $p = 0.0124$; S1 Table, l. 18). In contrast, HFD shorter than 24 wks did not lead to obvious differences (Fig 2A). Interestingly, already a change of diet from 12 wks HFD to 4- or 12-wks ND rescued this effect (Fig 2A). Similarly, only mice receiving HFD for 24 wks showed significantly less vibrissae compared to control mice (Fig 2B; Kruskal-Wallis test, $p < 0.0001$; S1 Table, l. 19). Further, a longer change to ND after mid-term HFD led to preservation of the vibrissae, while a short change of diet after long-term HFD was not sufficient (Fig 2B; Mann-Whitney test, $p = 0.0036$; S1 Table, l. 20). No differences were observed concerning the general activity (Fig 2C) or the touch escape reactivity (Fig 2D). Further, no obvious differences exist according to the appearance of the eyes, skin, tail and gait or fecal pellets after HFD or dietary change compared to ND (S1A–S1E Fig). In addition, young and old mice as well as animals on HFD and ND showed a similar sensory reactivity testing for the vibrissae (Fig 2E), of the pinna (Fig 2F) and a moderate motor reactivity indicated by the writhe reflex (S1F Fig).

3.3 HFD has no effect on short-term memory

A potential effect of diet and dietary change on short-term memory was studied applying the Y maze test. Number of spontaneous alternations neither differed significantly between diets or after dietary change nor between young and old mice (Fig 3A). Further, we found no difference in the number of double arm visits (errors) regarding diet/dietary change or age (Fig 3B). Analysis revealed a significant effect of diet/dietary change on activity between mice being 12 wks on HFD followed by 12 wks of ND compared to age-matched mice on ND and HFD (Fig 3C; One-way ANOVA, $p = 0.0021$; S1 Table, l. 22). Further, there was a significant effect of age in both control and HFD groups on general activity, indicated by a decreasing number of total arm entries in the maze (Kruskal-Wallis test, $p < 0.0001$; One-way ANOVA, $p = 0.0129$; S1 Table, ll. 23–24). There was a strong effect of HFD as well as dietary change and age on body weight, though a short period of ND after long-term HFD did not rescue the phenotype (Fig 3D). Therefore, we conclude that there is no effect of long-term HFD on working memory.

3.4 Learning is not affected by diet

Analyzing the control phase of the MWM test revealed no main effect of diet or dietary change or age on learning performance (Fig 4A). Latencies to find the target quadrant were significantly higher in mice on long-term HFD compared to age-matched mice on mid-term HFD followed by a return to ND on day one and two as well as on day three in comparison to age-matched control mice (Fig 4A; Two-way ANOVA, day $p < 0.0001$, diet $p = 0.0003$, interaction

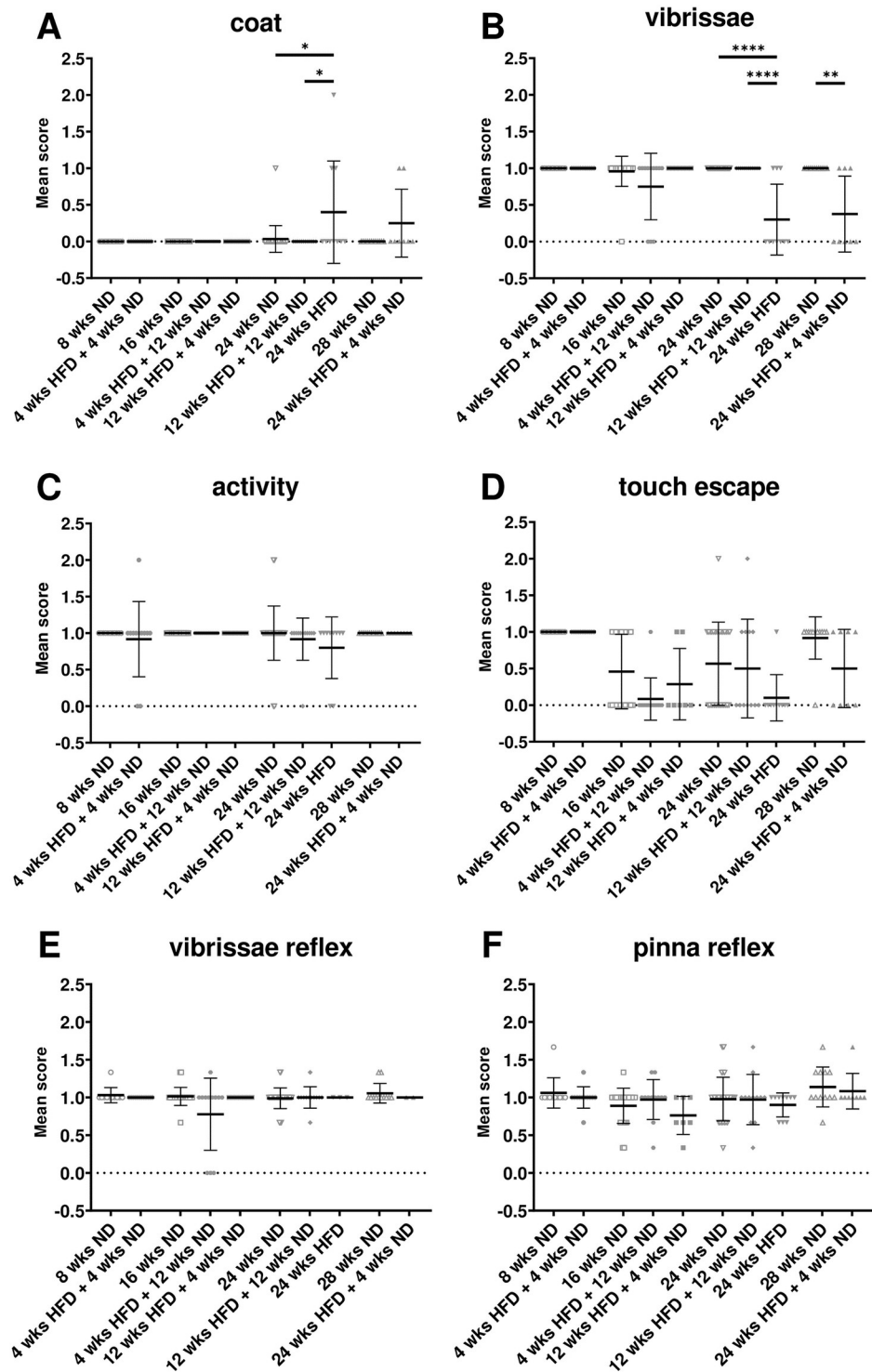


Fig 2. HFD leads to general health issues. (A-D) SHIRPA analysis was used to estimate general health of mice after ND or HFD. (A) Long-term HFD led to problems with the coat and (B) the loss of vibrissae, while there was more variance, but no significant difference after HFD in (C) general activity and (D) touch escape. Normal sensory reflexes as the (E) vibrissae and the (F) pinna reflex were observed in all groups irrespective of diet or age. Data are presented as mean values and error bars indicate SD; 8 wks ND n = 11, 4 wks HFD + 4 wks ND n = 12, 16 wks ND n = 24, 4 wks HFD + 12 wks ND n = 12, 12 wks HFD + 4 wks ND n = 7, 24 wks ND n = 30, 12 wks HFD + 12 wks ND n = 12, 24 wks HFD n = 10, 28 wks ND n = 12, 24 wks HFD + 4 wks ND n = 8; Kruskal-Wallis test, Mann-Whitney test; **** p < 0.0001; ** p < 0.01; * p < 0.05.

<https://doi.org/10.1371/journal.pone.0257921.g002>

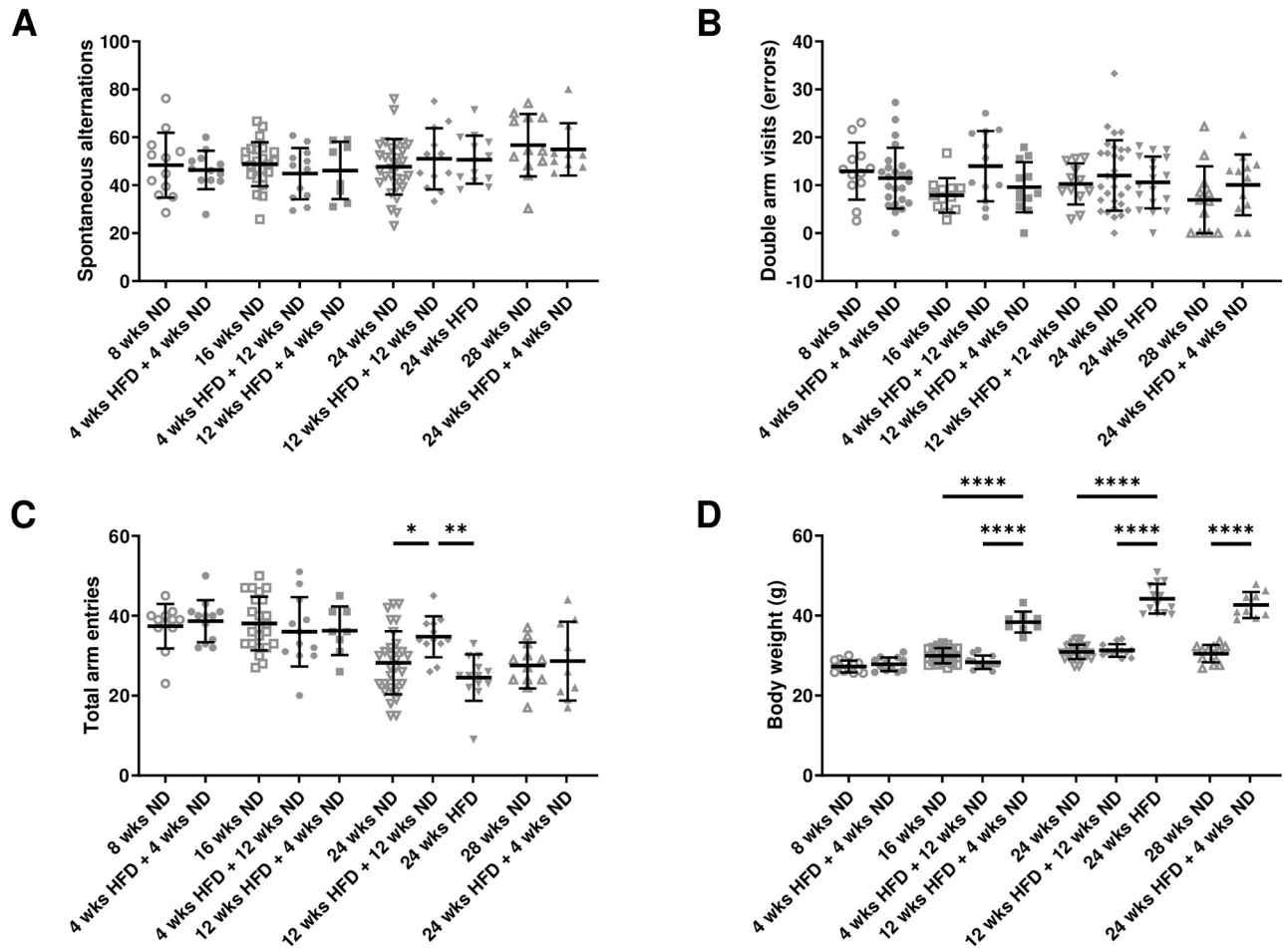


Fig 3. HFD has no effect on short-term memory in the Y maze test. (A) Spontaneous alternations were not affected by diet/dietary change. (B) No difference in the number of double arm visits (errors) regarding diet/dietary change was found. (C) Analysis of total arm entries revealed a significant effect of diet. (D) Mice gained more weight after longer HFD or rather lose weight after dietary change from HFD to ND. Data are presented as mean values and error bars indicate SD; 8 wks ND n = 11, 16 wks ND n = 24, 24 wks ND n = 30, 28 wks ND n = 12, 4 wks HFD + 4 wks ND n = 12, 12 wks HFD + 4 wks ND n = 8, 4 wks HFD + 12 wks ND n = 12, 12 wks HFD + 12 wks ND n = 12, 24 wks HFD n = 13, 24 wks HFD + 4 wks ND n = 9; (C) One-way ANOVA, (D) One-way ANOVA, Welch-ANOVA, unpaired t test; **** p < 0.0001; ** p < 0.01; * p < 0.05.

<https://doi.org/10.1371/journal.pone.0257921.g003>

p = 0.0432; [S1 Table](#), l. 34). However, mice fed with ND for 24 wks took more time to find the target quadrant than mice being 12 wks on HFD followed by 12 wks of ND. On all days, decreased latencies to find target quadrant and platform were observed for mice receiving 12 wks ND after 12 wks HFD compared to age-matched mice on ND or HFD ([Fig 4A and 4B](#)). Almost all groups showed an improvement in learning performance regarding the latency to find target quadrant and platform ([Fig 4A and 4B](#); [S1 Table](#), ll. 31–63). We found no effect of diet or dietary change on activity, but an impact of age on total distance in ND and HFD groups ([Fig 4C](#); [S1 Table](#), ll. 64–81). Therefore, we assumed similar preconditions of age-matched mice regarding vision, motor function and learning for lean and adipose mice.

The training phase was used to estimate the learning performance after different diets or dietary change. The significant main effect of diet/dietary change according to the latency to find the target quadrant counted for day one only ([Fig 4D](#); [S1 Table](#), ll. 82–90). Similarly, younger animals initially showed a shorter latency to find the target quadrant ([S1 Table](#), l. 91). Further, there was no main effect of diet on the latency to find the platform and an improvement

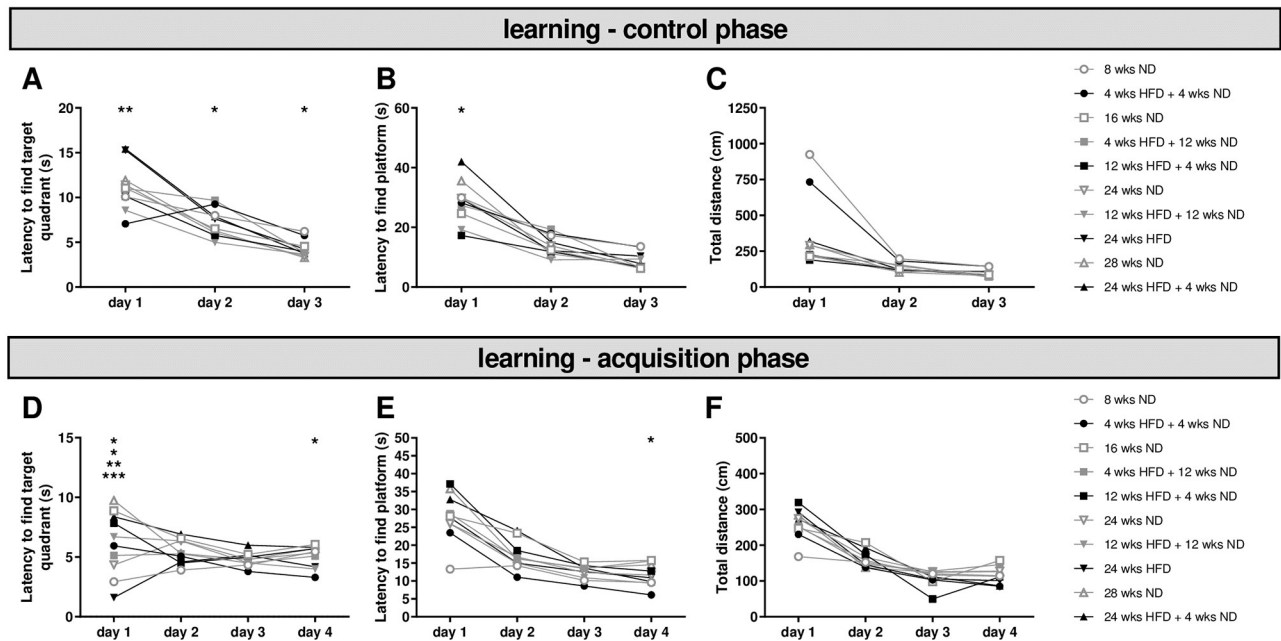


Fig 4. Learning is not affected by HFD. Before performing the MWM test, mice had three days to find the marked platform underneath the water by using visual information (control phase). (A) Diet had an effect on the latency to find the target quadrant. (B) We observed an effect on the latency to find the platform only on the first day regarding diet. (C) The motor activity was not affected by diet and general learning performance did not differ with respect to diet/dietary change. After the control phase, mice were trained for four days to perform the MWM test (acquisition phase). (D) Latency to find the target quadrant differed for some groups on day one and four, but learning did not change due to diet. (E) Latency to find the platform underneath the water surface showed no effect of diet. Performance up to day four did not differ relative to diet. (F) Motor activity was similar for mice on different diets. Data are presented as mean values and error bars indicate SD; 8 wks ND $n = 12$, 16 wks ND $n = 24$, 24 wks ND $n = 30$, 28 wks ND $n = 12$, 4 wks HFD + 4 wks ND $n = 12$, 12 wks HFD + 4 wks ND $n = 7$, 4 wks HFD + 12 wks ND $n = 12$, 12 wks HFD + 12 wks ND $n = 12$, 24 wks HFD $n = 11$, 24 wks HFD + 4 wks ND $n = 9$; Two-way ANOVA; *** $p < 0.001$; ** $p < 0.01$; * $p < 0.05$.

<https://doi.org/10.1371/journal.pone.0257921.g004>

in learning performance was observed in all groups with the exception of the study's youngest group on ND showing consistently short latencies to find the platform from day one (Fig 4E; S1 Table, ll. 94–111). Again, we observed a significant effect of age within ND and HFD groups on the first day (S1 Table, ll. 106, 109). However, the learning performance did not differ between groups (S1 Table, ll. 107, 110). Additionally, we found no main effect of diet/dietary change on total distance and all groups with the exception of the study's youngest group on ND increased similarly until day four (Fig 4F; S1 Table, ll. 112–123). The main effect of age on the total distance was limited to the first and third day within HFD groups and did not differ until the end of training (S1 Table, ll. 124–129). In line with the control phase, the training phase showed no differences of diet/dietary change or age on overall learning performance.

3.5 HFD-induced obesity does not lead to long-term memory deficits, but may alter cognitive flexibility

In probe trial one, we observed no effect of diet/dietary change on time spent in the target quadrant and all groups of mice showed a significant discrimination between the target and the opposite quadrant (Fig 5A; S1 Table, ll. 130–141). In contrast, mice with increasing age spent more time in the target and respectively less time in the opposite quadrant within HFD groups (S1 Table, ll. 142–147). Further, there was no effect of diet/dietary change or age on the latency to find the target quadrant (Fig 5B). Total distance decreased in mice on long-term HFD compared to age-matched control groups (Fig 5C; One-way ANOVA, $p = 0.0006$; S1

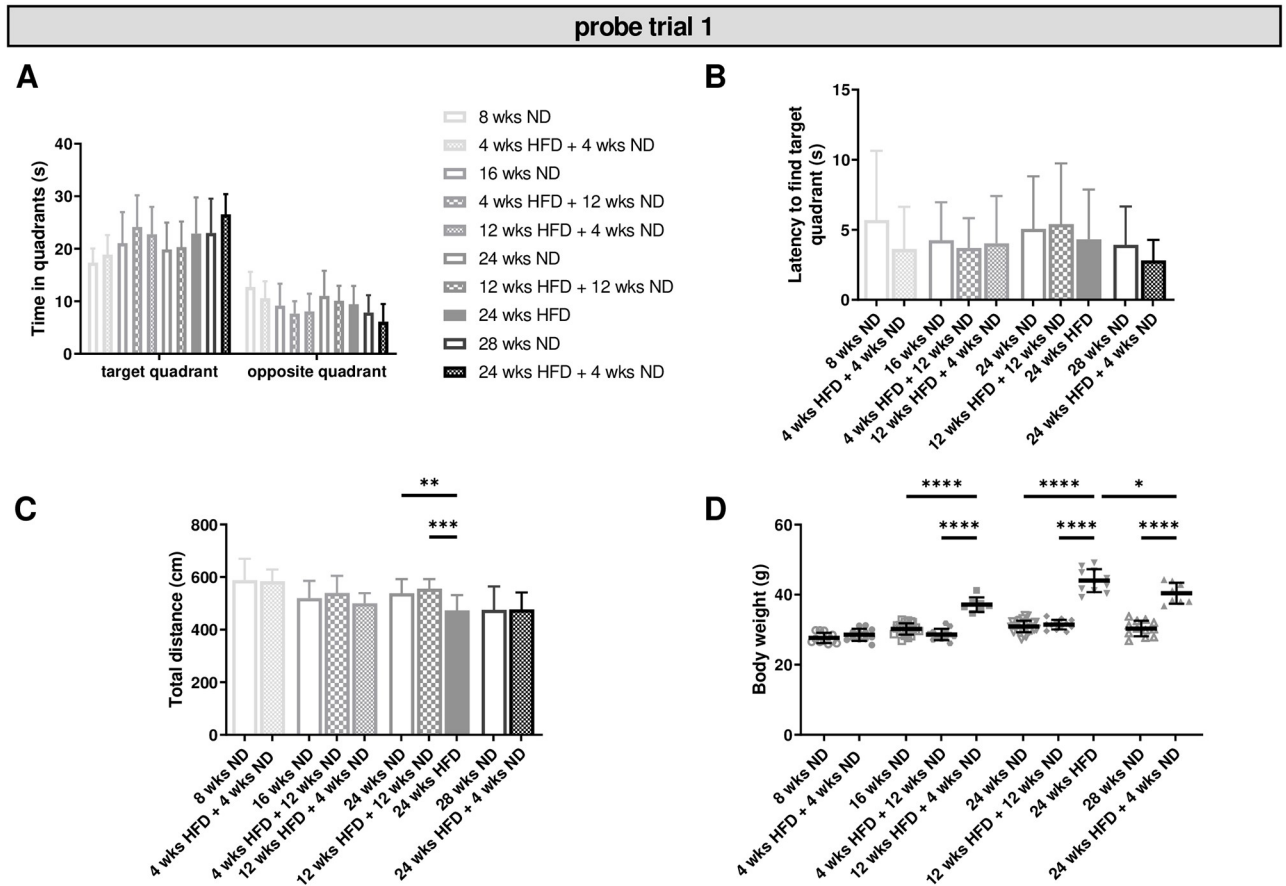


Fig 5. Diet-induced obesity causes no impairment of memory. Memory retention (probe trial one) was tested after four days of training in the MWM test. (A) Diet/dietary change had no effect on the time mice spent in quadrants, while older animals spent more time in the target quadrant. (B) No effect was found regarding the latency to find the target quadrant. (C) Motor activities were reduced in mice receiving 24 wks of HFD compared to age-matched control mice. (D) Diet had a significant effect on body weight and mice benefited from a change to ND after HFD. Data are presented as mean values and error bars indicate SD; 8 wks ND n = 12, 16 wks ND n = 24, 24 wks ND n = 30, 28 wks ND n = 12, 4 wks HFD + 4 wks ND n = 12, 12 wks HFD + 4 wks ND n = 7, 4 wks HFD + 12 wks ND n = 12, 12 wks HFD + 12 wks ND n = 12, 24 wks HFD n = 11, 24 wks HFD + 4 wks ND n = 8; (A): Two-way ANOVA, (B, C, D): One-way ANOVA, Welch-ANOVA, unpaired t test; ****, p < 0.0001; ***, p < 0.001; **, p < 0.01; *, p < 0.05.

<https://doi.org/10.1371/journal.pone.0257921.g005>

Table, I. 148). The motor activity also decreased with age within ND and HFD groups (S1 Table, II. 149–150). As expected, mice receiving HFD gained significant more weight than mice on ND and animals benefited significantly from dietary change (Fig 5D; S1 Table, II. 151–154). Body weight enhanced also with increasing age independent of diet (S1 Table, II. 155–157). No effect of diet/dietary change or age was found relative to the latency to find the platform location. In sum, we found no effect of diet/dietary change on test performance, but observed a negative effect of age within ND and HFD groups. However, our data revealed a strong effect of diet/dietary change and age on body weight. Further, long-term HFD and advanced age also resulted in decreased motor activity.

In a second probe trial, we observed no overall effect of diet/dietary change on time spent in the target or opposite quadrant. However, mice fed with HFD for 24 wks stayed significantly longer in the target quadrant compared to age-matched control groups (Fig 6A; two-way ANOVA, quadrant p < 0.0001, diet p = 0.3411, interaction p < 0.0001; S1 Table, II. 164–166). Just as in probe trial one, we observed no effect of diet and age relative to the latency to find

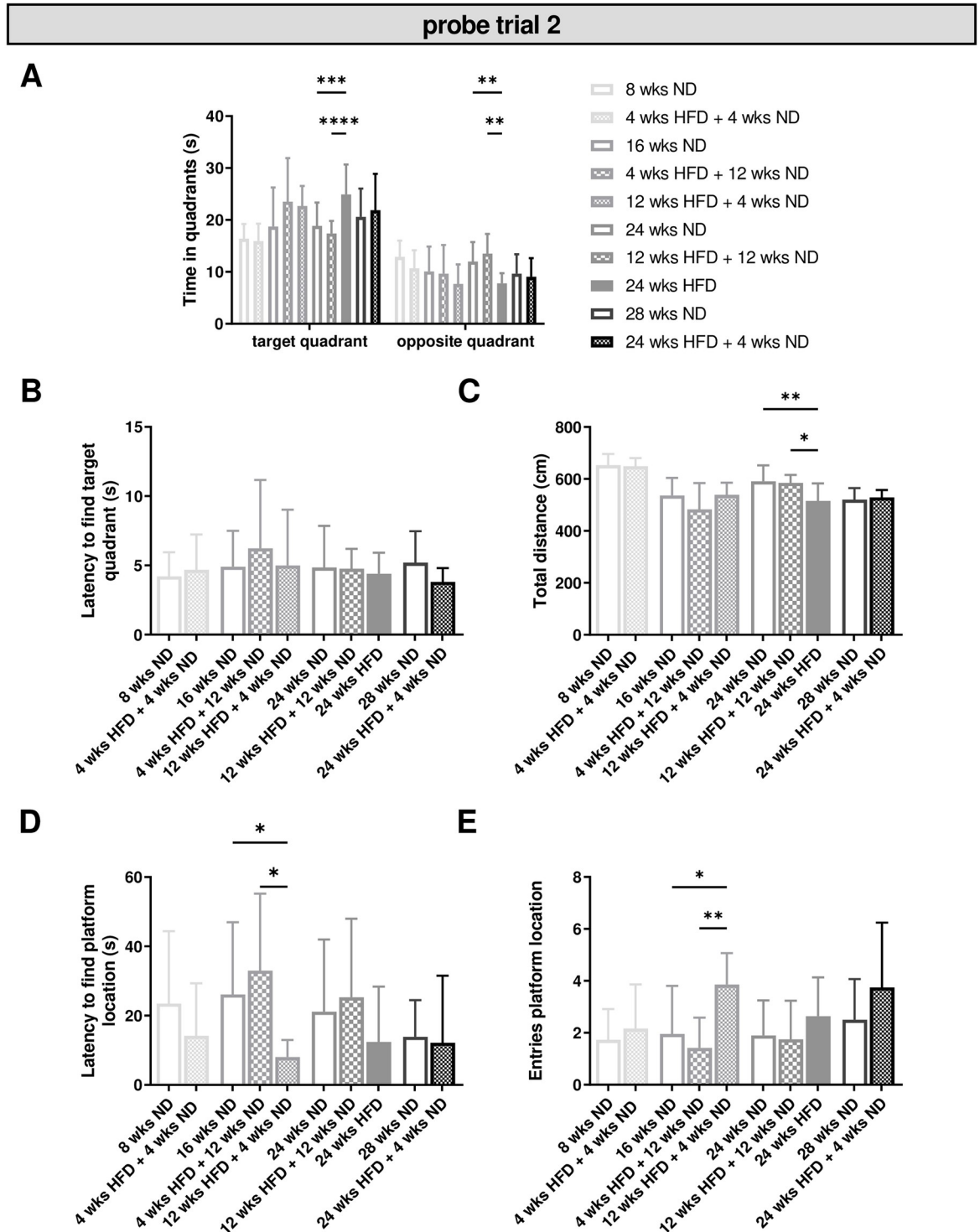


Fig 6. HFD leads to intact long-term memory, but may impair cognitive flexibility. Memory retention (probe trial two) was tested again after two days without any training in the MWM test. (A) Time mice spent in the target quadrant was significantly increased in mice receiving 24 wks of HFD compared to age-matched control mice. (B) No effect of diet was observed relative to the latency to find the target quadrant. (C) Diet had an effect on motor activity. (D, E) Dietary change showed a shorter latency to find the platform location and a significant effect on the entries to the platform location. Data are presented as mean values and error bars indicate SD; 8 wks ND n = 12, 16 wks ND n = 12, 24 wks ND n = 18, 28 wks ND n = 12, 4 wks HFD + 4 wks ND n = 12, 4 wks HFD + 12 wks ND n = 7, 4 wks HFD + 12 wks ND n = 12, 12 wks HFD + 12 wks ND n = 12, 24 wks HFD n = 10, 24 wks HFD + 4 wks ND n = 8; (A): Two-way ANOVA, (C): One-way ANOVA, (D, E): Kruskal-Wallis test; **** p < 0.0001; *** p < 0.001; ** p < 0.01; * p < 0.05.

<https://doi.org/10.1371/journal.pone.0257921.g006>

the target quadrant (Fig 6B). The motor activity was significantly reduced after long-term HFD of 24 wks compared to age-matched control animals (Fig 6C; One-way ANOVA, $p = 0.0016$; S1 Table, l. 173) and showed a significant effect of age within ND and HFD groups (S1 Table, ll. 174–175). Further, we observed a reduced latency and significant more entries of the platform location in mice with a short ND time after 12 wks of HFD compared to four wks of HFD followed by a longer ND period, while there was no effect of age (Fig 6D and 6E; Kruskal-Wallis test, latency $p = 0.0164$, entries $p = 0.0052$; S1 Table, ll. 176–177).

In sum, our investigations revealed no effect of diet/dietary change, but of age on memory performance with a strong effect of age and diet/dietary change on body weight. While we observed no effect of diet or age relative to the platform location during the first probe trial, there was an effect of dietary change in the probe trial two.

3.6 HFD has no consequences for the emotional state

In order to test whether HFD-induced obesity leads to alterations of the emotional condition (e.g. motivation), we conducted the tail suspension test. Healthy mice are meant to try to escape by active movements, when fixed and suspended by their tails. In our study no effect of diet/dietary change on activity was detected, while older mice within ND groups were more active in this test (S2A Fig; S1 Table, ll. 183–184). However, we observed no difference of diet/dietary change or between mice of different age according to the latency to inactivity (S2B Fig). Therefore, we conclude that there are no consequences of HFD on the emotional state in mice.

3.7 Increased microglial activation after long periods of HFD in the hypothalamus

We performed immunostaining on coronal brain sections of the youngest mice (8 wks ND vs. 4 wks HFD + 4 wks ND), animals that received mid-term HFD followed by a dietary change back to ND for the same period of time (24 wks ND vs. 12 wks HFD + 12 wks ND), older mice on long-term HFD (24 wks ND vs. 24 wks HFD) and with dietary change (28 wks ND vs. 24 wks HFD + 4 wks ND) to assess the effect of diet/dietary change on microglial and neuronal morphology in the hypothalamus ($n = 6$ –12 mice per condition). Microglial response determined by Iba1 signal intensity increased after 24 wks of HFD (Fig 7A and 7B; Welch-ANOVA, $p = 0.0069$; S1 Table, l. 178). Similarly, the area covered by Iba1-positive cells was significantly enhanced after 24 wks of HFD compared to ND for 24 wks (Fig 7C; One-way ANOVA, $p = 0.0003$; S1 Table, l. 180). Interestingly, long-term HFD (24 wks) followed by a dietary change back to ND resulted in lower Iba1 fluorescence intensity and smaller area of Iba1-positive cells (Fig 7B and 7C; S1 Table, ll. 179, 181). Short- and mid-term HFD (four and 12 wks) followed by a dietary change back to ND did not lead to higher fluorescence intensities and percentage of Iba1-stained area compared to age-matched control mice (Fig 7B and 7C). However, we could detect a trend towards higher fluorescence intensity and percentage of stained area with Iba1 after 12 wks on HFD followed by 12 wks on ND and 24 wks on HFD followed by four wks on ND compared to 24 wks on ND (Fig 7B and 7C). Indeed, in mice fed with ND or HFD followed by dietary change, we predominantly observed the ramified form of microglia exhibiting small somata and fine ramifications, while in the hypothalamus of mice on long-term HFD, many microglial cells displayed an activated morphology with thickened processes and bigger cell bodies. Number of Iba1-positive cells was slightly elevated following long-term HFD, but the difference between 24 wks on ND and 24 wks on HFD was not significant (Fig 7D; One-way ANOVA, $p = 0.1164$). Further, hypothalamic expression of mRNA encoding *Iba1* increased by 25% in mice fed a HFD for 24 wks (S3 Fig; Two-tailed unpaired t

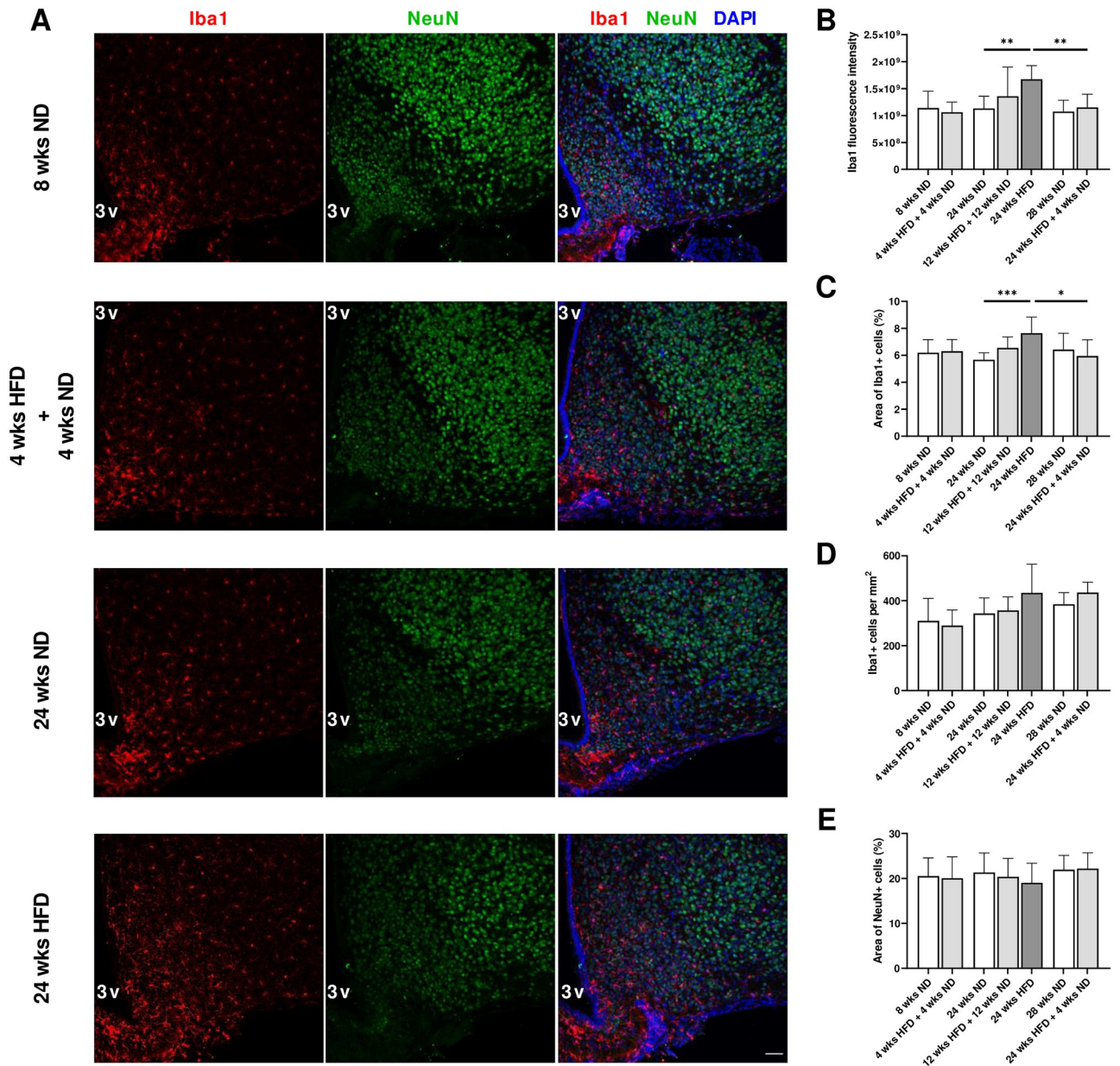


Fig 7. Increased microglial activation after long periods of HFD in the hypothalamus. (A) Representative confocal images of double-labeled immunofluorescence staining for Iba1 (red) and NeuN (green) within the mediobasal hypothalamus of male wild-type C57BL/6J mice fed with ND for eight wks, HFD for four wks followed by ND for four wks and ND or rather HFD for 24 wks. Nuclei were counterstained with DAPI. Scale bar corresponds to 50 μ m; 3v, third ventricle. (B) Fluorescence intensity measurements of Iba1, (C) quantification of percentage of area covered by Iba1 and (E) NeuN-immunoreactive profiles and (D) number of Iba1-immunoreactive cells revealed a microgliosis in response to long-term HFD exposure without effects on neurons. Data are presented as mean values and error bars indicate SD; 8 wks ND n = 6, 4 wks HFD + 4 wks ND n = 6, 24 wks ND n = 12, 12 wks HFD + 12 wks ND n = 6, 24 wks HFD n = 6, 28 wks ND n = 6, 24 wks HFD + 4 wks ND n = 6; (B): Welch-ANOVA, unpaired t test, (C): One-way ANOVA, unpaired t test; *** p < 0.001; ** p < 0.01; * p < 0.05.

<https://doi.org/10.1371/journal.pone.0257921.g007>

test, p = 0.0328; [S1 Table](#), l. 185). We did not observe morphological alterations in neurons within the mediobasal hypothalamus after a dietary change or a long-term HFD ([Fig 7A and 7E](#)). In summary, long periods of HFD increased microglial activation within the mediobasal hypothalamus without effects on neuronal morphology and NeuN-stained areas as a substitute for cell numbers.

3.8 HFD-induced obesity does not alter cortical and hippocampal morphology

There were no differences regarding fluorescence intensity and percentage of area of both Iba1 and NeuN immunosignals between the analyzed groups within the frontal motor cortex ([S4A–S4C and S4E Fig](#)). Number of Iba1-positive cells was not altered after diet/dietary change compared to age-matched mice ([S4D Fig](#)). Similarly, we found no alterations within hippocampal areas CA1, CA3 and dentate gyrus after HFD exposure and dietary change compared to age-matched control groups ([Fig 8A–8I](#)). Microglial cell density within hippocampal areas did not change neither after diet/dietary change nor with age ([S5 Fig](#)).

A more detailed quantitative analysis of microglial morphology in hippocampal brain regions revealed that in CA1, microglial cell area, perimeter, convex hull area and skeleton length were significantly elevated in animals that received mid-term HFD followed by a dietary change back to ND for the same time period compared to age-matched mice ([S6A–S6C and S6F Fig](#); One-way ANOVA, A) $p = 0.0240$, B) $p = 0.0305$, C) $p = 0.0226$, F) $p = 0.0349$; [S1 Table](#), ll. 186–189). On the other hand, averaged microglial cell solidity and soma size did not differ significantly between relevant groups in CA1 ([S6D and S6E Fig](#)). CA3 and hilar regions did not show significant alterations in morphological parameters of microglial cells after diet/dietary change ([S6G–S6R Fig](#)). However, microglial cell area, perimeter, convex hull area and skeleton length were also slightly elevated in animals that received mid-term HFD followed by a dietary change back to ND for the same time period compared to age-matched mice ([S6G–S6I, S6L–S6O and S6R Fig](#)). Microglial cells in these mice had slightly bigger cells of the ramified morphology showing similar cell solidities and soma size areas, but also longer skeleton lengths and higher branching indices compared to age-matched control mice leading to bigger cell area, perimeter and convex hull area ([S6G–S6R Fig](#); [S2 Table](#)). In general, ramified microglial cells have smaller soma areas, bigger cell perimeters and longer skeleton lengths than activated microglia. Microglial cell and soma area are expected to increase due to activation and soma enlargement yielding higher values of these morphological parameters for activated microglia. Soma size area was not higher in the group that received mid-term HFD followed by a dietary change back to ND for the same time period ([S6K and S6Q Fig](#)). Microglia of these mice had larger cell perimeters, which is estimated to be higher in ramified cells and its decrease is characteristic of fewer ramifications ([S6L and S6R Fig](#)). Increasingly ramified cells have larger convex hull areas and lower cell solidity. An increase of this parameter, also known as cell occupancy, reveals the tendency of microglial cells to be more compact indicating the transition toward activation. Cell circularity is expected to be higher for activated microglia. Typically, highly ramified microglial cells have a greater skeleton length, as well as many branch and end points. The branching index is an additional measurement of microglial branching complexity. For instance, a small ramified microglial cell and an activated microglial cell may have a similar cell volume, but the activated state occupies more of its surrounding, therefore the branching index measure will be smaller. Various important morphological parameters (or their appropriate combination) which indicate microglial activation did not differ in hippocampal regions between relevant groups [60]. Quantification of microglial morphological parameters revealed the most significant changes in the frontal cortex with age, but not with diet/dietary change ([S6S–S6X Fig](#)). Within cortical regions, microglia of older mice showed higher values for cell area ([S1 Table](#), ll. 190–191; [S2 Table](#)), cell perimeter ([S1 Table](#), ll. 192–193; [S2 Table](#)), convex hull area ([S1 Table](#), ll. 194–195; [S2 Table](#)) and skeleton length ([S1 Table](#), ll. 196–197; [S2 Table](#)). There were no detectable changes in relevant morphological parameters indicating microglial activation neither with age nor with diet/dietary change.

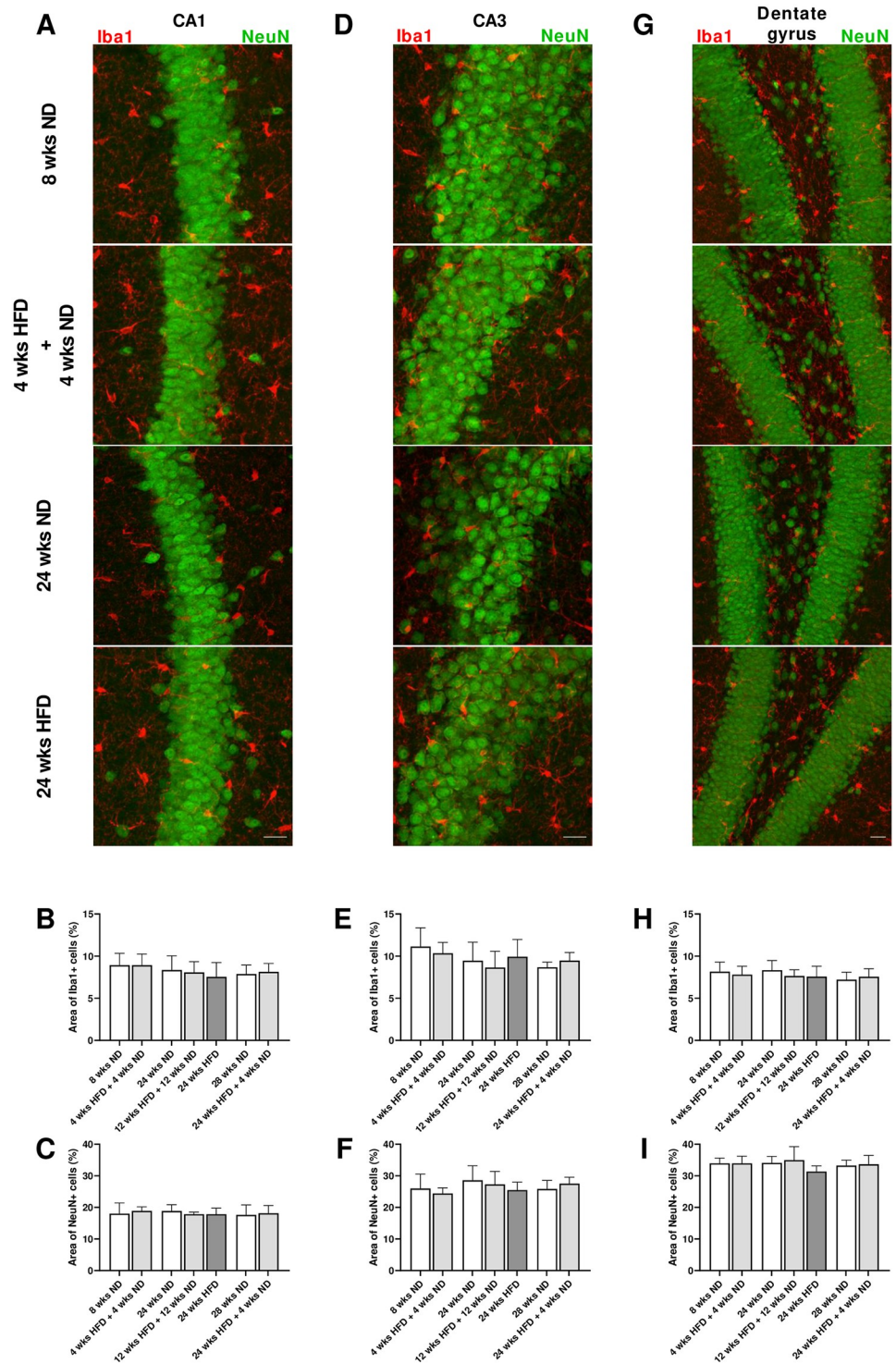


Fig 8. HFD-induced obesity does not alter hippocampal morphology. (A, D, G) Representative confocal images of double-labeled immunofluorescence staining for Iba1 (red) and NeuN (green) within the hippocampus, in particular CA1 and CA3 regions and dentate gyrus of male wild-type C57BL/6J mice fed with ND for eight wks, HFD for four wks followed by ND for four wks and ND or rather HFD for 24 wks. (B, E, H) Quantification of the area stained by Iba1 and (C, F, I) NeuN revealed no differences in hippocampal morphology in mice on HFD compared to ND-fed mice. Scale bar corresponds to 25 μ m. Data are presented as mean values and error bars indicate SD; 8 wks ND n = 6, 4 wks HFD + 4 wks ND n = 6, 24 wks ND n = 12, 12 wks HFD + 12 wks ND n = 6, 24 wks HFD n = 6, 28 wks ND n = 6, 24 wks HFD + 4 wks ND n = 6.

<https://doi.org/10.1371/journal.pone.0257921.g008>

Taken together, we conclude that brains of mice on ND and HFD have similar structural features within the frontal motor cortex and the hippocampus. Quantitative analysis of morphological parameters of microglial cells reveals no microglial activation within the hippocampus and cortex after long-term HFD.

3.9 Long-term HFD does not lead to lipid droplet accumulation and histological changes in the hippocampus

In order to find out whether dietary lipids reach the brain and accumulate there over time, we analyzed coronal brain sections stained with Oil Red O of the study's youngest group 8 wks ND vs. 4 wks HFD + 4 wks ND and the oldest group 24 wks ND vs. 24 wks HFD undergoing the longest period of HFD without dietary change. Oil Red O-stained droplets were predominantly distributed in the hippocampus, in particular in CA1, CA3 and hilar regions. However, lipid droplet accumulation did not increase in CA1 and CA3 neurons and hilar areas in HFD-fed mice compared to ND-fed mice (Fig 9A, 9C and 9E). Further, Oil Red O intensity of stained lipid droplets did not differ between ND- and HFD-fed mice (Fig 9B, 9D and 9F). Calculated ratios (lipid droplets per cell, per tissue, per cell area, and per tissue area) did not reveal any differences in lipid droplet accumulation neither after a long period of HFD nor with age (S7 Fig). Furthermore, ND- and HFD-fed mice had a normal histological appearance and neuronal distribution in CA1 and CA3 hippocampal regions (Fig 9A, 9C and 9E). Overall, results

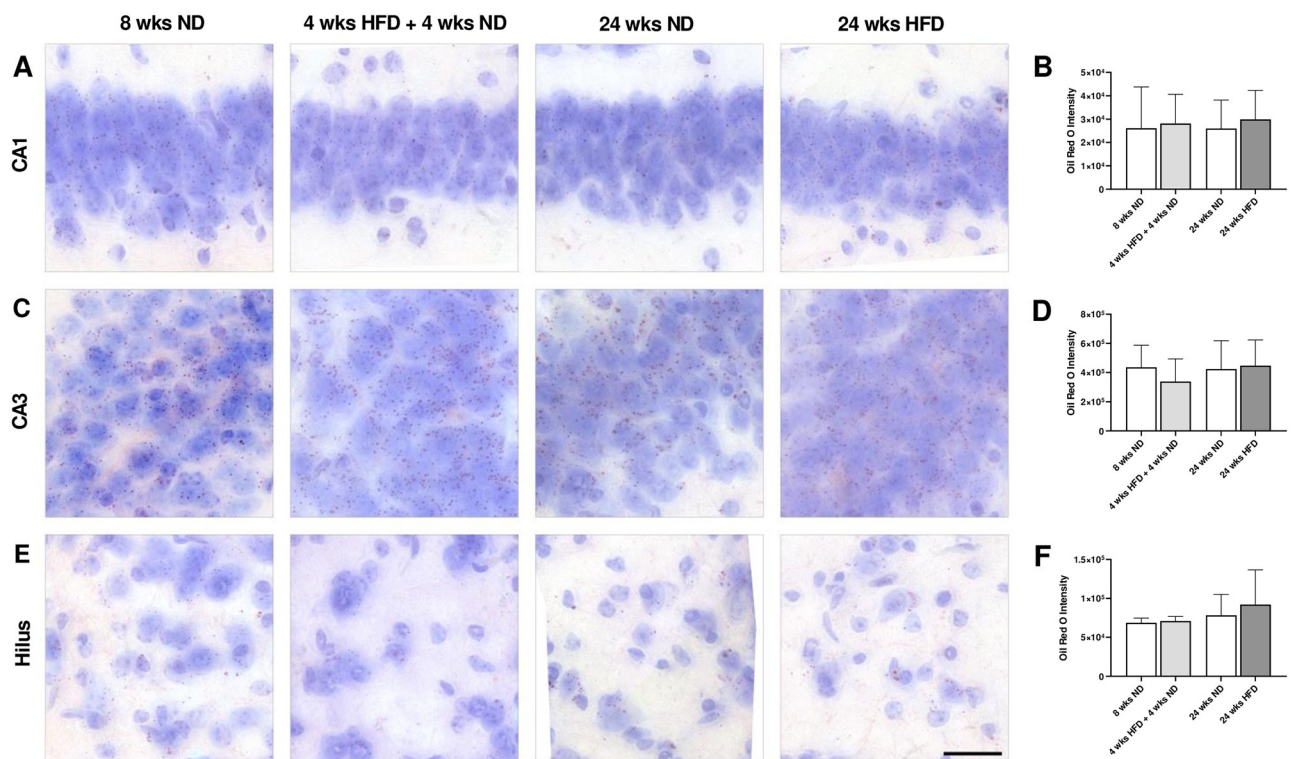


Fig 9. Long-term HFD does not lead to lipid droplet accumulation and histological changes in the hippocampus. (A, C, E) Representative photomicrographs showing Oil Red O stained CA1, CA3 and hilar regions of male wild-type C57BL/6J mice fed with ND for eight wks, HFD for four wks followed by ND for four wks, ND or rather HFD for 24 wks. (E) Scale bar corresponds to 25 μ m. Graphs display (B) Oil Red O intensity in CA1, (D) CA3 and (F) hilar regions. Dietary lipids do not accumulate within the hippocampus due to HFD. Data are presented as mean values and error bars indicate SD; 8 wks ND n = 4–5, 4 wks HFD + 4 wks ND n = 5–6, 24 wks ND n = 6, 24 wks HFD n = 6.

<https://doi.org/10.1371/journal.pone.0257921.g009>

of Oil Red O staining suggested that long-term HFD does not cause structural damage in CA1 and CA3 neuronal cells.

4. Discussion

4.1 Long periods of HFD induce microglial activation in the hypothalamus, but not in the hippocampus

Previous studies already reported about inflammatory microglial responses to variable durations of HFD in the hypothalamus, where microglia, the CNS analogs of macrophages, and astrocytes are involved in body weight homeostasis and obesity [37, 45, 65, 66]. However, hypothalamic inflammation and microgliosis, characterized by rapid morphological changes and microglial inflammatory signals, have been found to occur very early in response to a fat-dense diet [45, 66–69]. A study by Waise et al. (2015) showed that even one day of HFD induced inflammation in the hypothalamus exhibiting increased numbers of macrophages/microglia and upregulated mRNA expression levels of proinflammatory biomarkers [69]. Further, it was recently demonstrated that microglia, bone-marrow derived macrophages, may maintain their pool without significant substitution by circulating monocytes after their establishment in early postnatal life, even under conditions of chronic HFD feeding [70]. Here, for immunofluorescence labeling of microglial cells in hypothalamic sections, we used Iba1, which is a molecular marker for active microglia participating in membrane ruffling and phagocytosis [59]. Iba1 is also known to increase the expression of inflammatory chemokines and cytokines [71]. In our study, we found that long periods of HFD lead to microglial activation within the mediobasal hypothalamus. Interestingly, a dietary change after four, 12 and 24 wks of HFD back to ND rescued this effect already observed in the aforementioned HFD feeding studies for short- and mid-term HFD exposure (Valdearcos et al., 2014, 2017; Baufeld et al., 2016). Berkseth and colleagues (2014) previously reported that hypothalamic gliosis associated with 16 wks HFD exposure is largely reversible in rodents, consistent with reversal of the HFD-induced obesity phenotype [72]. This study also demonstrated that POMC neuronal cell number did not differ between ND, HFD, HFD/ND groups. Here, the activation of microglial cells after long-term HFD did not coincide with morphological alterations or signs of degeneration of neurons within the mediobasal hypothalamus. Unfortunately, the morphological analysis failed within the hypothalamus due to many overlapping cells and inadequate detection of cell bodies. However, this brain area was not the focus of our study and our results from Iba1 signal intensity and stained area quantification after HFD exposure are largely confirmatory of published studies [37, 45]. In contrast to our findings in the hypothalamus responsible for appetite and weight control, we did not discover morphological changes in microglia and neurons of the hippocampus, a brain region required for memory and learning, after long-lasting HFD exposure. In line, Agrimi et al. (2019) showed that 18 wks of HFD did not modify the morphology of the hippocampal formation in adult mice [73]. However, it was previously demonstrated that consumption of HFD during the juvenile period impaired hippocampal morphology and function, as reviewed by Del Olmo and Ruiz-Gayo (2018) [74]. Also, early exposure to HFD induces inflammatory changes in the mouse hippocampus [75]. In this study, six wks of HFD in three-wks-old C57BL/6J male mice increased Iba1-positive cells' soma area in the hilus and stratum radiatum when comparing to ND. Here, we focused on CA1, CA3 and dentate gyrus/hilar regions, where no microglial activation after long periods of HFD was observed. Hence, the starting age and duration of HFD need to be considered regarding the evaluation and comparison of microglial responses in specific brain regions.

4.2 HFD-induced obesity has no effects on hippocampal morphology and lipid droplet contents

Adequate nutritional status and dietary intake are essential for healthy brain functioning. Emotions, behavior, cognitive processes, neuroendocrine functions and synaptic plasticity can be affected by excessive nutritional intake with possible detrimental outcome on neuronal physiology. Lipids, in particular, have important effects on neuronal structure and function [76]. It is known that in metabolic diseases and during aging lipid droplets, which are cytoplasmic non-polar lipids with lipophilic constitutive proteins on their surface, accumulate in many organs including the liver, muscle and brain. Lipid droplets were identified in meningeal, cortical and neurogenic brain regions corresponding to distinct cellular phenotypes, including astrocytes, microglial and neuronal cells, during aging by Shimabukuro et al. (2016) [77]. In our study, we assessed the consequences of HFD-induced obesity on lipid droplet content in the brain using Oil Red O staining. Lipid droplets were predominantly distributed in the hippocampus in ND- and HFD-fed mice, but there was no evidence of an increased lipid droplet accumulation in CA1, CA3 and hilar regions after long-lasting HFD exposure. Thus, our results indicate that the lipid droplet contents within the hippocampus do not increase by long-term HFD and lipid droplets do not accumulate in hippocampal regions and neurons with age. In contrast to our findings, Zhao et al. (2017) described a slight increase in lipid contents by Oil Red O staining in CA3 of the hippocampus in apolipoprotein E-deficient (ApoE^{-/-}) mice after receiving HFD for 12 wks [78]. Unfortunately, quantitative analysis between ND and HFD is missing in this study. Further, they observed neuronal loss in the CA3 provoked by hyperlipidemia. In line, CA1 region was not affected by mid-term HFD exposure. The disagreements regarding the CA3 region are probably caused by the usage of the ApoE knockout mouse line, a suitable model to study hyperlipidemia, which is a risk factor for neurodegenerative diseases, including Alzheimer's disease. ApoE, the most abundant apolipoprotein in the CNS, is particularly implicated in cholesterol efflux and microglial phagocytosis. A review by Loving and Bruce (2020) suggested that increased ApoE production in microglia is a response to increased intracellular cholesterol accumulation [79]. The diet composition is another important aspect that needs to be considered when comparing feeding studies in general. In the study of Zhao et al. (2017), diet consisted of 10% lard, 2% cholesterol and 0.5% cholic acid [78], whereas our experimental diet, characterized by extremely high amounts of fat with middle-chain saturated fatty acids (coconut oil), contained 20.3% crude protein, 35.5% crude fat, 0.1% crude fiber, 5.3% crude ash, 0.2% starch, 17.0% sugar and no additional cholesterol. Maya-Monteiro and colleagues recently showed that lipid droplets accumulate in the hypothalamic third ventricle wall layer with similar heterogeneous distributions in human and mouse [80]. The HFD used in this study also contained high carbohydrates (17 kcal% protein, 42 kcal% carbohydrate, and 41 kcal% fat as well as a high-fructose corn syrup sweetened beverage), whereas our experimental diet consisted of less carbohydrates and more fat (59 kcal% fat, 26 kcal% carbohydrates, 15 kcal% protein). In contrast to our lipid staining, the authors used immunofluorescence labeling of the specific lipid droplet protein PLIN2 to visualize and quantify lipid droplets.

Moreover, in addition to histological analysis, we aimed to study effects after long-term HFD (24 wks) on general health, emotional state, learning and memory in mice. Further, we wanted to analyze potential improvement of health and behavioral performance after the diet has been changed back to a ND, which has hardly been described in the literature so far [72, 81].

4.3 Long-term HFD and obesity lead to health issues, without affecting reflexes or the emotional state in mice

It is known that a fat-dense diet and obesity can cause impairments of general health such as metabolic alterations and cardiac dysfunction [73, 82–84]. Using the SHIRPA protocol and body weight we assessed the consequences of long-term HFD and obesity, as well as dietary change, on appearance in mice. Here, we found that applying a fat-dense diet for mid- and long-term increased the body weight significantly. Further, a change of diet back to ND, after having HFD before, revealed a positive effect on the body weight and hepatic lipid accumulation. Long-term HFD led also to weak and scrubby fur and bare spots, which is an indication for health problems in animals. Interestingly, already a short dietary change to ND helped to avoid this consequence. Similarly, mice on long-term fat-dense diet showed significant more vibrissae loss, while already 12 wks of ND were sufficient for preservation of the whiskers. Loss of vibrissae is often a result of conflicts within the group of mice housed together [85–87]. Thus, long-term HFD may facilitate antisocial behavior and increase aggression, which can also affect general health later on. SHIRPA analysis indicated no differences in aggression toward the experimenter, while social behavior was not studied here. Future studies could apply the intruder paradigm with animals of the same group to investigate whether HFD increases aggression. Interestingly, we observed no further differences between mice on HFD compared to ND relative to eyes, skin, tail, gait, general activity or the touch escape. Also, sensory and motor reflexes were without any pathological findings, which is important to evaluate results from other behavioral tests. As an association between obesity and depression had already been described [88–90], we asked whether obese mice following HFD develop depressive-like features. A study by Vagena et al. (2019) with C57BL/6J mice showed that already three wks of fat-dense diet cause depressive-like behavior in the tail suspension and the forced swim test [91]. In order to test whether depressive-like behavior influences the motivation in cognitive and memory tests, we applied the tail suspension test as well. However, our data showed no evidence for depressive-like behavior in this test. Together, we could rule out that the motivation or performance in other behavioral tests were influenced by alterations of the emotional state, severe motor problems or constraints of sensory reflexes.

4.4 Diet-induced obesity has no effect on learning and memory, but may influence cognitive ability

Many studies describe a link between obesity and learning deficits, memory and cognitive impairments, as well as an increased risk for dementia and Alzheimer's disease [83, 92, 93]. Unfortunately, most studies refer to different study designs, applied tests and parameters to evaluate a diet-induced memory impairment. To assess an effect of long-term HFD and dietary change on working memory, which depends on hippocampal effort [94], we applied the Y maze test. Animals with impaired working memory show increased number of errors and altered spontaneous alternations in this test [95, 96]. Our study revealed no effect of HFD, dietary change or age on short-term memory regarding these parameters. But, a stable effect of age on activity was found in both HFD and ND groups, showing a decreasing number of arm entries. In line, Agrimi et al. (2019) described that 18 wks of HFD alone did not impair spatial memory in the Y maze test [73]. To develop cognitive deficits other co-existing risk factors such as psychosocial stress were needed. Also, no differences in the Y maze test were found in mice, whose mothers received HFD during gestation [97].

Further, learning and memory were analyzed using the MWM test. Thereby, we conducted a control phase, where mice were trained to swim to the labeled platform underneath the water first, which is in contrast to many other studies. This phase was used to evaluate the

qualification of obese mice to pass the test regarding vision, motor function and learning, compared to lean mice. In the control and in the acquisition phase, where mice were trained to find the platform underneath the water by visual cues in the environment, we observed no effect of diet or dietary change. Only initial effects were found relative to age. Similar to the control phase, performance improved over testing days and training revealed no effect of diet/dietary change or age on overall learning. Therefore, we could assure that aged-matched mice receiving ND and HFD possessed similar preconditions regarding vision, motor function and learning in the MWM test.

Directly after the acquisition phase, memory retention was tested in probe trial one in which the platform was removed. Analyzing latency and time in the target quadrant revealed no effect of diet or dietary change on test performance. As we observed also no effect of diet or age according to the latency to find the platform location, we suppose even long-term HFD does not cause memory impairment. Besides, long-lasting HFD and high age can affect the motor performance in mice. However, age-dependent effects were not the focus of our study. As before, we observed no effect of diet or dietary change on memory performance in probe trial two, performed after two days without any training. Contrary, in the second probe trial a tendency in latency and a difference in platform entries were found for mice on dietary change. Mice on longer HFD (12 wks HFD + 4 wks ND) seemed to stick to the old platform location learned during training, while age-matched mice on shorter HFD (4 wks HFD + 12 wks ND) rather ignored the previous platform location. Mice may have learned from the experience in probe trial one that the platform is not at the same position and could be located elsewhere. Further, compared to age-matched groups, mice on long-term HFD (24 wks) spent more time in the target quadrant, where the platform was supposed to be. Indeed, it could be more efficient to check other quadrants and use another searching strategy. According to this, we hypothesize that the cognitive flexibility and memory extinction may be impaired by HFD, so that these mice stick to their old searching strategy and prefer the known platform location [98–100]. In line, a study by Woo et al. (2013), measuring cognitive function-related proteins such as NGF (nerve growth factor) and BDNF (brain-derived neurotrophic factor), suggested a decrease in plasticity and cognitive function in the brain of rats maintained on HFD [101]. Further, they indicated enhanced protein and mRNA expression levels after dietary change. Supporting our data, Jurdak et al. (2008) showed that sugar-induced obesity leads to impairment in spatial learning and memory in the MWM in young rats, while fat-induced obesity is not sufficient for behavioral alterations [102].

Comparing studies of diet-induced obesity effects on learning and memory impairment showed a high discrepancy with reference to species, sex, age, analyzed parameters, applied tests, and particularly the feeding paradigm such as diet (high-fat, high-sugar or combined diets, start and duration). In terms of mouse line, a study with APP23 mice, a model for Alzheimer's disease, 12-month-old animals fed for 12 wks with HFD showed a learning deficit in the acquisition phase as well as a negative memory effect in the probe test of MWM compared to ND [103]. Further, Jones et al. (2019) studied the effect of HFD-induced obesity and the apolipoprotein E4 (APOE4), both high risk factors for Alzheimer's disease [3]. In contrast, they found no behavioral effect on spatial memory in the Barnes maze in APOE3 and APOE4 knock-in mice, after being on HFD for 12 wks. With regards to parameters in the MWM, Guo et al. (2020) used the distance during training and probe trial observing an obesity-induced memory reduction after 12 wks of HFD in mice [104]. In our study, we adducted this parameter rather to describe motor effort or activity. For evaluating memory impairments, the latency to find the target quadrant in the probe trial, directly after the acquisition phase, is used in most studies.

The effect of starting age and timing of HFD on the outcome of the study has been shown by Di Meco and Praticò (2019), where maternal fat-dense nutrition during gestation in mice had positive effects on brain health of the offspring in later life [97]. According to this, aged mice showed less tau pathology and caspase-3 activation in the brain. Additionally, they observed an improvement of learning and memory performance in the MWM test. Further, studies by Boitard et al. (2012, 2015) previously reported that mid-term exposure (8–12 wks) to HFD during adolescence, but not at adulthood, was linked to altered hippocampal function [105, 106], supporting the significance of starting age and duration of obesogenic diet for hippocampal-dependent memory. In line, other studies also proposed that HFD applied after the age of 8 wks did not induce harmful effects on spatial memory consolidation and spatial flexibility [23, 24].

Further differences in testing memory impairment are found relative to the applied test paradigm and the type of memory investigated. Gainey et al. (2016) described memory impairment using the Novel Object Recognition (NOR) and the Object Location Recognition (ORL) test already after one and three wks of HFD compared to low-fat diet in C57BL/6J mice [92]. The authors described this hippocampal-independent behavior which rapidly occurs after short-term HFD and normalizes with age. In line with our data, they state that hippocampal-sensitive memory develops not before long-term HFD. Next to the duration of the HFD, the composition can vary a lot between suppliers. However, most impact has the type of diet. A rather western diet, meaning a high-fat high-sugar diet (HFHSD), has been described to lead to cognitive impairment in humans and memory deficits in rodents [93]. In this study, even short-term HFHSD rapidly affected place recognition, but not object recognition memory in rats. Further, a dietary change back to ND recovered from this deficit. According to Jurdak et al. (2008) the brain seems to be more susceptible to sugar, leading rapidly to alterations in insulin and glucose metabolism causing cognitive impairment [102].

In conclusion, already mid-term HFD leads to a significant increase in body weight, which implicates further problems in general health. It has been shown that dietary change back to ND improves body weight and the appearance in mice. Here, long-term HFD alone does not cause learning deficits or spatial memory impairment in the Y maze and in the MWM test. However, long periods of excessive dietary fat intake increase microglial responses within the mediobasal hypothalamus, but not in the hippocampus showing neither neuroanatomical alterations nor dietary lipid accumulation, as is the case in the liver. HFD may have detrimental consequences for cognitive flexibility and mice may benefit from dietary change. Especially the type of diet—high-fat, high-sugar (sugar types) or western diet (containing high levels of fat and sugar)—and the precise diet composition are crucial for data interpretation and thus for therapeutic consequences of metabolic as well as cognitive diseases. In order to understand the correlation of different risk factors for cognitive impairment and Alzheimer's disease, it is necessary to compare similar diets and test paradigms to investigate the underlying mechanisms.

Supporting information

S1 Fig. HFD does not lead to other general health issues. (A-E) SHIRPA analysis was used to estimate general health of mice after ND or HFD. (A) Long-term HFD did not lead to problems with eyes, (B) skin, (C) tail and (D) gait, or (E) fecal pellets. (F) Young and old mice as well as animals on HFD and ND showed a moderate motor reactivity indicated by the writhe reflex. Data are presented as mean values and error bars indicate SD; 8 wks ND n = 11, 4 wks HFD + 4 wks ND n = 12, 16 wks ND n = 24, 4 wks HFD + 12 wks ND n = 12, 12 wks HFD + 4 wks ND n = 7, 24 wks ND n = 30, 12 wks HFD + 12 wks ND n = 12, 24 wks HFD n = 10, 28 wks ND n = 12, 24 wks HFD + 4 wks ND n = 8.

(TIF)

S2 Fig. Emotional state is not altered following long-term HFD. Depressive-like behavior following HFD was investigated applying the tail suspension test. (A) No effect of diet/dietary change was found on activity. (B) The latency to inactivity did not differ relative to diet. Data are presented as mean values and error bars indicate SD; 8 wks ND n = 12, 16 wks ND n = 24, 24 wks ND n = 30, 28 wks ND n = 12, 4 wks HFD + 4 wks ND n = 12, 12 wks HFD + 4 wks ND n = 7, 4 wks HFD + 12 wks ND n = 12, 12 wks HFD + 12 wks ND n = 12, 24 wks HFD n = 10, 24 wks HFD + 4 wks ND n = 9.
(TIF)

S3 Fig. Upregulated hypothalamic *Iba1* expression following long-term HFD. Relative mRNA expression levels of *Iba1* in the hypothalamus, hippocampus and cortex of mice fed with ND or HFD for 24 wks. Data are presented as mean values and error bars indicate SD; 24 wks ND n = 3, 24 wks HFD n = 3; unpaired t test; * p < 0.05.
(TIF)

S4 Fig. Long periods of HFD do not induce microglial activation in the frontal motor cortex. (A) Representative photomicrographs of double-labeled immunofluorescence staining for *Iba1* (red) and NeuN (green) within the frontal motor cortex of male wild-type C57BL/6J mice fed with ND for eight wks, HFD for four wks followed by ND for four wks and ND or rather HFD for 24 wks. Nuclei were counterstained with DAPI. Scale bar corresponds to 25 μ m. (B) Fluorescence intensity measurements of *Iba1*, (C) quantification of percentage of stained area with *Iba1* and (E) NeuN and (D) number of *Iba1*-immunoreactive cells revealed no effect of HFD on microglial and neuronal morphology in the frontal cortex. Data are presented as mean values and error bars indicate SD; 8 wks ND n = 6, 4 wks HFD + 4 wks ND n = 6, 24 wks ND n = 12, 12 wks HFD + 12 wks ND n = 6, 24 wks HFD n = 6, 28 wks ND n = 6, 24 wks HFD + 4 wks ND n = 6.
(TIF)

S5 Fig. HFD-induced obesity does not alter microglial density in the hippocampus. Microglial cell density did not change neither after diet/dietary change nor with age in CA1 (A) and CA3 (B) regions and dentate gyrus (C) of male wild-type C57BL/6J mice fed with ND for eight wks, HFD for four wks followed by ND for four wks and ND or rather HFD for 24 wks. Data are presented as mean values and error bars indicate SD; 8 wks ND n = 6, 4 wks HFD + 4 wks ND n = 6, 24 wks ND n = 12, 12 wks HFD + 12 wks ND n = 6, 24 wks HFD n = 6, 28 wks ND n = 6, 24 wks HFD + 4 wks ND n = 6.
(TIF)

S6 Fig. Quantitative analysis of six morphological parameters of microglial cells reveals no microglial activation within the hippocampus and cortex after long-term HFD compared to age-matched control mice. Quantification of (A, G, M, S) microglial cell area, (B, H, N, T) cell perimeter, (C, I, O, U) cell convex hull area, (D, J, P, V) cell solidity, (E, K, Q, W) soma area and (F, L, R, X) skeleton length in CA1 and CA3 regions, dentate gyrus and frontal motor cortex of male wild-type C57BL/6J mice fed with ND for eight wks, HFD for four wks followed by ND for four wks, HFD for 12 wks followed by ND for 12 wks, ND or rather HFD for 24 wks, ND for 28 wks and HFD for 24 wks followed by ND for four wks. At least 180 cells per group were used for quantification. Data are presented as mean values and error bars indicate SD; 8 wks ND n = 6, 4 wks HFD + 4 wks ND n = 6, 24 wks ND n = 12, 12 wks HFD + 12 wks ND n = 6, 24 wks HFD n = 6, 28 wks ND n = 6, 24 wks HFD + 4 wks ND n = 6; One-way ANOVA; * p < 0.05.
(TIF)

S7 Fig. Long-term HFD does not lead to lipid droplet accumulation within the hippocampus. Lipid droplets (A) per cell, (B) per tissue, (C) per cell area, (D) and per tissue area did not reveal any differences in lipid droplet accumulation neither after a long period of HFD nor with age in CA1, CA3 and dentate gyrus hippocampal regions. Data are presented as mean values and error bars indicate SD; 8 wks ND n = 4–5, 4 wks HFD + 4 wks ND n = 5–6, 24 wks ND n = 6, 24 wks HFD n = 6.

(TIF)

S1 Table. Statistical analyses for all figures including statistical significances. The table shows relevant results of statistical tests.

(DOCX)

S2 Table. Morphological parameters of microglial cells within the hippocampus and cortex in mice after HFD and/or ND exposure for varying weeks.

(DOCX)

Acknowledgments

We thank Constance Hobusch, Angela Ehrlich, Andreas Horn and the staff from the animal facility for their excellent technical assistance. We thank Susann Hähnel and Nicole Kaiser for critical reading of the manuscript.

Author Contributions

Conceptualization: Judith Leyh, Uta Ceglarek, Ingo Bechmann, Julia Landmann.

Data curation: Judith Leyh, Karsten Winter, Julia Landmann.

Formal analysis: Judith Leyh, Madlen Reinicke, Julia Landmann.

Funding acquisition: Uta Ceglarek, Ingo Bechmann.

Investigation: Judith Leyh, Julia Landmann.

Resources: Uta Ceglarek, Ingo Bechmann.

Supervision: Ingo Bechmann, Julia Landmann.

Validation: Karsten Winter, Julia Landmann.

Visualization: Judith Leyh, Karsten Winter, Julia Landmann.

Writing – original draft: Judith Leyh, Julia Landmann.

Writing – review & editing: Judith Leyh, Karsten Winter, Madlen Reinicke, Uta Ceglarek, Ingo Bechmann, Julia Landmann.

References

1. Mathieu P, Poirier P, Pibarot Philippe, Lemieux Isabelle, Després Jean-Pierre. Visceral Obesity. Hypertension. 2009; 53: 577–584. <https://doi.org/10.1161/HYPERTENSIONAHA.108.110320> PMID: [19237685](https://pubmed.ncbi.nlm.nih.gov/19237685/)
2. Neth BJ, Craft S. Insulin Resistance and Alzheimer's Disease: Bioenergetic Linkages. Front Aging Neurosci. 2017; 9. <https://doi.org/10.3389/fnagi.2017.00345> PMID: [29163128](https://pubmed.ncbi.nlm.nih.gov/29163128/)
3. Jones NS, Watson KQ, Rebeck GW. Metabolic Disturbances of a High-Fat Diet Are Dependent on APOE Genotype and Sex. eNeuro. 2019; 6. <https://doi.org/10.1523/ENEURO.0267-19.2019> PMID: [31554665](https://pubmed.ncbi.nlm.nih.gov/31554665/)

4. Bojková B, Winklewski PJ, Wszedybyl-Winklewska M. Dietary Fat and Cancer—Which Is Good, Which Is Bad, and the Body of Evidence. *International Journal of Molecular Sciences*. 2020; 21: 4114. <https://doi.org/10.3390/ijms21114114> PMID: [32526973](https://pubmed.ncbi.nlm.nih.gov/32526973/)
5. Besser LM, Gill DP, Monsell SE, Brenowitz W, Meranus DH, Kukull W, et al. Body Mass Index, Weight Change, and Clinical Progression in Mild Cognitive Impairment and Alzheimer Disease. *Alzheimer Disease & Associated Disorders*. 2014; 28: 36–43. <https://doi.org/10.1097/WAD.000000000000005> PMID: [24126214](https://pubmed.ncbi.nlm.nih.gov/24126214/)
6. Bloor ID, Symonds ME. Sexual dimorphism in white and brown adipose tissue with obesity and inflammation. *Hormones and Behavior*. 2014; 66: 95–103. <https://doi.org/10.1016/j.yhbeh.2014.02.007> PMID: [24589990](https://pubmed.ncbi.nlm.nih.gov/24589990/)
7. Leigh S-J, Morris MJ. Diet, inflammation and the gut microbiome: Mechanisms for obesity-associated cognitive impairment. *Biochimica et Biophysica Acta (BBA)—Molecular Basis of Disease*. 2020; 1866: 165767. <https://doi.org/10.1016/j.bbadis.2020.165767> PMID: [32171891](https://pubmed.ncbi.nlm.nih.gov/32171891/)
8. Squire LR, Genzel L, Wixted JT, Morris RG. Memory consolidation. *Cold Spring Harb Perspect Biol*. 2015; 7: a021766. <https://doi.org/10.1101/cshperspect.a021766> PMID: [26238360](https://pubmed.ncbi.nlm.nih.gov/26238360/)
9. Anacker C, Hen R. Adult hippocampal neurogenesis and cognitive flexibility—linking memory and mood. *Nature Reviews Neuroscience*. 2017; 18: 335–346. <https://doi.org/10.1038/nrn.2017.45> PMID: [28469276](https://pubmed.ncbi.nlm.nih.gov/28469276/)
10. Kanoski SE, Davidson TL. Western diet consumption and cognitive impairment: Links to hippocampal dysfunction and obesity. *Physiology & Behavior*. 2011; 103: 59–68. <https://doi.org/10.1016/j.physbeh.2010.12.003> PMID: [21167850](https://pubmed.ncbi.nlm.nih.gov/21167850/)
11. Yeomans MR. Adverse effects of consuming high fat–sugar diets on cognition: implications for understanding obesity. *Proceedings of the Nutrition Society*. 2017; 76: 455–465. <https://doi.org/10.1017/S0029665117000805> PMID: [28514983](https://pubmed.ncbi.nlm.nih.gov/28514983/)
12. Molteni R, Barnard RJ, Ying Z, Roberts CK, Gómez-Pinilla F. A high-fat, refined sugar diet reduces hippocampal brain-derived neurotrophic factor, neuronal plasticity, and learning. *Neuroscience*. 2002; 112: 803–814. [https://doi.org/10.1016/s0306-4522\(02\)00123-9](https://doi.org/10.1016/s0306-4522(02)00123-9) PMID: [12088740](https://pubmed.ncbi.nlm.nih.gov/12088740/)
13. Wu A, Molteni R, Ying Z, Gomez-Pinilla F. A saturated-fat diet aggravates the outcome of traumatic brain injury on hippocampal plasticity and cognitive function by reducing brain-derived neurotrophic factor. *Neuroscience*. 2003; 119: 365–375. [https://doi.org/10.1016/s0306-4522\(03\)00154-4](https://doi.org/10.1016/s0306-4522(03)00154-4) PMID: [12770552](https://pubmed.ncbi.nlm.nih.gov/12770552/)
14. Goldbart AD, Row BW, Kheirandish-Gozal L, Cheng Y, Brittan KR, Gozal D. High fat/refined carbohydrate diet enhances the susceptibility to spatial learning deficits in rats exposed to intermittent hypoxia. *Brain Research*. 2006; 1090: 190–196. <https://doi.org/10.1016/j.brainres.2006.03.046> PMID: [16674930](https://pubmed.ncbi.nlm.nih.gov/16674930/)
15. Stranahan AM, Norman ED, Lee K, Cutler RG, Telljohann RS, Egan JM, et al. Diet-induced insulin resistance impairs hippocampal synaptic plasticity and cognition in middle-aged rats. *Hippocampus*. 2008; 18: 1085–1088. <https://doi.org/10.1002/hipo.20470> PMID: [18651634](https://pubmed.ncbi.nlm.nih.gov/18651634/)
16. Khazen T, Hatoum OA, Ferreira G, Maroun M. Acute exposure to a high-fat diet in juvenile male rats disrupts hippocampal-dependent memory and plasticity through glucocorticoids. *Scientific Reports*. 2019; 9: 12270. <https://doi.org/10.1038/s41598-019-48800-2> PMID: [31439894](https://pubmed.ncbi.nlm.nih.gov/31439894/)
17. Murray AJ, Knight NS, Cochlin LE, McAleese S, Deacon RMJ, Rawlins JNP, et al. Deterioration of physical performance and cognitive function in rats with short-term high-fat feeding. *The FASEB Journal*. 2009; 23: 4353–4360. <https://doi.org/10.1096/fj.09-139691> PMID: [19667117](https://pubmed.ncbi.nlm.nih.gov/19667117/)
18. Beilharz JE, Maniam J, Morris MJ. Short exposure to a diet rich in both fat and sugar or sugar alone impairs place, but not object recognition memory in rats. *Brain, Behavior, and Immunity*. 2014; 37: 134–141. <https://doi.org/10.1016/j.bbi.2013.11.016> PMID: [24309633](https://pubmed.ncbi.nlm.nih.gov/24309633/)
19. Beilharz JE, Kaakoush NO, Maniam J, Morris MJ. The effect of short-term exposure to energy-matched diets enriched in fat or sugar on memory, gut microbiota and markers of brain inflammation and plasticity. *Brain, Behavior, and Immunity*. 2016; 57: 304–313. <https://doi.org/10.1016/j.bbi.2016.07.151> PMID: [27448745](https://pubmed.ncbi.nlm.nih.gov/27448745/)
20. Hargrave SL, Davidson TL, Zheng W, Kinzig KP. Western diets induce blood-brain barrier leakage and alter spatial strategies in rats. *Behavioral Neuroscience*. 2016; 130: 123–135. <https://doi.org/10.1037/bne0000110> PMID: [26595878](https://pubmed.ncbi.nlm.nih.gov/26595878/)
21. Spencer SJ, Korosi A, Layé S, Shukitt-Hale B, Barrientos RM. Food for thought: how nutrition impacts cognition and emotion. *npj Science of Food*. 2017; 1: 7. <https://doi.org/10.1038/s41538-017-0008-y> PMID: [31304249](https://pubmed.ncbi.nlm.nih.gov/31304249/)
22. Yaseen A, Shrivastava K, Zuri Z, Hatoum OA, Maroun M. Prefrontal Oxytocin is Involved in Impairments in Prefrontal Plasticity and Social Memory Following Acute Exposure to High Fat Diet in Juvenile Animals. *Cereb Cortex*. 2019; 29: 1900–1909. <https://doi.org/10.1093/cercor/bhy070> PMID: [29608644](https://pubmed.ncbi.nlm.nih.gov/29608644/)

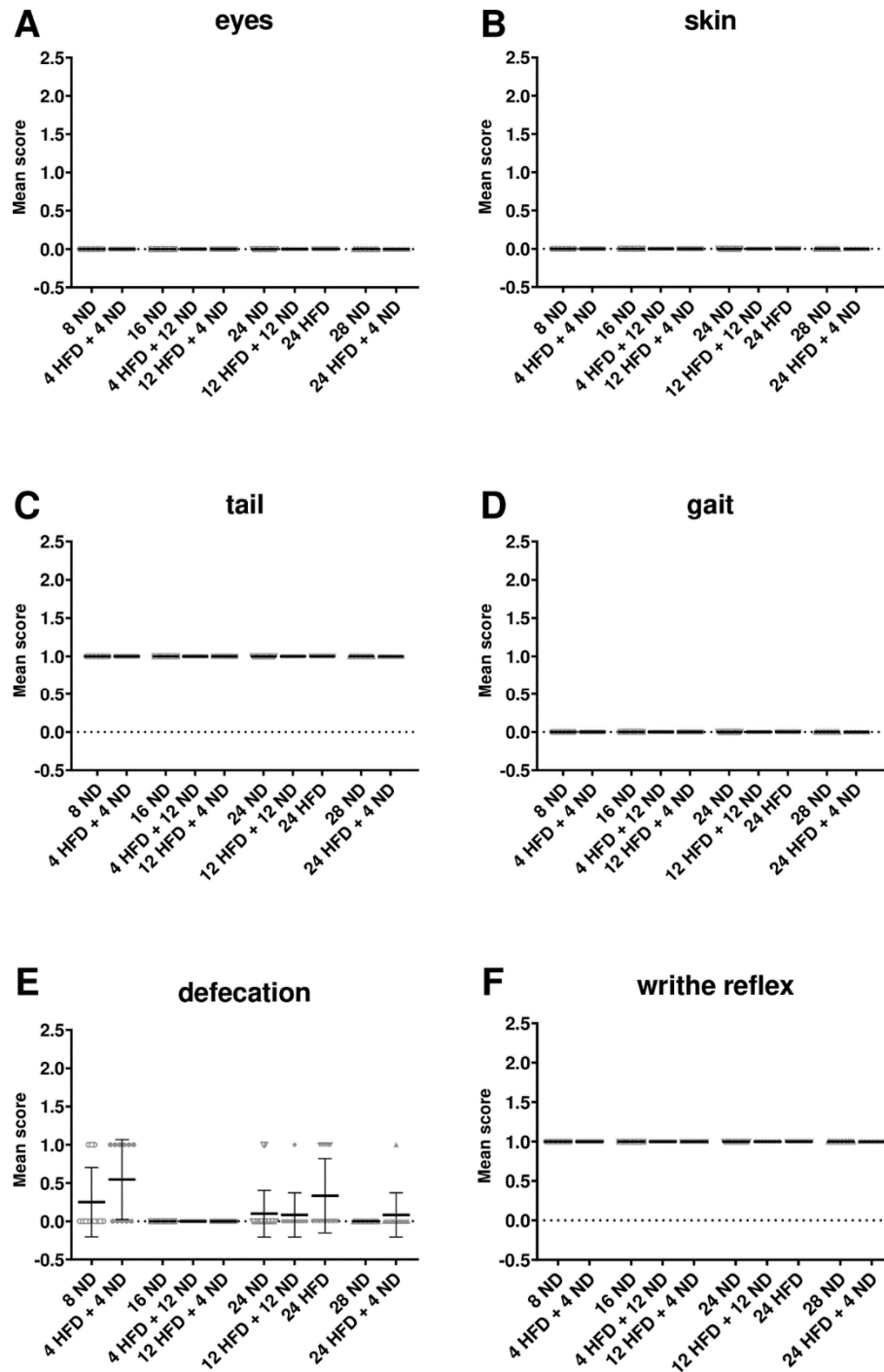
23. Valladolid-Acebes I, Fole A, Martín M, Morales L, Victoria Cano M, Ruiz-Gayo M, et al. Spatial memory impairment and changes in hippocampal morphology are triggered by high-fat diets in adolescent mice. Is there a role of leptin? *Neurobiology of Learning and Memory*. 2013; 106: 18–25. <https://doi.org/10.1016/j.nlm.2013.06.012> PMID: 23820496
24. Boitard C, Cavaroc A, Sauvart J, Aubert A, Castanon N, Layé S, et al. Impairment of hippocampal-dependent memory induced by juvenile high-fat diet intake is associated with enhanced hippocampal inflammation in rats. *Brain, Behavior, and Immunity*. 2014; 40: 9–17. <https://doi.org/10.1016/j.bbi.2014.03.005> PMID: 24662056
25. Vinuesa A, Pomilio C, Menafra M, Bonaventura MM, Garay L, Mercogliano MF, et al. Juvenile exposure to a high fat diet promotes behavioral and limbic alterations in the absence of obesity. *Psychoneuroendocrinology*. 2016; 72: 22–33. <https://doi.org/10.1016/j.psyneuen.2016.06.004> PMID: 27337091
26. Dutheil S, Ota KT, Wohleb ES, Rasmussen K, Duman RS. High-Fat Diet Induced Anxiety and Anhedonia: Impact on Brain Homeostasis and Inflammation. *Neuropsychopharmacology*. 2016; 41: 1874–1887. <https://doi.org/10.1038/npp.2015.357> PMID: 26658303
27. Cavaliere G, Trinchese G, Penna E, Cimmino F, Pirozzi C, Lama A, et al. High-Fat Diet Induces Neuroinflammation and Mitochondrial Impairment in Mice Cerebral Cortex and Synaptic Fraction. *Front Cell Neurosci*. 2019; 13. <https://doi.org/10.3389/fncel.2019.00509> PMID: 31798417
28. Chen T-J, Chen S-S, Wang D-C, Hung H-S. High-fat diet reduces novelty-induced expression of activity-regulated cytoskeleton-associated protein. *Journal of Cellular Physiology*. 2020; 235: 1065–1075. <https://doi.org/10.1002/jcp.29021> PMID: 31264208
29. Friedman JM, Halaas JL. Leptin and the regulation of body weight in mammals. *Nature*. 1998; 395: 763–770. <https://doi.org/10.1038/27376> PMID: 9796811
30. Elmquist JK, Elias CF, Saper CB. From Lesions to Leptin: Hypothalamic Control of Food Intake and Body Weight. *Neuron*. 1999; 22: 221–232. [https://doi.org/10.1016/s0896-6273\(00\)81084-3](https://doi.org/10.1016/s0896-6273(00)81084-3) PMID: 10069329
31. Seeley RJ, Woods SC. Monitoring of stored and available fuel by the CNS: implications for obesity. *Nature Reviews Neuroscience*. 2003; 4: 901–909. <https://doi.org/10.1038/nrn1245> PMID: 14595401
32. Horvath TL, Sarman B, García-Cáceres C, Enriori PJ, Sotonyi P, Shanabrough M, et al. Synaptic input organization of the melanocortin system predicts diet-induced hypothalamic reactive gliosis and obesity. *Proceedings of the National Academy of Sciences*. 2010; 107: 14875–14880. <https://doi.org/10.1073/pnas.1004282107> PMID: 20679202
33. Yi C-X, Habegger KM, Chowen JA, Stern J, Tschöp MH. A Role for Astrocytes in the Central Control of Metabolism. *NEN*. 2011; 93: 143–149. <https://doi.org/10.1159/000324888> PMID: 21372559
34. García-Cáceres C, Fuente-Martín E, Argente J, Chowen JA. Emerging role of glial cells in the control of body weight. *Molecular Metabolism*. 2012; 1: 37–46. <https://doi.org/10.1016/j.molmet.2012.07.001> PMID: 24024117
35. García-Cáceres C, Yi C-X, Tschöp MH. Hypothalamic Astrocytes in Obesity. *Endocrinology and Metabolism Clinics of North America*. 2013; 42: 57–66. <https://doi.org/10.1016/j.ecl.2012.11.003> PMID: 23391239
36. Grayson BE, Seeley RJ, Sandoval DA. Wired on sugar: the role of the CNS in the regulation of glucose homeostasis. *Nature Reviews Neuroscience*. 2013; 14: 24–37. <https://doi.org/10.1038/nrn3409> PMID: 23232606
37. Valdearcos M, Douglass JD, Robblee MM, Dorfman MD, Stifler DR, Bennett ML, et al. Microglial Inflammatory Signaling Orchestrates the Hypothalamic Immune Response to Dietary Excess and Mediates Obesity Susceptibility. *Cell Metabolism*. 2017; 26: 185–197.e3. <https://doi.org/10.1016/j.cmet.2017.05.015> PMID: 28683286
38. García-Cáceres C, Balland E, Prevot V, Luquet S, Woods SC, Koch M, et al. Role of astrocytes, microglia, and tanycytes in brain control of systemic metabolism. *Nature Neuroscience*. 2019; 22: 7–14. <https://doi.org/10.1038/s41593-018-0286-y> PMID: 30531847
39. Sofroniew MV, Vinters HV. Astrocytes: biology and pathology. *Acta Neuropathol*. 2010; 119: 7–35. <https://doi.org/10.1007/s00401-009-0619-8> PMID: 20012068
40. Bradl M, Lassmann H. Oligodendrocytes: biology and pathology. *Acta Neuropathol*. 2010; 119: 37–53. <https://doi.org/10.1007/s00401-009-0601-5> PMID: 19847447
41. Nutma E, van Gent D, Amor S, Peferoen LAN. Astrocyte and Oligodendrocyte Cross-Talk in the Central Nervous System. *Cells*. 2020; 9: 600. <https://doi.org/10.3390/cells9030600> PMID: 32138223
42. Goldmann T, Prinz M. Role of Microglia in CNS Autoimmunity. *Clinical and Developmental Immunology*. 2013; 2013: 1–8. <https://doi.org/10.1155/2013/208093> PMID: 23840238

43. Parkhurst CN, Yang G, Ninan I, Savas JN, Yates JR, Lafaille JJ, et al. Microglia Promote Learning-Dependent Synapse Formation through Brain-Derived Neurotrophic Factor. *Cell*. 2013; 155: 1596–1609. <https://doi.org/10.1016/j.cell.2013.11.030> PMID: [24360280](https://pubmed.ncbi.nlm.nih.gov/24360280/)
44. Traiffort E, Kassoussi A, Zahaf A, Laouarem Y. Astrocytes and Microglia as Major Players of Myelin Production in Normal and Pathological Conditions. *Front Cell Neurosci*. 2020; 14. <https://doi.org/10.3389/fncel.2020.00079> PMID: [32317939](https://pubmed.ncbi.nlm.nih.gov/32317939/)
45. Thaler JP, Yi C-X, Schur EA, Guyenet SJ, Hwang BH, Dietrich MO, et al. Obesity is associated with hypothalamic injury in rodents and humans. *J Clin Invest*. 2012; 122: 153–162. <https://doi.org/10.1172/JCI59660> PMID: [22201683](https://pubmed.ncbi.nlm.nih.gov/22201683/)
46. Graham LC, Harder JM, Soto I, de Vries WN, John SWM, Howell GR. Chronic consumption of a western diet induces robust glial activation in aging mice and in a mouse model of Alzheimer's disease. *Scientific Reports*. 2016; 6: 21568. <https://doi.org/10.1038/srep21568> PMID: [26888450](https://pubmed.ncbi.nlm.nih.gov/26888450/)
47. Emy D, Hrabě de Angelis AL, Jaitin D, Wieghofer P, Staszewski O, David E, et al. Host microbiota constantly control maturation and function of microglia in the CNS. *Nature Neuroscience*. 2015; 18: 965–977. <https://doi.org/10.1038/nn.4030> PMID: [26030851](https://pubmed.ncbi.nlm.nih.gov/26030851/)
48. Valdearcos M, Robblee MM, Benjamin DI, Nomura DK, Xu AW, Koliwad SK. Microglia Dictate the Impact of Saturated Fat Consumption on Hypothalamic Inflammation and Neuronal Function. *Cell Reports*. 2014; 9: 2124–2138. <https://doi.org/10.1016/j.celrep.2014.11.018> PMID: [25497089](https://pubmed.ncbi.nlm.nih.gov/25497089/)
49. Guillemot-Legris O, Muccioli GG. Obesity-Induced Neuroinflammation: Beyond the Hypothalamus. *Trends in Neurosciences*. 2017; 40: 237–253. <https://doi.org/10.1016/j.tins.2017.02.005> PMID: [28318543](https://pubmed.ncbi.nlm.nih.gov/28318543/)
50. Khan MSH, Hegde V. Obesity and Diabetes Mediated Chronic Inflammation: A Potential Biomarker in Alzheimer's Disease. *Journal of Personalized Medicine*. 2020; 10: 42. <https://doi.org/10.3390/jpm10020042> PMID: [32455946](https://pubmed.ncbi.nlm.nih.gov/32455946/)
51. Landmann J, Richter F, Classen J, Richter A, Penninger JM, Bechmann I. Behavioral phenotyping of calcium channel (CACN) subunit $\alpha 2\delta 3$ knockout mice: Consequences of sensory cross-modal activation. *Behavioural Brain Research*. 2019; 364: 393–402. <https://doi.org/10.1016/j.bbr.2017.12.032> PMID: [29305318](https://pubmed.ncbi.nlm.nih.gov/29305318/)
52. Magen I, Fleming SM, Zhu C, Garcia EC, Cardiff KM, Dinh D, et al. Cognitive deficits in a mouse model of pre-manifest Parkinson's disease. *European Journal of Neuroscience*. 2012; 35: 870–882. <https://doi.org/10.1111/j.1460-9568.2012.08012.x> PMID: [22356593](https://pubmed.ncbi.nlm.nih.gov/22356593/)
53. Uetani N, Kato K, Ogura H, Mizuno K, Kawano K, Mikoshiba K, et al. Impaired learning with enhanced hippocampal long-term potentiation in PTP δ -deficient mice. *The EMBO Journal*. 2000; 19: 2775–2785. <https://doi.org/10.1093/emboj/19.12.2775> PMID: [10856223](https://pubmed.ncbi.nlm.nih.gov/10856223/)
54. Vorhees CV, Williams MT. Morris water maze: procedures for assessing spatial and related forms of learning and memory. *Nature Protocols*. 2006; 1: 848–858. <https://doi.org/10.1038/nprot.2006.116> PMID: [17406317](https://pubmed.ncbi.nlm.nih.gov/17406317/)
55. Cryan JF, Mombereau C, Vassout A. The tail suspension test as a model for assessing antidepressant activity: Review of pharmacological and genetic studies in mice. *Neuroscience & Biobehavioral Reviews*. 2005; 29: 571–625. <https://doi.org/10.1016/j.neubiorev.2005.03.009> PMID: [15890404](https://pubmed.ncbi.nlm.nih.gov/15890404/)
56. Wang H, Blackall M, Sominsky L, Spencer SJ, Vlahos R, Churchill M, et al. Increased hypothalamic microglial activation after viral-induced pneumococcal lung infection is associated with excess serum amyloid A production. *Journal of Neuroinflammation*. 2018; 15: 200. <https://doi.org/10.1186/s12974-018-1234-1> PMID: [29980196](https://pubmed.ncbi.nlm.nih.gov/29980196/)
57. Harrison L, Pfuhlmann K, Schriever SC, Pfluger PT. Profound weight loss induces reactive astrogliosis in the arcuate nucleus of obese mice. *Molecular Metabolism*. 2019; 24: 149–155. <https://doi.org/10.1016/j.molmet.2019.03.009> PMID: [30979678](https://pubmed.ncbi.nlm.nih.gov/30979678/)
58. Winkler Z, Kuti D, Polyák Á, Juhász B, Gulyás K, Lénárt N, et al. Hypoglycemia-activated Hypothalamic Microglia Impairs Glucose Counterregulatory Responses. *Scientific Reports*. 2019; 9: 6224. <https://doi.org/10.1038/s41598-019-42728-3> PMID: [30996341](https://pubmed.ncbi.nlm.nih.gov/30996341/)
59. Kim YJ, Tu TH, Yang S, Kim JK, Kim JG. Characterization of Fatty Acid Composition Underlying Hypothalamic Inflammation in Aged Mice. *Molecules*. 2020; 25: 3170. <https://doi.org/10.3390/molecules25143170> PMID: [32664475](https://pubmed.ncbi.nlm.nih.gov/32664475/)
60. Leyh J, Paeschke S, Mages B, Michalski D, Nowicki M, Bechmann I, et al. Classification of Microglial Morphological Phenotypes Using Machine Learning. *Front Cell Neurosci*. 2021; 15: 701673. <https://doi.org/10.3389/fncel.2021.701673> PMID: [34267628](https://pubmed.ncbi.nlm.nih.gov/34267628/)
61. Sholl DA. Dendritic organization in the neurons of the visual and motor cortices of the cat. *J Anat*. 1953; 87: 387–406. PMID: [13117757](https://pubmed.ncbi.nlm.nih.gov/13117757/)

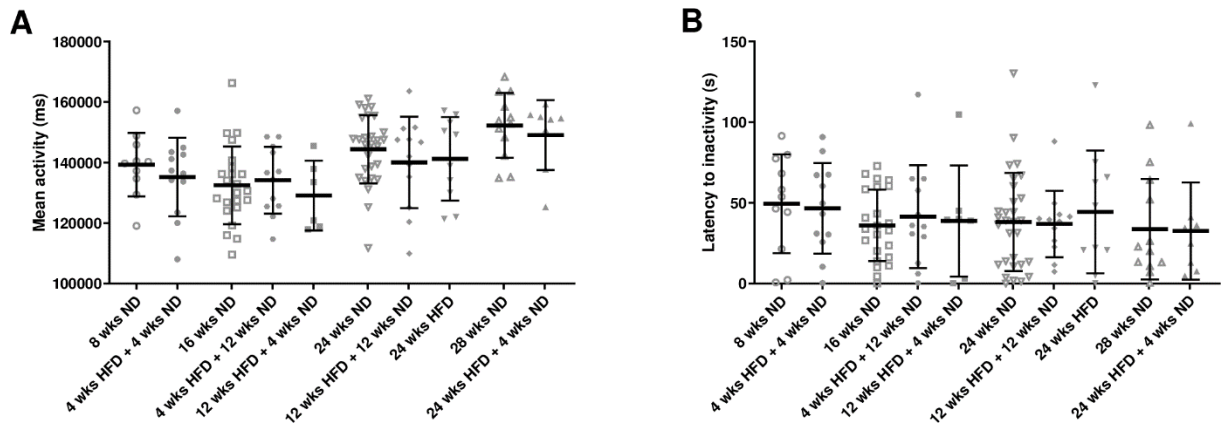
62. Garcia-Segura LM, Perez-Marquez J. A new mathematical function to evaluate neuronal morphology using the Sholl analysis. *J Neurosci Methods*. 2014; 226: 103–109. <https://doi.org/10.1016/j.jneumeth.2014.01.016> PMID: [24503022](https://pubmed.ncbi.nlm.nih.gov/24503022/)
63. Tsuru H, Osaka M, Hiraoka Y, Yoshida M. HFD-induced hepatic lipid accumulation and inflammation are decreased in Factor D deficient mouse. *Sci Rep*. 2020; 10: 17593. <https://doi.org/10.1038/s41598-020-74617-5> PMID: [33067533](https://pubmed.ncbi.nlm.nih.gov/33067533/)
64. Recena Aydos L, Aparecida do Amaral L, Serafim de Souza R, Jacobowski AC, Freitas dos Santos E, Rodrigues Macedo ML. Nonalcoholic Fatty Liver Disease Induced by High-Fat Diet in C57bl/6 Models. *Nutrients*. 2019; 11: 3067. <https://doi.org/10.3390/nu11123067> PMID: [31888190](https://pubmed.ncbi.nlm.nih.gov/31888190/)
65. Baufeld C, Osterloh A, Prokop S, Miller KR, Heppner FL. High-fat diet-induced brain region-specific phenotypic spectrum of CNS resident microglia. *Acta Neuropathol*. 2016; 132: 361–375. <https://doi.org/10.1007/s00401-016-1595-4> PMID: [27393312](https://pubmed.ncbi.nlm.nih.gov/27393312/)
66. Kim JD, Yoon NA, Jin S, Diano S. Microglial UCP2 Mediates Inflammation and Obesity Induced by High-Fat Feeding. *Cell Metabolism*. 2019; 30: 952–962.e5. <https://doi.org/10.1016/j.cmet.2019.08.010> PMID: [31495690](https://pubmed.ncbi.nlm.nih.gov/31495690/)
67. Buckman LB, Thompson MM, Lippert RN, Blackwell TS, Yull FE, Ellacott KLJ. Evidence for a novel functional role of astrocytes in the acute homeostatic response to high-fat diet intake in mice. *Molecular Metabolism*. 2015; 4: 58–63. <https://doi.org/10.1016/j.molmet.2014.10.001> PMID: [25685690](https://pubmed.ncbi.nlm.nih.gov/25685690/)
68. Balland E, Cowley MA. Short-term high-fat diet increases the presence of astrocytes in the hypothalamus of C57BL6 mice without altering leptin sensitivity. *Journal of Neuroendocrinology*. 2017; 29: e12504. <https://doi.org/10.1111/jne.12504> PMID: [28699230](https://pubmed.ncbi.nlm.nih.gov/28699230/)
69. Waise TMZ, Toshinai K, Naznin F, NamKoong C, Md Moin AS, Sakoda H, et al. One-day high-fat diet induces inflammation in the nodose ganglion and hypothalamus of mice. *Biochemical and Biophysical Research Communications*. 2015; 464: 1157–1162. <https://doi.org/10.1016/j.bbrc.2015.07.097> PMID: [26208455](https://pubmed.ncbi.nlm.nih.gov/26208455/)
70. Lee CH, Shin SH, Kang GM, Kim S, Kim J, Yu R, et al. Cellular source of hypothalamic macrophage accumulation in diet-induced obesity. *Journal of Neuroinflammation*. 2019; 16: 221. <https://doi.org/10.1186/s12974-019-1607-0> PMID: [31727092](https://pubmed.ncbi.nlm.nih.gov/31727092/)
71. Zhao Y-Y, Yan D-J, Chen Z-W. Role of AIF-1 in the regulation of inflammatory activation and diverse disease processes. *Cellular Immunology*. 2013; 284: 75–83. <https://doi.org/10.1016/j.cellimm.2013.07.008> PMID: [23948156](https://pubmed.ncbi.nlm.nih.gov/23948156/)
72. Berkseth KE, Guyenet SJ, Melhorn SJ, Lee D, Thaler JP, Schur EA, et al. Hypothalamic gliosis associated with high-fat diet feeding is reversible in mice: a combined immunohistochemical and magnetic resonance imaging study. *Endocrinology*. 2014; 155: 2858–2867. <https://doi.org/10.1210/en.2014-1121> PMID: [24914942](https://pubmed.ncbi.nlm.nih.gov/24914942/)
73. Agrimi J, Spalletti C, Baroni C, Keceli G, Zhu G, Caragnano A, et al. Obese mice exposed to psychosocial stress display cardiac and hippocampal dysfunction associated with local brain-derived neurotrophic factor depletion. *EBioMedicine*. 2019; 47: 384–401. <https://doi.org/10.1016/j.ebiom.2019.08.042> PMID: [31492565](https://pubmed.ncbi.nlm.nih.gov/31492565/)
74. Del Olmo N, Ruiz-Gayo M. Influence of High-Fat Diets Consumed During the Juvenile Period on Hippocampal Morphology and Function. *Front Cell Neurosci*. 2018; 12. <https://doi.org/10.3389/fncel.2018.00439> PMID: [30515083](https://pubmed.ncbi.nlm.nih.gov/30515083/)
75. Vinuesa A, Bentivegna M, Calfa G, Filipello F, Pomilio C, Bonaventura MM, et al. Early Exposure to a High-Fat Diet Impacts on Hippocampal Plasticity: Implication of Microglia-Derived Exosome-like Extracellular Vesicles. *Mol Neurobiol*. 2019; 56: 5075–5094. <https://doi.org/10.1007/s12035-018-1435-8> PMID: [30474797](https://pubmed.ncbi.nlm.nih.gov/30474797/)
76. Chianese R, Coccorello R, Viggiano A, Scafuro M, Fiore M, Coppola G, et al. Impact of Dietary Fats on Brain Functions. *CN*. 2018; 16: 1059–1085. <https://doi.org/10.2174/1570159X15666171017102547> PMID: [29046155](https://pubmed.ncbi.nlm.nih.gov/29046155/)
77. Shimabukuro MK, Langhi LGP, Cordeiro I, Brito JM, Batista CM de C, Mattson MP, et al. Lipid-laden cells differentially distributed in the aging brain are functionally active and correspond to distinct phenotypes. *Scientific Reports*. 2016; 6: 23795. <https://doi.org/10.1038/srep23795> PMID: [27029648](https://pubmed.ncbi.nlm.nih.gov/27029648/)
78. Zhao X-S, Wu Q, Peng J, Pan L-H, Ren Z, Liu H-T, et al. Hyperlipidemia-induced apoptosis of hippocampal neurons in apoE(-/-) mice may be associated with increased PCSK9 expression. *Molecular Medicine Reports*. 2017; 15: 712–718. <https://doi.org/10.3892/mmr.2016.6055> PMID: [28000893](https://pubmed.ncbi.nlm.nih.gov/28000893/)
79. Loving BA, Bruce KD. Lipid and Lipoprotein Metabolism in Microglia. *Front Physiol*. 2020; 11. <https://doi.org/10.3389/fphys.2020.00393> PMID: [32411016](https://pubmed.ncbi.nlm.nih.gov/32411016/)
80. Maya-Monteiro CM, Corrêa-da-Silva F, Hofmann SS, Hesselink MKC, la Fleur SE, Yi C-X. Lipid Droplets Accumulate in the Hypothalamus of Mice and Humans with and without Metabolic Diseases. *Neuroendocrinology*. 2021; 111: 263–272. <https://doi.org/10.1159/000508735> PMID: [32422642](https://pubmed.ncbi.nlm.nih.gov/32422642/)

81. Hao S, Dey A, Yu X, Stranahan AM. Dietary obesity reversibly induces synaptic stripping by microglia and impairs hippocampal plasticity. *Brain Behav Immun*. 2016; 51: 230–239. <https://doi.org/10.1016/j.bbi.2015.08.023> PMID: [26336035](https://pubmed.ncbi.nlm.nih.gov/26336035/)
82. Park EJ, Lee JH, Yu G-Y, He G, Ali SR, Holzer RG, et al. Dietary and Genetic Obesity Promote Liver Inflammation and Tumorigenesis by Enhancing IL-6 and TNF Expression. *Cell*. 2010; 140: 197–208. <https://doi.org/10.1016/j.cell.2009.12.052> PMID: [20141834](https://pubmed.ncbi.nlm.nih.gov/20141834/)
83. Beilharz JE, Maniam J, Morris MJ. Diet-Induced Cognitive Deficits: The Role of Fat and Sugar, Potential Mechanisms and Nutritional Interventions. *Nutrients*. 2015; 7: 6719–6738. <https://doi.org/10.3390/nu7085307> PMID: [26274972](https://pubmed.ncbi.nlm.nih.gov/26274972/)
84. Zeng H, Vaka VR, He X, Booz GW, Chen J-X. High-fat diet induces cardiac remodelling and dysfunction: assessment of the role played by SIRT3 loss. *Journal of Cellular and Molecular Medicine*. 2015; 19: 1847–1856. <https://doi.org/10.1111/jcmm.12556> PMID: [25782072](https://pubmed.ncbi.nlm.nih.gov/25782072/)
85. Kalueff AV, Minasyan A, Keisala T, Shah ZH, Tuohimaa P. Hair barbering in mice: Implications for neurobehavioural research. *Behavioural Processes*. 2006; 71: 8–15. <https://doi.org/10.1016/j.beproc.2005.09.004> PMID: [16236465](https://pubmed.ncbi.nlm.nih.gov/16236465/)
86. Kappel S, Hawkins P, Mendl MT. To Group or Not to Group? Good Practice for Housing Male Laboratory Mice. *Animals*. 2017; 7: 88. <https://doi.org/10.3390/ani7120088> PMID: [29186765](https://pubmed.ncbi.nlm.nih.gov/29186765/)
87. Lidster K, Owen K, Browne WJ, Prescott MJ. Cage aggression in group-housed laboratory male mice: an international data crowdsourcing project. *Scientific Reports*. 2019; 9: 15211. <https://doi.org/10.1038/s41598-019-51674-z> PMID: [31645617](https://pubmed.ncbi.nlm.nih.gov/31645617/)
88. Weber B, Schweiger U, Deuschle M, Heuser I. Major depression and impaired glucose tolerance. *Exp Clin Endocrinol Diabetes*. 2000; 108: 187–190. <https://doi.org/10.1055/s-2000-7742> PMID: [10926314](https://pubmed.ncbi.nlm.nih.gov/10926314/)
89. Hamer M, Batty GD, Kivimaki M. Risk of future depression in people who are obese but metabolically healthy: the English longitudinal study of ageing. *Molecular Psychiatry*. 2012; 17: 940–945. <https://doi.org/10.1038/mp.2012.30> PMID: [22525487](https://pubmed.ncbi.nlm.nih.gov/22525487/)
90. Hryhorczuk C, Sharma S, Fulton SE. Metabolic disturbances connecting obesity and depression. *Front Neurosci*. 2013; 7. <https://doi.org/10.3389/fnins.2013.00177> PMID: [24109426](https://pubmed.ncbi.nlm.nih.gov/24109426/)
91. Vagena E, Ryu JK, Baeza-Raja B, Walsh NM, Syme C, Day JP, et al. A high-fat diet promotes depression-like behavior in mice by suppressing hypothalamic PKA signaling. *Translational Psychiatry*. 2019; 9: 1–15. <https://doi.org/10.1038/s41398-018-0355-8> PMID: [30664621](https://pubmed.ncbi.nlm.nih.gov/30664621/)
92. Gainey SJ, Kwakwa KA, Bray JK, Pillote MM, Tir VL, Towers AE, et al. Short-Term High-Fat Diet (HFD) Induced Anxiety-Like Behaviors and Cognitive Impairment Are Improved with Treatment by Glycerburide. *Front Behav Neurosci*. 2016; 10. <https://doi.org/10.3389/fnbeh.2016.00156> PMID: [27563288](https://pubmed.ncbi.nlm.nih.gov/27563288/)
93. Tran DMD, Westbrook RF. A high-fat high-sugar diet-induced impairment in place-recognition memory is reversible and training-dependent. *Appetite*. 2017; 110: 61–71. <https://doi.org/10.1016/j.appet.2016.12.010> PMID: [27940315](https://pubmed.ncbi.nlm.nih.gov/27940315/)
94. Dellu F, Contarino A, Simon H, Koob GF, Gold LH. Genetic Differences in Response to Novelty and Spatial Memory Using a Two-Trial Recognition Task in Mice. *Neurobiology of Learning and Memory*. 2000; 73: 31–48. <https://doi.org/10.1006/nlme.1999.3919> PMID: [10686122](https://pubmed.ncbi.nlm.nih.gov/10686122/)
95. Holcomb LA, Gordon MN, Jantzen P, Hsiao K, Duff K, Morgan D. Behavioral changes in transgenic mice expressing both amyloid precursor protein and presenilin-1 mutations: lack of association with amyloid deposits. *Behav Genet*. 1999; 29: 177–185. <https://doi.org/10.1023/a:1021691918517> PMID: [10547924](https://pubmed.ncbi.nlm.nih.gov/10547924/)
96. Wall PM, Messier C. Infralimbic kappa opioid and muscarinic M1 receptor interactions in the concurrent modulation of anxiety and memory. *Psychopharmacology (Berl)*. 2002; 160: 233–244. <https://doi.org/10.1007/s00213-001-0979-9> PMID: [11889492](https://pubmed.ncbi.nlm.nih.gov/11889492/)
97. Di Meco A, Praticò D. Early-life exposure to high-fat diet influences brain health in aging mice. *Aging Cell*. 2019; 18: e13040. <https://doi.org/10.1111/acer.13040> PMID: [31560166](https://pubmed.ncbi.nlm.nih.gov/31560166/)
98. Gehring TV, Luksys G, Sandi C, Vasilaki E. Detailed classification of swimming paths in the Morris Water Maze: multiple strategies within one trial. *Sci Rep*. 2015; 5: 14562. <https://doi.org/10.1038/srep14562> PMID: [26423140](https://pubmed.ncbi.nlm.nih.gov/26423140/)
99. Shah D, Verhoye M, Van der Linden A, D'Hooge R. Acquisition of Spatial Search Strategies and Reversal Learning in the Morris Water Maze Depend on Disparate Brain Functional Connectivity in Mice. *Cereb Cortex*. 2019; 29: 4519–4529. <https://doi.org/10.1093/cercor/bhy329> PMID: [30590460](https://pubmed.ncbi.nlm.nih.gov/30590460/)
100. Schulz D, Morschel J, Schuster S, Eulenburg V, Gomeza J. Inactivation of the Mouse L-Proline Transporter PROT Alters Glutamatergic Synapse Biochemistry and Perturbs Behaviors Required to Respond to Environmental Changes. *Front Mol Neurosci*. 2018; 11: 279. <https://doi.org/10.3389/fnmol.2018.00279> PMID: [30177871](https://pubmed.ncbi.nlm.nih.gov/30177871/)

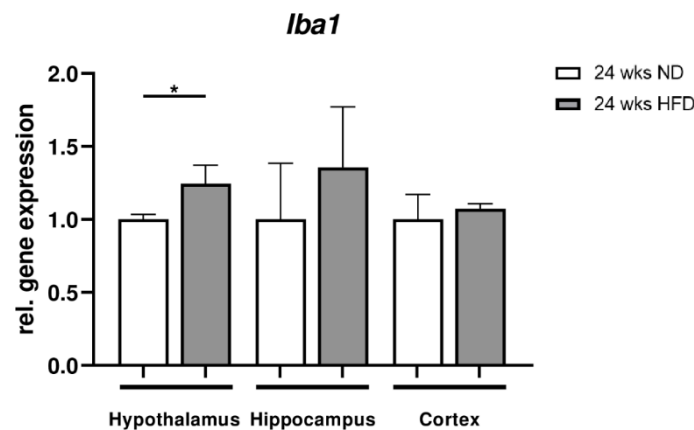
101. Woo J, Shin KO, Park SY, Jang KS, Kang S. Effects of exercise and diet change on cognition function and synaptic plasticity in high fat diet induced obese rats. *Lipids in Health and Disease*. 2013; 12: 144. <https://doi.org/10.1186/1476-511X-12-144> PMID: [24098984](https://pubmed.ncbi.nlm.nih.gov/24098984/)
102. Jurdak N, Lichtenstein AH, Kanarek RB. Diet-induced obesity and spatial cognition in young male rats. *Nutritional Neuroscience*. 2008; 11: 48–54. <https://doi.org/10.1179/147683008X301333> PMID: [18510803](https://pubmed.ncbi.nlm.nih.gov/18510803/)
103. Nam KN, Mounier A, Wolfe CM, Fitz NF, Carter AY, Castranio EL, et al. Effect of high fat diet on phenotype, brain transcriptome and lipidome in Alzheimer's model mice. *Scientific Reports*. 2017; 7: 4307. <https://doi.org/10.1038/s41598-017-04412-2> PMID: [28655926](https://pubmed.ncbi.nlm.nih.gov/28655926/)
104. Guo D-H, Yamamoto M, Hernandez CM, Khodadadi H, Baban B, Stranahan AM. Visceral adipose NLRP3 impairs cognition in obesity via IL-1R1 on CX3CR1⁺ cells. *J Clin Invest*. 2020; 130: 1961–1976. <https://doi.org/10.1172/JCI126078> PMID: [31935195](https://pubmed.ncbi.nlm.nih.gov/31935195/)
105. Boitard C, Etchamendy N, Sauviant J, Aubert A, Tronel S, Marighetto A, et al. Juvenile, but not adult exposure to high-fat diet impairs relational memory and hippocampal neurogenesis in mice. *Hippocampus*. 2012; 22: 2095–2100. <https://doi.org/10.1002/hipo.22032> PMID: [22593080](https://pubmed.ncbi.nlm.nih.gov/22593080/)
106. Boitard C, Maroun M, Tantot F, Cavaroc A, Sauviant J, Marchand A, et al. Juvenile Obesity Enhances Emotional Memory and Amygdala Plasticity through Glucocorticoids. *J Neurosci*. 2015; 35: 4092–4103. <https://doi.org/10.1523/JNEUROSCI.3122-14.2015> PMID: [25740536](https://pubmed.ncbi.nlm.nih.gov/25740536/)



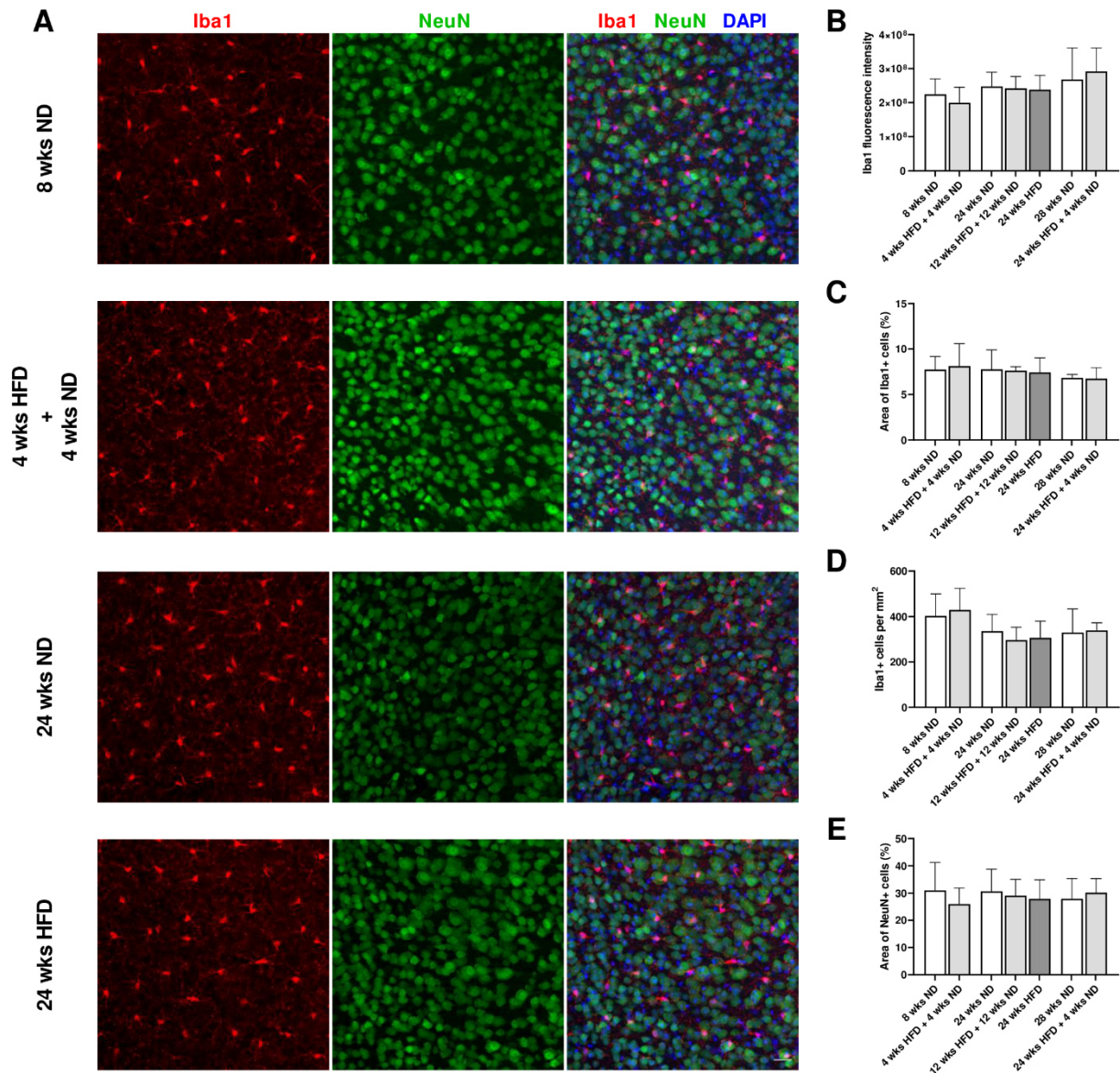
S1 Fig. HFD does not lead to other general health issues. (A-E) SHIRPA analysis was used to estimate general health of mice after ND or HFD. (A) Long-term HFD did not lead to problems with eyes, (B) skin, (C) tail and (D) gait, or (E) fecal pellets. (F) Young and old mice as well as animals on HFD and ND showed a moderate motor reactivity indicated by the writhe reflex. Data are presented as mean values and error bars indicate SD; 8 wks ND n = 11, 4 wks HFD + 4 wks ND n = 12, 16 wks ND n = 24, 4 wks HFD + 12 wks ND n = 12, 12 wks HFD + 4 wks ND n = 7, 24 wks ND n = 30, 12 wks HFD + 12 wks ND n = 12, 24 wks HFD n = 10, 28 wks ND n = 12, 24 wks HFD + 4 wks ND n = 8.



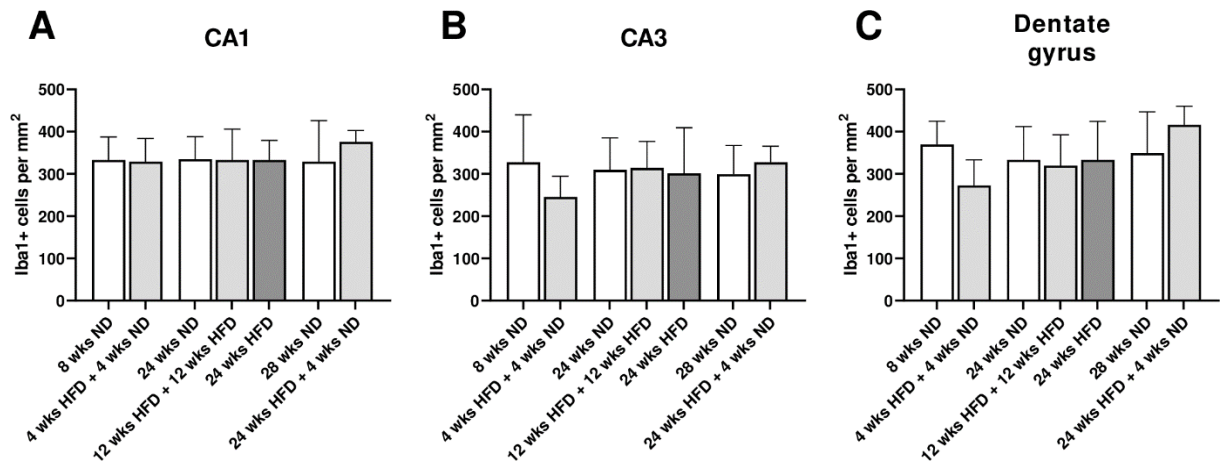
S2 Fig. Emotional state is not altered following long-term HFD. Depressive-like behavior following HFD was investigated applying the tail suspension test. (A) No effect of diet/dietary change was found on activity. (B) The latency to inactivity did not differ relative to diet. Data are presented as mean values and error bars indicate SD; 8 wks ND n = 12, 16 wks ND n = 24, 24 wks ND n = 30, 28 wks ND n = 12, 4 wks HFD + 4 wks ND n = 12, 12 wks HFD + 4 wks ND n = 7, 4 wks HFD + 12 wks ND n = 12, 12 wks HFD + 12 wks ND n = 12, 24 wks HFD n = 10, 24 wks HFD + 4 wks ND n = 9.



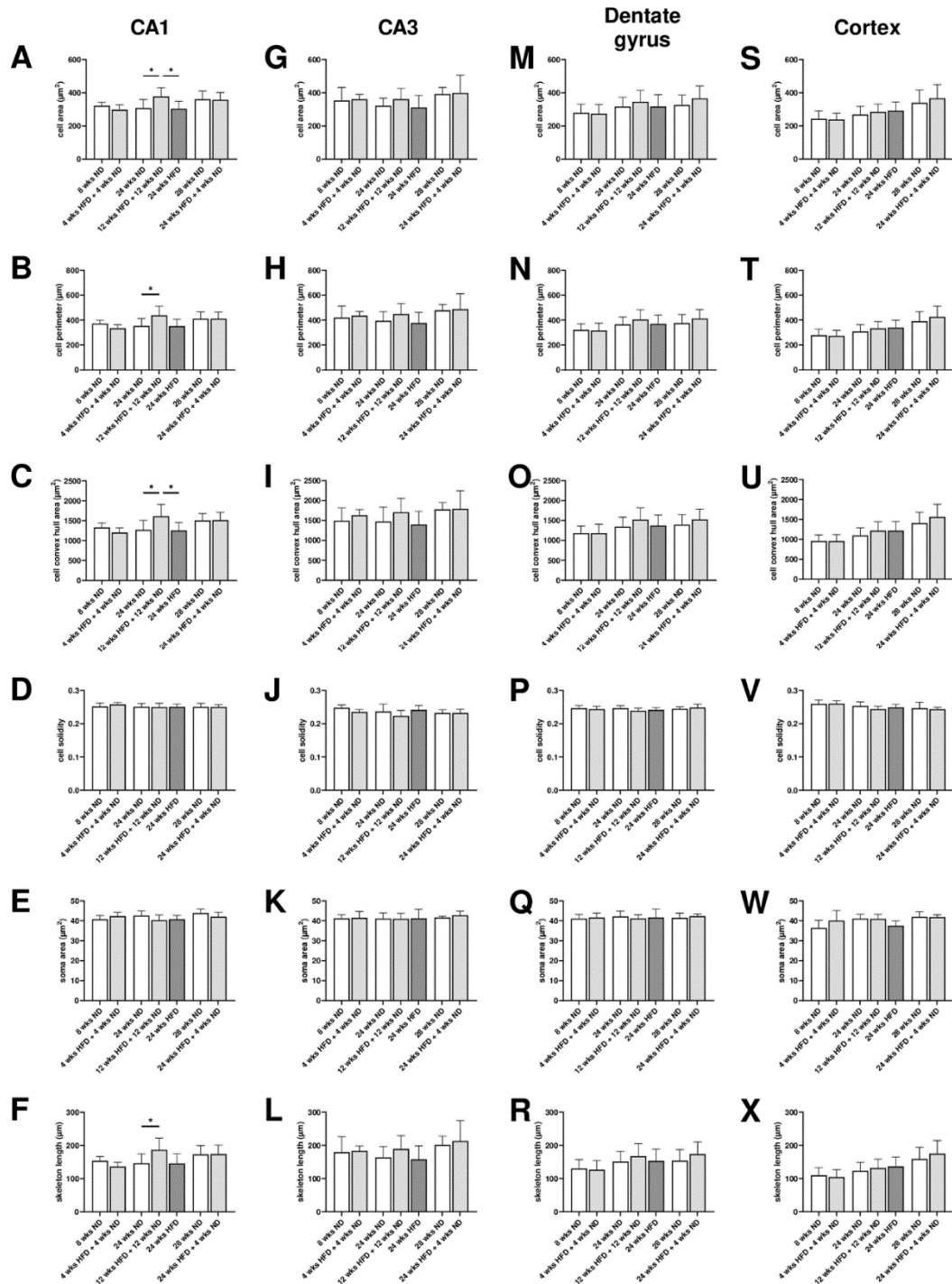
S3 Fig. Upregulated hypothalamic *Iba1* expression following long-term HFD. Relative mRNA expression levels of *Iba1* in the hypothalamus, hippocampus and cortex of mice fed with ND or HFD for 24 wks. Data are presented as mean values and error bars indicate SD; 24 wks ND n = 3, 24 wks HFD n = 3; unpaired t test; * $p < 0.05$.



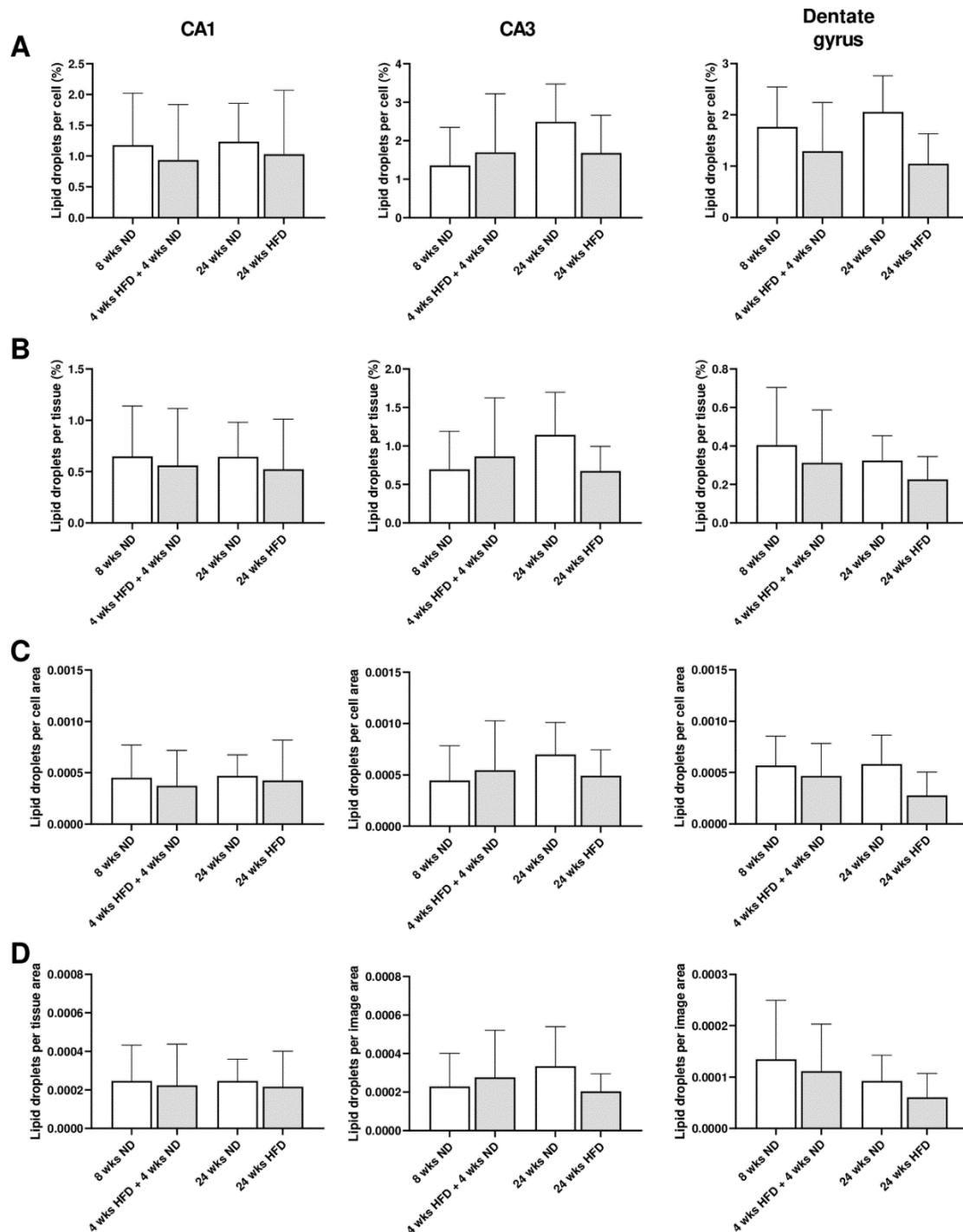
S4 Fig. Long periods of HFD do not induce microglial activation in the frontal motor cortex. (A) Representative photomicrographs of double-labeled immunofluorescence staining for Iba1 (red) and NeuN (green) within the frontal motor cortex of male wild-type C57BL/6J mice fed with ND for eight wks, HFD for four wks followed by ND for four wks and ND or rather HFD for 24 wks. Nuclei were counterstained with DAPI. Scale bar corresponds to 25 μ m. (B) Fluorescence intensity measurements of Iba1, (C) quantification of percentage of stained area with Iba1 and (E) NeuN and (D) number of Iba1-immunoreactive cells revealed no effect of HFD on microglial and neuronal morphology in the frontal cortex. Data are presented as mean values and error bars indicate SD; 8 wks ND n = 6, 4 wks HFD + 4 wks ND n = 6, 24 wks ND n = 12, 12 wks HFD + 12 wks ND n = 6, 24 wks HFD n = 6, 28 wks ND n = 6, 24 wks HFD + 4 wks ND n = 6.



S5 Fig. HFD-induced obesity does not alter microglial density in the hippocampus. Microglial cell density did not change neither after diet/dietary change nor with age in CA1 (A) and CA3 (B) regions and dentate gyrus (C) of male wild-type C57BL/6J mice fed with ND for eight wks, HFD for four wks followed by ND for four wks and ND or rather HFD for 24 wks. Data are presented as mean values and error bars indicate SD; 8 wks ND n = 6, 4 wks HFD + 4 wks ND n = 6, 24 wks ND n = 12, 12 wks HFD + 12 wks ND n = 6, 24 wks HFD n = 6, 28 wks ND n = 6, 24 wks HFD + 4 wks ND n = 6.



S6 Fig. Quantitative analysis of six morphological parameters of microglial cells reveals no microglial activation within the hippocampus and cortex after long-term HFD compared to age-matched control mice. Quantification of (A, G, M, S) microglial cell area, (B, H, N, T) cell perimeter, (C, I, O, U) cell convex hull area, (D, J, P, V) cell solidity, (E, K, Q, W) soma area and (F, L, R, X) skeleton length in CA1 and CA3 regions, dentate gyrus and frontal motor cortex of male wild-type C57BL/6J mice fed with ND for eight wks, HFD for four wks followed by ND for four wks, HFD for 12 wks followed by ND for 12 wks, ND or rather HFD for 24 wks, ND for 28 wks and HFD for 24 wks followed by ND for four wks. At least 180 cells per group were used for quantification. Data are presented as mean values and error bars indicate SD; 8 wks ND n = 6, 4 wks HFD + 4 wks ND n = 6, 24 wks ND n = 12, 12 wks HFD + 12 wks ND n = 6, 24 wks HFD n = 6, 28 wks ND n = 6, 24 wks HFD + 4 wks ND n = 6; One-way ANOVA; * p < 0.05.



S7 Fig. Long-term HFD does not lead to lipid droplet accumulation within the hippocampus. Lipid droplets (A) per cell, (B) per tissue, (C) per cell area, (D) and per tissue area did not reveal any differences in lipid droplet accumulation neither after a long period of HFD nor with age in CA1, CA3 and dentate gyrus hippocampal regions. Data are presented as mean values and error bars indicate SD; 8 wks ND n = 4–5, 4 wks HFD + 4 wks ND n = 5–6, 24 wks ND n = 6, 24 wks HFD n = 6.

S1 Table. Statistical analyses for all figures including statistical significances. The table shows relevant results of statistical tests.

Figure	Statistical significances	Statistical test	p-value
1C	16 wks ND vs. 12 wks HFD + 4 wks ND ****, 4 wks HFD + 12 wks ND vs. 12 wks HFD + 4 wks ND **** 24 wks ND vs. 24 wks HFD ****, 12 wks HFD + 12 wks ND vs. 24 wks HFD **** 28 wks ND vs. 24 wks HFD + 4 wks ND **** 24 wks HFD vs. 24 wks HFD + 4 wks ND **	One-way ANOVA Welch-ANOVA Unpaired t test Unpaired t test	< 0.0001 < 0.0001 < 0.0001 0.0024
5	8 wks ND vs. 16, 28 wks ND ***, 8 wks ND vs. 24 wks ND **** 4 wks HFD + 4 wks ND vs. 12 wks HFD + 4 wks ND, 24 wks HFD + 4 wks ND ****, 12 wks HFD + 4 wks ND vs. 24 wks HFD + 4 wks ND *	One-way ANOVA One-way ANOVA Unpaired t test	< 0.0001 < 0.0001 < 0.0001
1D	16 wks ND vs. 12 wks HFD + 4 wks ND ***, 4 wks HFD + 12 wks ND vs. 12 wks HFD + 4 wks ND **** 24 wks ND vs. 24 wks HFD ****, 12 wks HFD + 12 wks ND vs. 24 wks HFD **** 28 wks ND vs. 24 wks HFD + 4 wks ND **** 24 wks HFD vs. 24 wks HFD + 4 wks ND **	Kruskal-Wallis test Welch-ANOVA Unpaired t test Unpaired t test	< 0.0001 < 0.0001 < 0.0001 < 0.0001
13	8 wks ND vs. 16, 24, 28 wks ND ****, 16 wks ND vs. 24, 28 wks ND *** 4 wks HFD + 4 wks ND vs. 12 wks HFD + 4 wks ND *, 4 wks HFD + 4 wks ND vs. 24 wks HFD + 4 wks ND **** 4 wks HFD + 12 wks ND vs. 12 wks HFD + 12 wks ND **	One-way ANOVA Kruskal-Wallis test Welch's t test	< 0.0001 < 0.0001 0.0003
1F	24 wks ND vs. 24 wks HFD ** 24 wks HFD vs. 24 wks HFD + 4 wks ND **** 28 wks ND vs. 24 wks HFD + 4 wks ND **	Mann-Whitney test Unpaired t test Mann-Whitney test	0.0022 < 0.0001 0.0022
2A	24 wks ND vs. 24 wks HFD *, 12 wks HFD + 12 wks ND vs. 24 wks HFD *	Kruskal-Wallis test	0.0124
2B	24 wks ND vs. 24 wks HFD ****, 12 wks HFD + 12 wks ND vs. 24 wks HFD **** 28 wks ND vs. 24 wks HFD + 4 wks ND *	Kruskal-Wallis test Mann-Whitney test	< 0.0001 0.0036
21	4 wks HFD + 4 wks ND vs. 24 wks HFD + 4 wks ND **, 12 wks HFD + 4 wks ND vs. 24 wks HFD + 4 wks ND **	Kruskal-Wallis test	0.0012
3C	24 wks ND vs. 12 wks HFD + 12 wks ND *, 12 wks HFD + 12 wks ND vs. 24 wks HFD ** 8 wks ND vs. 24 wks ND **, 8 wks ND vs. 28 wks ND *, 16 wks ND vs. 28 wks ND ** 4 wks HFD + 4 wks ND vs. 24 wks HFD + 4 wks ND *	One-way ANOVA Kruskal-Wallis test One-way ANOVA	0.0021 < 0.0001 0.0129
3D	16 wks ND vs. 12 wks HFD + 4 wks ND ****, 4 wks HFD + 12 wks ND vs. 12 wks HFD + 4 wks ND **** 24 wks ND vs. 24 wks HFD ****, 12 wks HFD + 12 wks ND vs. 24 wks HFD **** 28 wks ND vs. 24 wks HFD + 4 wks ND ****	One-way ANOVA Welch-ANOVA Unpaired t test	< 0.0001 < 0.0001 < 0.0001
28	8 wks ND vs. 16, 28 wks ND ***, 8 wks ND vs. 24 wks ND ****	One-way ANOVA	< 0.0001
29	4 wks HFD + 4 wks ND vs. 12 wks HFD + 4 wks ND, 24 wks HFD + 4 wks ND ****, 12 wks HFD + 4 wks ND vs. 24 wks HFD + 4 wks ND **	One-way ANOVA	< 0.0001
30	4 wks HFD + 12 wks ND vs. 12 wks HFD + 12 wks ND **	Unpaired t test	0.0002
4A	1→3: 16 wks ND ****, 4 wks HFD + 12 wks ND ****, 12 wks HFD + 4 wks ND * Day 1: 12 wks HFD + 12 wks ND vs. 24 wks HFD **; Day 2: 12 wks HFD + 12 wks ND vs. 24 wks HFD *; Day 3: 24 wks ND vs. 24 wks HFD * 1→3: 24 wks ND ****, 12 wks HFD + 12 wks ND **, 24 wks HFD ** 1→3: 28 wks ND *, 24 wks HFD + 4 wks ND **	Two-way ANOVA Two-way ANOVA Two-way ANOVA	Day: < 0.0001 Diet: ns Interaction: ns Day: < 0.0001 Diet: 0.0003 Interaction: 0.0432 Day: < 0.0001 Diet: ns Interaction: ns
40	Day 3: 8 wks ND vs. 24, 28 wks ND *	Two-way ANOVA	Day: < 0.0001
41	1→3: 16 wks ND ****, 24 wks ND ****, 28 wks ND *	Two-way ANOVA	Age: ns Interaction: ns
42	Day 1: 4 wks HFD + 4 wks ND vs. 24 wks HFD + 4 wks ND ****, 12 wks HFD + 4 wks ND vs. 24 wks HFD + 4 wks ND *	Two-way ANOVA	Day: < 0.0001
44	1→3: 12 wks HFD + 4 wks ND *, 24 wks HFD + 4 wks ND **		Age: ns Interaction: 0.0001
46B	1→3: 8 wks ND **, 4 wks HFD + 4 wks ND ** 1→3: 16 wks ND ****, 4 wks HFD + 12 wks ND ***, 12 wks HFD + 4 wks ND * Day 1: 12 wks HFD + 12 wks ND vs. 24 wks ND * 1→3: 24 wks ND ****, 24 wks HFD ** 1→3: 28 wks ND ****, 24 wks HFD + 4 wks ND ****	Two-way ANOVA Two-way ANOVA Two-way ANOVA Two-way ANOVA	Day: < 0.0001 Diet: ns Interaction: ns Day: < 0.0001 Diet: ns Interaction: ns Day: < 0.0001 Diet: ns Interaction: ns Day: < 0.0001 Diet: ns Interaction: ns
58	Day 3: 8 wks ND vs. 16 wks ND *	Two-way ANOVA	Day: < 0.0001
59	1→3: 8 wks ND **, 16, 24 wks ND ****, 28 wks ND **	Two-way ANOVA	Age: ns Interaction: ns
60	Day 1: 4 wks HFD + 4 wks ND vs. 12 wks HFD + 4 wks ND *, 12 wks HFD + 4 wks ND vs. 24 wks HFD + 4 wks ND **	Two-way ANOVA	Day: < 0.0001
62	1→3: 4 wks HFD + 4 wks ND **, 12 wks HFD + 4 wks ND *, 24 wks HFD + 4 wks ND **	Two-way ANOVA	Age: 0.0021 Interaction: 0.0036
64C	1→3: 8 wks ND * 1→3: 16 wks ND ****, 4 wks HFD + 12 wks ND ***, 12 wks HFD + 4 wks ND ** 1→3: 24 wks ND ****, 12 wks HFD + 12 wks ND *, 24 wks HFD ** 1→3: 28 wks ND ****, 24 wks HFD + 4 wks ND **	Two-way ANOVA Two-way ANOVA Two-way ANOVA Two-way ANOVA	Day: 0.0009 Diet: ns Interaction: ns Day: < 0.0001 Diet: ns Interaction: ns Day: < 0.0001 Diet: ns Interaction: 0.0145 Day: < 0.0001 Diet: ns Interaction: ns
76	Day 1: 16 wks ND vs. 24 wks ND *; Day 3: 8 wks ND vs. 24, 28 wks ND *	Two-way ANOVA	Day: < 0.0001
77	1→3: 8 wks ND *, 16, 24, 28 wks ND ****	Two-way ANOVA	Age: < 0.0001 Interaction: < 0.0001
79	Day 1: 12 wks HFD + 4 wks ND vs. 24 wks HFD + 4 wks ND **	Two-way ANOVA	Day: 0.0067
80	1→3: 12 wks HFD + 4 wks ND **, 24 wks HFD + 4 wks ND **	Two-way ANOVA	Age: 0.0144 Interaction: ns
82D	Day 1: 8 wks ND vs. 4 wks HFD + 4 wks ND *; Day 4: 8 wks ND vs. 4 wks HFD + 4 wks ND * 1→4: 8 wks ND *	Two-way ANOVA	Day: ns Diet: ns Interaction: 0.0015
85	Day 1: 16 wks ND vs. 4 wks HFD + 12 wks ND *	Two-way ANOVA	Day: 0.0136 Diet: ns Interaction: ns
88	Day 1: 24 wks ND vs. 24 wks HFD **, 12 wks HFD + 12 wks ND vs. 24 wks HFD **	Two-way ANOVA	Day: ns Diet: ns

90			Interaction: 0.0059
91		Day 1: 8 wks ND vs. 16 wks ND ****, 16 wks ND vs. 24 wks ND **; Day 2: 8 wks ND vs. 16 wks ND *	Day: ns
92		1→4: 8 wks ND *	Age: 0.0155
93			Interaction: 0.0010
94	4E	Day 4: 8 wks ND vs. 4 wks HFD + 4 wks ND *	Day: < 0.0001
95		1→4: 4 wks HFD + 4 wks ND **	Diet: ns
96			Interaction: 0.0002
97		1→4: 16 wks ND **, 12 wks HFD + 4 wks ND **	Day: < 0.0001
98			Diet: ns
99			Interaction: ns
100		1→4: 24 wks ND ****, 12 wks HFD + 12 wks ND *, 24 wks HFD **	Day: < 0.0001
101			Diet: ns
102			Interaction: ns
103		1→4: 28 wks ND **, 24 wks HFD + 4 wks ND **	Day: < 0.0001
104			Diet: ns
105			Interaction: ns
106		Day 1: 8 wks ND vs. 16, 24, 28 wks ND **; Day 2: 8 wks ND vs. 16 wks ND *; Day 4: 8 wks ND vs. 16 wks ND **	Day: < 0.0001
107		1→4: 16, 28 wks ND **, 24 wks ND ****	Age: 0.0006
108			Interaction: 0.0101
109		Day 1: 4 wks HFD + 4 wks ND vs. 12 wks HFD + 4 wks ND *	Day: < 0.0001
110		1→4: 4 wks HFD + 4 wks ND **, 12 wks HFD + 4 wks ND **, 24 wks HFD + 4 wks ND **	Age: 0.0003
111			Interaction: ns
112	4F	1→4: 4 wks HFD + 4 wks ND **	Day: < 0.0001
113			Diet: ns
114		1→4: 16 wks ND ****, 4 wks HFD + 12 wks ND **, 12 wks HFD + 4 wks ND ****	Interaction: 0.0346
115			Day: < 0.0001
116			Diet: ns
117		1→4: 24 wks ND ****, 12 wks HFD + 12 wks ND **, 24 wks HFD ***	Interaction: 0.0336
118			Day: < 0.0001
119			Diet: ns
120		1→4: 28 wks ND **, 24 wks HFD + 4 wks ND **	Interaction: ns
121			Day: < 0.0001
122			Diet: ns
123			Interaction: ns
124		Day 4: 8 wks ND vs. 16 wks ND *	Day: < 0.0001
125		1→4: 16 wks ND ****, 24 wks ND ****, 28 wks ND **	Age: ns
126			Interaction: 0.0046
127		Day 1: 4 wks HFD + 4 wks ND vs. 12 wks HFD + 4 wks ND *	Day: < 0.0001
128		Day 3: 4 wks HFD + 4 wks ND vs. 12 wks HFD + 4 wks ND **, 12 wks HFD + 4 wks ND vs. 24 wks HFD + 4 wks ND **	Age: 0.0188
129		1→4: 4 wks HFD + 4 wks ND **, 12 wks HFD + 4 wks ND **, 24 wks HFD + 4 wks ND **	Interaction: 0.0141
130	5A	Target quadrant – opposite quadrant: 8 wks ND *, 4 wks HFD + 4 wks ND ***	Quadrant: < 0.0001
131			Diet: ns
132		Target quadrant – opposite quadrant: 16 wks ND ****, 4 wks HFD + 12 wks ND ****, 12 wks HFD + 4 wks ND ***	Interaction: ns
133			Diet: ns
134			Quadrant: < 0.0001
135			Interaction: ns

136		Target quadrant – opposite quadrant: 24 wks ND ****, 12 wks HFD + 12 wks ND ***, 24 wks HFD ****	Two-way ANOVA	Quadrant: < 0.0001
137				Diet: ns
138		Target quadrant – opposite quadrant: 28 wks ND ****, 24 wks HFD + 4 wks ND ****	Two-way ANOVA	Interaction: ns
139				Diet: ns
140				Quadrant: < 0.0001
141				Interaction: ns
142		Target quadrant: 8 wks ND vs. 28 wks ND *	Two-way ANOVA	Quadrant: < 0.0001
143				Age: ns
144				Interaction: 0.0191
145		Target quadrant: 4 wks HFD + 4 wks ND vs. 24 wks HFD + 4 wks ND ***	Two-way ANOVA	Quadrant: < 0.0001
146		Opposite quadrant: 4 wks HFD + 4 wks ND vs. 24 wks HFD + 4 wks ND *		Age: ns
147				Interaction: 0.0021
148	5C	24 wks ND vs. 24 wks HFD **, 12 wks HFD + 12 wks ND vs. 24 wks HFD ***	One-way ANOVA	0.0006
149		8 wks ND vs. 16 wks ND **, 8 wks ND vs. 28 wks ND ****	Kruskal-Wallis test	0.0002
150		4 wks HFD + 4 wks ND vs. 12 wks HFD + 4 wks ND **, 4 wks HFD + 4 wks ND vs. 24 wks HFD + 4 wks ND ***	One-way ANOVA	0.0002
151	5D	16 wks ND vs. 12 wks HFD + 4 wks ND ****, 4 wks HFD + 12 wks ND vs. 12 wks HFD + 4 wks ND ****	One-way ANOVA	< 0.0001
152		24 wks ND vs. 24 wks HFD ****, 12 wks HFD + 12 wks ND vs. 24 wks HFD ****	Welch-ANOVA	< 0.0001
153		28 wks ND vs. 24 wks HFD + 4 wks ND ****	Unpaired t test	< 0.0001
154		24 wks HFD vs. 24 wks HFD + 4 wks ND *	Unpaired t test	0.0268
155		8 wks ND vs. 16 wks ND ***, 8 wks ND vs. 24 wks ND ****, 8 wks ND vs. 28 wks ND **	One-way ANOVA	< 0.0001
156		4 wks HFD + 4 wks ND vs. 12 wks HFD + 4 wks ND, 24 wks HFD + 4 wks ND ****, 12 wks HFD + 4 wks ND vs. 24 wks HFD + 4 wks ND *	One-way ANOVA	< 0.0001
157		4 wks HFD + 12 wks ND vs. 12 wks HFD + 12 wks ND ***	Unpaired t test	0.0001
158	6A	Target quadrant – opposite quadrant: 4 wks HFD + 4 wks ND **	Two-way ANOVA	Quadrant: 0.0007
159				Diet: ns
160		Target quadrant – opposite quadrant: 16 wks ND **, 4 wks HFD + 12 wks ND ***, 12 wks HFD + 4 wks ND **	Two-way ANOVA	Interaction: ns
161				Quadrant: < 0.0001
162				Diet: ns
163				Interaction: ns
164		Target quadrant – opposite quadrant: 24 wks ND ****, 24 wks HFD ****	Two-way ANOVA	Quadrant: < 0.0001
165		Target quadrant: 24 wks ND vs. 24 wks HFD **, 12 wks HFD + 12 wks ND vs. 24 wks HFD ****		Diet: ns
166		Opposite quadrant: 24 wks ND vs. 24 wks HFD **, 12 wks HFD + 12 wks ND vs. 24 wks HFD **	Two-way ANOVA	Interaction: < 0.0001
167		Target quadrant – opposite quadrant: 28 wks ND **, 24 wks HFD + 4 wks ND **		Quadrant: < 0.0001
168				Diet: ns
169				Interaction: ns
170		Target quadrant: 4 wks HFD + 4 wks ND vs. 12 wks HFD + 4 wks ND **, 4 wks HFD + 4 wks ND vs. 24 wks HFD + 4 wks ND **	Two-way ANOVA	Quadrant: < 0.0001
171				Age: ns
172				Interaction: 0.0153
173	6C	24 wks ND vs. 24 wks HFD **, 12 wks HFD + 12 wks ND vs. 24 wks HFD *	One-way ANOVA	0.0016
174		8 wks ND vs. 16, 28 wks ND ****, 8 wks ND vs. 24 wks ND *, 16 wks ND vs. 24 wks ND **, 24 wks ND vs. 28 wks ND **	One-way ANOVA	< 0.0001
175		4 wks HFD + 4 wks ND vs. 12 wks HFD + 4 wks ND ****, 4 wks HFD + 4 wks ND vs. 24 wks HFD + 4 wks ND ****	One-way ANOVA	< 0.0001
176	6D	16 wks ND vs. 12 wks HFD + 4 wks ND *, 4 wks HFD + 12 wks ND vs. 12 wks HFD + 4 wks ND *	Kruskal-Wallis test	0.0164
177	6E	16 wks ND vs. 12 wks HFD + 4 wks ND *, 4 wks HFD + 12 wks ND vs. 12 wks HFD + 4 wks ND **	Kruskal-Wallis test	0.0052
178	7B	24 wks ND vs. 24 wks HFD **	Welch-ANOVA	0.0069
179		24 wks HFD vs. 24 wks HFD + 4 wks ND **	Unpaired t test	0.0047
180	7C	24 wks ND vs. 24 wks HFD ***	One-way ANOVA	0.0003
181		24 wks HFD vs. 24 wks HFD + 4 wks ND *	Unpaired t test	0.0346

4. Zusammenfassung

Nach Angaben der Weltgesundheitsorganisation (WHO) hat sich die Prävalenz von Adipositas seit 1975 nahezu verdreifacht, wofür neben der genetischen Disposition Sozial- und Umweltfaktoren wie die Kombination aus gesteigerter Fettaufnahme über die Nahrung sowie eine Abnahme der körperlichen Aktivität verantwortlich sind ^{172,174,255}. Der Verzehr einer fettreichen Nahrung und Adipositas sind mit zahlreichen Krankheiten wie Herz-Kreislauf-Erkrankungen, Krebs, Störungen des Glukosestoffwechsels und Typ-2-Diabetes verbunden ^{168,256–259}. Darüber hinaus geht eine (ernährungsbedingte) Adipositas mit kognitiven Defiziten und einem erhöhten Risiko für neurodegenerative Erkrankungen, einschließlich der Alzheimer-Krankheit, einher, indem Entzündungen im Gehirn verstärkt und die Gehirnalterung beschleunigt werden ^{210,246,260}. Der westliche Lebensstil und die ernährungsbedingte Adipositas beeinflussen zudem den funktionalen und morphologischen Phänotyp von Mikrogliazellen ^{183,184}. Mikroglia sind immunkompetente Makrophagen des zentralen Nervensystems (ZNS), die das Hirnparenchym fortlaufend mit ihren hochdynamischen und mobilen Zellfortsätzen auf Gewebeschäden, Infektionen oder homöostatische Störungen hin überwachen. Indem sie Krankheitserreger, apoptotische Zellen, synaptische Überreste, Toxine und Myelintrümmer aufnehmen, tragen Mikrogliazellen entscheidend zur Homöostase, Plastizität und zum Lernen bei ^{11,13,51,52,261,262}. Die auffällige morphologische Plastizität der Mikroglia ist eine der herausragenden Eigenschaften dieser Zellen und die Kategorisierung der Funktion von Mikrogliazellen auf Grundlage der Morphologie ist gut etabliert. Häufig wird eine automatische Klassifizierung der morphologischen Phänotypen von Mikrogliazellen anhand quantitativer Parameter vorgenommen. Diese Ansätze sind allerdings auf einige wenige und vor allem manuell ausgewählte Kriterien beschränkt, was das Risiko eines Selektionsbias birgt und die resultierenden Klassifizierungen beeinträchtigen kann.

Im ersten Teil dieser Arbeit wurden Mikroglia mit Hilfe eines maschinellen Lernansatzes vier morphologischen Kategorien (verzweigt, stäbchenförmig, aktiviert, amöboid) zugeordnet. Hierfür wurde ein neuronales Faltungsnetzwerk (Convolutional Neural Network (CNN)) mit manuell ausgewählten Mikrogliazellen im Hippocampus und Kortex verschiedener Mausstämmen (C57BL/6J-, *db/db*- und *db/+*-Mäuse) angewendet. Die entwickelte Methode zur Klassifizierung mikroglialer morphologischer Phänotypen wurde in einem Mausmodell des ischämischen Schlaganfalls, bei dem nachgewiesenermaßen Mikrogliazellen in den betroffenen Hirnregionen aktiviert sind ^{263–265}, überprüft und bestätigt. Die vom ischämischen Schlaganfall betroffenen Areale im Hippocampus und Neokortex wiesen mehr aktivierte und stäbchenförmige Mikrogliazellen und folglich weniger verzweigte Mikroglia auf als die relevanten Hirnareale der kontralateralen Hemisphäre. Bereits kleine morphologische Unterschiede in Mikrogliazellen sind mit Hilfe eines CNNs nachweisbar und können

auf eine beginnende Veränderung des Aktivierungszustands von Mikrogliazellen und damit auf pathologische Prozesse im Gehirn hinweisen. Zur weiteren Verifizierung dieser auf einem CNN basierenden Klassifizierungsmethode wurden zahlreiche morphologische Parameter (u. A. Zellfläche, Zellumfang, konvexe Fläche und Umfang der Zellhülle, Zellsolidität, Zellkonvexität, Zellzirkularität, Fläche und Umfang des Somas, Somazirkularität, Anzahl und Länge der Fortsätze, Verzweigungs- und Endpunkte der Fortsätze) von etwa 16.000 Iba1-positiven Zellen gemessen und quantitativ analysiert. Damit kann im Anschluss an die Klassifizierung eine detaillierte morphologische Charakterisierung der Mikrogliazellen erfolgen. Übereinstimmend mit vorangegangenen parameterbasierten Studien wurden beispielsweise größere Zellflächen für aktivierte und stäbchenförmige Mikroglia sowie kleinere Somaflächen für verzweigte Mikroglia bestätigt.

Im Gegensatz zur konventionellen parameterbasierten Klassifizierung, bei der vor Einteilung der Zellen in morphologische Klassen ausgewählte Parameter berechnet werden müssen, erfordert die auf einem CNN basierende Klassifizierung keine Parameter oder eine Kombination von diesen, sondern lediglich Bildausschnitte einzelner Zellen. Beim Vergleich beider Klassifizierungsmethoden wurde deutlich, dass sich die Festlegung geeigneter Parameterkombinationen und Schwellenwerte als schwierig gestaltet, da es teils sehr große Überlappungen von Parameterwerten zwischen den einzelnen Klassen gibt. Damit bietet die CNN-Klassifizierung, die sich ausschließlich auf den morphologischen Phänotyp stützt, eine leistungsstarke Alternative zur parameterbasierten Klassifizierung.

Die im Rahmen dieser Arbeit entwickelte Methode zur Klassifizierung und Quantifizierung morphologischer Phänotypen von Mikrogliazellen erfordert einerseits eine komplexe Bildvorbereitung (einschließlich Kontrastausgleich, Detektion von Soma und Fortsätzen, Zellrekonstruktion und -trennung), bevor das maschinelle Lernmodell für jede beliebige Hirnregion anwendbar ist. Andererseits vermag die Methode effizient, zeitsparend und objektiv postmortale mikrogliale Veränderungen in gesunden und kranken Tiermodellen sowie zukünftig für Hirnautopsieproben von Menschen zu charakterisieren.

Im zweiten Teil der Arbeit wurden die Auswirkungen einer langfristigen fettreichen Ernährung auf Verhaltensmerkmale, Mikroglia und Neuronen bei Mäusen und etwaige reversible Effekte nach einer Ernährungsumstellung untersucht. Hierfür wurden 8 Wochen alte männliche C57BL/6J-Mäuse genutzt, bei denen für 24 Wochen eine normale Diät (11 kcal% Fett), eine fettreiche Diät (59 kcal% Fett) oder ein Ernährungswechsel durchgeführt wurde. Die Folgen der ernährungsbedingten Adipositas und der Ernährungsumstellung für den allgemeinen Gesundheitszustand (Fellbeschaffenheit, Vorhandensein von Vibrissen), die sensorischen und motorischen Fähigkeiten, das Lernen sowie das Gedächtnis wurden anhand eines angepassten Protokolls zur Bewertung des

Phänotyps sowie unter Verwendung von Y-Maze-, Morris-Water-Maze- und Tail-Suspension-Tests untersucht. Neuronen und Mikroglia wurden im mediobasalen Hypothalamus, im Hippocampus und im frontalen motorischen Kortex nach einer langfristigen fettreichen Ernährung sowie einer anschließenden Ernährungsumstellung histologisch analysiert.

Eine gesteigerte mikrogliale Reaktion (erhöhte Iba1-Fluoreszenzintensität, gesteigerter Anteil der Iba1-gefärbten Fläche und höhere Genexpression von *Iba1*) auf eine 24-wöchige fettreiche Ernährung war auf den Hypothalamus begrenzt und bestätigte vorangegangene Studien. Die detaillierte quantitative Analyse der mikroglialen Morphologie unter Verwendung des im ersten Teil dieser Arbeit beschriebenen und für Fluoreszenzaufnahmen angepassten Ansatzes zeigte bei Mikrogliazellen im Kortex und Hippocampus adipöser Mäuse keine Veränderungen in relevanten morphologischen Parametern. Eine Vergrößerung von Zell- und Somafläche oder eine verringerte Länge der Fortsätze der Mikrogliazellen hätte z. B. auf einen aktivierten morphologischen Phänotyp hingedeutet. In keiner der drei analysierten Hirnregionen wurden dystrophe Mikrogliazellen, eine Neurodegeneration oder eine Anhäufung intrazellulärer Lipidtröpfchen, wie in der Leber untersucht und nachgewiesen, beobachtet.

Eine fettreiche Ernährung für 24 Wochen führte zu allgemeinen Gesundheitsproblemen in Form von Fellveränderungen (struppiges Fell mit kahlen Stellen) und Vibrissenverlust. Sensorische oder motorische Fähigkeiten und der emotionale Zustand (z. B. Motivation) adipöser Mäuse waren nicht eingeschränkt verglichen mit altersentsprechenden Kontrollmäusen (normale Ernährung oder kürzere Zeit auf fettreicher Ernährung mit anschließender Ernährungsumstellung). Dadurch konnte ausgeschlossen werden, dass die Motivation oder Leistung in den weiteren Verhaltenstests durch Veränderungen des emotionalen Zustands, schwere motorische Probleme oder eingeschränkte Reflexe beeinflusst wurde. Das Kurz- und Langzeitgedächtnis der Versuchstiere war durch eine lang anhaltende fettreiche Ernährung nicht beeinträchtigt. Mäuse, denen für längere Zeit eine fettreiche Ernährung verabreicht wurde, hielten allerdings im Vergleich zu Kontrolltieren beim Morris-Water-Maze-Test an ihrer alten Suchstrategie fest, indem sie den alten, bekannten Standort der Plattform bevorzugten, anstatt andere Quadranten zu überprüfen. Die ernährungsbedingte Adipositas hatte demzufolge bei Mäusen dieser Studie, die ab einem Alter von 8 Wochen eine fettreiche Ernährung erhielten, zwar keine Defizite beim Lernen und Langzeitgedächtnis zur Folge, könnte aber die kognitive Flexibilität beeinflusst haben.

Mäuse profitierten erwartungsgemäß hinsichtlich ihres Gewichts von einer Ernährungsumstellung auf eine normale Diät. Eine morphologische Aktivierung mikroglialer Zellen im mediobasalen Hypothalamus, wie nach 24 Wochen fettreicher Diät beobachtet, wurde bei Mäusen, die nach einer

24-wöchigen fettreichen Ernährung auf eine normale Ernährung für 4 Wochen umgestellt wurden, nicht beobachtet und war demnach reversibel.

Zusammenfassend wurde festgestellt, dass lange Zeiträume mit übermäßigem Fett in der Nahrung allein keine Lerndefizite oder Beeinträchtigungen des räumlichen Gedächtnisses verursachen, obwohl eine ernährungsbedingte Adipositas nachteilige Folgen für die kognitive Flexibilität haben kann und Mäuse von einer Ernährungsumstellung profitieren. Keine Defizite im Kurz- und Lachzeitgedächtnis nach einer langfristigen fettreichen Ernährung stehen nicht im Einklang mit Ergebnissen anderer Studien^{232–235}, was auf unterschiedliche Diäten, abweichendes Alter der Mäuse oder Überinterpretation zurückzuführen sein könnte. Insbesondere die Art der Nahrung – fettreich, zuckerreich oder die westliche Ernährungsform mit hohem Fett- und Zuckergehalt – sowie die genaue Zusammensetzung des Futters sind entscheidend für die Interpretation von Daten und somit für die therapeutischen Konsequenzen für Stoffwechselerkrankungen und kognitive Störungen. Zum besseren Verständnis des Zusammenhangs unterschiedlicher Risikofaktoren für neurodegenerative Erkrankungen wie M. Alzheimer und zur Untersuchung der zugrunde liegenden Mechanismen im Mausmodell ist es nach Betrachtung der aktuellen Studienlage notwendig, den Fokus auf die Futterzusammensetzung und das Alter bei Beginn der Fütterungsstudie zu legen.

5. Literaturverzeichnis

1. Bear, M. F., Connors, B. W. & Paradiso, M. A. *Neurowissenschaften: ein grundlegendes Lehrbuch für Biologie, Medizin und Psychologie*. (Springer Spektrum, 2012).
2. Dos Santos, S. E. *et al.* Similar Microglial Cell Densities across Brain Structures and Mammalian Species: Implications for Brain Tissue Function. *J. Neurosci.* 40, 4622–4643 (2020).
3. Del Rio-Hortega, P. El tercer elemento de los centros nerviosos I La microglia en estado normal II Intervención de la microglia en los procesos patológicos III Naturaleza probable de la microglia. *Bol Soc Esp Biol* 69–120 (1919).
4. Sierra, A. *et al.* The “Big-Bang” for modern glial biology: Translation and comments on Pío del Río-Hortega 1919 series of papers on microglia: 1919 Río-Hortega Papers on Microglia. *Glia* 64, 1801–1840 (2016).
5. Bohlen, C. J., Friedman, B. A., Dejanovic, B. & Sheng, M. Microglia in Brain Development, Homeostasis, and Neurodegeneration. *Annu. Rev. Genet.* 53, 263–288 (2019).
6. Eyo, U. B. & Wu, L.-J. Microglia: Lifelong patrolling immune cells of the brain. *Prog. Neurobiol.* 179, 101614 (2019).
7. Prinz, M., Jung, S. & Priller, J. Microglia Biology: One Century of Evolving Concepts. *Cell* 179, 292–311 (2019).
8. Ginhoux, F. *et al.* Fate Mapping Analysis Reveals That Adult Microglia Derive from Primitive Macrophages. *Science* 330, 841–845 (2010).
9. Nimmerjahn, A., Kirchhoff, F. & Helmchen, F. Resting Microglial Cells Are Highly Dynamic Surveillants of Brain Parenchyma in Vivo. *Science* 308, 1314–1318 (2005).
10. Prinz, M., Priller, J., Sisodia, S. S. & Ransohoff, R. M. Heterogeneity of CNS myeloid cells and their roles in neurodegeneration. *Nat. Neurosci.* 14, 1227–1235 (2011).
11. Goldmann, T. & Prinz, M. Role of Microglia in CNS Autoimmunity. *Clin. Dev. Immunol.* 2013, 1–8 (2013).
12. Welsch, U., Kummer, W. & Deller, T. *Histologie: Zytologie, Histologie und mikroskopische Anatomie: das Lehrbuch*. (Elsevier, 2018).
13. Parkhurst, C. N. *et al.* Microglia Promote Learning-Dependent Synapse Formation through Brain-Derived Neurotrophic Factor. *Cell* 155, 1596–1609 (2013).
14. Yang, S. *et al.* Microglia reprogram metabolic profiles for phenotype and function changes in central nervous system. *Neurobiol. Dis.* 152, 105290 (2021).
15. Prinz, M., Erny, D. & Hagemeyer, N. Ontogeny and homeostasis of CNS myeloid cells. *Nat. Immunol.* 18, 385–392 (2017).
16. Brioschi, S., Zhou, Y. & Colonna, M. Brain Parenchymal and Extraparenchymal Macrophages in Development, Homeostasis, and Disease. *J. Immunol.* 204, 294–305 (2020).
17. Tan, Y.-L., Yuan, Y. & Tian, L. Microglial regional heterogeneity and its role in the brain. *Mol. Psychiatry* 25, 351–367 (2020).
18. Kierdorf, K. *et al.* Microglia emerge from erythromyeloid precursors via Pu.1- and Irf8-dependent pathways. *Nat. Neurosci.* 16, 273–280 (2013).
19. Füger, P. *et al.* Microglia turnover with aging and in an Alzheimer’s model via long-term in vivo single-cell imaging. *Nat. Neurosci.* 20, 1371–1376 (2017).
20. Huang, Y. *et al.* Repopulated microglia are solely derived from the proliferation of residual microglia after acute depletion. *Nat. Neurosci.* 21, 530–540 (2018).
21. Li, Q. & Barres, B. A. Microglia and macrophages in brain homeostasis and disease. *Nat. Rev. Immunol.* 18, 225–242 (2018).
22. Askew, K. *et al.* Coupled Proliferation and Apoptosis Maintain the Rapid Turnover of Microglia in the Adult Brain. *Cell Rep.* 18, 391–405 (2017).
23. Tay, T. L. *et al.* A new fate mapping system reveals context-dependent random or clonal expansion of microglia. *Nat. Neurosci.* 20, 793–803 (2017).
24. Butovsky, O. *et al.* Identification of a unique TGF- β -dependent molecular and functional signature in microglia. *Nat. Neurosci.* 17, 131–143 (2014).

25. Grabert, K. *et al.* Microglial brain region-dependent diversity and selective regional sensitivities to aging. *Nat. Neurosci.* 19, 504–516 (2016).
26. Galatro, T. F. *et al.* Transcriptomic analysis of purified human cortical microglia reveals age-associated changes. *Nat. Neurosci.* 20, 1162–1171 (2017).
27. Gosselin, D. *et al.* An environment-dependent transcriptional network specifies human microglia identity. *Science* 356, eaal3222 (2017).
28. Bennett, M. L. *et al.* New tools for studying microglia in the mouse and human CNS. *Proc. Natl. Acad. Sci.* 113, E1738–E1746 (2016).
29. Zrzavy, T. *et al.* Loss of ‘homeostatic’ microglia and patterns of their activation in active multiple sclerosis. *Brain* 140, 1900–1913 (2017).
30. Butovsky, O. & Weiner, H. L. Microglial signatures and their role in health and disease. *Nat. Rev. Neurosci.* 19, 622–635 (2018).
31. Villa, A. *et al.* Sex-Specific Features of Microglia from Adult Mice. *Cell Rep.* 23, 3501–3511 (2018).
32. Stevens, B. *et al.* The Classical Complement Cascade Mediates CNS Synapse Elimination. *Cell* 131, 1164–1178 (2007).
33. Wake, H., Moorhouse, A. J., Jinno, S., Kohsaka, S. & Nabekura, J. Resting Microglia Directly Monitor the Functional State of Synapses In Vivo and Determine the Fate of Ischemic Terminals. *J. Neurosci.* 29, 3974–3980 (2009).
34. Sierra, A. *et al.* Microglia Shape Adult Hippocampal Neurogenesis through Apoptosis-Coupled Phagocytosis. *Cell Stem Cell* 7, 483–495 (2010).
35. Paolicelli, R. C. *et al.* Synaptic Pruning by Microglia Is Necessary for Normal Brain Development. *Science* 333, 1456–1458 (2011).
36. Schafer, D. P. *et al.* Microglia Sculpt Postnatal Neural Circuits in an Activity and Complement-Dependent Manner. *Neuron* 74, 691–705 (2012).
37. Zhan, Y. *et al.* Deficient neuron-microglia signaling results in impaired functional brain connectivity and social behavior. *Nat. Neurosci.* 17, 400–406 (2014).
38. Miyamoto, A. *et al.* Microglia contact induces synapse formation in developing somatosensory cortex. *Nat. Commun.* 7, 12540 (2016).
39. Selkoe, D. J. Alzheimer’s Disease Is a Synaptic Failure. *Science* 298, 789–791 (2002).
40. Stephan, A. H., Barres, B. A. & Stevens, B. The Complement System: An Unexpected Role in Synaptic Pruning During Development and Disease. *Annu. Rev. Neurosci.* 35, 369–389 (2012).
41. Vasek, M. J. *et al.* A complement–microglial axis drives synapse loss during virus-induced memory impairment. *Nature* 534, 538–543 (2016).
42. Kettenmann, H., Kirchhoff, F. & Verkhratsky, A. Microglia: New Roles for the Synaptic Stripper. *Neuron* 77, 10–18 (2013).
43. Alexaki, V. I. *et al.* DHEA inhibits acute microglia-mediated inflammation through activation of the TrkA-Akt1/2-CREB-Jmjd3 pathway. *Mol. Psychiatry* 23, 1410–1420 (2018).
44. Rizzi, C. *et al.* NGF steers microglia toward a neuroprotective phenotype. *Glia* 66, 1395–1416 (2018).
45. Fodelianaki, G. *et al.* Nerve Growth Factor modulates LPS - induced microglial glycolysis and inflammatory responses. *Exp. Cell Res.* 377, 10–16 (2019).
46. Yilmaz, C. *et al.* Neurosteroids as regulators of neuroinflammation. *Front. Neuroendocrinol.* 55, 100788 (2019).
47. Wu, S.-Y. *et al.* BDNF reverses aging-related microglial activation. *J. Neuroinflammation* 17, 210 (2020).
48. Harley, S. B. R. *et al.* Selective Ablation of BDNF from Microglia Reveals Novel Roles in Self-Renewal and Hippocampal Neurogenesis. *J. Neurosci.* 41, 4172–4186 (2021).
49. Kierdorf, K. & Prinz, M. Factors regulating microglia activation. *Front. Cell. Neurosci.* 7, (2013).
50. Prinz, M. & Priller, J. Microglia and brain macrophages in the molecular age: from origin to neuropsychiatric disease. *Nat. Rev. Neurosci.* 15, 300–312 (2014).

51. Nutma, E., van Gent, D., Amor, S. & Peferoen, L. A. N. Astrocyte and Oligodendrocyte Cross-Talk in the Central Nervous System. *Cells* 9, 600 (2020).
52. Traiffort, E., Kassoussi, A., Zahaf, A. & Laouarem, Y. Astrocytes and Microglia as Major Players of Myelin Production in Normal and Pathological Conditions. *Front. Cell. Neurosci.* 14, 79 (2020).
53. Galloway, D. A., Phillips, A. E. M., Owen, D. R. J. & Moore, C. S. Phagocytosis in the Brain: Homeostasis and Disease. *Front. Immunol.* 10, 790 (2019).
54. Mike, J. K. & Ferriero, D. M. Efferocytosis Mediated Modulation of Injury after Neonatal Brain Hypoxia-Ischemia. *Cells* 10, 1025 (2021).
55. Kotter, M. R. Myelin Impairs CNS Remyelination by Inhibiting Oligodendrocyte Precursor Cell Differentiation. *J. Neurosci.* 26, 328–332 (2006).
56. Safaiyan, S. *et al.* Age-related myelin degradation burdens the clearance function of microglia during aging. *Nat. Neurosci.* 19, 995–998 (2016).
57. Hill, R. A., Li, A. M. & Grutzendler, J. Lifelong cortical myelin plasticity and age-related degeneration in the live mammalian brain. *Nat. Neurosci.* 21, 683–695 (2018).
58. Sierra, A., Gottfried-Blackmore, A. C., McEwen, B. S. & Bulloch, K. Microglia derived from aging mice exhibit an altered inflammatory profile. *Glia* 55, 412–424 (2007).
59. Floden, A. M. & Combs, C. K. Microglia Demonstrate Age-Dependent Interaction with Amyloid- β Fibrils. *J. Alzheimers Dis.* 25, 279–293 (2011).
60. Hefendehl, J. K. *et al.* Homeostatic and injury-induced microglia behavior in the aging brain. *Aging Cell* 13, 60–69 (2014).
61. Cantuti-Castelvetri, L. *et al.* Defective cholesterol clearance limits remyelination in the aged central nervous system. *Science* 359, 684–688 (2018).
62. Mawuenyega, K. G. *et al.* Decreased Clearance of CNS β -Amyloid in Alzheimer's Disease. *Science* 330, 1774–1774 (2010).
63. Wildsmith, K. R., Holley, M., Savage, J. C., Skerrett, R. & Landreth, G. E. Evidence for impaired amyloid β clearance in Alzheimer's disease. *Alzheimers Res. Ther.* 5, 33 (2013).
64. Hickman, S., Izzy, S., Sen, P., Morsett, L. & El Khoury, J. Microglia in neurodegeneration. *Nat. Neurosci.* 21, 1359–1369 (2018).
65. Madore, C., Yin, Z., Leibowitz, J. & Butovsky, O. Microglia, Lifestyle Stress, and Neurodegeneration. *Immunity* 52, 222–240 (2020).
66. Tay, T. L. *et al.* Microglia Gone Rogue: Impacts on Psychiatric Disorders across the Lifespan. *Front. Mol. Neurosci.* 10, 421 (2018).
67. Brisch, R. *et al.* The role of microglia in neuropsychiatric disorders and suicide. *Eur. Arch. Psychiatry Clin. Neurosci.* (2021) doi:10.1007/s00406-021-01334-z.
68. Streit, W. J. Microglial senescence: does the brain's immune system have an expiration date? *Trends Neurosci.* 29, 506–510 (2006).
69. Streit, W. J., Braak, H., Xue, Q.-S. & Bechmann, I. Dystrophic (senescent) rather than activated microglial cells are associated with tau pathology and likely precede neurodegeneration in Alzheimer's disease. *Acta Neuropathol.* 118, 475–485 (2009).
70. Bussian, T. J. *et al.* Clearance of senescent glial cells prevents tau-dependent pathology and cognitive decline. *Nature* 562, 578–582 (2018).
71. Dixon, S. J. *et al.* Ferroptosis: An Iron-Dependent Form of Nonapoptotic Cell Death. *Cell* 149, 1060–1072 (2012).
72. Angelova, D. M. & Brown, D. R. Microglia and the aging brain: are senescent microglia the key to neurodegeneration? *J. Neurochem.* 151, 676–688 (2019).
73. Kapralov, A. A. *et al.* Redox lipid reprogramming commands susceptibility of macrophages and microglia to ferroptotic death. *Nat. Chem. Biol.* 16, 278–290 (2020).
74. Damani, M. R. *et al.* Age-related alterations in the dynamic behavior of microglia. *Aging Cell* 10, 263–276 (2011).
75. Perry, V. H. & Holmes, C. Microglial priming in neurodegenerative disease. *Nat. Rev. Neurol.* 10, 217–224 (2014).

76. Keren-Shaul, H. *et al.* A Unique Microglia Type Associated with Restricting Development of Alzheimer's Disease. *Cell* 169, 1276-1290.e17 (2017).
77. Krasemann, S. *et al.* The TREM2-APOE Pathway Drives the Transcriptional Phenotype of Dysfunctional Microglia in Neurodegenerative Diseases. *Immunity* 47, 566-581.e9 (2017).
78. Song, W. M. & Colonna, M. The identity and function of microglia in neurodegeneration. *Nat. Immunol.* 19, 1048–1058 (2018).
79. Jordão, M. J. C. *et al.* Single-cell profiling identifies myeloid cell subsets with distinct fates during neuroinflammation. *Science* 363, eaat7554 (2019).
80. Srinivasan, K. *et al.* Alzheimer's Patient Microglia Exhibit Enhanced Aging and Unique Transcriptional Activation. *Cell Rep.* 31, 107843 (2020).
81. Alexaki, V. I. The Impact of Obesity on Microglial Function: Immune, Metabolic and Endocrine Perspectives. *Cells* 10, 1584 (2021).
82. Sala Frigerio, C. *et al.* The Major Risk Factors for Alzheimer's Disease: Age, Sex, and Genes Modulate the Microglia Response to A β Plaques. *Cell Rep.* 27, 1293-1306.e6 (2019).
83. Ransohoff, R. M. How neuroinflammation contributes to neurodegeneration. *Science* 353, 777–783 (2016).
84. Salter, M. W. & Stevens, B. Microglia emerge as central players in brain disease. *Nat. Med.* 23, 1018–1027 (2017).
85. Dokalis, N. & Prinz, M. Resolution of neuroinflammation: mechanisms and potential therapeutic option. *Semin. Immunopathol.* 41, 699–709 (2019).
86. Cunha, M. I. *et al.* Pro-inflammatory activation following demyelination is required for myelin clearance and oligodendrogenesis. *J. Exp. Med.* 217, e20191390 (2020).
87. Davalos, D. *et al.* ATP mediates rapid microglial response to local brain injury in vivo. *Nat. Neurosci.* 8, 752–758 (2005).
88. Tremblay, M.-E. *et al.* The Role of Microglia in the Healthy Brain. *J. Neurosci.* 31, 16064–16069 (2011).
89. Nimmerjahn, A. Two-Photon Imaging of Microglia in the Mouse Cortex In Vivo. *Cold Spring Harb. Protoc.* 2012, pdb.prot069294 (2012).
90. Huang, H. *et al.* Damage-associated molecular pattern-activated neutrophil extracellular trap exacerbates sterile inflammatory liver injury: LIVER INJURY/REGENERATION. *Hepatology* 62, 600–614 (2015).
91. Colonna, M. & Butovsky, O. Microglia Function in the Central Nervous System During Health and Neurodegeneration. *Annu. Rev. Immunol.* 35, 441–468 (2017).
92. Doorn, K. J. *et al.* Increased Amoeboid Microglial Density in the Olfactory Bulb of Parkinson's and Alzheimer's Patients: Microglia in Olfactory Bulb of AD and PD Patients. *Brain Pathol.* 24, 152–165 (2014).
93. Stence, N., Waite, M. & Dailey, M. E. Dynamics of microglial activation: A confocal time-lapse analysis in hippocampal slices. *Glia* 33, 256–266 (2001).
94. Fumagalli, S., Perego, C., Ortolano, F. & De Simoni, M.-G. CX3CR1 deficiency induces an early protective inflammatory environment in ischemic mice: Fractalkine Receptor and Ischemic Environment. *Glia* 61, 827–842 (2013).
95. Salamanca, L. *et al.* MIC-MAC: An automated pipeline for high-throughput characterization and classification of three-dimensional microglia morphologies in mouse and human postmortem brain samples. *Glia* 67, 1496–1509 (2019).
96. Nissl, F. Über einige Beziehungen zwischen Nervenzellerkrankungen und gliösen Erscheinungen bei ver-schiedenen Psychosen. *Arch F Psychiatr U Nervenkrankh* 656 (1899).
97. Ziebell, J. M., Taylor, S. E., Cao, T., Harrison, J. L. & Lifshitz, J. Rod microglia: elongation, alignment, and coupling to form trains across the somatosensory cortex after experimental diffuse brain injury. *J. Neuroinflammation* 9, 247 (2012).
98. Rojas, B. *et al.* Microglia in mouse retina contralateral to experimental glaucoma exhibit multiple signs of activation in all retinal layers. *J. Neuroinflammation* 11, 133 (2014).

99. Bachstetter, A. D. *et al.* Rod-shaped microglia morphology is associated with aging in 2 human autopsy series. *Neurobiol. Aging* 52, 98–105 (2017).
100. Holloway, O. G., Canty, A. J., King, A. E. & Ziebell, J. M. Rod microglia and their role in neurological diseases. *Semin. Cell Dev. Biol.* 94, 96–103 (2019).
101. Taylor, S. E., Morganti-Kossmann, C., Lifshitz, J. & Ziebell, J. M. Rod Microglia: A Morphological Definition. *PLoS ONE* 9, e97096 (2014).
102. Streit, W., J. Microglial degeneration in the aging brain - bad news for neurons? *Front. Biosci.* 3423–38 (2008) doi:10.2741/2937.
103. Spittau, B. Aging Microglia—Phenotypes, Functions and Implications for Age-Related Neurodegenerative Diseases. *Front. Aging Neurosci.* 9, 194 (2017).
104. Streit, W. J., Sammons, N. W., Kuhns, A. J. & Sparks, D. L. Dystrophic microglia in the aging human brain. *Glia* 45, 208–212 (2004).
105. Prokop, S. *et al.* Impact of TREM2 risk variants on brain region-specific immune activation and plaque microenvironment in Alzheimer’s disease patient brain samples. *Acta Neuropathol.* 138, 613–630 (2019).
106. Streit, W. J., Xue, Q.-S., Tischer, J. & Bechmann, I. Microglial pathology. *Acta Neuropathol. Commun.* 2, 142 (2014).
107. Streit, W. J., Khoshbouei, H. & Bechmann, I. Dystrophic microglia in late-onset Alzheimer’s disease. *Glia* 68, 845–854 (2020).
108. Tischer, J. *et al.* Inhomogeneous distribution of Iba-1 characterizes microglial pathology in Alzheimer’s disease: Inhomogeneous Distribution of Iba-1 in AD. *Glia* 64, 1562–1572 (2016).
109. Soreq, L. *et al.* Major Shifts in Glial Regional Identity Are a Transcriptional Hallmark of Human Brain Aging. *Cell Rep.* 18, 557–570 (2017).
110. Sousa, A. M. M. *et al.* Molecular and cellular reorganization of neural circuits in the human lineage. *Science* 358, 1027–1032 (2017).
111. Heindl, S. *et al.* Automated Morphological Analysis of Microglia After Stroke. *Front. Cell. Neurosci.* 12, 106 (2018).
112. Masuda, T., Sankowski, R., Staszewski, O. & Prinz, M. Microglia Heterogeneity in the Single-Cell Era. *Cell Rep.* 30, 1271–1281 (2020).
113. Ito, D. *et al.* Microglia-specific localisation of a novel calcium binding protein, Iba1. *Mol. Brain Res.* 57, 1–9 (1998).
114. Lier, J., Streit, W. J. & Bechmann, I. Beyond Activation: Characterizing Microglial Functional Phenotypes. *Cells* 10, 2236 (2021).
115. Sasaki, Y., Ohsawa, K., Kanazawa, H., Kohsaka, S. & Imai, Y. Iba1 Is an Actin-Cross-Linking Protein in Macrophages/Microglia. *Biochem. Biophys. Res. Commun.* 286, 292–297 (2001).
116. Walker, D. G. & Lue, L.-F. Immune phenotypes of microglia in human neurodegenerative disease: challenges to detecting microglial polarization in human brains. *Alzheimers Res. Ther.* 7, 56 (2015).
117. Kim, Y. J., Tu, T. H., Yang, S., Kim, J. K. & Kim, J. G. Characterization of Fatty Acid Composition Underlying Hypothalamic Inflammation in Aged Mice. *Molecules* 25, 3170 (2020).
118. Leone, C. *et al.* Characterization of human monocyte-derived microglia-like cells. *Glia* 54, 183–192 (2006).
119. Köhler, C. Allograft inflammatory factor-1/Ionized calcium-binding adapter molecule 1 is specifically expressed by most subpopulations of macrophages and spermatids in testis. *Cell Tissue Res.* 330, 291–302 (2007).
120. Buckman, L. B. *et al.* Obesity induced by a high-fat diet is associated with increased immune cell entry into the central nervous system. *Brain. Behav. Immun.* 35, 33–42 (2014).
121. Schwabenland, M. *et al.* Analyzing microglial phenotypes across neuropathologies: a practical guide. *Acta Neuropathol.* 142, 923–936 (2021).
122. Zhao, Y.-Y., Yan, D.-J. & Chen, Z.-W. Role of AIF-1 in the regulation of inflammatory activation and diverse disease processes. *Cell. Immunol.* 284, 75–83 (2013).

123. Minten, C., Terry, R., Deffrasnes, C., King, N. J. C. & Campbell, I. L. IFN Regulatory Factor 8 Is a Key Constitutive Determinant of the Morphological and Molecular Properties of Microglia in the CNS. *PLoS ONE* 7, e49851 (2012).
124. Masuda, T. *et al.* IRF8 Is a Critical Transcription Factor for Transforming Microglia into a Reactive Phenotype. *Cell Rep.* 1, 334–340 (2012).
125. Masuda, T. *et al.* IRF8 is a transcriptional determinant for microglial motility. *Purinergic Signal.* 10, 515–521 (2014).
126. Kozlowski, C. & Weimer, R. M. An Automated Method to Quantify Microglia Morphology and Application to Monitor Activation State Longitudinally In Vivo. *PLoS ONE* 7, e31814 (2012).
127. Valous, N. A., Lahrmann, B., Zhou, W., Veltkamp, R. & Grabe, N. Multistage histopathological image segmentation of Iba1-stained murine microglia in a focal ischemia model: Methodological workflow and expert validation. *J. Neurosci. Methods* 213, 250–262 (2013).
128. Kongsui, R., Beynon, S. B., Johnson, S. J. & Walker, F. R. Quantitative assessment of microglial morphology and density reveals remarkable consistency in the distribution and morphology of cells within the healthy prefrontal cortex of the rat. *J. Neuroinflammation* 11, 182 (2014).
129. Rey-Villamizar, N. *et al.* Large-scale automated image analysis for computational profiling of brain tissue surrounding implanted neuroprosthetic devices using Python. *Front. Neuroinformatics* 8, (2014).
130. Johnson, S. J. & Walker, F. R. Strategies to improve quantitative assessment of immunohistochemical and immunofluorescent labelling. *Sci. Rep.* 5, 10607 (2015).
131. Zanier, E. R., Fumagalli, S., Perego, C., Pischiutta, F. & De Simoni, M.-G. Shape descriptors of the ‘never resting’ microglia in three different acute brain injury models in mice. *Intensive Care Med. Exp.* 3, 39 (2015).
132. Morrison, H., Young, K., Qureshi, M., Rowe, R. K. & Lifshitz, J. Quantitative microglia analyses reveal diverse morphologic responses in the rat cortex after diffuse brain injury. *Sci. Rep.* 7, 13211 (2017).
133. York, E. M., LeDue, J. M., Bernier, L.-P. & MacVicar, B. A. 3DMorph Automatic Analysis of Microglial Morphology in Three Dimensions from *Ex Vivo* and *In Vivo* Imaging. *eneuro* 5, ENEURO.0266-18.2018 (2018).
134. York, E. M., LeDue, J. M., Bernier, L.-P. & MacVicar, B. A. 3DMorph Automatic Analysis of Microglial Morphology in Three Dimensions from *Ex Vivo* and *In Vivo* Imaging. *eNeuro* 5, ENEURO.0266-18.2018 (2018).
135. Kyriazis, A. D. *et al.* An End-to-end System for Automatic Characterization of Iba1 Immunopositive Microglia in Whole Slide Imaging. *Neuroinformatics* 17, 373–389 (2019).
136. Fernández-Arjona, M. del M., Grondona, J. M., Granados-Durán, P., Fernández-Llebrez, P. & López-Ávalos, M. D. Microglia Morphological Categorization in a Rat Model of Neuroinflammation by Hierarchical Cluster and Principal Components Analysis. *Front. Cell. Neurosci.* 11, 235 (2017).
137. Fernández-Arjona, M. del M., Grondona, J. M., Fernández-Llebrez, P. & López-Ávalos, M. D. Microglial Morphometric Parameters Correlate With the Expression Level of IL-1 β , and Allow Identifying Different Activated Morphotypes. *Front. Cell. Neurosci.* 13, 472 (2019).
138. Döbel, I. *et al.* Maschinelles Lernen. Eine Analyse zu Kompetenzen, Forschung und Anwendung. https://www.bigdata-ai.fraunhofer.de/content/dam/bigdata/de/documents/Publikationen/Fraunhofer_Studie_ML_201809.pdf. (2018).
139. Nielsen, M. A. *Neural Networks and Deep Learning*. (Determination Press, 2015).
140. Ertel, W. *Grundkurs Künstliche Intelligenz: eine praxisorientierte Einführung*. (Springer Vieweg, 2016).
141. Yamashita, R., Nishio, M., Do, R. K. G. & Togashi, K. Convolutional neural networks: an overview and application in radiology. *Insights Imaging* 9, 611–629 (2018).
142. Wuttke, L. Künstliche Neuronale Netzwerke: Definition, Einführung, Arten und Funktion. <https://datasolut.com/neuronale-netzwerke-einfuehrung/> (2020).

143. Oei, R. W. *et al.* Convolutional neural network for cell classification using microscope images of intracellular actin networks. *PLOS ONE* 14, e0213626 (2019).
144. Dürr, O. & Sick, B. Single-Cell Phenotype Classification Using Deep Convolutional Neural Networks. *J. Biomol. Screen.* 21, 998–1003 (2016).
145. Hölter, S. M. Verhaltensphänotypisierung von Mäusen. *BIOspektrum* 23, 138–141 (2017).
146. Landmann, J. *et al.* Behavioral phenotyping of calcium channel (CACN) subunit $\alpha 2\delta 3$ knockout mice: Consequences of sensory cross-modal activation. *Behav. Brain Res.* 364, 393–402 (2019).
147. Hölter, S. M. *et al.* Tests for Anxiety-Related Behavior in Mice: Tests for Anxiety-Related Behavior. *Curr. Protoc. Mouse Biol.* 5, 291–309 (2015).
148. Cryan, J. F., Mombereau, C. & Vassout, A. The tail suspension test as a model for assessing antidepressant activity: Review of pharmacological and genetic studies in mice. *Neurosci. Biobehav. Rev.* 29, 571–625 (2005).
149. World Health Organization. Dementia. *WHO* <https://www.who.int/news-room/fact-sheets/detail/dementia> (2021).
150. Bundesministerium für Gesundheit. Ratgeber Demenz. (2021).
151. Więckowska-Gacek, A., Mietelska-Porowska, A., Wydrych, M. & Wojda, U. Western diet as a trigger of Alzheimer’s disease: From metabolic syndrome and systemic inflammation to neuroinflammation and neurodegeneration. *Ageing Res. Rev.* 70, 101397 (2021).
152. Aisen, P. S. *et al.* On the path to 2025: understanding the Alzheimer’s disease continuum. *Alzheimers Res. Ther.* 9, 60 (2017).
153. Husain, M. A., Laurent, B. & Plourde, M. APOE and Alzheimer’s Disease: From Lipid Transport to Physiopathology and Therapeutics. *Front. Neurosci.* 15, 630502 (2021).
154. Wolfe, C., Fitz, N., Nam, K., Lefterov, I. & Koldamova, R. The Role of APOE and TREM2 in Alzheimer’s Disease—Current Understanding and Perspectives. *Int. J. Mol. Sci.* 20, 81 (2018).
155. Lanfranco, M. F., Sepulveda, J., Kopetsky, G. & Rebeck, G. W. Expression and secretion of APOE isoforms in astrocytes and microglia during inflammation. *Glia* 69, 1478–1493 (2021).
156. Liu, C.-C., Kanekiyo, T., Xu, H. & Bu, G. Apolipoprotein E and Alzheimer disease: risk, mechanisms and therapy. *Nat. Rev. Neurol.* 9, 106–118 (2013).
157. Bos, M. M. *et al.* The ApoE $\epsilon 4$ Isoform: Can the Risk of Diseases be Reduced by Environmental Factors? *J. Gerontol. Ser. A* 74, 99–107 (2019).
158. Qian, J. *et al.* APOE-related risk of mild cognitive impairment and dementia for prevention trials: An analysis of four cohorts. *PLOS Med.* 14, e1002254 (2017).
159. Louwersheimer, E. *et al.* Rare Genetic Variant in SORL1 May Increase Penetrance of Alzheimer’s Disease in a Family with Several Generations of APOE- $\epsilon 4$ Homozygosity. *J. Alzheimers Dis.* 56, 63–74 (2017).
160. Riphagen, J. M. *et al.* Linking APOE- $\epsilon 4$, blood-brain barrier dysfunction, and inflammation to Alzheimer’s pathology. *Neurobiol. Aging* 85, 96–103 (2020).
161. Sullivan, P. M. Influence of Western diet and APOE genotype on Alzheimer’s disease risk. *Neurobiol. Dis.* 138, 104790 (2020).
162. Torres-Perez, E., Ledesma, M., Garcia-Sobreviela, M. P., Leon-Latre, M. & Arbones-Mainar, J. M. Apolipoprotein E4 association with metabolic syndrome depends on body fatness. *Atherosclerosis* 245, 35–42 (2016).
163. Zhao, N. *et al.* Alzheimer’s Risk Factors Age, APOE Genotype, and Sex Drive Distinct Molecular Pathways. *Neuron* 106, 727-742.e6 (2020).
164. World Health Organization. Noncommunicable diseases. *WHO* <https://www.who.int/news-room/fact-sheets/detail/noncommunicable-diseases> (2021).
165. Fontaine, K. R., Redden, D. T., Wang, C., Westfall, A. O. & Allison, D. B. Years of Life Lost Due to Obesity. *JAMA* 289, 187 (2003).
166. Prospective Studies Collaboration. Body-mass index and cause-specific mortality in 900 000 adults: collaborative analyses of 57 prospective studies. *The Lancet* 373, 1083–1096 (2009).
167. Berrington de Gonzalez, A. *et al.* Body-Mass Index and Mortality among 1.46 Million White Adults. *N. Engl. J. Med.* 363, 2211–2219 (2010).

168. Blüher, M. Obesity: global epidemiology and pathogenesis. *Nat. Rev. Endocrinol.* 15, 288–298 (2019).
169. World Health Organization. Obesity and overweight. *WHO* <https://www.who.int/news-room/fact-sheets/detail/obesity-and-overweight> (2021).
170. World Health Organization. Diabetes. *WHO* <https://www.who.int/en/news-room/fact-sheets/detail/diabetes> (2021).
171. Global BMI Mortality Collaboration *et al.* Body-mass index and all-cause mortality: individual-participant-data meta-analysis of 239 prospective studies in four continents. *Lancet Lond. Engl.* 388, 776–786 (2016).
172. The Lancet Gastroenterology & Hepatology. Obesity: another ongoing pandemic. *Lancet Gastroenterol. Hepatol.* 6, 411 (2021).
173. Bray, G. A. & Popkin, B. M. Dietary fat intake does affect obesity! *Am. J. Clin. Nutr.* 68, 1157–1173 (1998).
174. Schrauwen, P. & Westerterp, K. R. The role of high-fat diets and physical activity in the regulation of body weight. *Br. J. Nutr.* 84, 417–427 (2000).
175. Nguyen, D. M. & El-Serag, H. B. The Epidemiology of Obesity. *Gastroenterol. Clin. North Am.* 39, 1–7 (2010).
176. Chooi, Y. C., Ding, C. & Magkos, F. The epidemiology of obesity. *Metabolism* 92, 6–10 (2019).
177. George, V., Tremblay, A., Després, J. P., Leblanc, C. & Bouchard, C. Effect of dietary fat content on total and regional adiposity in men and women. *Int. J. Obes.* 14, 1085–1094 (1990).
178. Tucker, L. A. & Kano, M. J. Dietary fat and body fat: a multivariate study of 205 adult females. *Am. J. Clin. Nutr.* 56, 616–622 (1992).
179. Golay, A. & Bobbioni, E. The role of dietary fat in obesity. *Int. J. Obes. Relat. Metab. Disord. J. Int. Assoc. Study Obes.* 21 Suppl 3, S2-11 (1997).
180. Saris, W. *et al.* Randomized controlled trial of changes in dietary carbohydrate/fat ratio and simple vs complex carbohydrates on body weight and blood lipids: the CARMEN study. *Int. J. Obes.* 24, 1310–1318 (2000).
181. Frayling, T. M. *et al.* A Common Variant in the *FTO* Gene Is Associated with Body Mass Index and Predisposes to Childhood and Adult Obesity. *Science* 316, 889–894 (2007).
182. Christakis, N. A. & Fowler, J. H. The Spread of Obesity in a Large Social Network over 32 Years. *N. Engl. J. Med.* 357, 370–379 (2007).
183. Thaler, J. P. *et al.* Obesity is associated with hypothalamic injury in rodents and humans. *J. Clin. Invest.* 122, 153–162 (2012).
184. Graham, L. C. *et al.* Chronic consumption of a western diet induces robust glial activation in aging mice and in a mouse model of Alzheimer’s disease. *Sci. Rep.* 6, 21568 (2016).
185. Erny, D. *et al.* Host microbiota constantly control maturation and function of microglia in the CNS. *Nat. Neurosci.* 18, 965–977 (2015).
186. Waise, T. M. Z. *et al.* One-day high-fat diet induces inflammation in the nodose ganglion and hypothalamus of mice. *Biochem. Biophys. Res. Commun.* 464, 1157–1162 (2015).
187. Baufeld, C., Osterloh, A., Prokop, S., Miller, K. R. & Heppner, F. L. High-fat diet-induced brain region-specific phenotypic spectrum of CNS resident microglia. *Acta Neuropathol.* 132, 361–375 (2016).
188. Valdearcos, M. *et al.* Microglial Inflammatory Signaling Orchestrates the Hypothalamic Immune Response to Dietary Excess and Mediates Obesity Susceptibility. *Cell Metab.* 26, 185-197.e3 (2017).
189. Lee, C. H. *et al.* Cellular source of hypothalamic macrophage accumulation in diet-induced obesity. *J. Neuroinflammation* 16, 221 (2019).
190. Kim, J. D., Yoon, N. A., Jin, S. & Diano, S. Microglial UCP2 Mediates Inflammation and Obesity Induced by High-Fat Feeding. *Cell Metab.* 30, 952-962.e5 (2019).
191. Kanoski, S. E. & Davidson, T. L. Western diet consumption and cognitive impairment: Links to hippocampal dysfunction and obesity. *Physiol. Behav.* 103, 59–68 (2011).

192. Squire, L. R., Genzel, L., Wixted, J. T. & Morris, R. G. Memory consolidation. *Cold Spring Harb. Perspect. Biol.* 7, a021766 (2015).
193. Anacker, C. & Hen, R. Adult hippocampal neurogenesis and cognitive flexibility — linking memory and mood. *Nat. Rev. Neurosci.* 18, 335–346 (2017).
194. Yeomans, M. R. Adverse effects of consuming high fat–sugar diets on cognition: implications for understanding obesity. *Proc. Nutr. Soc.* 76, 455–465 (2017).
195. Vinuesa, A. *et al.* Early Exposure to a High-Fat Diet Impacts on Hippocampal Plasticity: Implication of Microglia-Derived Exosome-like Extracellular Vesicles. *Mol. Neurobiol.* 56, 5075–5094 (2019).
196. Lu, J. *et al.* Ursolic acid improves high fat diet-induced cognitive impairments by blocking endoplasmic reticulum stress and I κ B kinase β /nuclear factor- κ B-mediated inflammatory pathways in mice. *Brain. Behav. Immun.* 25, 1658–1667 (2011).
197. Jeon, B. T. *et al.* Resveratrol Attenuates Obesity-Associated Peripheral and Central Inflammation and Improves Memory Deficit in Mice Fed a High-Fat Diet. *Diabetes* 61, 1444–1454 (2012).
198. De Luca, S. N. *et al.* Early life overfeeding impairs spatial memory performance by reducing microglial sensitivity to learning. *J. Neuroinflammation* 13, 112 (2016).
199. Gzielo, K. *et al.* Long-Term Consumption of High-Fat Diet in Rats: Effects on Microglial and Astrocytic Morphology and Neuronal Nitric Oxide Synthase Expression. *Cell. Mol. Neurobiol.* 37, 783–789 (2017).
200. Lopes, K. O., Sparks, D. L. & Streit, W. J. Microglial dystrophy in the aged and Alzheimer’s disease brain is associated with ferritin immunoreactivity. *Glia* 56, 1048–1060 (2008).
201. Imperatore, R. *et al.* Immunohistochemical Analysis of Intestinal and Central Nervous System Morphology in an Obese Animal Model (Danio rerio) Treated with 3,5-T2: A Possible Farm Management Practice? *Animals* 10, 1131 (2020).
202. Luchsinger, J. A. *et al.* Relation of Diabetes to Mild Cognitive Impairment. *Arch. Neurol.* 64, 570 (2007).
203. Knopman, D. S. & Roberts, R. Vascular Risk Factors: Imaging and Neuropathologic Correlates. *J. Alzheimers Dis.* 20, 699–709 (2010).
204. Iadecola, C. & Davisson, R. L. Hypertension and Cerebrovascular Dysfunction. *Cell Metab.* 7, 476–484 (2008).
205. Beydoun, M. A., Beydoun, H. A. & Wang, Y. Obesity and central obesity as risk factors for incident dementia and its subtypes: a systematic review and meta-analysis. *Obes. Rev.* 9, 204–218 (2008).
206. Whitmer, R. A. *et al.* Central obesity and increased risk of dementia more than three decades later. *Neurology* 71, 1057–1064 (2008).
207. Pedditizi, E., Peters, R. & Beckett, N. The risk of overweight/obesity in mid-life and late life for the development of dementia: a systematic review and meta-analysis of longitudinal studies. *Age Ageing* 45, 14–21 (2016).
208. Armstrong, R. A. Risk factors for Alzheimer’s disease. *Folia Neuropathol.* 57, 87–105 (2019).
209. Livingston, G. *et al.* Dementia prevention, intervention, and care: 2020 report of the Lancet Commission. *The Lancet* 396, 413–446 (2020).
210. Besser, L. M. *et al.* Body Mass Index, Weight Change, and Clinical Progression in Mild Cognitive Impairment and Alzheimer Disease. *Alzheimer Dis. Assoc. Disord.* 28, 36–43 (2014).
211. Baranowski, B. J., Hayward, G. C., Fajardo, V. A. & MacPherson, R. E. K. Increased Prevalence of Obesity/Type 2 Diabetes and Lower Levels of Lithium in Rural Texas Counties May Explain Greater Alzheimer’s Disease Risk. *J. Alzheimers Dis.* 64, 303–308 (2018).
212. Baranowski, B. J., Marko, D. M., Fenech, R. K., Yang, A. J. T. & MacPherson, R. E. K. Healthy brain, healthy life: a review of diet and exercise interventions to promote brain health and reduce Alzheimer’s disease risk. *Appl. Physiol. Nutr. Metab.* 45, 1055–1065 (2020).
213. Chong, C. P., Shahar, S., Haron, H. & Din, N. C. Habitual sugar intake and cognitive impairment among multi-ethnic Malaysian older adults. *Clin. Interv. Aging* 14, 1331–1342 (2019).

214. Kivipelto, M. *et al.* Obesity and Vascular Risk Factors at Midlife and the Risk of Dementia and Alzheimer Disease. *Arch. Neurol.* 62, (2005).
215. Kivipelto, M., Mangialasche, F. & Ngandu, T. Lifestyle interventions to prevent cognitive impairment, dementia and Alzheimer disease. *Nat. Rev. Neurol.* 14, 653–666 (2018).
216. Rasmussen Eid, H. *et al.* Smoking and Obesity as Risk Factors in Frontotemporal Dementia and Alzheimer's Disease: The HUNT Study. *Dement. Geriatr. Cogn. Disord. Extra* 9, 1–10 (2019).
217. Li, X.-Y. *et al.* Midlife Modifiable Risk Factors for Dementia: A Systematic Review and Meta-analysis of 34 Prospective Cohort Studies. *Curr. Alzheimer Res.* 16, 1254–1268 (2020).
218. Sun, Z. *et al.* Late-life obesity is a protective factor for prodromal Alzheimer's disease: a longitudinal study. *Aging* 12, 2005–2017 (2020).
219. Ma, L.-Z. *et al.* Metabolically healthy obesity reduces the risk of Alzheimer's disease in elders: a longitudinal study. *Aging* 11, 10939–10951 (2019).
220. Isaac, V. *et al.* Adverse Associations between Visceral Adiposity, Brain Structure, and Cognitive Performance in Healthy Elderly. *Front. Aging Neurosci.* 3, (2011).
221. Shefer, G., Marcus, Y. & Stern, N. Is obesity a brain disease? *Neurosci. Biobehav. Rev.* 37, 2489–2503 (2013).
222. Coppin, G., Nolan-Poupart, S., Jones-Gotman, M. & Small, D. M. Working memory and reward association learning impairments in obesity. *Neuropsychologia* 65, 146–155 (2014).
223. Dye, L., Boyle, N. B., Champ, C. & Lawton, C. The relationship between obesity and cognitive health and decline. *Proc. Nutr. Soc.* 76, 443–454 (2017).
224. Espeland, M. A. *et al.* Long-term Impact of Behavioral Weight Loss Intervention on Cognitive Function. *J. Gerontol. A. Biol. Sci. Med. Sci.* 69, 1101–1108 (2014).
225. Espeland, M. A. *et al.* Long-term Impact of Weight Loss Intervention on Changes in Cognitive Function: Exploratory Analyses from the Action for Health in Diabetes Randomized Controlled Clinical Trial. *J. Gerontol. Ser. A* 73, 484–491 (2018).
226. Barron, A. M., Rosario, E. R., Elteriefi, R. & Pike, C. J. Sex-Specific Effects of High Fat Diet on Indices of Metabolic Syndrome in 3xTg-AD Mice: Implications for Alzheimer's Disease. *PLoS ONE* 8, e78554 (2013).
227. Knight, E. M., Martins, I. V. A., Gümüşgöz, S., Allan, S. M. & Lawrence, C. B. High-fat diet-induced memory impairment in triple-transgenic Alzheimer's disease (3xTgAD) mice is independent of changes in amyloid and tau pathology. *Neurobiol. Aging* 35, 1821–1832 (2014).
228. Niu, L. *et al.* A high-sugar high-fat diet induced metabolic syndrome shows some symptoms of Alzheimer's disease in rats. *J. Nutr. Health Aging* 20, 509–513 (2016).
229. Haleem, D. J. & Mahmood, K. Brain serotonin in high-fat diet-induced weight gain, anxiety and spatial memory in rats. *Nutr. Neurosci.* 24, 226–235 (2021).
230. Nissankara Rao, L. S., Kilari, E. K. & Kola, P. K. Protective effect of *Curcuma amada* acetone extract against high-fat and high-sugar diet-induced obesity and memory impairment. *Nutr. Neurosci.* 24, 212–225 (2021).
231. Więckowska-Gacek, A. *et al.* Western Diet Induces Impairment of Liver-Brain Axis Accelerating Neuroinflammation and Amyloid Pathology in Alzheimer's Disease. *Front. Aging Neurosci.* 13, 654509 (2021).
232. Molteni, R., Barnard, R. J., Ying, Z., Roberts, C. K. & Gómez-Pinilla, F. A high-fat, refined sugar diet reduces hippocampal brain-derived neurotrophic factor, neuronal plasticity, and learning. *Neuroscience* 112, 803–814 (2002).
233. Wu, A., Molteni, R., Ying, Z. & Gomez-Pinilla, F. A saturated-fat diet aggravates the outcome of traumatic brain injury on hippocampal plasticity and cognitive function by reducing brain-derived neurotrophic factor. *Neuroscience* 119, 365–375 (2003).
234. Goldbart, A. D. *et al.* High fat/refined carbohydrate diet enhances the susceptibility to spatial learning deficits in rats exposed to intermittent hypoxia. *Brain Res.* 1090, 190–196 (2006).
235. Stranahan, A. M. *et al.* Diet-induced insulin resistance impairs hippocampal synaptic plasticity and cognition in middle-aged rats. *Hippocampus* 18, 1085–1088 (2008).

236. Murray, A. J. *et al.* Deterioration of physical performance and cognitive function in rats with short-term high-fat feeding. *FASEB J.* 23, 4353–4360 (2009).
237. Beilharz, J. E., Maniam, J. & Morris, M. J. Short exposure to a diet rich in both fat and sugar or sugar alone impairs place, but not object recognition memory in rats. *Brain. Behav. Immun.* 37, 134–141 (2014).
238. Beilharz, J. E., Kaakoush, N. O., Maniam, J. & Morris, M. J. The effect of short-term exposure to energy-matched diets enriched in fat or sugar on memory, gut microbiota and markers of brain inflammation and plasticity. *Brain. Behav. Immun.* 57, 304–313 (2016).
239. Hargrave, S. L., Davidson, T. L., Zheng, W. & Kinzig, K. P. Western diets induce blood-brain barrier leakage and alter spatial strategies in rats. *Behav. Neurosci.* 130, 123–135 (2016).
240. Spencer, S. J., Korosi, A., Layé, S., Shukitt-Hale, B. & Barrientos, R. M. Food for thought: how nutrition impacts cognition and emotion. *Npj Sci. Food* 1, 7 (2017).
241. Khazen, T., Hatoum, O. A., Ferreira, G. & Maroun, M. Acute exposure to a high-fat diet in juvenile male rats disrupts hippocampal-dependent memory and plasticity through glucocorticoids. *Sci. Rep.* 9, 12270 (2019).
242. Yaseen, A., Shrivastava, K., Zuri, Z., Hatoum, O. A. & Maroun, M. Prefrontal Oxytocin is Involved in Impairments in Prefrontal Plasticity and Social Memory Following Acute Exposure to High Fat Diet in Juvenile Animals. *Cereb. Cortex* 29, 1900–1909 (2019).
243. Valladolid-Acebes, I. *et al.* Spatial memory impairment and changes in hippocampal morphology are triggered by high-fat diets in adolescent mice. Is there a role of leptin? *Neurobiol. Learn. Mem.* 106, 18–25 (2013).
244. Boitard, C. *et al.* Impairment of hippocampal-dependent memory induced by juvenile high-fat diet intake is associated with enhanced hippocampal inflammation in rats. *Brain. Behav. Immun.* 40, 9–17 (2014).
245. Vinuesa, A. *et al.* Juvenile exposure to a high fat diet promotes behavioral and limbic alterations in the absence of obesity. *Psychoneuroendocrinology* 72, 22–33 (2016).
246. Leigh, S.-J. & Morris, M. J. Diet, inflammation and the gut microbiome: Mechanisms for obesity-associated cognitive impairment. *Biochim. Biophys. Acta BBA - Mol. Basis Dis.* 1866, 165767 (2020).
247. Duthel, S., Ota, K. T., Wohleb, E. S., Rasmussen, K. & Duman, R. S. High-Fat Diet Induced Anxiety and Anhedonia: Impact on Brain Homeostasis and Inflammation. *Neuropsychopharmacology* 41, 1874–1887 (2016).
248. Cavaliere, G. *et al.* High-Fat Diet Induces Neuroinflammation and Mitochondrial Impairment in Mice Cerebral Cortex and Synaptic Fraction. *Front. Cell. Neurosci.* 13, (2019).
249. Chen, T.-J., Chen, S.-S., Wang, D.-C. & Hung, H.-S. High-fat diet reduces novelty-induced expression of activity-regulated cytoskeleton-associated protein. *J. Cell. Physiol.* 235, 1065–1075 (2020).
250. Guillemot-Legris, O. & Muccioli, G. G. Obesity-Induced Neuroinflammation: Beyond the Hypothalamus. *Trends Neurosci.* 40, 237–253 (2017).
251. Khan, M. S. H. & Hegde, V. Obesity and Diabetes Mediated Chronic Inflammation: A Potential Biomarker in Alzheimer's Disease. *J. Pers. Med.* 10, 42 (2020).
252. Kanasaki, K. & Koya, D. Biology of Obesity: Lessons from Animal Models of Obesity. *J. Biomed. Biotechnol.* 2011, 1–11 (2011).
253. Ingalls, A. M., Dickie, M. M. & Snell, G. D. Obese, a new mutation in the house mouse*. *J. Hered.* 41, 317–318 (1950).
254. Gao, Y. *et al.* Hormones and diet, but not body weight, control hypothalamic microglial activity: Hypothalamic Microglia in Obesity. *Glia* 62, 17–25 (2014).
255. Lee, A., Cardel, M. & Donahoo, W. T. Social and Environmental Factors Influencing Obesity. in *Endotext* (eds. Feingold, K. R. *et al.*) (MDText.com, Inc., 2000).
256. Mathieu, P., Poirier, P., Pibarot, P., Lemieux, I. & Després, J.-P. Visceral Obesity. *Hypertension* 53, 577–584 (2009).

257. Neth, B. J. & Craft, S. Insulin Resistance and Alzheimer's Disease: Bioenergetic Linkages. *Front. Aging Neurosci.* 9, (2017).
258. Jones, N. S., Watson, K. Q. & Rebeck, G. W. Metabolic Disturbances of a High-Fat Diet Are Dependent on APOE Genotype and Sex. *eNeuro* 6, (2019).
259. Bojková, B., Winklewski, P. J. & Wszedybyl-Winklewska, M. Dietary Fat and Cancer—Which Is Good, Which Is Bad, and the Body of Evidence. *Int. J. Mol. Sci.* 21, 4114 (2020).
260. Bloor, I. D. & Symonds, M. E. Sexual dimorphism in white and brown adipose tissue with obesity and inflammation. *Horm. Behav.* 66, 95–103 (2014).
261. Bradl, M. & Lassmann, H. Oligodendrocytes: biology and pathology. *Acta Neuropathol.* 119, 37–53 (2010).
262. Sofroniew, M. V. & Vinters, H. V. Astrocytes: biology and pathology. *Acta Neuropathol.* 119, 7–35 (2010).
263. del Zoppo, G. J. Inflammation and the neurovascular unit in the setting of focal cerebral ischemia. *Neuroscience* 158, 972–982 (2009).
264. Härtig, W. *et al.* Damaged Neocortical Perineuronal Nets Due to Experimental Focal Cerebral Ischemia in Mice, Rats and Sheep. *Front. Integr. Neurosci.* 11, 15 (2017).
265. Zhang, S. Microglial activation after ischaemic stroke. *Stroke Vasc. Neurol.* 4, 71–74 (2019).

6. Darstellung des eigenen wissenschaftlichen Beitrags

Hiermit erkläre ich, dass die unten genannten Darstellungen des eigenen Beitrags für die Publikationen von mir erbracht wurden.


Publikation: Leyh J*, Paeschke S*, Mages B, Michalski D, Nowicki M, Bechmann I, Winter K. Classification of Microglial Morphological Phenotypes Using Machine Learning. Front Cell Neurosci. 2021 Jun 29;15:701673. doi: 10.3389/fncel.2021.701673. PMID: 34267628; PMCID: PMC8276040.

* These authors have contributed equally to this work and share first authorship.

Beitrag des Promovenden:


- Mitkonzipierung und Durchführung der Experimente
- Entnahme von Gewebeproben und Aufarbeitung von Proben der C57BL/6J-Mäuse
- Anfertigung immunhistochemischer Färbungen von Hirngewebe der C57BL/6J-Mäuse
- Manuelle Klassifizierung der mikroglialen Zellen
- Erstellung von Abbildungen und Tabellen
- Statistische Auswertung der Daten
- Verfassen des Manuskriptes und Mitarbeit bei späterer Überarbeitung

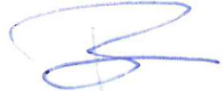
Folgende Personen bestätigen die Richtigkeit meiner Darstellung des eigenen Beitrags:

Korrespondierender Autor/Seniorautor: 
Dr. rer. hum. Karsten Winter

Ko-Erstautor: 
M. Sc. Sabine Paeschke

Ausgewählte Ko-Autoren: 
Dr. rer. med. Bianca Mages


PD Dr. Marcin Nowicki


Prof. Dr. med. Ingo Bechmann

Publikation: Leyh J, Winter K, Reinicke M, Ceglarek U, Bechmann I, Landmann J. Long-term diet-induced obesity does not lead to learning and memory impairment in adult mice. PLoS One. 2021 Sep 29;16(9):e0257921. doi: 10.1371/journal.pone.0257921. PMID: 34587222; PMCID: PMC8480843.

Beitrag des Promovenden:

- Mitkonzipierung und Durchführung der Experimente
- Entnahme von Gewebeproben und Aufarbeitung der Proben für die angewendeten Methoden
- Planung und Auswertung der Verhaltenstests
- Durchführung und Auswertung folgender Methoden:
 - Immunhistochemische Färbungen
 - Immunfluoreszenzfärbungen
 - RT-qPCR
- Erstellung (konfokal-) mikroskopischer Aufnahmen
- Erstellung von Abbildungen und Tabellen
- Statistische Auswertung der Daten
- Verfassen des Manuskriptes und Mitarbeit bei späterer Überarbeitung

Folgende Personen bestätigen die Richtigkeit meiner Darstellung des eigenen Beitrags:

Korrespondierender Autor/Seniorautor:



Dr. rer. med. Julia Landmann

Ko-Autoren:



Dr. rer. hum. Karsten Winter



Dr. rer. nat. Madlen Reinicke



Prof. Dr. rer. nat. Uta Ceglarek



Prof. Dr. med. Ingo Bechmann

Ort, Datum

Judith Leyh

7. Erklärung über die eigenständige Abfassung der Arbeit

Hiermit erkläre ich, dass ich die vorliegende Arbeit selbstständig und ohne unzulässige Hilfe oder Benutzung anderer als der angegebenen Hilfsmittel angefertigt habe. Ich versichere, dass Dritte von mir weder unmittelbar noch mittelbar eine Vergütung oder geldwerte Leistungen für Arbeiten erhalten haben, die im Zusammenhang mit dem Inhalt der vorgelegten Dissertation stehen, und dass die vorgelegte Arbeit weder im Inland noch im Ausland in gleicher oder ähnlicher Form einer anderen Prüfungsbehörde zum Zweck einer Promotion oder eines anderen Prüfungsverfahrens vorgelegt wurde. Alles aus anderen Quellen und von anderen Personen übernommene Material, das in der Arbeit verwendet wurde oder auf welches direkt Bezug genommen wird, wurde als solches kenntlich gemacht. Insbesondere wurden alle Personen genannt, die direkt an der Entstehung der vorliegenden Arbeit beteiligt waren. Die aktuellen gesetzlichen Vorgaben in Bezug auf die Zulassung der klinischen Studien, die Bestimmungen des Tierschutzgesetzes, die Bestimmungen des Gentechnikgesetzes und die allgemeinen Datenschutzbestimmungen wurden eingehalten. Ich versichere, dass ich die Regelungen der Satzung der Universität Leipzig zur Sicherung guter wissenschaftlicher Praxis kenne und eingehalten habe.

Ort, Datum

Judith Leyh

9. Publikationsliste

Reinicke M, **Leyh J**, Zimmermann S, Chey S, Brkovic IB, Wassermann C, Landmann J, Lütjohann D, Isermann B, Bechmann I, Ceglarek U. Plant Sterol-Poor Diet Is Associated with Pro-Inflammatory Lipid Mediators in the Murine Brain. *Int J Mol Sci*. 2021 Dec 8;22(24):13207. doi: 10.3390/ijms222413207. PMID: 34948003; PMCID: PMC8707069.

Leyh J, Winter K, Reinicke M, Ceglarek U, Bechmann I, Landmann J. Long-term diet-induced obesity does not lead to learning and memory impairment in adult mice. *PLoS One*. 2021 Sep 29;16(9):e0257921. doi: 10.1371/journal.pone.0257921. PMID: 34587222; PMCID: PMC8480843.

Leyh J*, Paeschke S*, Mages B, Michalski D, Nowicki M, Bechmann I, Winter K. Classification of Microglial Morphological Phenotypes Using Machine Learning. *Front Cell Neurosci*. 2021 Jun 29;15:701673. doi: 10.3389/fncel.2021.701673. PMID: 34267628; PMCID: PMC8276040.

*These authors have contributed equally to this work and share first authorship.

Reinicke M, Dorow J, Bischof K, **Leyh J**, Bechmann I, Ceglarek U. Tissue pretreatment for LC-MS/MS analysis of PUFA and eicosanoid distribution in mouse brain and liver. *Anal Bioanal Chem*. 2020 Apr;412(10):2211-2223. doi: 10.1007/s00216-019-02170-w. Epub 2019 Dec 21. PMID: 31865417; PMCID: PMC7118053.

Streit WJ, Braak H, Del Tredici K, **Leyh J**, Lier J, Khoshbouei H, Eisenlöffel C, Müller W, Bechmann I. Microglial activation occurs late during preclinical Alzheimer's disease. *Glia*. 2018 Dec;66(12):2550-2562. doi: 10.1002/glia.23510. Epub 2018 Nov 11. PMID: 30417428.

10. Danksagung

An dieser Stelle möchte ich nachstehenden Personen meinen großen Dank entgegenbringen, ohne deren Mithilfe diese Dissertation niemals zustande gekommen wäre.

Mein besonderer Dank gilt meinem Betreuer und Doktorvater, Prof. Dr. Ingo Bechmann, für die Überlassung des Themas der vorliegenden Arbeit, seine wissenschaftliche Expertise, seine konstruktive Kritik und seine Ermutigung.

Insbesondere danken möchte ich Dr. Karsten Winter für die produktiven und lehrreichen Gespräche, seine wissenschaftlichen Anregungen sowie für seine anschaulichen, laienverständlichen Erläuterungen informatischer und statistischer Gegebenheiten und damit für seinen essentiellen Beitrag zu beiden Publikationen.

Großer Dank gilt Dr. Julia Landmann, die mich methodisch unterstützte und mir mit viel Rat und Motivation zur Seite stand. Für ihren Beitrag zur zweiten Publikation trotz Mutterschutz und Elternzeit danke ich ihr sehr.

Ferner möchte ich den technischen Mitarbeitern des anatomischen Instituts für ihre hervorragende technische Unterstützung und für angenehme Stunden im Labor danken. Besonderer Dank gilt Angela Ehrlich, Constance Hobusch und Andreas Horn, die mir immer helfend und mit aufmunternden Worten beistanden.

Ich danke allen Ko-Autoren für die Realisierung der Projekte und allen Mitarbeitern der Anatomie für die Unterstützung während der letzten Jahre.

Susann Hähnel, Dr. Nicole Kaiser, Beatrice Böhme und Dr. Elke Brylla danke ich von Herzen, nicht nur für das sehr hilfreiche Korrekturlesen, ihre kritischen Betrachtungen und differenzierten Anmerkungen, sondern ausdrücklich für die bleibenden Gespräche und Momente abseits von Labor und Wissenschaft.

Schließlich möchte ich meinen Freunden, meiner Familie, meinen Eltern und insbesondere meinem Freund für ihre unermüdliche Unterstützung, ihre Geduld, ihre Zusprüche und ihr großes Verständnis ein riesengroßes Dankeschön aussprechen. Sie sind der Schlüssel zur Fertigstellung dieser Doktorarbeit, die sonst niemals in diesem Zeitrahmen und in dieser Qualität hätte fertiggestellt werden können.